MONASH University

Rheology and Linear Dichroism of Dilute Solutions of Flexible and Semiflexible Polymers in Shear Flow

Isaac Pincus

Doctor of Philosophy

A Thesis Submitted for the Degree of Doctor of Philosophy at
Monash University in 2022
Department of Chemical and Biological Engineering

To my parents, Nena and Simon, for their unending support

and

to my friends at Monash, who made my PhD years all the more enjoyable

Copyright notice

Abstract

Although the non-equilibrium behaviour of polymer solutions is generally well understood, particularly in extensional flow, there remain several unanswered questions for dilute solutions in simple shear flow, and full parameter-free, quantitative agreement with experiments has not been achieved. For example, experimental viscosity data exhibit qualitative differences in shear-thinning exponents, shear rate for onset of shear-thinning and high-shear Newtonian plateaus depending on polymer semiflexibility, contour length and solvent quality. While polymer models are able to incorporate all of these effects through various spring force laws, bending potentials, excluded volume (EV) potentials, and hydrodynamic interaction (HI), the inclusion of each piece of physics has not been systematically matched to experimentally observed behaviour. Furthermore, attempts to develop multiscale models which can make quantitative predictions are hindered by the lack of ability to fully match the results of bead-rod models, often used to represent a polymer chain at the Kuhn step level, with bead-spring models, which take into account the entropic elasticity. In light of these difficulties, this work aims to develop a general model based on the so-called FENE-Fraenkel spring, originally formulated by Larson and coworkers (Hsieh et al., 2006, J. Chem. Phys., 124(4)), which can span the range from rigid rod to traditional entropic spring, as well as include a bending potential, EV and HI. As we show, this model can reproduce, and smoothly move between, a wide range of previously observed polymer solution rheology in shear flow. Further, by showing that one can correctly capture the solvent quality for semiflexible polymer models using Yamakawa's Quasi-Two-Parameter (QTP) theory, we develop a successive-fine-graining scheme for predicting polymer rheology and conformation, particularly focusing on correctly capturing the experimentally measured Linear Dichroism (LD) for semiflexible polymers. Following the approach of earlier authors, our multiscale model can be used to relate the dichroism of each segment in our bead-spring chain to the extension of the spring, giving quantitative agreement with experimental LD data.

Declaration

This thesis is an original work of my research and contains no material which has been accepted for the award of any other degree or diploma at any university or equivalent institution and that, to the best of my knowledge and belief, this thesis contains no material previously published or written by another person, except where due reference is made in the text of the thesis.

Signature: _____

Print Name: Isaac Pincus

Date: _____

Publications during enrolment

Journal publications:

1) Isaac Pincus, Alison Rodger and J. Ravi Prakash, *Viscometric functions and rheo-optical properties of dilute polymer solutions: Comparison of FENE-Fraenkel dumbbells with rodlike models*, **Journal of Non-Newtonian Fluid Mechanics**, 2020, 285, 104395.

2) Isaac Pincus, Alison Rodger and J. Ravi Prakash, *Dilute polymer solutions under shear flow: comprehensive qualitative analysis using a bead-spring chain model with a FENE-Fraenkel spring*, submitted to **Journal of Rheology** (under review). Preprint can be found on arXiv at https://doi.org/10.48550/arXiv.2206.01870.

3) Isaac Pincus and J. Ravi Prakash, *Successive fine graining of semiflexible polymers using quasi-two-parameter theory.* (In preparation).

4) Isaac Pincus, Alison Rodger and J. Ravi Prakash, *Quantitative prediction of DNA flow dichroism through multiscale polymer modelling.* (In preparation).

Conference presentations:

1) Isaac Pincus, Alison Rodger and J. Ravi Prakash, *Viscometric functions and rheo-optical properties of dilute polymer solutions: Comparison of FENE-Fraenkel dumbbells with rodlike models*, **Statistical Mechanics of Soft Matter Meeting**, 16-17 December, 2019, Adelaide, Australia.

2) Isaac Pincus, Alison Rodger and J. Ravi Prakash, *Qualitative rheology of dilute solutions of flexible and semiflexible polymers*, **18th International Congress on Rheology**, 12-17 December, 2020, Rio De Janeiro, Brazil (virtual attendance).

Acknowledgements

I would firstly like to thank my supervisor, Prof. Ravi Jagadeeshan, to whom I wish to extend my deepest gratitude for accepting me as a student and guiding me through my PhD research. I have not only learnt an enormous amount and grown as a scientist and chemical engineer, but have always felt valued, supported and encouraged as part of Prof. Ravi's research group. Our technical discussions were always enlightening, whether it was about my own research, how to most effectively learn and apply prior work, or even undergraduate teaching and laboratories. I also very much enjoyed our discussion of non-technical topics, with group meetings often continuing beyond the scheduled end time as we talked about politics, current events and anecdotes about research and life as an academic. Prof. Ravi has been an exceptional supervisor and it has been a privilege to study under him. Without him, my PhD would not have been nearly as productive or enjoyable as it was.

I would also like to thank my co-supervisor, Prof. Alison Rodger, who helped me to apply my research to experimental problems, and always offered a fresh perspective. It was wonderful to be able to discuss not only the rheological work that made up the bulk of my thesis, but also learn about optics and spectroscopy, and how my research could be applied in those fields. Prof. Alison was endlessly supportive, for which I am very grateful. Prof. Peter Daivis and Assoc. Prof. Rico Tabor provided excellent feedback at each of my milestones, including detailed notes on my reports, as well as several important technical suggestions. Additionally, Prof. Burkhard Dünweg provided helpful early guidance, and some of the key insights for my second chapter were developed during his visit to Monash in 2019.

I'd particularly like to thank my colleagues and friends in the Molecular Rheology Group, including Aritra, Kailash, Kiran, Silpa and Nick. Their contributions are evident in many places throughout my thesis in the form of shared algorithms and code, discussions of theory, and suggestions for analysing or interpreting data. I'm also grateful to all my friends at Monash and in Melbourne, who made my time away from my desk a lot of fun, an in particular my roommates and fellow PhD students during the COVID-19 months, Ed and Nathan. I also had wonderful support from the staff in the Department of Chemical and Biological Engineering, in particular Lilyanne Price, Tracy Groves and Laura McManus, who not only helped with administrative matters but were instrumental in helping setup and run department student conferences.

This research was supported by an Australian Government Research Training Program (RTP) Scholarship. I also take this opportunity to acknowledge computer time grants from the National Computational Infrastructure (NCI), as well as the High-Performance Computing Facility team at Monash University, who provided access to the MonARCH and MASSIVE supercomputing clusters, as well as technical support.

Contents

List of Figures

Chapter 1

Introduction

This thesis research seeks to develop polymer physics models which can predict the Linear Dichroism (LD) of a semiflexible macromolecule in shear flow, which many authors have previously studied [1–8]. LD is the polarisation-dependent absorption of light by an ensemble of oriented molecules, such that

$$\mathrm{LD} = A_{\parallel} - A_{\perp} \tag{1.1}$$

where $A_{\parallel}$ and $A_{\perp}$ represent the absorption of light polarised in perpendicular directions relative to some laboratory axis (the $\parallel$ direction). Sample orientation can be achieved in a variety of ways [9]. In this work, the focus is on shear orientation in a Couette cell, in which the sample is placed in solution and sheared between concentric cylinders. Couette flow LD has a fairly significant disadvantage, namely that sample orientation under shear flow is both imperfect and configurationally complex due to the combination of rotational and elongational velocity components. Thus, data interpretation is often restricted to being qualitative or semi-quantitative, and attempts to calculate the orientation parameter have been either crude approximations or limited to rigid rods [2, 3]. If this difficulty could be overcome and sample orientations determined for a particular macromolecular sample at a particular shear rate, it would be possible to considerably improve the quantitative accuracy of LD spectroscopy analysis [9, 10]. Since a full analytical theory for the conformation of a flexible polymer chain in shear flow is infeasible, these treatments have previously relied on approximations regarding the chain connectivity, perturbation due to shear flow, and physical effects such as solvent-polymer interactions and hydrodynamic forces on beads [4, 11, 12]. Recent advances in modelling of dilute polymer solutions, most notably the development and refinement of simulation methods such as Brownian dynamics (BD), allow one to avoid many of the earlier approximations [13]. It is now possible to qualitatively recover much of the key behaviour of polymers in shear flows (although quantitative predictions remain challenging), and even obtain quantitative, parameter-free predictions in extensional flows [12, 14–16].

Prediction of LD presents something of a challenge compared to prediction of polymer solution material properties such as e.g. viscosity. This is because it is the interaction of light with the individual chromophores in a given macromolecule which leads to the LD, not the overall stresses or conformation of the chain. One must be able to capture not only the large-scale structure of the polymer in flow, but also the average orientation of the individual monomers along the chain backbone. Additionally, available LD data generally span an extremely wide range of macromolecule sizes; for example, Simonson and Kubista measured the flow LD of DNA fragments from 300 base pairs (bp) to 164 kbp [17]. This problem requires multiscale modelling, since it is computationally intractable to simply scale up a model which is capable of representing a 300 base pair DNA fragment to the level of tens or even hundreds of thousands of base pairs. While models of this sort have been developed [18–21], they have not been applied directly to prediction of properties in shear flow. Furthermore, it is somewhat unclear, when using these models, how one would properly include the polymer-solvent interactions, namely the hydrodynamic interactions and excluded volume, which are known to be important effects [11, 12].

Despite the maturity of the field of polymer solution modelling, there still remain several unanswered questions regarding the qualitative behaviour of polymer solutions in shear flow [12, 22]. One key difficulty is correctly describing the change in viscosity as shear rate is increased, for which experiments and simulations give confusingly varied results [12, 22]. For example, changes in polymer molecular weight, backbone semiflexibility and sovlent-polymer interactions contribute to differences in shear-thinning exponents, shear rates for onset of shear-thinning, and appearance of a high-shear plateau. On the other hand, simulated and theoretical models show considerable differences in behaviour depending on the type of bead-bead connection (rod or spring), inclusion of hydrodynamic interactions (HI) or excluded volume effects (EV), as well as use of a bending potential. Clearly, it would be useful to have a single model which can span the entire range of previously-modelled behaviour, in order to systematically investigate the effects of each piece of added physics. Not only would this allow for improved qualitative understanding of experimental behaviour, but it would also aid in development of multiscale modelling approaches at different levels of polymer coarse-graining.

This thesis studies these issues; in particular, the quantitative prediction of LD for DNA molecules, as well as the qualitative behaviour of polymer models in shear flow. Our method involves applying Brownian dynamics (BD) simulation techniques to a bead-spring-chain polymer model with a judiciously chosen spring force law, a bending potential to model semiflexibility, as well as hydrodynamic interactions (HI) and excluded volume forces (EV) between the beads. Specifically, the key object of our investigation is the so-called FENE-Fraenkel spring force law, first introduced by Larson and coworkers as a way of reproducing the behaviour of a bead-rod chain [23]. This force law has the useful property that it is not only able to model a rigid rod, but also, through proper choice of parameters, behave identically to a traditional

FENE spring, which has been widely used in the literature as a coarse-grained model for extremely long polymer chains [11, 12, 14, 16]. Therefore, the FENE-Fraenkel spring is useful as a tool to bridge the gap between different modelling scales, being able to both shed light on the qualitative differences in behaviour between bead-spring and bead-rod models in shear flow, as well as, in theory, model a real polymer segment of arbitrary length.

The thesis is organised as follows. In Chapter 2, we describe the properties of the FENE-Fraenkel dumbbell, focusing on the crossover between bead-spring and bead-rod behaviour. We also show how it is possible to use the FENE-Fraenkel dumbbell to match experimental measurements of the properties of short, rigid polymers, such as the viscosity of PBLG and the LD of M13 bacteriophage. In Chapter 3, we extend this model to chains with multiple springs, showing how one can reproduce the full range of previously-observed experimental and theoretical behaviour via the FENE-Fraenkel spring as well as a bending potential, HI and EV. Chapter 4 discusses the proper choice of HI and EV parameters in a polymer model when a bending potential is included. Specifically, we use the method of successive fine graining (SFG, originally developed by Prakash and coworkers [14, 16]) as well as Yamakawa's quasi-two-parameter theory (QTP) in order to obtain a correct measure of solvent quality as the underlying bending stiffness of the model is altered. In Chapter 5, a multi-scale model is developed which can quantitatively predict the experimental DNA flow LD data of Simonson and Kubista [17]. Importantly, we show how one can draw upon the earlier theories of Wilson and Schellman [1, 2] in order to match the extension of individual springs in our model to the overall measured dichroism. Finally, the key conclusions are summarised in Chapter 6, along with a brief discussion of potential future avenues to extend this research.

Chapter 2

Rheology of FENE-Fraenkel Dumbbells and Comparison with Rodlike Models

2.1 Introduction

While both bead-rod and bead-spring models are able to successfully predict certain rheological properties of polymer chains in dilute solution, their relative usefulness continues to be debated. This debate began with the theoretical finding by Kramers [24] that the equilibrium distribution of the included angle of a trimer differs depending on whether the monomer links are represented as constrained rods or infinitely stiff springs (the reason for which is discussed by Van Kampen [25] and Lodder *et al.* [26]). It is often argued that true constraints do not exist in nature and therefore stiff springs should be preferred, but in fact the form of the spring potential can also affect the included angle, such that a quantum mechanical treatment appears to be necessary for a fully correct solution given a real polymer [25, 27]. Nevertheless, the practical difference is small, as both models yield results in qualitative agreement with experimental studies [11, 28], while direct quantitative comparisons are sparse for bead-rod chains [12, 22].

Some of the most stark differences between predictions of bead-rod and bead-spring models arise for dilute polymer solutions in shear flow, as described by Pan et al. [22]. For example, there is no clear consensus on the shear-thinning exponent of the viscosity with shear rate for high molecular weight polymers. Some experimental studies using viscometers show a $-(2/3)$ power law scaling in the viscosity of high molecular weight flexible polymers under shear flow, followed by a high-shear Newtonian viscosity plateau [29]. Other studies of single fluorescently stained DNA molecules show a power law decay of viscosity with shear rate,

with a shear thinning exponent around -0.54 [30, 31]. Confusingly, bead-spring and bead-rod models each show different aspects of this experimental behaviour, depending on whether effects such as finite extensibility, chain flexibility, hydrodynamic interactions or excluded volume are included.

Early calculations by Stewart and Sorensen [32] for a rigid dumbbell with hydrodynamic interactions included found an eventual $-(1/3)$ power law scaling in the viscosity with shear rate after an initial Newtonian plateau. Using a similar method for FENE dumbbells without hydrodynamic interactions, Fan [33] found a shear-thinning exponent of -0.607, while the analytical pre-averaged FENE-P dumbbell model gives an asymptotic exponent of $-(2/3)$ [34]. These dumbbell models cannot reproduce the high-shear second Newtonian plateau. For moderate-length (20 to 100 bead) bead-rod chains without hydrodynamic interactions, an exponent of $-(1/2)$ was found[35, 36] (which appears to change to -0.3 as hydrodynamic interactions are included [37]), along with a second Newtonian plateau at high shear. However, in the presence of both hydrodynamic and excluded volume interactions, Petera and Muthukumar found no high-shear Newtonian viscosity plateau [37]. For finitely extensible bead-spring chains with hydrodynamic interactions and excluded volume, there is an intermediate $-(1/2)$ power law regime, followed by a $-(2/3)$ [38] or -0.61 [31] exponent at very high shear rates. Clearly, although both the bead-spring and bead-rod models purport to represent the physics of the same underlying polymer, there are fundamental differences in the high-shear viscosity scaling.

Additionally, rods exhibit an instantaneous stress jump at the inception of flow (which is also found in experimental studies [39]) arising from the viscous fourth-order contribution to the stress tensor [34, 36, 40]. Bead-spring models do not contain this term for any form of the spring force law, so that additional physics in the form of a parallel dissipative dashpot is needed to produce an instantaneous stress jump [41–43].

In general, it is unclear whether these differences between bead-rod and bead-spring models arise due to the form of the spring force law, the effects of rigid constraints, or additional physics such as excluded volume or hydrodynamic interactions [22]. These differences are difficult to investigate systematically, as there is currently no model which can represent the full range of possible parameters. For example, the FENE and Marko-Siggia WLC force laws are used to coarse-grain many Kuhn lengths of a polymer chain into a single bead-spring segment, and so are physically unrealistic or unusable as representations of short, rigid, inextensible sections of chain. While spring force laws have been developed which can be used at the level of a single Kuhn segment [18, 21], they go smoothly to zero force at low extensions, rather than having a ‘negative’ force which opposes compression and keeps the spring length constrained as for a rod. A model with a non-zero natural length, such as the Fraenkel force law, is able to approximate a rigid chain segment in the high-stiffness limit, but its strictly linear behaviour

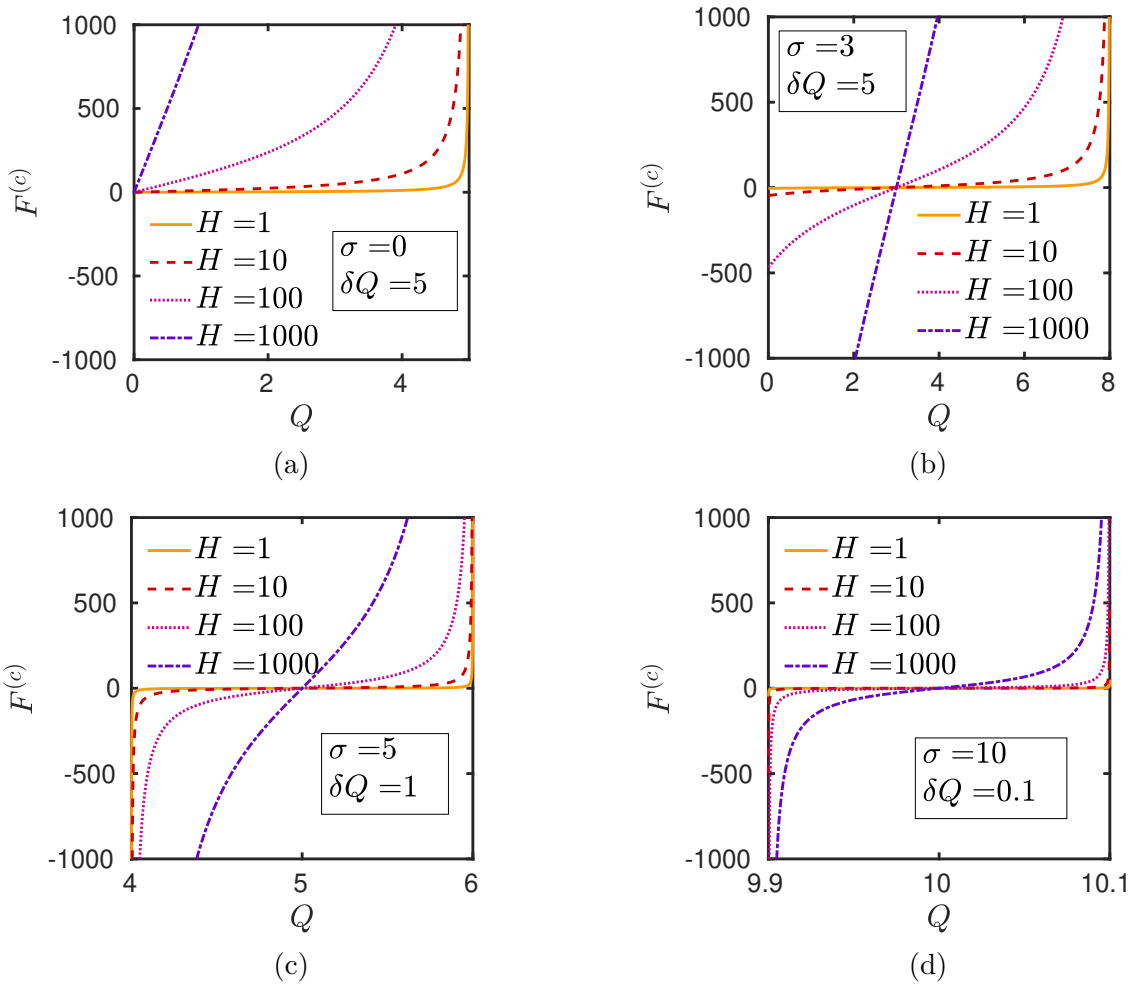

FIGURE 2.1: Visualisation of the spring force for a FENE-Fraenkel spring with varying values of spring stiffness H, natural length σ and extensibility δQ. The force is linear around $Q = \sigma$, but quickly approaches $\pm\infty$ as $Q \to Q \pm \delta Q$. (a) Corresponds to the limit of a FENE spring. (b) $\delta Q > \sigma > 0$, leading to a negative, but not infinite force for $Q < \sigma$. (c) Approximate limit of a Fraenkel spring for large δQ. (d) Large σ and small δQ leads to tightly constrained Q and hence approximation of inextensible rod.

means it cannot model a finitely extensible section of chain. By developing a spring force law which can represent both a stiff, inextensible rod, as well as a finitely extensible entropic spring, it may be possible to directly examine many of the observed differences which arise when using either a bead-rod or bead-spring model of a flexible polymer molecule.

The so-called FENE-Fraenkel spring force law [23] may be viable as a way to model both rods and entropic springs, as well as the crossover between the two. For this spring, the force between connected beads at a given extension Q (where the bead-bead vector is denoted by $\boldsymbol{Q}$) is

$$\boldsymbol{F}^{(c)} = \frac{H(Q-\sigma)}{1-(Q-\sigma)^2/(\delta Q)^2}\frac{\boldsymbol{Q}}{Q} \tag{2.1}$$

where $\boldsymbol{F}^{(c)}$ is the force vector between the beads, σ is the natural length of the spring ($Q = \sigma$

in the absence of any additional forces), δQ is the maximum extensibility around σ, and H is the spring stiffness. By examining Figure 2.1, we can see that the spring length (Q) will never extend more than a distance $\pm\delta Q$ from the 'natural' length $Q = \sigma$. In addition, the spring is approximately linear close to $Q = \sigma$. Note that we can recover the FENE force law by setting $\sigma = 0$, in which case we can identify that $\delta Q \equiv Q_0$, where Q_0 is the maxmimum extensibility of the FENE spring, as displayed in Figure 2.1 (a). When σ is further increased such that $\delta Q > \sigma > 0$, the spring behaves similarly to a FENE spring at large extensions but has a non-zero rest length and a negative, but not divergent force at $Q < \sigma$, as seen in Figure 2.1 (b). Furthermore, in the limit that $\delta Q \to \infty$, we recover the Fraenkel spring, as can be seen approximately in Figure 2.1 (c). Finally, setting $\delta Q \to \infty$ and $\sigma = 0$ gives the simple Hookean spring. In order to simulate a rod, a large σ and small δQ can be used as in Figure 2.1 (d), such that the spring length is constrained to lie between the two limits with a divergent force at $Q = \sigma \pm \delta Q$, leading to an approximation of an inextensible rod. An alternative explanation of the various limits of the FENE-Fraenkel spring, as well as comparison with the Marko-Siggia worm-like-chain force law [44], is given in Section 3.2.1 and Figure 3.4.

The FENE-Fraenkel spring was first introduced by Larson and coworkers [23] as a way to mimic a freely jointed bead-rod chain without the significant computational complexities associated with constrained Brownian dynamics simulations necessitated by the use of a rod as connector between beads. They were able to show that the free-draining material properties of a FENE-Fraenkel spring chain match those of a bead-rod chain in shear and extensional flow with reduced CPU time when the spring parameters are chosen appropriately, namely with sufficiently high H and low δQ. However, when hydrodynamic interactions were included, there were differences in the shear rate dependent viscosity between the bead-rod chain and bead-FENE-Fraenkel spring chain [11]. Since there are no analytical results for rods or springs with this model and flow geometry, it was unclear whether the differences were due to simulation artefacts, or whether the differences were intrinsic to the models. Later in Chapter 3, we will see that this apparent disagreement is likely due to either large statistical error bars in the bead-rod results, or incorrectly chosen FENE-Fraenkel spring parameters and simulation timestep. Additionally, Larson and coworkers only used the FENE-Fraenkel spring as a way to represent a rod, and did not explicitly explore the crossover between a spring and a rod.

In the current work, the properties of a simple dumbbell connected via a FENE-Fraenkel spring will be examined, which can be used to address several of the open questions mentioned above. Specifically, we investigate whether a stiff and inextensible FENE-Fraenkel spring can be used as a replacement for a rod in shear flow in terms of material property scaling with shear rate, the stress jump, and failure to adhere to the stress-optical law. Since the full distribution function of a bead-rod dumbbell with HI can be determined semi-analytically in shear flow [32, 34], simulations can be compared with exact results. Once similarities between bead-spring and bead-rod dumbbells are established, the differences induced by altering spring stiffness and

extensibility can be systematically examined, eventually converging on the FENE, Fraenkel and Hookean spring limits.

There are also a variety of experimental results for the viscosity of rigid molecules with high aspect ratios, such as poly(γ-benzyl L-glutamate) [45] and tobacco mosaic virus [46], for which the rigid-rod model has been shown to be qualitatively and reasonably quantitatively accurate (for example, see Fig. 14.4 in [34] or Fig. 5 in [47]). These filamentous molecules with contour lengths on the order of persistence length have traditionally been modelled as rods [48], while they do in fact exhibit some flexibility and finite extensibility about their equilibrium end-to-end distance. The form of the FENE-Fraenkel spring force law allows for investigation of the independent effects of spring stiffness, natural length and extensibility through variation of H, σ and δQ, such that it may be a better qualitative model of the extensibility of these molecules compared to rigid rod models. However, note that the FENE-Fraenkel spring is not being developed in this chapter as an actual physical model of a length of semiflexible polymer chain, as the form of the FENE-Fraenkel force law cannot accurately reproduce either the high-extension or high-compression behaviour of a short section of a wormlike chain [49], and chain bending is not accounted for. Note that in Chapter 5, we are indeed able to include a bending potential into our model, such that a FENE-Fraenkel bead-spring chain with a bending potential between the beads can be used as an accurate model of a DNA chain of arbitrary length.

Besides viscometric functions and rheo-optical properties derived from the stress and gyration tensors, the predicted linear dichroism (LD) of the dumbbell ensemble is computed. Linear dichroism refers to the difference in absorption of parallel and perpendicularly polarised light by an oriented ensemble of molecules, and can be used to investigate the structure and interaction of large, flexible macromolecules which are hard to characterise using traditional techniques such as crystallography or NMR. As an analytic technique, LD may be useful for high-throughput screening of potential drug targets to DNA or cytoskeletal proteins [9], however difficulty in predicting the orientation of large, flexible molecules inhibits its quantitative accuracy [3]. Since the LD signal is related to molecular orientation, it provides a useful experimental test of models of polymer behaviour in flow, and these models may in turn be crucial for future progress in improving the LD technique. To our knowledge, our current work represents the first direct comparison of a BD simulation with experimental LD data, although BD appears to have been used both to compute orientation of semiflexible chains for comparison with LD data [8], and also to interpret previous experimental data for LD of biomolecules in lipid membranes [50]. Additionally, the semi-analytical rod models used in this chapter have previously been applied to rigid bacteriophage LD by McLachlan et al. [3].

This chapter is split into 3 further sections. In section 2, we set up the theoretical treatment of both bead-spring and bead-rod dumbbells which will inform simulations and describe our

methods for numerically evaluating the distribution functions. In section 3, we discuss our simulation results, particularly highlighting the comparison between bead-rod and bead-spring dumbbell material functions. Finally, we conclude with the key findings of our work and future plans for bead-FENE-Fraenkel-spring-chain simulations.

2.2 Methods

2.2.1 Governing Equations for Dumbbell Models

The general dumbbell model consists of two massless beads of radius a, connected by either a spring, or a rod with length L. We describe the co-ordinates of the two beads by $\boldsymbol{r}_1$ and $\boldsymbol{r}_2$, with the connector vector between the beads given by $\boldsymbol{Q} = \boldsymbol{r}_2 - \boldsymbol{r}_1$. For a rod, this vector can be simplified as $\boldsymbol{Q} = L\boldsymbol{u}$, where $\boldsymbol{u}$ is the radial unit vector in spherical coordinates. For a spring, the unit vector in the direction of the spring is $\boldsymbol{u} = \boldsymbol{Q}/Q$, where Q is the dumbbell length.

The dumbbell is suspended in an incompressible Newtonian solvent of viscosity η_s, with a velocity field imposed by shear flow expressed in the form:

$$\boldsymbol{v}(\boldsymbol{r}, t) = \boldsymbol{v}_0(t) + \boldsymbol{\kappa}(t) \cdot \boldsymbol{r} \tag{2.2}$$

Here $\boldsymbol{r}$ is a position given with respect to a fixed reference frame (the laboratory frame), $\boldsymbol{v}_0$ is a position-invariant vector and $\boldsymbol{\kappa}(t)$ is a tensor given by the transpose of the velocity field gradient, which is also position-invariant. Both $\boldsymbol{v}_0$ and $\boldsymbol{\kappa}$ can in general be a function of time.

If we include hydrodynamic interactions in the form of a diffusion tensor $\boldsymbol{\Omega}$ (which we have chosen as the Rotne-Prager-Yamakawa tensor), then the differential equation for the time evolution of the bead-spring dumbbell connector vector distribution function $\psi = \psi(t, \boldsymbol{Q})$ is given by the following Fokker-Planck equation [34]:

$$\frac{\partial \psi^*_{\mathrm{H}}}{\partial t^*_{\mathrm{H}}} = -\frac{\partial}{\partial \boldsymbol{Q}^*_{\mathrm{H}}} \cdot \left\{ \boldsymbol{\kappa}^*_{\mathrm{H}} \cdot \boldsymbol{Q}^*_{\mathrm{H}} - (\boldsymbol{\delta} - \zeta\boldsymbol{\Omega}) \cdot \frac{1}{2}\boldsymbol{F}^{*(c)}_{\mathrm{H}} \right\} \psi^*_{\mathrm{H}} + \frac{1}{2}\frac{\partial}{\partial \boldsymbol{Q}^*_{\mathrm{H}}}\frac{\partial}{\partial \boldsymbol{Q}^*_{\mathrm{H}}} : [\boldsymbol{\delta} - \zeta\boldsymbol{\Omega}]\psi^*_{\mathrm{H}} \tag{2.3}$$

where $\boldsymbol{\delta}$ denotes the unit tensor and length, time and force variables have been re-scaled in terms of 'Hookean' units respectively, such that

$$l_{\mathrm{H}} \equiv \sqrt{\frac{k_{\mathrm{B}}T}{H}}, \lambda_{\mathrm{H}} \equiv \frac{\zeta}{4H}, F_{\mathrm{H}} \equiv \sqrt{k_{\mathrm{B}}TH} \tag{2.4}$$

and non-dimensional variables are denoted with a star superscript, such as $Q^*_{\mathrm{H}} = Q/l_{\mathrm{H}}$ or $t^*_{\mathrm{H}} = t/\lambda_{\mathrm{H}}$. The friction coefficient ζ is equivalent to that for a sphere in Stokes flow, so that

$\zeta = 6\pi\eta_s a$. It is also possible to use another system for non-dimensionalising our simulations and results, which we denote the 'rodlike' unit system and identify:

$$l_{\mathrm{R}} \equiv \sigma, \lambda_R \equiv \frac{\sigma^2\zeta}{k_{\mathrm{B}}T}, F_R \equiv \frac{k_{\mathrm{B}}T}{\sigma} \tag{2.5}$$

Note that in this unit system, the rodlike FENE-Fraenkel spring stiffness is given by $H^*_R = H\sigma^2/k_{\mathrm{B}}T$. This system is commonly used for bead-rod models, with rod length L instead of natural length σ in Equation 2.5 above. Since the times, length and forces are scaled in the same way between FENE-Fraenkel springs and rods in this unit system, we can compare results directly between these two models without having to convert back to dimensional form.

It is fairly straightforward to convert between the 'rodlike' and 'Hookean' unit systems via substitution, for example for lengths we have

$$Q^*_{\mathrm{H}} = \frac{Q}{l_{\mathrm{H}}} = \frac{Q}{\sqrt{k_{\mathrm{B}}T/H}} = Q^*_{\mathrm{R}}\sigma \cdot \sqrt{\frac{k_{\mathrm{B}}TH^*_{\mathrm{R}}}{k_{\mathrm{B}}T\sigma^2}} = Q^*_{\mathrm{R}}\sqrt{H^*_{\mathrm{R}}} \tag{2.6}$$

$$Q^*_{\mathrm{R}} = \frac{Q}{\sigma} = \frac{Q^*_{\mathrm{H}}\sqrt{k_{\mathrm{B}}T/H}}{\sigma^*_{\mathrm{H}}\sqrt{k_{\mathrm{B}}T/H}} = \frac{Q^*_{\mathrm{H}}}{\sigma^*_{\mathrm{H}}} \tag{2.7}$$

and for times we have

$$t^*_H = \frac{t}{\lambda_H} = t^*_R\frac{4H}{\zeta}\frac{\sigma^2\zeta}{k_{\mathrm{B}}T} = 4H^*_R t^*_R \tag{2.8a}$$

$$t^*_R = \frac{t}{\lambda_R} = t^*_H\frac{\zeta}{4H}\frac{k_{\mathrm{B}}T}{\sigma^2\zeta} = \frac{1}{4{\sigma^*_H}^2}t^*_H \tag{2.8b}$$

Finally, we also define rodlike and Hookean hydrodynamic interaction parameters h^*_H and h^*_R, which are essentially dimensionless bead radii, as:

$$h^*_H = \frac{a}{\sqrt{\pi}l_H} \equiv \frac{a^*_H}{\sqrt{\pi}} \tag{2.9a}$$

$$h^*_R = \frac{3a}{4\sigma} \equiv \frac{3a^*_R}{4} \tag{2.9b}$$

This implies that $h^*_H = 4/3h^*_R\sqrt{H^*_R/\pi}$, or equivalently that $h^*_R = 3/4h^*_H\sqrt{\pi/\sigma^*_H}$.

The Fokker-Planck Equation 2.3 can be expressed as an equivalent stochastic differential equation via Itô's calculus [13], which is then integrated over thousands to millions of trajectories using a semi-implicit predictor-corrector scheme. This numerical scheme has been detailed by other authors for both FENE [51–53] as well as FENE-Fraenkel [23] springs. A full description of the derivation of distribution functions and numerical integration procedures used here for both the FENE-Fraenkel bead-spring dumbbell and rodlike models can be found in Appendices A.1 and A.2. A given FENE-Fraenkel dumbbell simulation for a single trajectory therefore requires specification of two dimensionless spring parameters, either σ^*_H and δQ^*_H for Hookean

units or H_R^* and δQ_R^* for rodlike units; the timestep Δt_H^* or Δt_R^*, with the conversion between the two influenced by the choice of spring parameters as per Equation 2.8; the flow field $\boldsymbol{\kappa}_H^*$ or $\boldsymbol{\kappa}_R^*$, which varies with inverse time and therefore follows similar scaling to that in Equation 2.8; and finally the hydrodynamic interaction parameter h_R^* or h_H^*, which again are proportional to each other based on the spring parameters as per Equation 2.9. To ensure sufficient sampling for low error, the ensemble of dumbbells was allowed to reach steady-state, and then data was collected for tens to hundreds of relaxation times. Ensemble size was generally of order 10^6 to 10^8 dumbbells.

The rodlike distribution function is solved semi-analytically via a harmonic expansion, as was originally done by Stewart and Sorensen [32]. This method was extended to include RPY HI between beads as per Bird *et al.* [34], and to solve for the transient distribution function as detailed by McLachlan and coworkers [3]. Note that the same solution method can be used for a variety of rodlike models which have the same general form of the diffusion equation, such as multibead-rods, prolate spheroids and slender bodies. A full description of the semi-analytical solution method used here can be found in Appendix A.1.2.

2.2.2 Measured Quantities

Viscometric properties of the solution are calculated using the Kramers form of the stress tensor [34]. For springs, this tensor has the form

$$\boldsymbol{\tau}_p = \boldsymbol{\tau} + \eta_s \dot{\boldsymbol{\gamma}} = -n\langle \boldsymbol{QF} \rangle + nk_{\mathrm{B}}T\boldsymbol{\delta} \tag{2.10}$$

where $\boldsymbol{\delta}$ is the unit tensor, η_s is the solvent viscosity and $\boldsymbol{\tau}_p$ is the polymer contribution to the stress tensor. For rods, the stress tensor is given by

$$\boldsymbol{\tau}_p = -3nkT\langle \boldsymbol{uu} \rangle - nkT\lambda\{\boldsymbol{\kappa} : \langle \boldsymbol{uuuu} \rangle\} + nkT\boldsymbol{\delta} \tag{2.11}$$

where λ is a time constant which varies with the specific rod model and form of HI [34]. The viscosity η_p, first and second normal stress differences Ψ_1 and Ψ_2 and an angle χ_τ characterising the tensor orientation can be calculated using this stress tensor. In shear flow, these quantities have the form:

$$-\eta_p = \frac{\tau_{xy}}{\dot{\gamma}} \tag{2.12a}$$

$$-\Psi_1 = \frac{\tau_{xx} - \tau_{yy}}{\dot{\gamma}^2} \tag{2.12b}$$

$$-\Psi_2 = \frac{\tau_{yy} - \tau_{zz}}{\dot{\gamma}^2} \tag{2.12c}$$

$$\chi_\tau = \frac{1}{2}\arctan\frac{2\tau_{xy}}{\tau_{xx} - \tau_{yy}} = \frac{1}{2}\arctan\frac{2\eta_p}{\Psi_1\dot{\gamma}} \tag{2.13}$$

A similar characteristic angle χ_G can be found for the second moment $\langle \boldsymbol{QQ} \rangle$:

$$\chi_G = \frac{1}{2} \arctan \frac{2\langle Q_{xy} \rangle}{\langle Q_{xx} - Q_{yy} \rangle} \tag{2.14}$$

where $Q_{mn} \equiv Q_m Q_n$.

While χ_G and χ_τ are equal at equilibrium, they may differ in the presence of flow. Since the χ_G parameter is related to the measured optical birefringence through the refractive index tensor [54, 55], while the χ_τ parameter gives the orientation of the stress tensor, when χ_G and χ_τ are not equal, the stress optical rule will not hold. The stress optical rule is generally found to hold for small extensions of high molecular weight, highly extensible polymers, but does not hold for dilute solutions of rigid rods [55].

In addition to these viscometric functions, the predicted orientation parameter S of the ensemble will also be measured. For shear flow along the x-axis, the S-parameter is defined as [3, 56]:

$$S = \frac{1}{2}\Big[3\langle \cos^2 \theta_s \rangle - 1\Big] \tag{2.15}$$

where θ_s is the angle between the flow direction and the molecular orientation axis, such that in this case $\cos\theta_s = \boldsymbol{\delta}_x \cdot \boldsymbol{u}$ where $\boldsymbol{\delta}_x$ is the unit vector in the x-direction.

The S-parameter is proportional to the measured Linear Dichroism (LD) of a sample. The LD of a sample arises from the transition dipole moment of its constituent molecules, which will absorb light polarised parallel to the moment vector but does not interact with light polarised perpendicularly [9, 56]. The molecular chemistry determines the direction of the transition dipole moment at a particular wavelength and can often be determined a-priori [56]. Shear flow in a Couette cell is commonly used as an orientation method for LD, since it is relatively easy to measure the absorbance of a sample in a cell and only small volumes of sample are needed [3, 9].

In general, the overall LD signal of an oriented sample can be separated into two contributions, one from the angle the transition dipole moment makes with the molecular axis (α) and one from the average orientation of the molecules (S):

$$\frac{LD}{A_{\text{iso}}} = LD_{\text{r}} = \frac{3}{2} S(3\cos^2\alpha - 1) \tag{2.16}$$

where A_{iso} is the isotropic absorbance of the sample (prior to orientation). Therefore, by using experimental shear flow LD data for dilute solutions of rodlike or semi-flexible macromolecules for which α is known, the S-parameter can be extracted and compared against S predictions from polymer models.

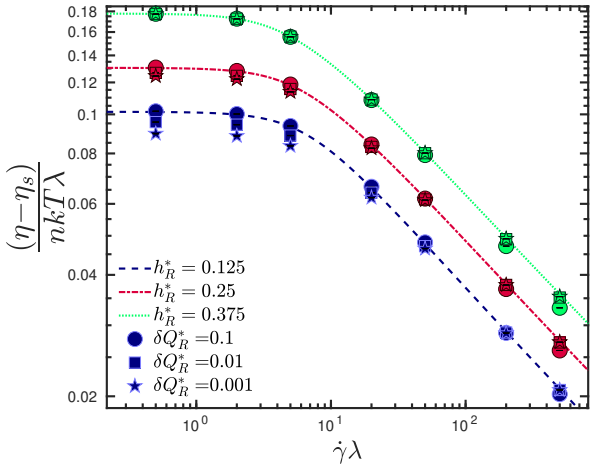

FIGURE 2.2: Comparison of FENE-Fraenkel dumbbell viscosity with bead-rod dumbbell viscosity at a range of shear rate values showing deviations at small h^* and δQ_R^*. Coloured lines are rodlike results at 3 different values of h_{R}^*. Symbol colour represents value of the HI parameter h_{R}^*, while symbol shape denotes different values of the extensibility δQ_{R}^*. Error bars are smaller than symbol size.

In order to reduce error bars on measured quantities, variance reduction has been used in some of the simulation results reported here. This involves simulating a second ensemble of dumbbells at equilibrium, each of which is matched with the non-equilibrium simulation by using the same random numbers for each pair [13]. When material functions are measured for the ensemble in flow, values from the equilibrium ensemble are individually subtracted from their matched dumbbell in flow, which serves to eliminate noise while keeping the same average value.

2.3 Results and Discussion

2.3.1 Code Validation

The semi-analytical solution for the rodlike distribution function was computed using MATLAB ODE solvers. The results were compared with those of Stewart and Sorensen [32] as well as McLachlan *et al.* [3] and found to be identical.

Since there is no previous work on FENE-Fraenkel dumbbells against which to compare results, the code was validated against the expected equilibrium distribution, as well as viscometric functions of FENE dumbbells from Kailasham *et al.* [43], who used the same semi-implicit predictor corrector method with a cubic polynomial solver and RPY HI. The results are identical to within error. Further details of these comparisons and graphs of results are given in Appendix A.3.

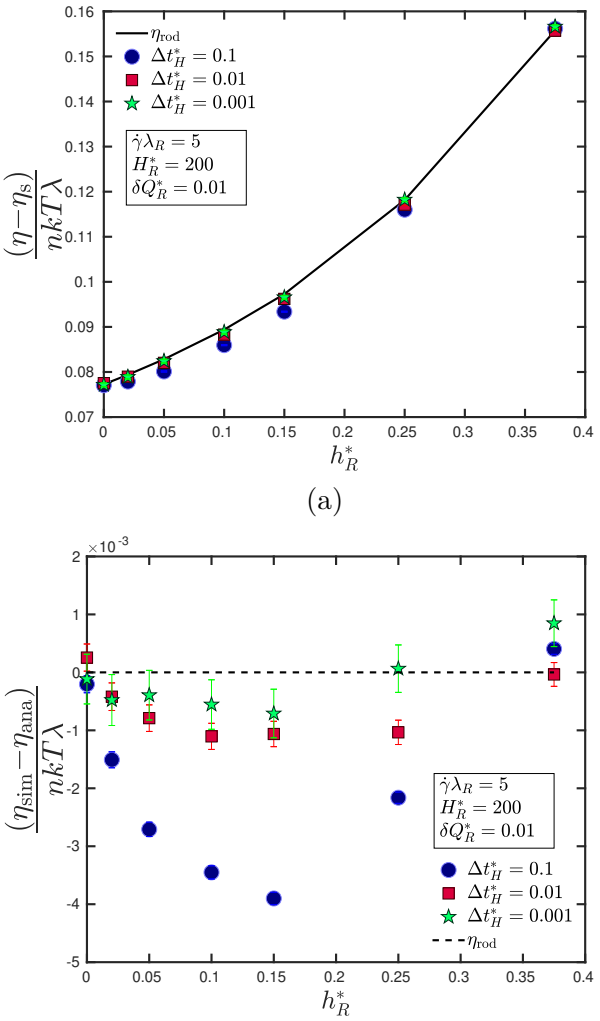

FIGURE 2.3: Timestep convergence as h_R^* is varied at low δQ_R^*. Plot (a) shows simulated FENE-Fraenkel viscosity for three different Δt compared with bead-rod viscosity at the same shear rate. Plot (b) shows difference between FENE-Fraenkel and bead-rod viscosity at the same timestep values, and with the same parameters. Where not displayed, error bars are smaller than symbol size.

However, there is a subtle timestep convergence issue which appears at only certain values of the hydrodynamic interaction parameter h^*. As seen in Figure 2.2, the low-shear viscosity appears nearly identical (and equal to the bead-rod value) at all values of the extensibility δQ_R^* for $h_R^* = 0.375$, but for $h_R^* = 0.125$, the zero-shear viscosity of the FENE-Fraenkel spring appears to deviate further from the bead-rod result with decreasing extensibility, which is a counter-intuitive result.

All simulations used to generate Figure 2.2 used the same $\Delta t_H^* = 0.2$ (equivalently $\Delta t_R^* = 0.00025$), which was small enough to ensure timestep convergence for $h_R^* = 0.375$. However, as can be seen in Figure 2.3, timestep convergence actually varies considerably and non-monotonically with the value of h^*. Specifically, at $h_R^* = 0$ and $h_R^* = 0.375$ (representing no HI or osculating beads respectively), a change from $\Delta t_H^* = 0.1$ to $\Delta t_H^* = 0.001$ makes very

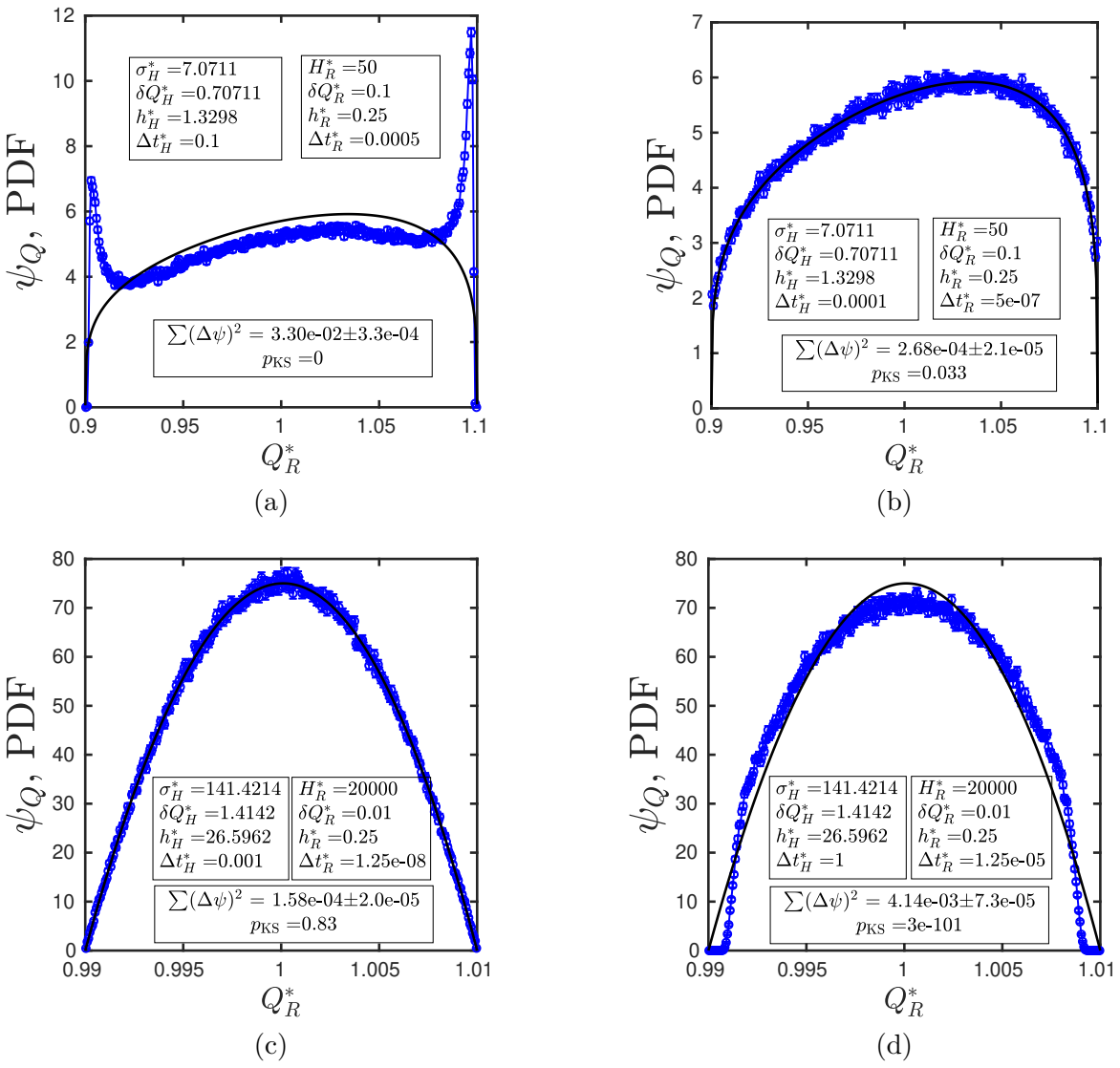

FIGURE 2.4: Examples of distribution functions at several timestep values. The black line represents the analytical probability distribution function, while the blue circles ● are binned dumbbell length frequencies from BD simulations. Error bars assume a Poisson distribution for each bin. Spring parameters are displayed in both rodlike and Hookean units. Summed squared error between the analytical and simulated distribution functions ($\sum(\Delta\psi)^2$, see Eq. (31) in S.I. for expression) is displayed for each plot. The p_{KS} value is the p-value for a Kolmogorov-Smirnov hypothesis test, with the null hypothesis that the two distributions are the same (high p_{KS} implies a closer match).

little difference to the measured viscosity, while for $h_R^* = 0.15$, the viscosity varies significantly. While one might expect that this is due to some numerical error at intermediate h^*, comparison of the simulated probability distribution function of dumbbell lengths $\psi(Q)$ at equilibrium with the analytical result seems to suggest that the convergence at low and high h^* is a simple coincidence, as will be shown below.

Figure 2.4 gives some examples of these distribution function plots. The sum of squared differences between the simulated and analytical distributions is denoted by $\sum(\Delta\psi)^2$ (the precise

definition of which is given in Equation A.31), while the p_{KS} value reported in the figure is the p-value for a Kolmogorov-Smirnov hypothesis test, with the null hypothesis that the two distributions are the same. High p_{KS} implies a closer match (details are given in Appendix A.3.2). Figures 2.4 (a) and (c) are not converged, with a $p_{\mathrm{KS}} < 0.01$, while Figures 2.4 (b) and (d) are converged (based on $p_{\mathrm{KS}} > 0.01$). By examining these distribution function plots for a range of possible FENE-Fraenkel spring parameters and timestep widths, it appears that convergence depends primarily upon the balance between δQ_H^* and Δt_H^*, with other parameters playing a minor role (Note that in non-dimensional form, the FENE-Fraenkel spring is characterised by two parameters, as can be seen by manipulating Equation 2.1 with Equation 2.6, and so δQ_R^* and δQ_H^* are sufficient to fully characterise the spring force). This can be seen clearly in Figure 2.5, which plots the summed difference for a wide range of FENE-Fraenkel springs and timestep widths. From Figure 2.5 (a) with constant Δt_H^* and varied h_R^*, δQ_H^* and δQ_R^*, it's clear that for a particular timestep, the δQ_H^* value is by far the most impactful parameter, with h_R^* and δQ_R^* having only minor effects. Figure 2.5 (b) then plots the timestep convergence for constant h_R^*, showing a levelling off of the summed difference at low Δt_H^*.

The conclusion is that we can be reasonably certain of equilibrium timestep convergence of the distribution functions if we choose a sufficiently small Δt_H^* given a particular δQ_H^*, with other parameters being relatively unimportant. Figure 2.6 quantifies this relationship, giving the approximate Δt_H^* required for $p_{\mathrm{KS}} > 0.01$ in the Kolmogorov-Smirnov test such that the simulated distribution is the same as the analytical distribution at a particular value of δQ_H^*. A Δt_H^* larger than that in the figure may give unpredictable results, as evidenced by Figure 2.3. Note, however, that a value of Δt_H^* smaller than that in Figure 2.6 is necessary but not sufficient to guarantee convergence away from equilibrium. Particularly at very high shear rates, a smaller Δt_H^* may be required.

Notably, this issue may be the reason Larson and coworkers [23] were unable to reproduce the zero-shear viscosity of a bead-rod model with a FENE-Fraenkel spring when HI is included, since they used $\delta Q_H^* < 0.1$ and $\Delta t_H^* = 4$, which appears too large to ensure timestep convergence on the distribution functions. It would be worth revisiting the problem for the bead-spring-chain to determine if this is the case (and in fact this has been done in Chapter 3).

2.3.2 Comparison of Rodlike Models with FENE-Fraenkel Dumbbell

One of the key aims of using the FENE-Fraenkel spring is to reproduce the rheological behaviour of a rigid rod. In this section the material properties of a rigid dumbbell are compared to those of a FENE-Fraenkel-spring dumbbell simulated using BD. In general, the rodlike system of non-dimensionalisation is adopted for the FENE-Fraenkel dumbbell results, which enables direct comparisons between bead-spring and bead-rod results without normalisation

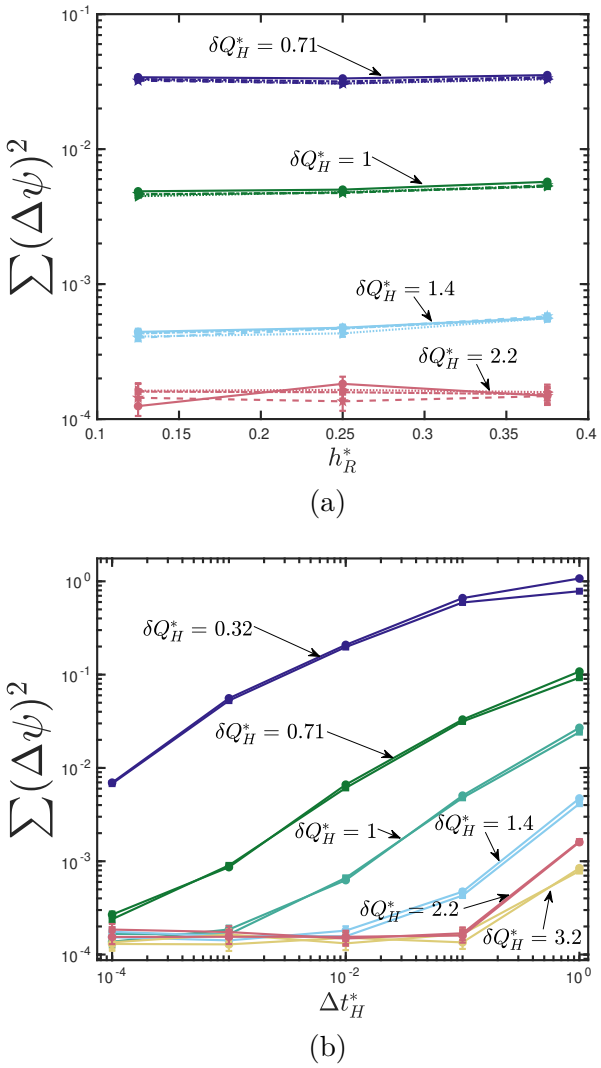

FIGURE 2.5: Changes in summed differences between simulated and analytical distribution functions (as seen in Figure 2.4) with FENE-Fraenkel spring simulation parameters. In both plots colour represents δQ_H^* value, as labelled. (a) Δt_H^* is held fixed at 0.1, with full lines for $\delta Q_R^* = 0.1$, dot-dashed lines for $\delta Q_R^* = 0.05$, dashed lines for $\delta Q_R^* = 0.02$, and dotted lines for $\delta Q_R^* = 0.01$. (b) h_R^* is held fixed at 0.25, with circle symbols for $\delta Q_R^* = 0.1$ and square symbols for $\delta Q_R^* = 0.01$. Where not displayed, error bars are smaller than symbol size.

or re-scaling of variables. Note that the spring stiffness and extensibility δQ_R^* and H_R^* are chosen such that $\delta Q_H^* = \sqrt{2}$ or $\sqrt{5}$ (i.e. $\delta Q_H^* > 1$), so that when $\Delta t_H^* < 10^{-2}$ the underlying length distribution function is timestep converged. These choices of δQ_H^* give a reasonable balance between required computational time and accuracy with respect to reproducing bead-rod results. The effects of varying δQ, H and σ systematically will be investigated in later sections.

In the following discussion, the term 'accuracy' is used to refer to how well the FENE-Fraenkel spring reproduces the bead-rod results. For example, a lower spring extensibility is said to give a more accurate viscosity than a spring with higher extensibility if the simulated viscosity is closer to the bead-rod viscosity for the lower extensibility.

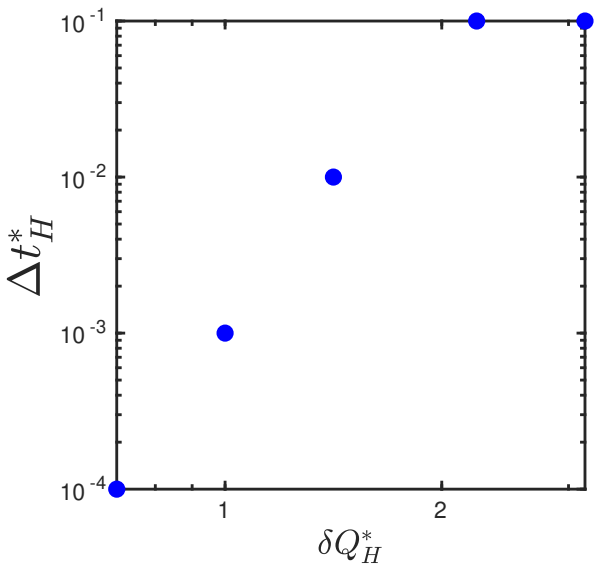

FIGURE 2.6: Effect of δQ_H^* on the Δt_H^* required for convergence of the BD distribution function to the analytical result at equilibrium based on a Kolmogorov-Smirnov test. This is based only on the five Δt values used in Figure 2.5 (b), such that the value plotted in this figure is the highest Δt_H^* in the set $\{10^{-4}, 10^{-3}, \ldots, 1\}$ for which $p_{\mathrm{KS}} < 0.01$. For example, a FENE-Fraenkel spring with $\delta Q_H^* = 1$ should have a timestep Δt_H^* no larger than 10^{-3} for distribution function convergence.

2.3.2.1 Stress Jump

Comparing the expression for the stress tensor of bead-rod dumbbells in Equation 2.11 with that of bead-spring dumbbells in Equation 2.10, both expressions share a term which varies with $\langle \boldsymbol{uu} \rangle$, since $\boldsymbol{Q}$ and $\boldsymbol{F}$ are both directed along $\boldsymbol{u}$. If flow is switched on at $t = 0$, this term must be isotropic (i.e. equal to the unit tensor $\boldsymbol{\delta}$) at $t \leq 0$, since the dumbbells will be in their equilibrium configuration prior to flow and at the first instant. Therefore, the off-diagonal elements of the stress tensor must be uniformly 0 at the inception of flow for any form of the spring potential. On the other hand, the stress tensor for the rod contains an additional term, $\{\boldsymbol{\kappa} : \langle \boldsymbol{uuuu} \rangle\}$, often referred to as the 'viscous' contribution to the stress tensor [36], which scales with the flow tensor and the fourth power of the dumbbell orientation. As this term has non-zero cross-terms (i.e. $\{\boldsymbol{\kappa} : \langle \boldsymbol{uuuu} \rangle\}_{x,y} \neq 0$) for an equilibrium $\psi(\boldsymbol{u})$, the viscosity of a rod is non-zero at $t = 0$, giving an instantaneous 'stress jump' at the inception of shear flow. This seems to be a fundamental difference between unconstrained bead-spring and constrained bead-rod models.

In spite of the absence of this term for FENE-Fraenkel springs, they were found to exhibit a 'pseudo-stress-jump', with an extremely rapid rise in viscosity to match that of bead-rod dumbbells at the inception of flow. Figure 2.7 shows BD simulation results for the transient behaviour of FENE-Fraenkel springs as flow is switched on. The sets of parameters used in Figure 2.7 all lead to an asymptotic convergence to the bead-rod results on a timescale which is a small fraction of the total time to reach steady-state (steady state is reached at $t \approx 0.25\lambda_R$

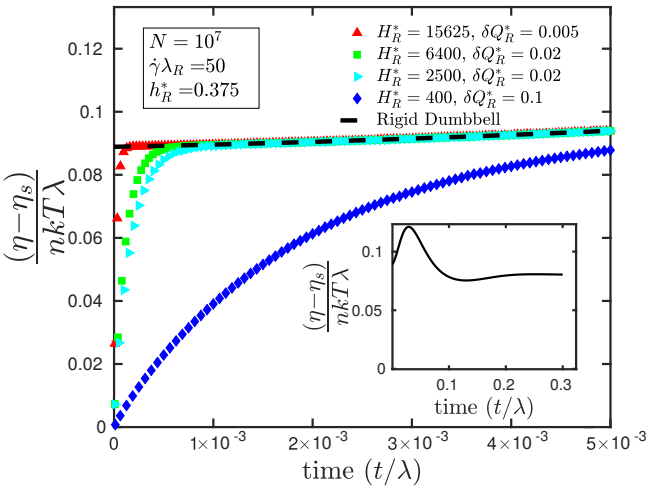

FIGURE 2.7: Stress jump in a FENE-Fraenkel spring at various values of spring stiffness and extensibility. Inset shows full transient viscosity curve for bead-rod dumbbell, which FENE-Fraenkel simulations follow accurately after initial stress jump. Error bars are smaller than symbol size.

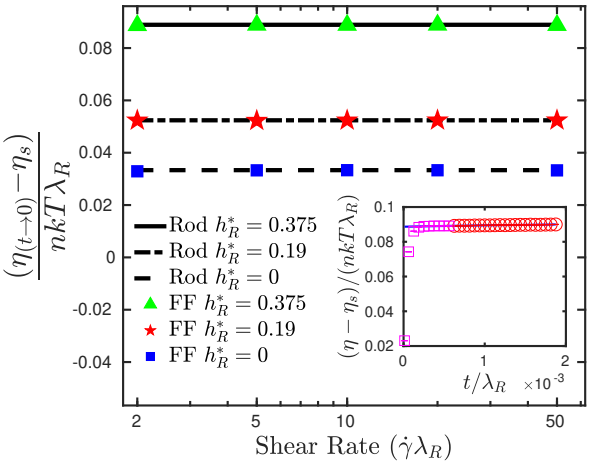

FIGURE 2.8: Shear rate independence of stress jump in both bead-rod dumbbells and FENE-Fraenkel spring dumbbells. FENE-Fraenkel springs have $H_R^* = 400$ and $\delta Q_R^* = 0.005$. Values for the FENE-Fraenkel dumbbell were calculated using a fourth-order polynomial fit extrapolated to zero time, as shown in the inset. The rigid dumbbell values are given directly by Equation 2.11. In the inset, Red circles ● represent data points used for the extrapolation, while magenta squares ■ represent data obtained from BD simulations but not used in the extrapolation, since the viscosity had not leveled off to the linear region. Blue line is a 4th-order polynomial fit to the red circles. Error bars are smaller than symbol size.

for $\dot{\gamma}\lambda R = 50$, as displayed in Figure 2.7 inset). As one would intuitively expect, this pseudo-stress-jump occurs over a shorter period of time when the spring stiffness is increased or the extensibility is decreased.

For bead-rod dumbbells, the magnitude of the stress jump should be independent of shear rate but still vary with the hydrodynamic interaction parameter, as predicted by theory [34]. Figure 2.8 shows that this relation holds for FENE-Fraenkel dumbbells when the viscosity is extrapolated to $t = 0$. An example of this extrapolation is shown in the inset of Figure 2.8,

where the data points used for a polynomial fit are chosen in the approximately linear region immediately after the initial rapid stress jump.

Note that in the context of experimental measurements, the fact that this stress jump is not strictly instantaneous is mostly irrelevant, since it is generally on the order of microseconds and can be made arbitrarily small by decreasing the extensibility or increasing the spring stiffness. For example, later in section 2.3.4.1 it will be shown that an 800 nm contour length bacteriophage with an aspect ratio of ≈ 100 can be reasonably modelled by a FENE-Fraenkel spring with $a = 20.9$ nm, $\sigma = 727$ nm, $H_R^* = 200$, $\delta Q_R^* = 0.1$ and hence $\delta Q \approx 73$. For this parameter set, the stress jump occurs over approximately 300 μs, which is shorter than the step-change time of most widely used rheometers (generally on the order of milliseconds). Therefore, although the FENE-Fraenkel spring is not a perfect reproduction of the rodlike stress jump, it should be able to reproduce any experimental measurement of the stress jump given appropriately chosen parameters.

2.3.2.2 Material Functions

Figures 2.9 (a) to 2.11 (a) show the scaling of material functions η, Ψ_1 and Ψ_2 with shear rate for the FENE-Fraenkel spring at various values of the spring stiffness H_R^* and extensibility δQ_R^*. Note that the semi-analytical solution method for bead-rod dumbbells is unstable beyond $\dot{\gamma}\lambda_R = 10^3$ (since an increasingly ill-conditioned matrix at high shear rates must be inverted), and so bead-rod curves are only displayed up to this shear rate. Power law extrapolations are provided as a guide to the eye for higher shear rates. Figures 2.9 (b) to 2.11 (b) also show the relative error between the bead-rod dumbbell material functions and the FENE-Fraenkel spring, as it is hard to discern the difference on the log scales. Although results are given only for $h_R^* = 0.25$, plots for other values of the HI parameter give qualitatively similar results with respect to the scaling of viscometric functions as H_R^* and δQ_R^* are varied.

These results show that the FENE-Fraenkel spring is able to reproduce the shear-rate-scaling behaviour of all three measured viscometric functions over three decades of shear rates given appropriately chosen spring parameters. A stiffer spring (with larger H_R^* and/or smaller δQ_R^*) appears to uniformly give more accurate results for all shear rates. At high shear rates, the material properties of the less stiff spring ($H_R^* = 200$, $\delta Q_R^* = 0.1$) deviate significantly from the bead-rod results, while at lower shear rates there is less difference. It appears that the 'spring-like' nature of the FENE-Fraenkel dumbbells is being revealed at high shear rates, which causes a deviation from the $-1/3$ power law scaling in the viscosity.

For the FENE-Fraenkel dumbbell, the steady-shear second normal stress difference is strictly positive for the parameter set used here, matching with the bead-rod predictions as in Figure 2.11. While this is consistent with the previous calculations of Stewart and Sorenson [32],

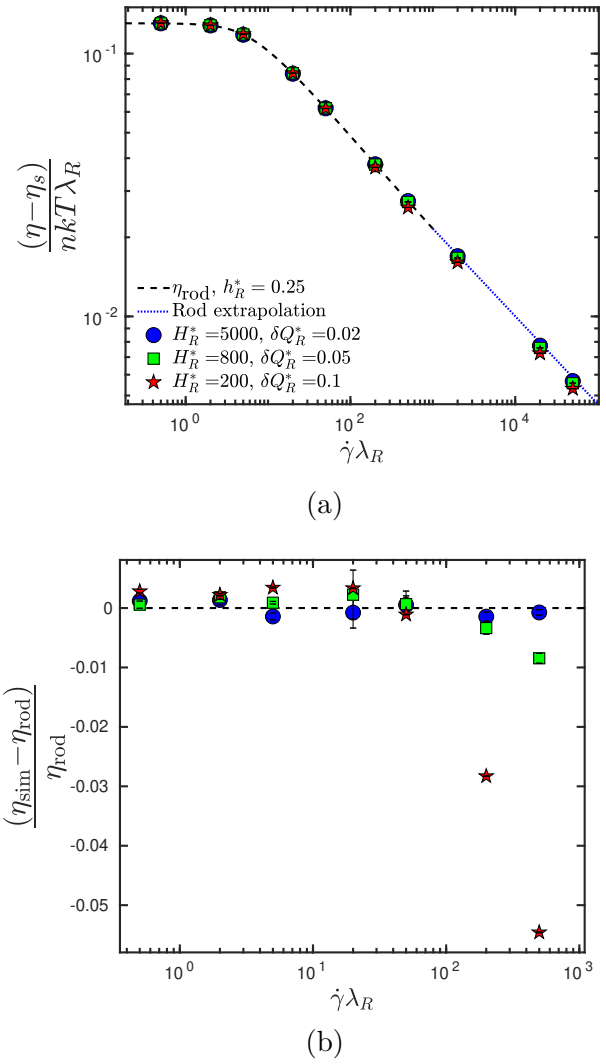

FIGURE 2.9: Non-dimensional viscosity against non-dimensional shear rate for bead-rod dumbbells (dashed lines) and bead-FENE-Fraenkel-spring dumbbells (symbols). Error bars are smaller than symbol size. Fig. (a) shows direct comparison, while Fig. (b) gives the relative error between the BD simulations and rodlike semi-analytical result, with the symbols having the same meaning in both (a) and (b). Blue dotted line is a power-law extrapolation from the tail of the bead-rod curve, with exponent $-1/3$.

note that this behaviour is different from that of springs. For example, Hookean springs give a negative Ψ_2 when fluctuating hydrodynamic interactions are included [57], and it is this Hookean behaviour which is consistent with careful experimental measurements of polymer solutions [58]. It will later be shown that the FENE-Fraenkel spring does in fact give a negative Ψ_2 for sufficiently 'spring-like' sets of parameters.

The first and second normal stress differences of the FENE-Fraenkel spring show considerably more deviation from the rodlike results than the viscosity for all spring parameters. This is particularly noticeable at high shear rates, such that to obtain a maximum of 10% error in the measured material parameters with respect to the rodlike results requires $H_R^* > 5000$, $\delta Q_R^* < 0.02$ for Ψ_2 in Figure 2.11, and $H_R^* > 800$, $\delta Q_R^* < 0.05$ for Ψ_1 in Figure 2.10, while

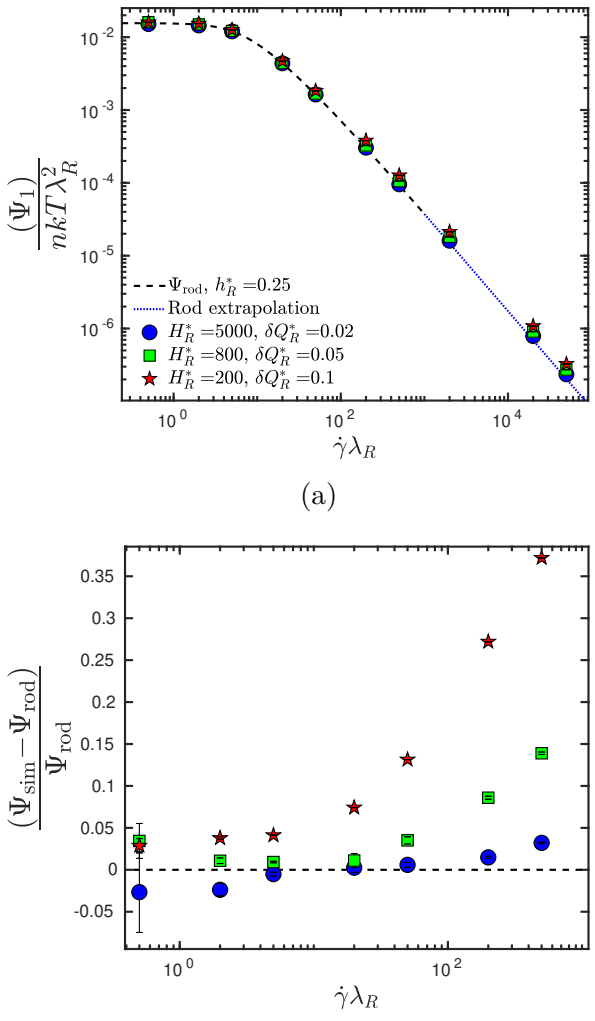

FIGURE 2.10: Non-dimensional first normal stress difference against non-dimensional shear rate for bead-rod dumbbells (dashed lines) and bead-FENE-Fraenkel-spring dumbbells (symbols). Error bars are smaller than symbol size. Fig. (a) shows direct comparison, while Fig. (b) gives the relative error between the BD simulations and rodlike semi-analytical result, with the symbols having the same meaning in both (a) and (b). Blue dotted line is a power-law extrapolation from the tail of the bead-rod curve, with exponent $-4/3$.

only $H_R^* > 200$, $\delta Q_R^* < 0.1$ in Figure 2.9 for η. There appears to be no universal 'safe' set of parameters to ensure convergence to rodlike results, with the degree of accuracy instead depending on the shear rate and measured observable.

2.3.2.3 χ_G and χ_τ scaling with shear rate

As previously discussed, the two χ parameters, χ_G and χ_τ, represent the orientation of the gyration tensor and the stress tensor respectively. These should be identical at equilibrium (or at sufficiently low shear rates), since when there is no shear the stress tensor is directly proportional to the gyration tensor. In general, at higher shear rates χ_G and χ_τ may separate,

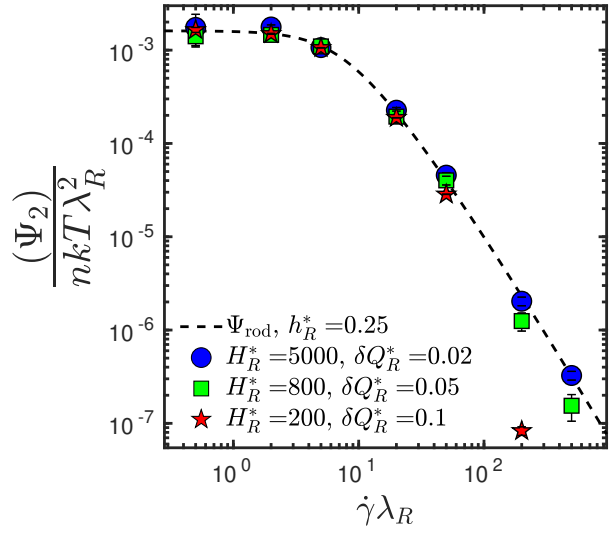

(a)

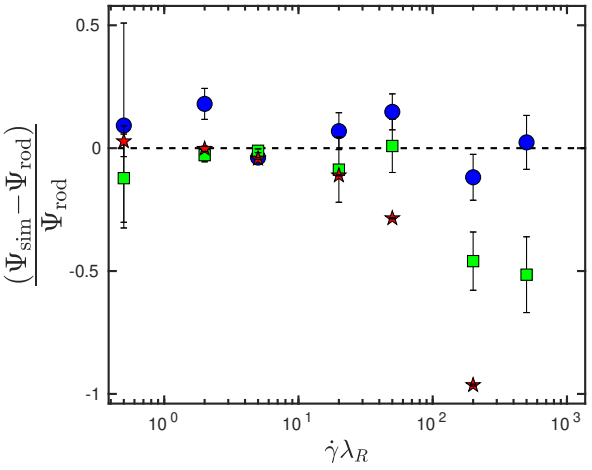

(b)

FIGURE 2.11: Non-dimensional second normal stress difference against non-dimensional shear rate for bead-rod dumbbells (dashed lines) and bead-FENE-Fraenkel-spring dumbbells (symbols). Error bars are smaller than symbol size. Fig. (a) shows direct comparison, while Fig. (b) gives the relative error between the BD simulations and rodlike semi-analytical result, with the symbols having the same meaning in both (a) and (b). Ψ_2 is not displayed beyond $\dot{\gamma}\lambda_R = 500$ as error is too large to give meaningful results.

indicating that these two tensors are no longer directly proportional and hence the stress optical rule no longer holds.

Figure 2.12 compares simulation results for FENE-Fraenkel dumbbells with the semi-analytical bead-rod solution. A lower extensibility or higher stiffness seems to uniformly give more accurate results over the whole range of shear rates for both χ_τ and χ_G. For the spring parameters chosen here, the stress-optical rule clearly does not hold, as for the bead-rod dumbbell. Furthermore, all three parameter sets show the same qualitative behaviour as a rod, with a continuously decreasing χ_G and a plateau in χ_τ at high shear rates. This plateau

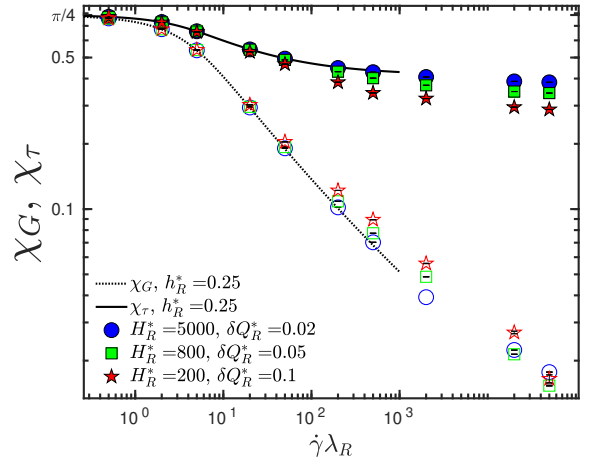

(a)

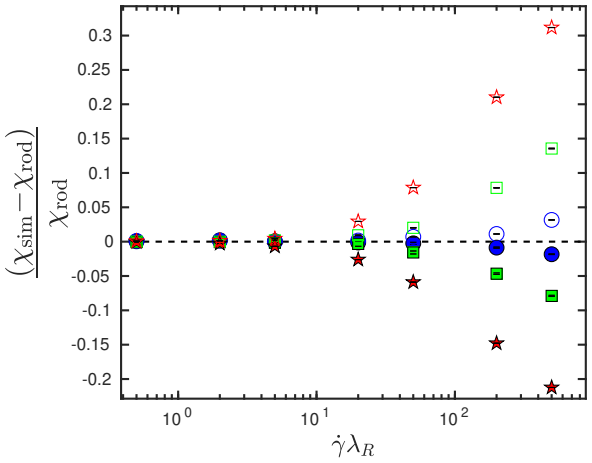

(b)

FIGURE 2.12: Black lines show χ_G (dotted line) and χ_τ (filled line) for a bead-rod dumbbell. Filled in shapes are FENE-Fraenkel simulation averages for χ_τ, while open shapes are those for χ_G. Fig. (a) gives a direct comparison of BD simulations with rodlike semi-analytical calculations, while Fig. (b) shows the relative error between the two at each shear rate, with the symbols having the same meaning in both (a) and (b).

is a feature of the power-law scaling of η and Ψ_1, as follows from Equation 2.13. Since η has a $\approx -1/3$ scaling, while Ψ_1 has a $\approx -4/3$ scaling, $2\eta_p/\Psi_1\dot{\gamma}$ will be approximately constant at high shear rates, and hence χ_τ will also be constant. This is not the general behaviour of a Hookean or FENE spring, which display a power-law decay in both χ_G and χ_τ, as will be seen in section 2.3.3.3.

2.3.3 Effects of increased extensibility

The FENE-Fraenkel spring is able to not only represent a rod in the limit of low δQ and high H, but also an entropic spring such as a FENE spring in the limit of $\sigma \to 0$. The range of

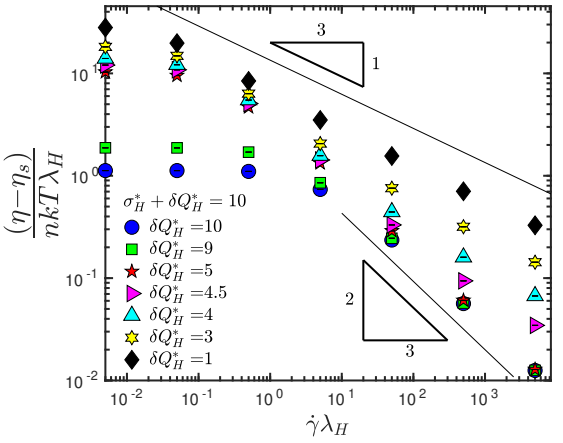

(a)

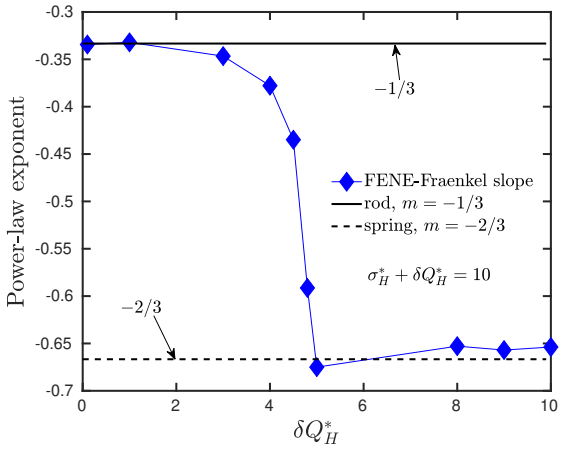

(b)

FIGURE 2.13: Viscosity scaling with shear rate of FENE-Fraenkel dumbbells with a constant $\sigma^*_H + \delta Q^*_H = 10$ and $h^*_H = 0.15$. Fig. (a) gives the viscosity curves for several δQ^*_H, while Fig. (b) gives the high-shear power law exponent in the viscosity scaling at each δQ^*_H, determined by a linear fit to the last 3 data points. Lines are only guides for the eye and do not represent fits to the data. Note that quantities are scaled using Hookean units.

possible σ, δQ and H values between these two limits can therefore mimic a variety of possible force-extension relations.

2.3.3.1 Rod to FENE-spring crossover in viscosity

A FENE-Fraenkel spring with $\sigma = 0$ is identical to a FENE spring with the FENE b-parameter $b = {\delta Q^*_H}^2 \equiv HQ_0^2/k_\mathrm{B}T$, where Q_0 is the maximum spring extensibility corresponding to δQ for the FENE-Fraenkel spring when $\sigma = 0$. At high shear rates, a FENE spring will show a $-2/3$ power-law scaling in the viscosity, while a rod (or a sufficiently stiff FENE-Fraenkel spring, as seen previously) will show a $-1/3$ scaling. In order to compare these two regimes, Hookean non-dimensionalisation must be used, as there is no 'FENE-limit' in the rodlike unit

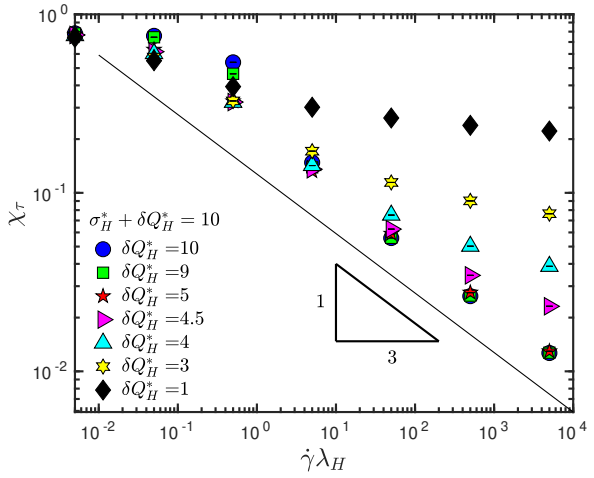

(a)

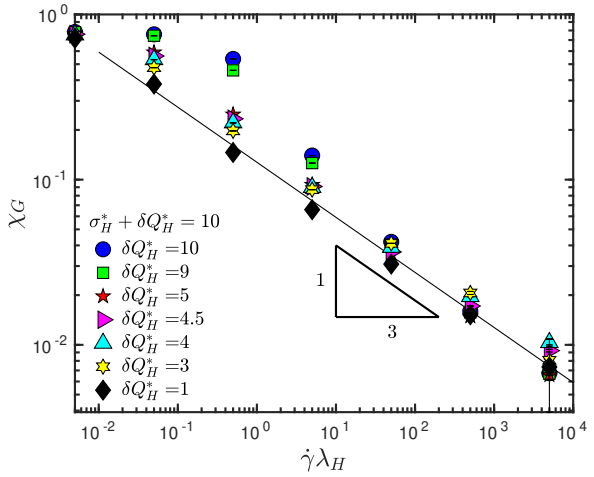

(b)

FIGURE 2.14: Plot of χ_τ (a) and χ_G (b) for the same parameter set as in Figure 2.13. Lines are a guide to the eye and not fits to the data. Quantities are scaled using Hookean units.

system. A more extensible or less rodlike spring then corresponds to a lower σ_H^* and a higher δQ_H^*, so that a natural way to compare a 'rodlike' and 'FENE-like' FENE-Fraenkel spring is to keep $\sigma_H^* + \delta Q_H^*$ constant. This is shown in Figure 2.13, where $\sigma_H^* + \delta Q_H^* = 10$, such that the $\sigma_H^* = 0$ case corresponds to a FENE spring with $b = 100$, and the $\sigma_H^* = 9.9$ case corresponds to $H_R^* = 98.01$ and $\delta Q_R^* = 0.0101$. Note that this does imply δQ_R^* can be greater than 1, in which case δQ_R^* can be thought of as a maximum fractional extension, but the spring clearly still cannot compress to $Q < 0$. Physically, one could interpret this as a very rough model of a set of polymers with constant contour length when fully stretched, but different distributions of end-to-end distances. The bead-rod case then corresponds to a delta-function peaked at $Q = \sigma$.

Examining Figure 2.13 (a), two major changes in the viscosity-shear rate curve are apparent as the spring is made more extensible (higher δQ_H^* and hence lower σ_H^*). The first is a drop in

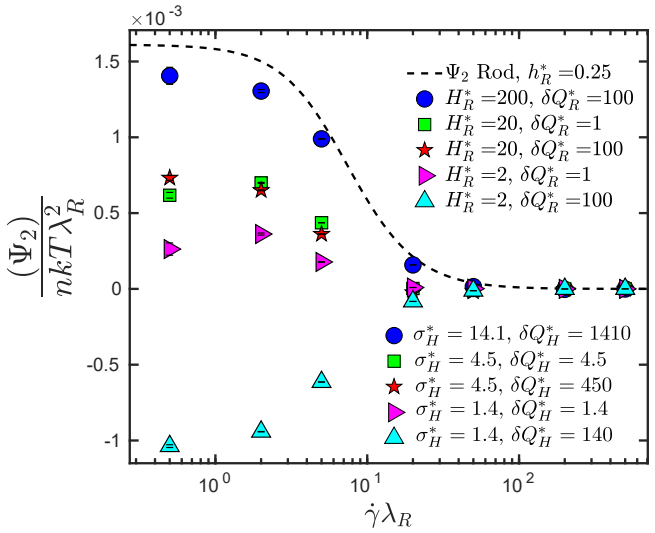

FIGURE 2.15: Second normal stress difference against shear rate for various spring extensibilities and stiffnesses at $h_R^* = 0.15$. Dotted line is Ψ_2 for the bead-rod dumbbell. This figure uses rodlike non-dimensionalisation. Error bars are smaller than symbol size.

the apparent zero-shear viscosity. This is easily explained by the decreased average end-to-end distance of the dumbbell as σ_H^* is decreased, since the zero-shear viscosity is proportional to the equilibrium dumbbell length. The second change is in the high-shear behaviour, where the power-law slope of the viscosity curve goes from $-1/3$ to $-2/3$. Interestingly, at the shear rates investigated here, this crossover happens fairly suddenly at around $\delta Q_H^* = 5$ to $\delta Q_H^* = 4.5$, as the $\delta Q_H^* > 5$ viscosities converge at high shear rates. This effect is seen clearly in Figure 2.13 (b), which shows that the crossover from $-2/3$ to $-1/3$ power law exponent begins suddenly around $\delta Q_H^* \approx \sigma_H^* \approx 5$. The exponent then goes smoothly to the rodlike limit of $-1/3$ as δQ_H^* decreases further. Furthermore, this crossover also corresponds to a leveling off in χ_τ, as seen in Figure 2.14. In other words, the value of δQ_H^* at which the shear-thinning slope deviates from $-2/3$ (in this case, $\delta Q_H^* \approx 5$) is the same at which χ_τ shows a high-shear plateau similar to that seen in the rodlike results of Figure 2.12.

Finally, as expected, a spring with low σ_H^* ($\sigma_H^* = 1$, $\delta Q_H^* = 9$) is approximately equivalent to a FENE spring of similar extensibility ($\sigma_H^* = 0$, $\delta Q_H^* = 10$). In other words, there is no discontinuity between the $\sigma \to 0$ and $\sigma = 0$ cases.

2.3.3.2 Changing sign of Ψ_2

If fluctuations in hydrodynamic interactions are accounted for, either in BD simulations or using a Gaussian approximation, the second normal stress difference Ψ_2 of a Hookean dumbbell in shear flow will be strictly negative [13, 57]. However, bead-rod dumbbells show a positive Ψ_2, so we should expect to see some sort of crossover as the extensibility is increased or the stiffness is decreased of the FENE-Fraenkel spring. Figure 2.15 shows that this is in fact the case, where both a low stiffness and high extensibility is required to observe a negative Ψ_2.

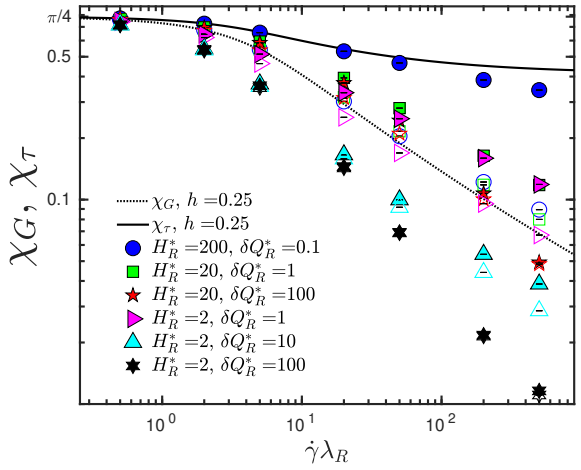

FIGURE 2.16: Scaling of χ_G and χ_τ with shear rate as extensibility and stiffness of the FENE-Fraenkel spring are varied at $h_R^* = 0.25$. Filled shapes are FENE-Fraenkel simulations of χ_τ, while hollow shapes are χ_G. Rodlike units are used for comparison with rodlike results. Error bars are smaller than symbol size.

In other words, only an analogue of a highly flexible polymer shows a negative Ψ_2, with more rigid models giving positive Ψ_2. This figure again uses rodlike units to allow comparisons with bead-rod results.

This finding is significant given the history of theoretical and experimental determinations of Ψ_2 for high molecular weight polymers. Up to about 1962, the 'Weissenberg hypothesis' that $\Psi_2 = 0$ was thought to be correct, until several measurements showed that Ψ_2 may be positive [58, 59]. This was then found to be due to subtle hole pressure effects, leading to a consensus that for flexible polymer solutions, $\Psi_2 < 0$. This has been found in both rheometer force-based measurements using different plate geometries, as well as optical and shape-based measurements of channel flow [58, 60, 61]. There seems to be a lack of similar measurements for rodlike molecules, with Ψ_2 changing sign with shear rate for highly concentrated solutions [62], but no clear results for dilute solutions.

Given the results of this computational study, it appears likely that a negative Ψ_2 is not a universal property of all polymer solutions, but instead a function of flexibility. Further simulations of multi-bead chains with tunable flexibility may be necessary for investigation of this effect. These results could be compared to experimental measurements of Ψ_2 for polymer solutions with a range of concentrations, flexibilities and morphologies (for example, using rigid macromolecules such as bacteriophages).

2.3.3.3 χ_G and χ_τ scaling with extensibility

The relative orientation of the gyration tensor (represented by χ_G) and the stress tensor (represented by χ_τ) show complex behaviour depending on the stiffness and extensibility of the

FENE-Fraenkel spring. As Figure 2.16 shows, a low stiffness ($H_R^* = 2$) and highly extensible ($\delta Q_R^* = 100$) FENE-Fraenkel spring has similar χ_G and χ_τ at all shear rates. The slope of the χ_G and χ_τ curves continue to decrease as H is decreased or δQ is increased, as the behaviour is fundamentally different in the Hookean limit. As the extensibility is decreased, χ_G and χ_τ move further apart, while increasing stiffness appears to change the absolute magnitude of χ_G and χ_τ at a particular shear rate. This suggests that the FENE-Fraenkel spring captures behaviour which cannot be replicated individually by a FENE or Fraenkel spring.

As previously mentioned in section 2.3.2.3, we should expect a high-shear plateau of the bead-rod χ_τ at high shear rates due to the $-1/3$ power law scaling in η and $-4/3$ power law scaling in Ψ_1. For a FENE spring, the power law scaling in Ψ_1 remains at $-4/3$, while the viscosity now scales as $-2/3$, leading to an overall $-1/3$ scaling in χ_τ. This can be seen in Figure 2.14 (a), where a more extensible spring leads to a power-law scaling in χ_τ. Additionally, Figure 2.16 shows the same $-1/3$ scaling (similar to χ_G) for FENE-Fraenkel dumbbells with low extensibility and low stiffness, but low stiffness and high extensibility (for example $H_R^* = 2$, $\delta Q_R^* = 100$, approaching a Hookean dumbbell) seems to lead to a further decrease in the power law exponent.

2.3.4 Comparison with experimental data

Here we show that the FENE-Fraenkel dumbbell model is able to give a reasonable description of the viscosity and S-parameter of semiflexible molecules with persistence length on the order of contour length. We also compare results with rodlike models of the same aspect ratio and length as the experimentally measured molecules. Although the FENE-Fraenkel spring is compared with real semiflexible polymers, the aim is not to develop this force law as a replacement for wormlike chain polymer models, or to suggest that the FENE-Fraenkel spring dumbbell can reproduce all the physics of these chains. Instead, we wish to show that the FENE-Fraenkel dumbbell is at least as useful as a bead-rod dumbbell in modelling rigid polymers. Additionally, the FENE-Fraenkel spring's adjustable extensibility may offer qualitative advantages over a rigid rod when the contour length is greater than the persistence length, since the variability in end-to-end distance of the true polymer chain may be somewhat captured by this extensiblity.

2.3.4.1 Linear Dichroism Comparisons

Figure 2.17 compares the S-parameter prediction of three models (a FENE-Fraenkel spring dumbbell, a rigid multibead-rod and a prolate spheriod) with experimental data on the Linear Dichroism of M13 bacteriophage, which is filamentous with a persistence length ($\approx$ 1250 nm

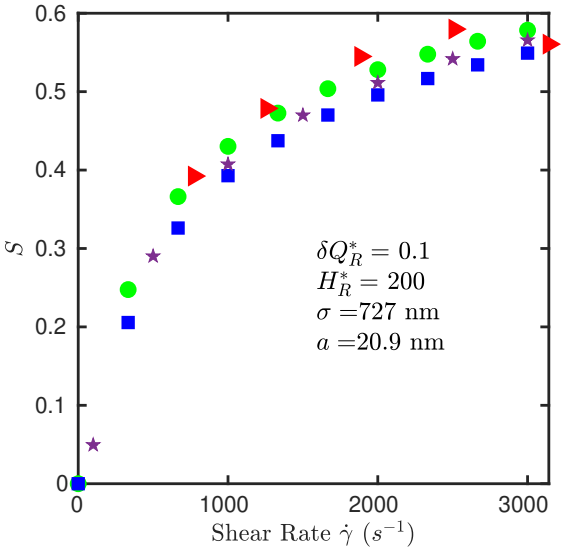

FIGURE 2.17: Comparison of various rodlike models with experimental LD data for M13 bacteriophage with contour length 800 nm and aspect ratio 100. Red triangles ▶ are experimental LD measurements from [3], where the transition dipole moment was assumed to be $\alpha = 31°$ to obtain the S-parameter values. Green circles ● are numerical calculations for an osculating multibead-rod model with bead diameter 8 nm [34]. Blue squares ■ are numerical calculations for a prolate spheroid with minor axis 4 nm and major axis 400 nm, identical to those of McLachlan et al. [3]. Purple stars ★ are FENE-Fraenkel simulations with bead parameters displayed in the figure. Error bars are smaller than symbol size for the FENE-Fraenkel simulation, but were not provided for the experimental data.

[63]) longer than its contour length ($\approx$ 800 nm) and a diameter of $\approx$ 8 nm. The experimental data is taken from Ref. [3], where a microvolume Couette cell was used to shear M13 bacteriophage at several shear rates. As described in the paper from which this data was taken, the transition dipole moment angle for this bacteriophage can be determined via the protein structure of the phage to be $\alpha = 31°$. Given the provided LD_r data, the experimental S-parameter can be extracted and is plotted here. However, quantitative comparisons should be made cautiously, since experimental error and uncertainty in α were not specified.

The multibead-rod and prolate spheroid models can be applied without any fitting, given the aspect ratio and length of the original bacteriophage [3, 34]. However, the bead radius of the FENE-Fraenkel dumbbell must be fit in some manner, as setting $a = 4$ nm gives completely inaccurate results. This can be done by noting that for S-parameter prediction, the bead-rod dumbbell and multibead-rod are identical up to a factor proportional to the bead radius, such that the time constants characterising the two models can be equated using a simple analytical expression. The bead radius $a = 20.9$ nm of the FENE-Fraenkel dumbbell was therefore chosen such that a bead-rod dumbbell with $a = 20.9$ nm would give exactly the same time constant and hence S-parameter prediction as the multibead-rod model with $a = 8$ nm. A more detailed explanation of this procedure can be found in Appendix A.5. The values $H_R^* = 200$ and $\delta Q_R^* = 0.1$ were chosen based on the results of section 2.3.2.2, given that this set of parameters appears to fairly accurately reproduce a bead-rod dumbbell for moderate

shear rates. The value of σ in dimensional form was then chosen such that $\sigma + \delta Q = 800$ nm, which gives $\sigma \approx 727$ nm.

As can be seen in Figure 2.17, both the prolate spheroid and osculating multibead-rod, when given an aspect ratio equal to that of the bacteriophage, give results which appear quantitatively correct. This suggests that some form of slender rod is a suitable model for rigid macromolecules with persistence length close to or greater than contour length. This result is somewhat surprising given the persistence length of M13 is ≈ 1250 nm [63] compared to its contour length of 800 nm. Observed under a microscope, this molecule would appear quite bendy and flexible rather than perfectly rigid. This provides an example of the suitability of a rigid segment in describing the behaviour of a polymer on length scales lower than the Kuhn length, while also suggesting that a segment model with some extensibility is no less physically reasonable than a perfectly rigid bead-bead link. Specifically, the FENE-Fraenkel spring is able to predict the S-parameter, even though the extensibility is reasonably high (10% of the natural length σ). It seems that bead size and rodlike model parameters are more influential than the specific form of the force-extension curve or the connector model in general. This shows that even without an extremely high H or small δQ to ensure strict matching to bead-rod results, the FENE-Fraenkel spring is a reasonable qualitative model of a fairly rigid molecule.

2.3.4.2 Prediction of shear-dependent viscosity

Yang [47] has previously measured the shear-dependent intrinsic viscosity of Poly-γ-benzyl-L-glutamate (PBLG) in m-cresol solvent, which can be compared with our theoretical predictions. This is displayed in Figure 2.18, which compares several FENE-Fraenkel spring dumbbells and a multibead-rod model with viscosity data for PBLG in m-cresol. The FENE-Fraenkel spring parameters were chosen to roughly imitate a short wormlike chain with the same contour length and persistence length as PBLG (with contour length $L = 143$ nm and persistence length $l_p = 90$ nm respectively [45, 47]). The end-to-end distance distribution function for a short wormlike chain is given by Frey and Wilhelm [64], from which the equilibrium extension $\sqrt{\langle Q^2 \rangle_{\text{eq}}}$ can be easily derived. For the FENE-Fraenkel spring, σ and δQ were chosen such that $\sigma + \delta Q = L = 143$ nm and $\sigma = \sqrt{\langle Q^2_{\text{WLC}} \rangle_{\text{eq}}}$, giving $\sigma = 115$ nm and $\delta Q = 28$ nm. Finally, the bead radius a was chosen in a similar way to that for the M13 bacteriophage comparisons in section 2.3.4.1, except that for viscosity there are two characteristic time constants for the bead-rod and multibead-rod models which cannot be directly equated. A bead-rod dumbbell radius of $a = 8.58$ nm was found to give results visually closest to a multibead-rod model with an aspect ratio of ≈ 94 (the same aspect ratio as PBLG), so this bead radius was used for the FENE-Fraenkel spring dumbbell. A more detailed explanation

of this procedure can be found in Appendix A.5. Figure 2.18 then shows results with three possible values of the spring stiffness H_R^*.

The stiffest spring, with $H_R^* = 500$, falls closest to the multibead-rod model, as would be expected for a more rodlike FENE-Fraenkel spring. Interestingly, the springs with lower stiffness seem to predict the experimental results more accurately at high shear rates. While it is difficult to draw solid conclusions from this single viscosity curve, it may be that the extensibility of the PBLG molecule is being revealed at higher shear rates, similar to the deviation of the extensible FENE-Fraenkel spring from rodlike viscosity at high shear rates. In this way, a 'rodlike' model which has finite extensibility, such as the FENE-Fraenkel spring, may be more useful than a true rigid rod when predicting shear viscosity of certain polymers. Therefore, the FENE-Fraenkel spring is a promising force law with which to investigate the differences in high shear-rate behaviour of bead-rod and bead-spring chains. Further research on FENE-Fraenkel spring chains may provide insight into why different models are only able to predict some behaviours of certain true polymer chains and not others.

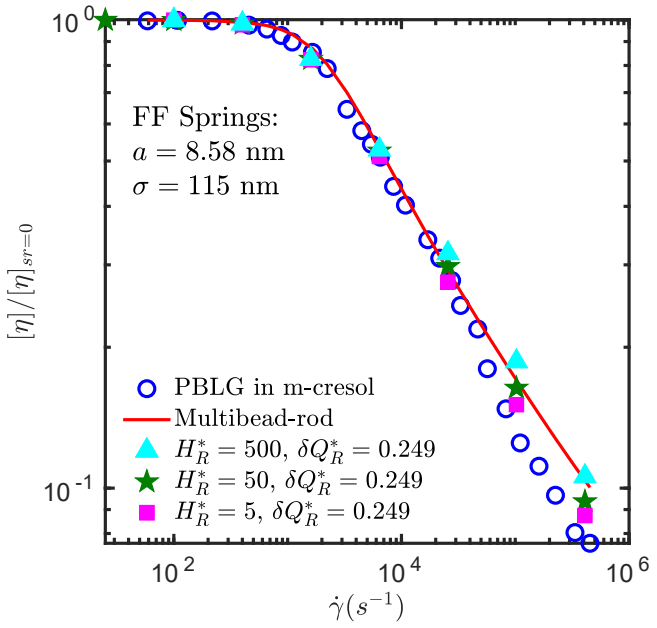

FIGURE 2.18: Comparison of experimental shear-rate dependent intrinsic viscosity $[\eta]$ for PBLG with a multibead-rod and FENE-Fraenkel spring. Experimental data is Poly-γ-benzyl-L-glutamate (PBLG) in m-cresol at 25.5°C, where the contour length is $L = 143$ nm and the persistence length is 90 nm with an aspect ratio of ≈ 94 [45, 47]. FENE-Fraenkel dumbbell bead radius was chosen to give a best fit to the experimental data.

2.4 Conclusions

The FENE-Fraenkel spring has been shown to be a viable replacement for a rod in terms of the stress jump, material functions and rheo-optical properties. However, there is no set of spring parameters which give universal adherence to bead-rod results. Instead, the particular

measured property and the shear rate also affect the calculated accuracy, such that stiffer and less extensible springs are needed for higher shear rates and parameters such as Ψ_1 and Ψ_2 as opposed to η and χ. For example, using $H_R^* = 200$ and an extensibility of $\delta Q_R^* = 0.1$ is sufficient to obtain η_{rod} to within 1% accuracy up to $\dot{\gamma}_R^* = 50$ (Figure 2.9), while a far stiffer $H_R^* = 5000$ and $\delta Q_R^* = 0.02$ is required to obtain $\Psi_{2,\text{rod}}$ to within 10% for $\dot{\gamma}_R^* > 50$ (Figure 2.11).

There is also the issue of timestep convergence, which should be checked explicitly for each h^*, δQ_H^* and $\dot{\gamma}$, which were found to be the key factors influencing the required timestep for convergence of the equilibrium distribution function and non-equilibrium averages. In general, as δQ_H^* is lowered a smaller Δt_H^* is needed for distribution function convergence at equilibrium, as seen in Figure 2.6. This gives a good starting point to check timestep convergence at non-zero shear rates.

As the spring stiffness and extensibility are relaxed towards the FENE, Fraenkel and Hookean limits, the FENE-Fraenkel spring begins to show more traditionally 'spring-like' behaviour. This manifests itself most clearly in a change in the shear-thinning exponent of the viscosity, which moves from $-1/3$ to $-2/3$ as H is decreased and δQ is increased. It appears that any FENE-Fraenkel spring will eventually deviate from the $-1/3$ scaling at sufficiently high shear rates, with a higher stiffness or lower extensibility causing this change in scaling to occur at higher and higher $\dot{\gamma}$. Therefore, higher shear rates appear to reveal more of the 'spring-like' nature of a stiff and inextensible FENE-Fraenkel spring. Additionally, the second normal stress difference appears negative for the FENE-Fraenkel spring only when both H_R^* is small and δQ_R^* is large, converging towards Hookean behaviour. Significantly, the FENE-Fraenkel spring is able to represent both positive and negative Ψ_2 with a single form of the spring potential. This is also the case for χ_τ and χ_G, where the stress optical law does not hold if either H_R^* is large or δQ_R^* is small. Once again this demonstrates that the FENE-Fraenkel spring is able to represent both spring and rod regimes with correctly chosen parameters.

Comparisons with experimental data show the FENE-Fraenkel spring is also able to qualitatively reproduce the behaviour of rigid filamentous molecules. With spring parameters of $H_R^* = 200$ and $\delta Q_R^* = 0.1$, which were sufficient to reproduce bead-rod behaviour at low shear rates, the FENE-Fraenkel spring can accurately model the linear dichroism of M13 bacteriophage, given an appropriately chosen bead radius a. Of particular note is data on the shear-thinning of PBLG polymer in m-cresol solvent, which displays a slight deviation from the classic $-1/3$ power law exponent at very high shear rates. This may be due to the fact that this polymer is not truly rigid and has some flexibility and extensibility, which the FENE-Fraenkel spring is able to qualitatively capture. This suggests that the deviation of the FENE-Fraenkel spring from bead-rod material properties at high shear rates may not be an issue when used

as a model for links in a semi-flexible polymer, as experimental measurements also display this behaviour.

Future work will focus on two main areas. Firstly, whether the results obtained for the dumbbell case when comparing a FENE-Fraenkel spring and rod remain valid in the bead-spring-chain case. Secondly, whether the FENE-Fraenkel spring can be used, along with a bending potential, as a model of a semiflexible polymer chain such as DNA in the context of modelling the Linear Dichroism signal in shear flow. In this second case, the ability of the FENE-Fraenkel spring to represent both a rod and an entropic spring may be useful when comparing different possible levels of coarse-graining to use in the model. As will be seen in Chapter 3 and Chapter 5, the FENE-Fraenkel spring in does fact succeed on both counts.

Chapter 3

FENE-Fraenkel bead-spring chains

3.1 Introduction

Decades of research have resulted in a mature understanding of the behaviour of dilute polymer solutions in flow, to the point where direct quantitative comparisons with experimental data in extensional flow are possible [14–16]. However, there remain several unresolved qualitative questions regarding behaviour in shear flow, and complete quantitative analysis of experimental results continues to be challenging [11, 12, 31]. One key difficulty is in correctly describing the change in viscosity as shear rate is increased, where experiments and simulations give confusingly varied results [12, 22]. For example, changes in polymer molecular weight, backbone semiflexibility and sovlent-polymer interactions contribute to differences in shear-thinning exponents, shear rates for onset of shear-thinning, and appearance of a high-shear plateau, as depicted in Figure 3.1. On the other hand, Figure 3.2 gives several results derived from simulated and theoretical models, with considerable differences in behaviour depending on the type of bead-bead connection (rod or spring), inclusion of hydrodynamic interactions (HI) or excluded volume effects (EV), as well as use of a bending potential. Clearly, it would be useful to have a single model which can span the entire range of previously-modelled behaviour, in order to systematically investigate the effects of each piece of added physics. Not only would this allow for improved qualitative understanding of experimental behaviour, but it would also aid in development of multiscale modelling approaches at different levels of polymer coarse-graining. In this paper, we summarise prior research on shear rheology of dilute polymer solutions, and present a model with full fluctuating HI and EV based on the FENE-Fraenkel spring force law [23, 65] and a bending potential between springs. This model can move smoothly between all the regimes of behaviour described in Figure 3.2, demonstrating several novel results in the process.

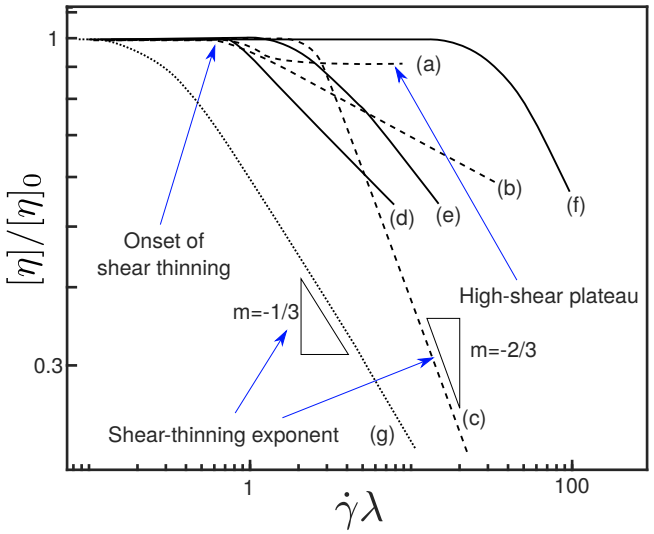

FIGURE 3.1: Schematic of observed experimental shear-thinning behaviour in polymer solutions. Here $[\eta]/[\eta]_0$ is the intrinsic viscosity at some shear rate divided by the intrinsic viscosity at zero shear. The shear rate is $\dot{\gamma}$, normalised by the polymer relaxation time λ. The value of λ is determined from the zero-shear viscosity via $\lambda = [\eta]_0 \eta_s M / N_A k_B T$, where η_s is the solvent viscosity, M is the polymer molecular weight, k_B is Boltzmann's constant and T is the temperature. Data is traced from plots of several authors [22, 29, 47, 66]. Values should not be considered exact, only qualitatively correct. Dashed lines (curves a, b and c) are polystyrene of 13.6×10^6 g/mol in a theta solvent (a) and good solvent [66] (b), as as well as 2×10^6 g/mol in a theta solvent [29] (c). Solid lines (curves d, e and f) are DNA at various solvent qualities [22] with lengths 25 kbp (d), 48.5 kbp (e), and 165.6 kbp (f). Dotted line (curve g) is PBLG (a rigid molecule) of $M = 2.08 \times 10^5$ g/mol in m-cresol solvent [47]. Note the differences in onset of shear thinning, shear thinning exponent, and high-shear plateau as polymer length, flexibility and solvent quality are changed.

While chains with Hookean springs and preaveraged hydrodynamic interactions (the Zimm model) are able to accurately describe the linear viscoelastic properties of many polymer solutions, their infinite stretchability leads to inaccurate predictions in flow [34]. The finite extensibility of a chain is generally included in one of two ways, either using rigid rods to represent each Kuhn step of the backbone individually, or a finitely extensible entropic spring which approximates the force-extension behaviour of a large segment of the underlying molecule [21]. Bead-rod dumbbells are known to have a shear-thinning exponent of $(-1/3)$ (Figure 3.2, curve d) and approximate the behaviour of highly rigid molecules [32, 65], while FENE-spring dumbbells show a $(-2/3)$ exponent (Figure 3.2, curve c) and are able to qualitatively predict the shear-thinning behaviour of some flexible polymer solutions [33, 34, 70]. Additionally, the Weissenberg number for onset of shear-thinning increases with increasing extensibility (quantified by the FENE b-parameter) [68], a behaviour which is also found as the molecular weight of experimental systems is increased [22, 66] (Figure 3.1 curves d, e and f).

For chains, a well-known and somewhat counter-intuitive result is that a bead-rod chain with connections modelled as hard constraints gives a different distribution from an infinitely-stiff Fraenkel chain [25, 26, 34], although the difference seems unimportant in practice [23].

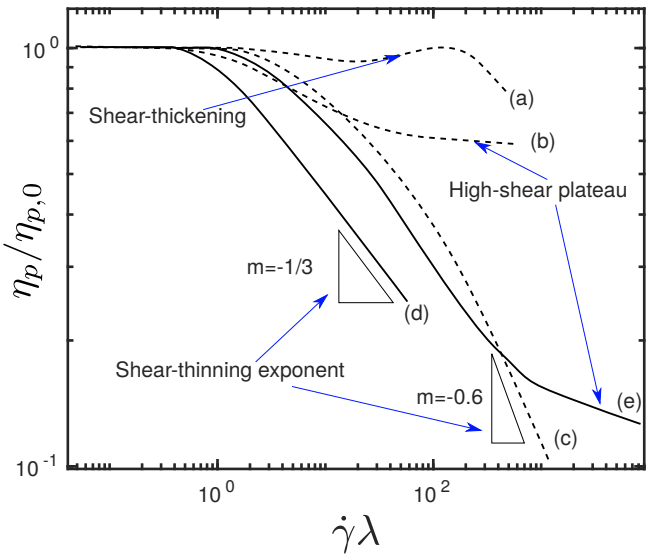

FIGURE 3.2: Schematic of theoretical and simulation findings, traced from previous works and not exact. Dashed lines (curves a, b and c) are 'spring-like' results for FENE chains with HI [67] (a), Hookean chains with EV [68] (b) and Marko-Siggia force-law [44] chains with EV and HI [31] (c). Solid lines (curves d and e) are 'rod-like' results, namely stiff Fraenkel springs with a strong bending potential [69] (d), and a bead-rod chain with HI but no EV [37] (e).

In the following discussion, we will refer to both simply as 'bead-rod' chains, except where explicitly distinguished. While finitely extensible bead-spring chains show a $(-1/2)$ to (-0.6) shear-thinning exponent in the viscosity (without excluded volume effects) [31, 36, 37, 71–74], bead-rod chains display some unexpected behaviours at high shear rates. Most notably, there is an apparent second Newtonian plateau in the viscosity at high shear rates, which appears to be exacerbated by the inclusion of HI [36, 37]. This behaviour is generally not seen in experimental studies, although there are some hints of it in the polystyrene data of Hua et al. [29], and of Noda for much longer polymer chains [66].

This viscosity plateau is somewhat correlated with a decrease in polymer extension in the flow direction at high shear rates [37, 71, 75]. In general, all models show a compression (measured in terms of the components of the gyration tensor) in the gradient and neutral direction, which is also seen in single-molecule imaging of DNA [31]. However, the compression in flow direction is unexpected, and was explored in detail first by Netz and Sedner [76] and then by Dalal and coworkers [77–79]. The conclusion is that HI increases this effect, while an appropriately chosen EV potential largely eliminates it, as does fine-graining beyond the Kuhn-step level in the form of a stiff bending potential between segments [78, 79]. Since these extremely high shear rates are largely out of the reach of experiments, it's unclear the extent to which this effect is a real physical result and not an artefact of the coarse-graining. These authors did not study the effects of this behaviour on the viscosity or normal stress, however they did examine the end-on-end tumbling behaviour of chains, deriving power-law expressions for the tumbling time as a function of shear rate based on the segmental diffusion and convection [78]. Some

studies seem to suggest a $(-3/4)$ power law slope in tumbling period with shear rate [79] (or -1.1 on inclusion of HI but with no EV), while others show a $(-2/3)$ slope for experimental and simulation data [80].

We note that it is possible to include a parallel dashpot in a bead-spring model, which models the internal viscosity (IV) of a polymer chain [34, 41, 43, 81–84]. Such models display a $-1/3$ slope in the viscosity for bead-spring-dashpot dumbbells [43], a high-shear plateau in viscosity which depends on the IV parameter [82], and instantaneous stress jumps [41, 43], all of which are also characteristic features of bead-rod models. However, including them in a BD simulation is extremely complicated without preaveraging [81–83], and measuring the strength of IV experimentally so as to determine dashpot viscosity is not common or straightforward [85]. While this is a promising avenue of investigation, in this paper we will restrict our focus to bead-spring models without IV.

Briefly returning to the entropic bead-spring models, there is again some uncertainty in the power-law exponent, with bead FENE-spring chains showing a $(-2/3)$ or -0.6 power-law slope [71, 72], while some results suggest a Cohen-Pade or Marko-Siggia wormlike-chain (MS-WLC) force law could give a $(-1/2)$ power-law slope [31, 73]. However, it is important to consider whether the slope is truly 'terminal', as these models tend to have a large crossover region between the low-shear Newtonian plateau and the high-shear behaviour. For example, Schroeder et al. [31] report a $(-1/2)$ power-law exponent in the viscosity for comparisons with experimental data, but note a -0.61 exponent at very high shear rates for the MS-WLC spring force law when carrying out BD simulations.

While the chain connectivity is crucially important to the shear-flow behaviour, there has also been a large body of work incorporating the effects of hydrodynamic interactions (HI) and excluded volume (EV). It's well known that a bead-Hookean-spring chain with preaveraged HI (Zimm model) does not lead to shear-thinning. However, when consistently-averaged, treated using a Gaussian or similar approximation, or with full fluctuating effects [67, 86–88], a chain of Hookean springs shows slight shear-thinning and then shear-thickening. The intuitive explanation of this behaviour is that the Zimm zero-shear viscosity is lower than the Rouse zero-shear viscosity, but shear flow pulls the beads apart and lessens the effects of HI. Therefore, the chain thins slightly due to the 'backflow' from HI, then thickens to reach the Rouse viscosity at high shear rates. This shear-thickening is also seen for sufficiently extensible non-Hookean springs at sufficiently high bead numbers, before the onset of further shear-thinning due to finite extensibility [67, 73]. However, this behaviour has not been seen in experimental measurements of dilute polymer solutions - the thickening for semidilute solutions is thought to be related to entanglements rather than HI [67, 89]. As has been mentioned, HI also causes a compression of bead-rod models at high shear rates, as well as a second Newtonian plateau in the viscosity [35, 37, 76, 79]. Additionally, as predicted by the Zimm

model, zero-shear viscosity is reduced when HI is included, despite no change in the equilibrium structure. Note that the intermediate-shear-rate viscosity thickening of bead-spring models due to HI has not been observed in bead-rod models, however it is possible that longer chains are required. For example, there are slight hints of the effect in the bead-rod simulations of Khomami and Moghani [75] who used 350 beads, although their findings are not definitive.

The effects of excluded volume are generally characterised via the chain swelling at equilibrium, which is related to the solvent quality parameter z [12, 90]. Rigorous theoretical developments treating EV using a delta function potential and renormalisation group approaches [90] find that the EV contribution to the shear-thinning exponent should be $(-1/4)$ for sufficiently long Rouse chains [91]. In simulations, EV potentials can generally be grouped into soft-core repulsive (such as the Gaussian potential [92, 93]), hard-core repulsive (such as the Weeks-Chandler-Andersen (WCA) potential [37]), or hard-core potentials with repulsive and attractive components (such as the Lennard-Jones (LJ) [79] or Soddemann-Dünweg-Kremer (SDK) [94, 95] potentials). A theta-solvent is one either without any EV interactions, or with a potential equal parts repulsive and attractive such that there is no swelling at equilibrium - importantly, Dalal et al. [79] showed that these are emphatically NOT equivalent away from equilibrium for bead-rod chains. In fact, several authors have shown that besides causing chain-swelling at equilibrium, a hard-core EV potential also suppresses the high-shear decrease in chain stretch seen in bead-rod chains, as well as the high-shear plateau in viscosity [37, 75, 77, 79]. This effect occurs even using a theta-solvent LJ potential, constructed as to cause no swelling at equilibrium [79]. For Rouse chains and FENE chains, BD simulations show the expected $(-1/4)$ decrease in viscosity with shear rate for sufficiently strong EV in the long-chain limit [53, 96].

The inclusion of semiflexibility, generally modelled through a potential energy cost for backbone bending or twisting [49], also has somewhat uncertain effects upon the shear-flow behaviour. Generally, a strong bending potential is associated with a $(-1/3)$ power law slope in the viscosity with shear rate for BD simulations of bead-rod models [69, 71], although it appears to approach $(-1/2)$ for a sufficiently weak bending potential [97]. This is expected, as a bead-rod chain with a very strong bending potential is essentially a rigid multibead-rod, which has a $(-1/3)$ power-law shear-thinning exponent. However, the mean-field model of Winkler [98, 99] suggests a $(-2/3)$ slope irrespective of bending stiffness, which may be due to the backbone extensibility inherent to the model. Additionally, as has already been mentioned, the use of a bending potential to increase the level of fine-graining in a bead-rod model beyond the Kuhn length, in order to accurately model the true polymer persistence length, reduces the compression of the bead-rod chain at high shear rates [78, 79].

To conclude our discussion of prior results, we briefly touch upon a few additional measures of chain behaviour in shear flow which have been explored in the literature. The first and

second normal stress coefficients Ψ_1 and Ψ_2, are the two experimentally observable viscometric functions besides viscosity. The first normal stress coefficient Ψ_1 is generally found to show a $(-4/3)$ power-law scaling with shear rate irrespective of the model [31–33, 35–37, 71, 73], however some long bead-rod-chains with HI and EV seem to display a -1.1 power law slope [75, 100]. The second normal stress difference is difficult to get accurate statistics on, both in experiments [58] and simulations, but is thought to have a positive value for bead-rod chains [100] and a negative value for bead-spring chains [73]. One can also measure optical properties, such as the birefringence [36], extinction or orientation angles [31, 36, 65, 72, 96, 99], or linear dichroism [17, 100]. Generally, these give similar results to single-molecule imaging, which shows an extension in the flow direction and contraction in the gradient direction. Finally, we have the power spectral density, which essentially allows one to examine frequency components belonging to different time scales of polymer motion [31]. This can be matched with experimental data [80], and was analysed extensively by Hur et al. [101], but will not be calculated directly here.

In light of the wide variety of expected behaviour based on the physics included in a given polymer model, it can be difficult to predict what effect a given component will have on the qualitative shear-flow behaviour. This ambiguity may be resolved by using a singular model which can span the entire range of previously-identified behaviour, as well as move smoothly between each limit, allowing one to successively add each piece of physics in turn to investigate the effects. In Section 3.2, we will describe such a model based on the so-called FENE-Fraenkel spring, along with a bending potential, EV, and full hydrodynamic interactions. Additionally, we will give a brief overview of the Brownian dynamics (BD) simulation algorithm, as well as expressions for our measured rheological, conformation and optical properties. We will then present results in Section 3.3, first showing that our FENE-Fraenkel-spring chain can reproduce both FENE-spring behaviour, as well as show exact agreement with the bead-rod simulations of Petera and Muthukumar [37]. The behaviour of viscosity, gyration tensor components and tumbling frequency is then carefully investigated in the crossover between bead-rod and bead-spring behaviour, and as a function of bending stiffness, EV and HI. Finally, to conclude in Section 3.4, we will qualitatively compare our simulations with the previous experimental, theoretical and numerical results in Figure 3.1 and Figure 3.2. We show that the whole range of behaviour can be qualitatively reproduced by our model, although further work is needed for exact quantitative predictions.

3.2 Methods

Our current model is a bead-spring chain of N beads and $N_\mathrm{s} = N - 1$ segments with bead μ at position $\boldsymbol{r}_\mu$ relative to the chain center of mass, bead-bead vectors $\boldsymbol{Q}_\mu = \boldsymbol{r}_\mu - \boldsymbol{r}_{\mu-1}$ and segment

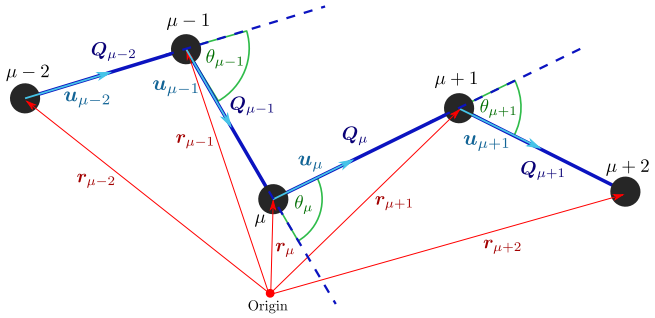

FIGURE 3.3: Diagram of bead, segment and segment angle labelling scheme. Bead μ is at position $\boldsymbol{r}_\mu$ relative to the center of mass, with some angle θ_μ. The segment from μ to $\mu+1$ has unit vector $\boldsymbol{\mu}$, with length Q_μ. Note that for N beads, the beads are numbered from $\mu = 1, 2, 3, \ldots, N$, the segments from $\mu = 1, 2, 3, \ldots, N-1$, and the angles from $\mu = 2, 3, 4, \ldots, N-1$.

angles θ_μ. This is displayed schematically in Figure 3.3, which also gives the numbering scheme for beads, segments and angles. We impose some connector force law $\boldsymbol{F}_\mu^{(c)}(\boldsymbol{Q}_\mu)$ which acts along the segments, as well as bending forces between segments, EV forces between every set of spatially nearby beads, and HI perturbations to represent the effects of the implicit solvent, all of which will be described in detail shortly. The solvent is represented implicitly such that beads have solvent friction $\zeta = 6\pi\eta_s a$, where η_s is the solvent viscosity and a is the effective bead radius. Flow is imposed through the tensor $\boldsymbol{\kappa}$, where the velocity field of the Newtonian solvent is $\boldsymbol{v} = \boldsymbol{\kappa}\cdot\boldsymbol{r}$, assuming the background flow $\boldsymbol{v}_0 = 0$. For the case of shear flow considered here, the only non-zero component of $\boldsymbol{\kappa}$ is $\kappa_{x,y} = \dot{\gamma}$, the shear rate.

3.2.1 FENE-Fraenkel force law

The connector forces act along the segments, and we will predominately use the FENE-Fraenkel form. This force law was introduced by Hsieh et al. in a 2006 paper with the purpose of reproducing a bead-rod chain while avoiding the complications of BD simulations with constraints [23]. However, this force law also has the useful property that it can simultaneously represent other commonly-used force laws, such as the FENE, Hookean and Fraenkel springs. In a previous paper, we have discussed the properties of a FENE-Fraenkel dumbbell in detail, including how to correctly choose a timestep during simulations, how various rheological properties scale with shear rate, and how one can smoothly move between bead-rod and bead-spring behaviour [65]. Here, we show that it is possible to use a bead-FF-spring-chain to recover the full range of bead-spring-chain and bead-rod-chain behaviour, including all the qualitative features of Figure 3.1 and Figure 3.2.

Written in dimensional form, the FENE-Fraenkel spring force law is given by:

$$\boldsymbol{F}^{(c)} = \frac{H(Q-\sigma)}{1-(Q-\sigma)^2/(\delta Q)^2}\frac{\boldsymbol{Q}}{Q} \tag{3.1}$$

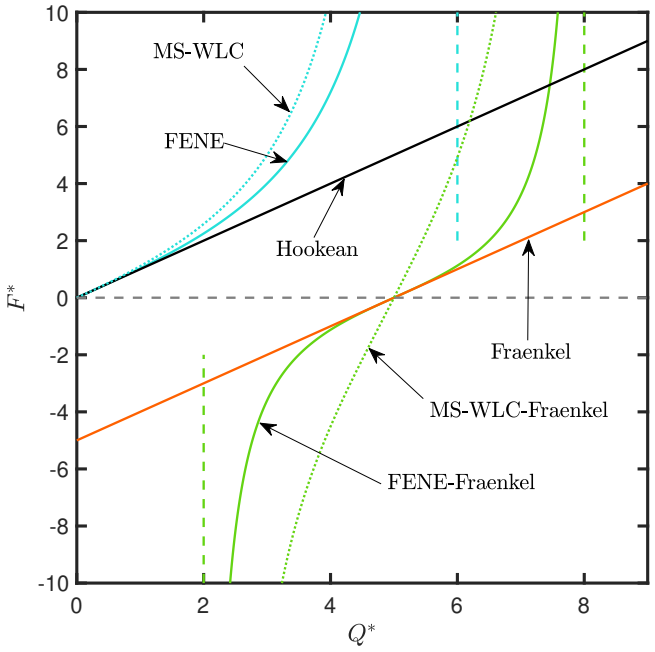

FIGURE 3.4: FENE-Fraenkel (full lines, Equation 3.2) and MS-WLC-Fraenkel (dotted lines, Equation 3.5) force limits. Vertical lines show maximum and minimum extensibilities. 'Hookean' spring has $\delta Q^* = 10000$, $\sigma^* = 0$. Fraenkel spring has $\delta Q^* = 10000$, $\sigma^* = 5$. FENE and MS-WLC springs have $\delta Q^* = 6$, $\sigma^* = 0$. FENE-Fraenkel spring has $\delta Q^* = 3$, $\sigma^* = 5$, while MS-WLC-Fraenkel spring has $\delta Q^* = 8$, $\sigma^* = 5$ (which has equivalent minimum and maximum extensibility compared to the shown FENE-Fraenkel spring).

Here $\boldsymbol{F}^{(c)}$ is the force vector between the beads with bead-bead vector $\boldsymbol{Q}$ and length Q, σ is the natural length of the spring ($Q = \sigma$ in the absence of any additional forces), δQ is the maximum extensibility around σ, and H is the effective elastic modulus of the spring (with units of force per length). Furthermore, we generally rescale lengths to a non-dimensional form using the spring length, namely $l_H = \sqrt{k_\mathrm{B}T/H}$, where k_B is Boltzmann's constant and T is the solution temperature. Since energies are also scaled by $k_\mathrm{B}T$, forces are additionally non-dimensionalised by $\sqrt{k_\mathrm{B}TH}$. In this form, the spring force law reads:

$$\boldsymbol{F}^{(c)*} = \frac{(Q^* - \sigma^*)}{1 - (Q^* - \sigma^*)^2/(\delta Q^*)^2} \frac{\boldsymbol{Q}^*}{Q^*} \tag{3.2}$$

with non-dimensional qualtities denoted by an asterisk (e.g. $Q^* = Q/l_H$). As can be seen in Figure 3.4, setting $\sigma^* = 0$ recovers the FENE and Hookean (in the limit $\delta Q^* \to \infty$) force laws, while $\delta Q^* \to \infty$ for finite σ^* gives the Fraenkel force law. Note that in the $\sigma = 0$ (FENE) case, the parameter δQ is equivalent to the more common label Q_0, and the non-dimensional δQ^* is equivalent to the square root of the FENE b-parameter, $\sqrt{b} = Q_0/l_H$.

We also briefly investigate the properties of a new spring force law, which we have called

the 'MS-WLC-Fraenkel' (Marko-Siggia Wormlike-Chain Fraenkel) spring, which has force-extension behaviour given by:

$$\boldsymbol{F}^{(c)} = H\boldsymbol{Q}\frac{2}{3}\frac{\delta Q}{Q}\left\{\frac{(1-\alpha)^{-2}-1}{4}+\alpha-\frac{\sigma}{\delta Q}\left[\frac{(1+\alpha)^{-2}-1}{4}-\alpha\right]\right\} \tag{3.3}$$

where α is a non-dimensional quantity given by:

$$\alpha = \frac{Q-\sigma}{\delta Q-\sigma} \tag{3.4}$$

Therefore, scaling lengths by l_H as for the FENE-Fraenkel spring, this can be written as:

$$\boldsymbol{F}^{(c)*} = \boldsymbol{Q}^*\frac{2}{3}\frac{\delta Q^*}{Q^*}\left\{\frac{(1-\alpha)^{-2}-1}{4}+\alpha-\frac{\sigma^*}{\delta Q^*}\left[\frac{(1+\alpha)^{-2}-1}{4}-\alpha\right]\right\} \tag{3.5}$$

with α defined as before via σ^* and δQ^*. If we identify that $H \equiv (3k_{\mathrm{B}}T)/(2Ll_p)$, where l_p is the polymer persistence length (discussed shortly) and $L \equiv \delta Q$ is the contour length, the $\sigma = 0$ limit of this force law is equivalent to that given by Marko and Siggia, the so-called MS-WLC spring [44]. This is show in Figure 3.4, for both the $\sigma^* = 0$, $\delta Q^* = 6$ and $\sigma^* = 5$, $\delta Q^* = 8$ cases. Note that compared to the FENE-Fraenkel force law, we see a different approach to the maximum-extensibility limit, as well as increased effective stiffness around σ^* for $\sigma^* > 0$. The MS-WLC-Fraenkel force law is considerably harder to deal with analytically, as its distribution function must be found numerically, but is used to show that results depend more on the extensibility, compressibility and average length than the fine-grained details of the force law in question.

3.2.2 Bending potential, EV and HI

One important feature of polymer chains which we wish to model is the semiflexibility, related to the energetic resistance to bending along the backbone. This semiflexibility is represented by the persistence length, which can be thought of as the exponential decay constant for the autocorrelation of the tangent vector direction along the backbone curve [49]:

$$\langle \boldsymbol{u}(s)\boldsymbol{u}(s')\rangle = e^{\frac{-|s-s'|}{l_p}} \tag{3.6}$$

where l_p is the persistence length, and $\boldsymbol{u}(s)$ is the tangent vector to the curve at position s, if the backbone is imagined as a continuous space-curve analogue of Figure 3.3. This is also often expressed in terms of the measure of chain size more common for flexible chains, the number of Kuhn steps $N_k \equiv L/(2l_p)$, where L is the total polymer contour length.

In a continous chain, the inverse of the persistence length can be identified as a so-called stiffness parameter, essentially a flexural modulus which describes the energetic cost for chain

bending. For discrete models, we can use an equivalent potential which imposes an energetic cost based on the angle θ_μ. In our case, the bending potential is given by:

$$\phi_{\mathrm{b},\mu}/k_\mathrm{B}T = C(1-\cos\theta_\mu) \tag{3.7}$$

where C is the bending stiffness, while θ_μ and $\phi_{\mathrm{b},\mu}$ are the included angle and bending potential between vectors $\boldsymbol{Q}_\mu$ and $\boldsymbol{Q}_{\mu+1}$ respectively. An expression for the force on bead μ due to the bending potential is given in Appendix D, as well as an analytical expression for the angular distribution function. For this form of the bending potential, Saadat and Khomami give a useful relation for the bending stiffness C as a function of the ratio of contour length L and persistence length l_p, represented by the number of Kuhn steps in each segment $N_{\mathrm{K,s}} = L/(2N_\mathrm{s}l_p)$ [18]:

$$C = \frac{1 + p_{\mathrm{b},1}(2N_{\mathrm{K,s}}) + p_{\mathrm{b},2}(2N_{\mathrm{K,s}})^2}{2N_{\mathrm{K,s}} + p_{\mathrm{b},3}(2N_{\mathrm{K,s}})^2 + p_{\mathrm{b},4}(2N_{\mathrm{K,s}})^3} \tag{3.8}$$

where $p_{\mathrm{b,i}} = -1.237, 0.8105, -1.0243, 0.4595$ for $i = 1,2,3,4$ respectively. This is a Pade approximation chosen to exactly match the nearest neighbour correlation of a continuous wormlike chain at $N_{\mathrm{K,s}} = \{0,1,2,4,15,\infty\}$ [18], while providing a good approximation for other $N_{\mathrm{K,s}}$. Note that this form is technically only exact for Saadat and Khomami's specific force law [18], but we find it gives the correct segment-segment correlation irrespective of the FENE-Fraenkel parameters used. This allows us to express our chain semiflexibility in terms of the more physically relevant l_p, rather than simply as a function of the parameter C.

Experimentally, we measure our solvent quality by the equilibrium swelling, for example of the gyration radius [102]. This is caused by the effective strength of polymer-solvent interactions, such that increased polymer-solvent attraction increases the equilibrium coil size. This is a function of the so-called solvent quality z, which describes the universal swelling of a wide variety of experimental systems, based on renormalisation group calculations [90]. In theory and simulations, the EV force is modelled through some effective bead-bead interaction strength, given by the EV potential.

In our simulations, the excluded volume force between beads is given by one of two potentials, the first of which is a truncated, purely repulsive LJ potential, what we will call the 'hard-core' form as it does not allow bead overlap. Specifically, we use the SDK potential [95] with $\varepsilon = 0$, which has the exact form:

$$U_{\mathrm{SDK}} = \begin{cases} 4\left[\left(\frac{d}{Q}\right)^{12} - \left(\frac{d}{Q}\right)^{6} + \frac{1}{4}\right] - \varepsilon, & Q \leq 2^{1/6}d \\ \frac{1}{2}\varepsilon\left[\cos\left(\alpha Q^2 + \beta\right) - 1\right], & 2^{1/6}d \leq Q \leq 1.82d \\ 0, & Q \geq 1.82d \end{cases} \tag{3.9}$$

where d is the range of the potential (similar to the well-known σ of the LJ potential), ε is the attractive well depth and α and β are chosen such that the potential smoothly goes to zero

at the cuttoff radius $1.82d$ [95]. Note that while we use $\varepsilon = 0$, which can only model a good solvent (similar to the WCA potential [103]), one can choose some ε such that the attractive and repulsive forces balance, leading to a 'hard-core' θ-solvent with no net solvent-polymer interaction [94], or even a poor solvent. The second EV potential is the 'soft-core' Gaussian potential, of the form:

$$U_{\text{Gauss}} = \frac{\nu_{\text{ev}} k_{\text{B}} T}{(2\pi d_{\text{ev}}^2)^{3/2}} \exp\left\{-\frac{1}{2}\frac{Q^2}{d_{\text{ev}}^2}\right\} \tag{3.10}$$

where ν_{ev} is the strength of the excluded volume potential (with units of volume) and d_{ev} is the range of the potential [13, 104]. In the limit of $d_{\text{ev}} \to 0$, the Guassian potential approaches the delta-function potential. This 'soft' form of the excluded volume allows for bead overlap, but has the useful feature that the solvent quality, z, can be represented exactly in terms of the chain expansion caused by a particular choice of ν_{ev} [104]. This potential will generally be used in non-dimensional form, with:

$$z^* = \nu_{\text{ev}} \left(\frac{k_{\text{B}} T}{2\pi H}\right)^{3/2} \tag{3.11}$$

which allows the solvent quality z to be expressed approximately as:

$$z^* = z\chi^3/\sqrt{N} \tag{3.12}$$

where the parameter χ is a scaled dimensionless spring length, which will be described shortly in Equation 3.16. As $N \to \infty$ with z^* corrected for χ as above, Equation 3.12 is no longer an approximation but instead gives the exact universal swelling, which is a known function of z from analytical renormalisation group theories [96].

Hydrodynamic interactions are included via the RPY tensor, a regularisation of the Oseen-Burgers tensor, describing how the force on one bead influences the motion of the others:

$$\boldsymbol{\Omega}(\boldsymbol{r}) = \frac{3a}{4\zeta r}\left(A\boldsymbol{\delta} + B\frac{\boldsymbol{rr}}{r^2}\right) \tag{3.13}$$

where the values of A and B depend on the bead separation:

$$A = 1 + \frac{2}{3}\left(\frac{a}{r}\right)^2, B = 1 - 2\left(\frac{a}{r}\right)^2 \text{ for } r \geq 2a \tag{3.14a}$$

$$A = \frac{4}{3}\left(\frac{r}{a}\right) - \frac{3}{8}\left(\frac{r}{a}\right)^2, B = \frac{1}{8}\left(\frac{r}{a}\right)^2 \text{ for } r < 2a \tag{3.14b}$$

where a is the effective hydrodynamic bead radius, as in the definition of the bead friction ζ. Note that we usually represent the strength of HI in terms of the parameter h^*, essentially a

reduced bead radius. This is given by:

$$h^* = \sqrt{\frac{k_\mathrm{B}T}{H}} a\sqrt{\pi} \tag{3.15}$$

the form of which comes from its use in the Zimm model with preaveraged HI [34].

In general, calculations are performed and results are presented in the Hookean system of non-dimensionalisation, where we have length and force scales as described above, and time scale $\lambda_H = \zeta/4H$ (the first two of which we have already noted when discussing force laws). Non-dimensional properties are denoted with an asterisk, for example the polymer viscosity is given by $\eta_p^* \equiv (\eta - \eta_s)/n_p k_\mathrm{B} T \lambda_H$, where n_p is the number density of polymers in solution. From here on, all quantities are presented in non-dimensional form, except where explicitly noted otherwise. Non-dimensionalisation of chains using the FENE-Fraenkel spring is discussed more thoroughly in Chapter 2.

Parameters are often expressed in terms of the quantity χ, which is the ratio of the average length of a non-Hookean spring to that of a Hookean spring. This quantity is useful as a natural way to express how parameters such as HI strength h^* or EV radius d should change as the spring force law is altered [16]. It is best calculated in Hookean units, and is defined by:

$$\chi^2 = \frac{1}{3} \frac{\int Q^{*4} e^{\phi^*}}{\int Q^{*2} e^{\phi^*}} \tag{3.16}$$

where Q^* and ϕ^* are the non-dimensional spring length and spring potential respectively. Although it is in principle possible to derive this value analytically for the FENE-Fraenkel spring, it has different forms depending on the values of σ and δQ (which cause the lower limit of integration to be either $\sigma - \delta Q$ or 0). In practice, it is straightforward to calculate numerically by quadrature. For the MS-WLC-Fraenkel spring force law, there is no analytical expression for χ, and so the integrations must be performed numerically, with careful attention paid to avoid reaching floating-point infinities due to the exponentiation.

3.2.3 Brownian dynamics simulation methodology

By including all of these physical effects in our equation of motion for the chain, we can derive the following Fokker-Planck equation for the evolution of the distribution function $\psi(\boldsymbol{r}_1, \ldots, \boldsymbol{r}_N)$ [13, 34, 53]:

$$\frac{\partial \psi^*}{\partial t^*} = -\sum_{\nu=1}^{N} \frac{\partial}{\partial \boldsymbol{r}_\nu^*} \cdot \left\{ \boldsymbol{\kappa}^* \cdot \boldsymbol{r}_\nu^* + \frac{1}{4} \sum_\mu \boldsymbol{D}_{\nu\mu} \cdot \boldsymbol{F}_\mu^{\phi *} \right\} \psi^* + \frac{1}{4} \sum_{\nu,\mu=1}^{N} \frac{\partial}{\partial \boldsymbol{r}_\nu^*} \cdot \boldsymbol{D}_{\nu\mu} \cdot \frac{\partial \psi^*}{\partial \boldsymbol{r}_\mu^*} \tag{3.17}$$

where $\boldsymbol{F}_{\mu}^{\phi *}$ is the total force on bead μ due to the sum of the spring, bending and EV forces, and the tensor $\boldsymbol{D}_{\nu\mu} = \delta_{\nu\mu}\boldsymbol{\delta} + \zeta\boldsymbol{\Omega}_{\nu\mu}$ takes into account hydrodynamic interactions between beads μ and ν.

The numerical integration of Equation 3.17 is undertaken on the basis of the equivalent Itô stochastic differential equation for the chain configuration [13], which we give in the same form as Prabhakar and Prakash [53]:

$$\mathrm{d}\boldsymbol{R} = \left[\boldsymbol{K}\cdot\boldsymbol{R} + \frac{1}{4}\boldsymbol{D}\cdot\boldsymbol{F}^{\phi}\right]\mathrm{d}t^{*} + \frac{1}{\sqrt{2}}\boldsymbol{B}\cdot\mathrm{d}\boldsymbol{W} \tag{3.18}$$

where $\boldsymbol{R}$ is a $3\times N$ matrix containing bead co-ordinates, $\boldsymbol{K}$ is a $3N\times 3N$ block matrix with the diagonal blocks containing $\boldsymbol{\kappa}^{*}$ and others equal to 0, $\boldsymbol{F}^{\phi}$ is a $3\times N$ matrix containing total force vectors on each bead (due to spring, bending, and EV potentials), $\boldsymbol{D}$ is a $3N\times 3N$ block matrix where the $\nu\mu$ block contains the $\boldsymbol{D}_{\nu\mu}$ tensor components, $\boldsymbol{W}$ is a $3\times N$ dimensional Wiener process and $\boldsymbol{B}$ is a matrix such that $\boldsymbol{D} = \boldsymbol{B}\cdot\boldsymbol{B}^{\mathrm{T}}$. The matrix $\boldsymbol{B}$ is not calculated directly, but instead the product $\boldsymbol{B}\cdot\mathrm{d}\boldsymbol{W}$ is evaluated using a Chebyshev approximation, as originally proposed by Fixman [53, 105]. We give details of this approximation, as well as alternative methods of calculating the required matrix square root, in Appendix E. Additionally, the stochastic differential equation is integrated using a semi-implicit predictor-corrector method with a lookup table for the spring force law, the algorithm for which has been detailed extensively elsewhere [13, 23, 51–53]. We have given the details of the semi-implicit solution steps, as well as the implementation of lookup tables, in Appendix B.

Simulations are generally run with $\mathcal{O}(10^{3})$ trajectories for 50 relaxation times or 5000 strain units, whichever is shorter. This ensures plenty of sampling at steady state for all runs besides the most extensible FENE and Hookean springs, which were run for 50 relaxation times at all shear rates.

Several conformational, rheological and optical properties are extracted from our BD simulations. The overall contribution of the polymers to the stress tensor is given by the Kramers expression [34]:

$$\boldsymbol{\tau}_{p} - \eta_{s}\dot{\boldsymbol{\gamma}} = -n_{p}\sum_{\nu=1}^{N}\langle\boldsymbol{r}_{\nu}\boldsymbol{F}_{\nu}^{\phi}\rangle + n_{p}k_{\mathrm{B}}T\boldsymbol{\delta} \tag{3.19}$$

where again $\boldsymbol{F}_{\nu}^{\phi}$ is the sum of the spring, EV and bending forces on each bead, and n_{p} is the number density of polymers. From this the following material functions can be extracted:

$$-\eta_{p} = \frac{\tau_{p,xy} - \eta_{s}\dot{\gamma}}{\dot{\gamma}} \tag{3.20a}$$

$$-\Psi_{1} = \frac{\tau_{p,xx} - \tau_{p,yy}}{\dot{\gamma}^{2}} \tag{3.20b}$$

$$-\Psi_2 = \frac{\tau_{p,yy} - \tau_{p,zz}}{\dot{\gamma}^2} \tag{3.20c}$$

namely the polymer contribution to the viscosity η_p, and the first and second normal stress coefficients Ψ_1 and Ψ_2 respectively. Additionally, we measure the polymer extension in each direction using the gyration tensor, defined as:

$$\boldsymbol{G} = \frac{1}{N}\left\langle \sum_{\nu=1}^{N} \boldsymbol{r}_\nu \boldsymbol{r}_\nu \right\rangle \tag{3.21}$$

with the radius of gyration given by the trace of this tensor, and with the components:

$$R_{g,\alpha} = G_{\alpha\alpha} \tag{3.22}$$

where $\alpha = \{x, y, z\}$.

Two orientation angles (often referred to as extinction angles) can be defined based on $\boldsymbol{G}$ and $\boldsymbol{\tau}_p$. These are unfortunately also represented by χ in the literature, not to be confused with the equilibrium spring length from Equation 3.16. They are denoted χ_τ and χ_G, and are essentially the orientation of the stress tensor and gyration tensor respectively, with the forms:

$$\chi_G = \frac{1}{2}\arctan\frac{2\langle G_{xy}\rangle}{\langle G_{xx} - G_{yy}\rangle} \tag{3.23}$$

$$\chi_\tau = \frac{1}{2}\arctan\frac{2\tau_{xy}}{\tau_{xx} - \tau_{yy}} = \frac{1}{2}\arctan\frac{2\eta_p}{\Psi_1\dot{\gamma}} \tag{3.24}$$

Finally, we have the tumbling period (denoted τ_{tumble}), which can be measured in one of two ways. The first is to essentially count the total revolutions of the end-to-end vector of the polymer as a function of time, and so derive a kind of angular velocity. This method was employed by Dalal et al. in a BD simulation study [78], and also by Huber et al. in an experimental study directly imaging actin molecules [106]. However, it is also possible to define a tumbling period related to the cross-correlation between conformational changes in flow and gradient directions [30, 107, 108]. These quantities are reasonably straightforward to calculate in our simulations, but require some detailed explanation, and so we refer the reader to Appendix G for details.

Results are often plotted in terms of Weissenberg number $Wi = \dot{\gamma}^*\eta^*_{0,p}$, also referred to as reduced shear rate β in the literature [34]. The zero-shear viscosity scales similarly to the end-to-end relaxation time up to a constant factor, and so results adjusted by this relaxation time rather than viscosity are qualitatively similar [34]. The zero-shear viscosity is determined predominately from the Newtonian plateau at low shear rates for models with HI, although initial estimates are derived using Green-Kubo relations over the stress autocorrelation at equilibrium. We have compared several methods for determining zero-shear viscosity and

relaxation times in Appendix F, such as autocorrelation, step strain procedures, and stretch-relaxation. We also note that it is possible to calculate low-shear material properties using so-called transient time correlation functions (TTCF) [109, 110], which to our knowledge have not been used in the context of BD previously, but which are used extensively in non-equilibrium molecular dynamics approaches, which we have also described in Appendix F.

Note that for models without HI, the zero-shear viscosity can be expressed directly in terms of the radius of gyration [111]:

$$\eta_{p,0} = \frac{n_p \zeta}{6} N \langle R_g^2 \rangle_{\text{eq}} \tag{3.25}$$

and further, for chains without EV, HI or a bending potential, the radius of gyration can be given analytically in terms of the number of beads and equilibrium spring length [112]:

$$\langle R_g^2 \rangle_{\text{eq}} = \frac{N^2 - 1}{6N} \langle Q^2 \rangle_{\text{eq}} \tag{3.26}$$

These expressions are also used to validate the BD predictions.

Finally, we employ variance reduction (VR) techniques at low shear rates to obtain more precise predictions [13, 93, 113].

3.3 Results

We begin by summarising previous results for Hookean and FENE springs using our model with HI and EV, systematically displaying the effects of each piece of physics, as seen in Figure 3.5. Although these are certainly not novel findings, having been detailed for example by Ahn et al. in 1993 [68], they represent a wider range of parameter space than is currently in the literature, and are furthermore useful to inform later results.

Figure 3.5 (a) and (b) give η_p^* and $R_{g,x}^*$ curves for 20-bead Hookean and FENE chains without EV, but with and without HI, for a variety of FENE b-parameters (here identified as the total extensibility, $\delta Q \equiv \sqrt{b}$). The Hookean chain without HI shows no deviation from the Rouse zero-shear viscosity with shear rate, as expected for an infinitely extensible chain. Adding HI causes slight shear-thinning away from the Zimm viscosity, then shear-thickening towards the Rouse viscosity, due to HI being effectively weakened as the chain is stretched.

A highly extensible ($\delta Q > 100$) FENE chain with HI also displays this behaviour, following the Hookean + HI result up until shear rate $\dot{\gamma}^* \approx 1$, after which the finite extensibility of the FENE chain begins to be felt, and the model displays a terminal shear-thinning slope of approximately -0.6. This corresponds to a plateau in the chain extension in Figure 3.5 (b), showing the relationship between extension and viscosity, caused by orientation and stretching

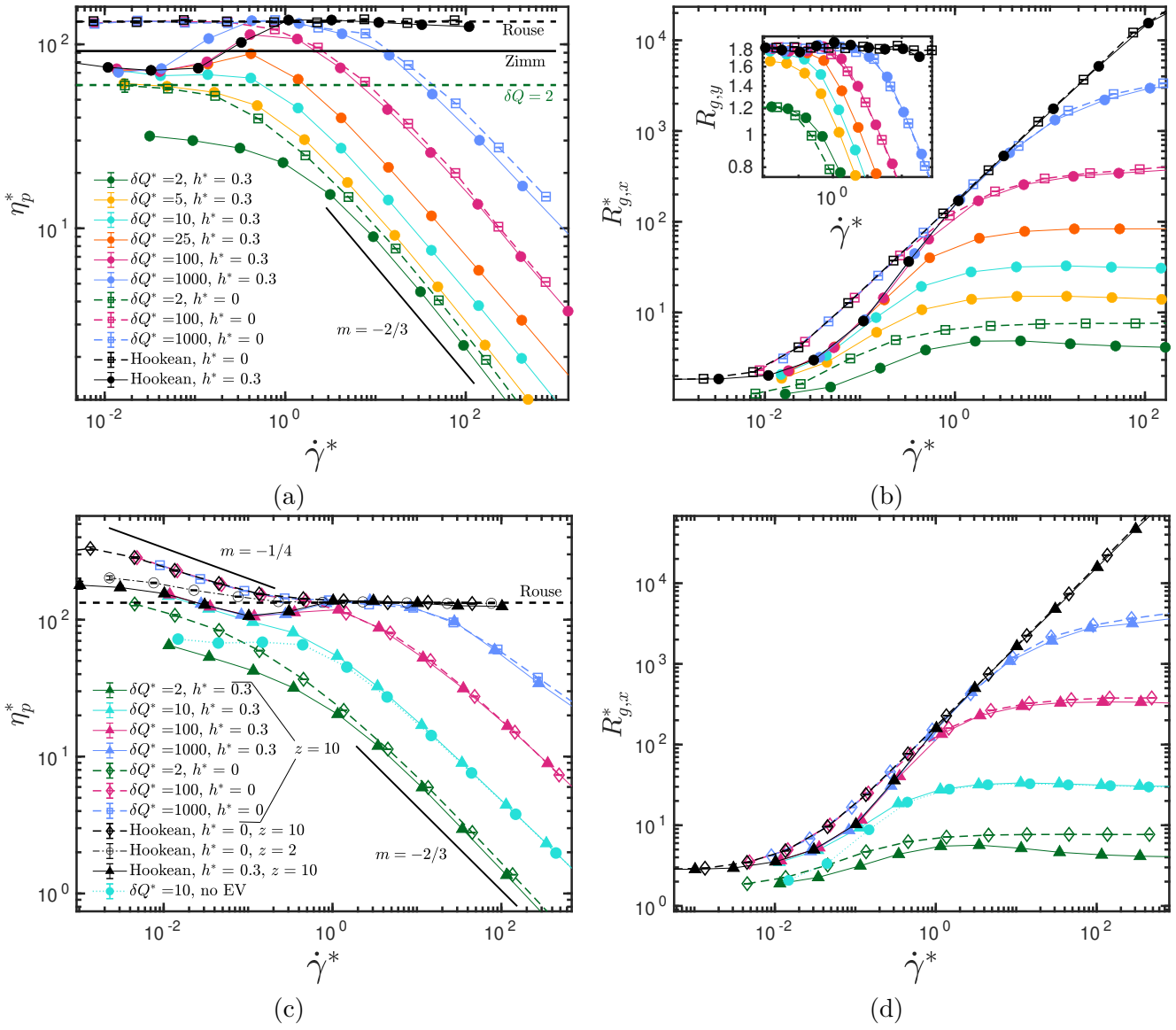

FIGURE 3.5: FENE springs of varying δQ, displaying both shear viscosity (a and c) and the xx-component of the gyration tensor (b and d) for 20-bead chains. Inset in (b) shows the scaling of the yy-component of the gyration tensor. Horizontal lines in (a) and (c) correspond to analytical results based on Equation 3.25, which can be calculated analytically with no HI, or using pre-averaged HI for the Zimm result. Labelled slopes ($m = -2/3$ and $m = -1/4$) are guides to the eye and do not imply exact terminal scaling with shear rate. For (c) and (d), all FENE chains include EV, with $z = 10$, with z^* calculated via Equation 3.12 and $d^* = z^{*1/5}$. Where not visible, error bars are smaller than symbol size.

of each link in the chain. The inset to Figure 3.5 (b) displays the $(-2/3)$ slope in $R_{g,y}$ for the FENE chains (not shown), notably the same as the shear-thinning exponent. This can be intuitively understood in terms of the Giesekus expression for the stress tensor of a chain without HI, where the stress tensor is essentially proportional to the averaged gyration tensor [34]. As δQ is decreased, the shear-thickening vanishes, apparently due to the simultaneous decrease in the shear rate for onset of shear-thinning - in other words, the shear thinning kicks in before the HI has a chance to cause shear thickening. Alternatively, one could reason that

the chain can't stretch enough to reach the Rouse viscosity before the finite extensibility of the chain is reached. Once δQ is small enough, the finite extensibility causes a decrease in the coil size at equilibrium, leading to a lower zero-shear viscosity [111], as seen in the $\delta Q = 2$ and $\delta Q = 5$ cases both with and without HI.

Once we switch on EV (through a soft Gaussian potential), the low and intermediate shear behaviour changes, as shown in Figure 3.5 (c) and (d). This potential is set with z^* as in Equation 3.12, and $d^* = z^{*1/5}$, as per previous suggestions [16, 96], giving a particular solvent quality z. This EV potential causes a swelling at zero shear both in the viscosity and gyration radius, as can be seen by comparing the Hookean EV chain with the Rouse viscosity, and also the cyan dotted-line circles and cyan full-line triangles ($\delta Q = 10$, $z = 0$ and 10) in Figure 3.5 (c) and (d). It is this swelling which defines the solvent quality, such that a smaller z leads to less swelling as expected.

Beyond equilibrium, as the effective solvent quality is increased from $z = 0 \rightarrow 2 \rightarrow 10$, we see some shear thinning prior to the $(-2/3)$ terminal exponent from the FENE springs. This 'intermediate' shear-thinning approaches a power-law slope of $-1/4$ as the solvent quality approaches infinity, which previous work has demonstrated exactly in the long-chain limit using BD and also renormalisation group approaches [14, 91, 96]. For the Hookean and highly extensible FENE chains ($\delta Q > 100$), there is something of a second Newtonian plateau at high shear rates, which is caused by the effect of EV lessening as beads are pulled apart due to flow. At higher shear rates, the FENE springs show the expected $\approx (-2/3)$ power-law slope in viscosity, essentially unchanged by the addition of EV. This can be seen particularly in the behaviour of the $\delta Q = 10$ FENE chains with and without EV (cyan symbols), where Figure 3.5 (c) and (d) show a difference in zero-shear behaviour, but identical high-shear properties.

Overall, our results match with previous theoretical and computational findings for FENE and Hookean springs both with and without HI and EV. In summary, the key features are an $\approx (-2/3)$ slope in viscosity at high shear rates for finite extensibility, and an $\approx (-1/4)$ power law slope in viscosity at intermidiate shear rates due to EV, slight shear-thickening due to HI, and differences in onset of shear thinning due to finite extensibility.

3.3.1 FENE-Fraenkel spring results

Now that we have outlined the behaviour of FENE and Hookean springs with HI and EV, we can 'stiffen' our FENE-Fraenkel springs by increasing σ to head towards the bead-rod limit. We first note that our model is indeed able to reproduce the bead-rod results of Petera and Muthukumar [37] in the 'rodlike' limit, even when HI is included (see Figure 3.6), in contrast to the previous results of Hsieh and Larson [23]. We suspect that this difference is due to

their unsuitably large timestep [65], noting that our model is able to reproduce the bead-rod results with both a 5× smaller spring constant, as well as a 10× larger extensibility. As we will see, this finding is not surprising given the range of crossover between bead-spring and bead-rod behaviour. We also note that a recent paper by Kumar and Dalal has demonstrated that a Fraenkel spring is indeed also able to reproduce bead-rod behaviour when sufficiently stiff [114].

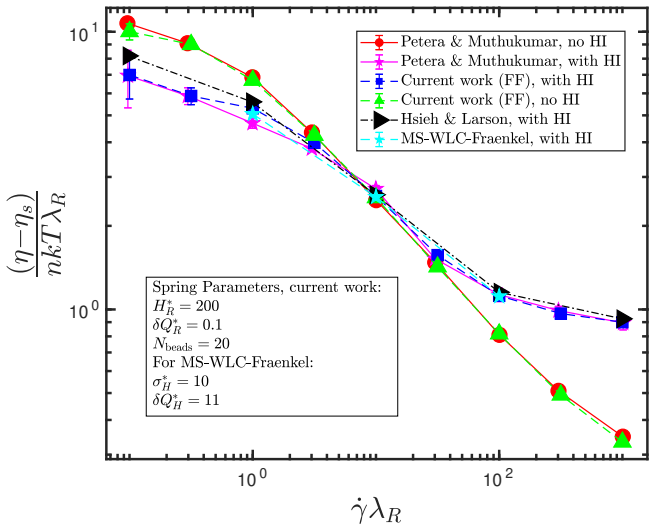

FIGURE 3.6: Comparisons between the FENE-Fraenkel spring in the current work and the bead-rod simulations of Petera and Muthukumar [37], as well as the previous FENE-Fraenkel simulations of Hsieh and Larson [23]. The timestep used was $\Delta t_H^* = 0.01$. Note that results are given in the 'rodlike' system of non-dimensionalisation, where $\lambda_R = \sigma^2\zeta/k_BT$, $H_R^* = H\sigma^2/k_BT$, and $\delta Q_R^* = \delta Q/\sigma$. In these units, the equivalent spring parameters used by Hsieh and Larson were $H_R^* = 1000$, $\delta Q_R^* = 0.01$, and $\Delta t_H^* = 4$. The MS-WLC-Fraenkel spring parameters are chosen to have the same relative extensibility around σ as our FENE-Fraenkel chain. Where not visible, error bars are smaller than symbol size.

Guided by previous results for FENE-Fraenkel dumbbells [65], we will principally investigate the change in power-law slope in viscosity with shear rate, as well as the compression in gyration radius at high shear seen in bead-rod models. For the following sets of figures, namely Figures 3.7, 3.12, 3.13, 3.14 and 3.15, we go from bead-spring to bead-rod behaviour by keeping $\sigma+\delta Q = 10$ fixed, while changing σ. For example, the cyan symbols in Figure 3.7 (a) with $\sigma = 0$ and $\delta Q = 10$ are exactly the same as our cyan-coloured FENE spring results in Figure 3.5, while the green-coloured symbols have $\sigma = 9$ and $\delta Q = 1$. This is following the procedure from our previous paper on FENE-Fraenkel dumbbells [65], which showed a smooth crossover from bead-spring to bead-rod behaviour using this arrangement.

We first examine Figure 3.7 (a), which gives the normalised viscosity as a function of Weissenberg number for $N = 20$. Alongside it, Figure 3.7 (c) displays the log-log gradient of the lines in (a). Pure FENE springs (cyan symbols) give the expected $(-2/3)$ slope in viscosity at high shear rates, as seen in Figure 3.5. This same 'spring-like' terminal slope is observed for $\sigma = 1$, 4, and 5. However, at $\sigma = 6$ and beyond, we see an increase in the power-law exponent,

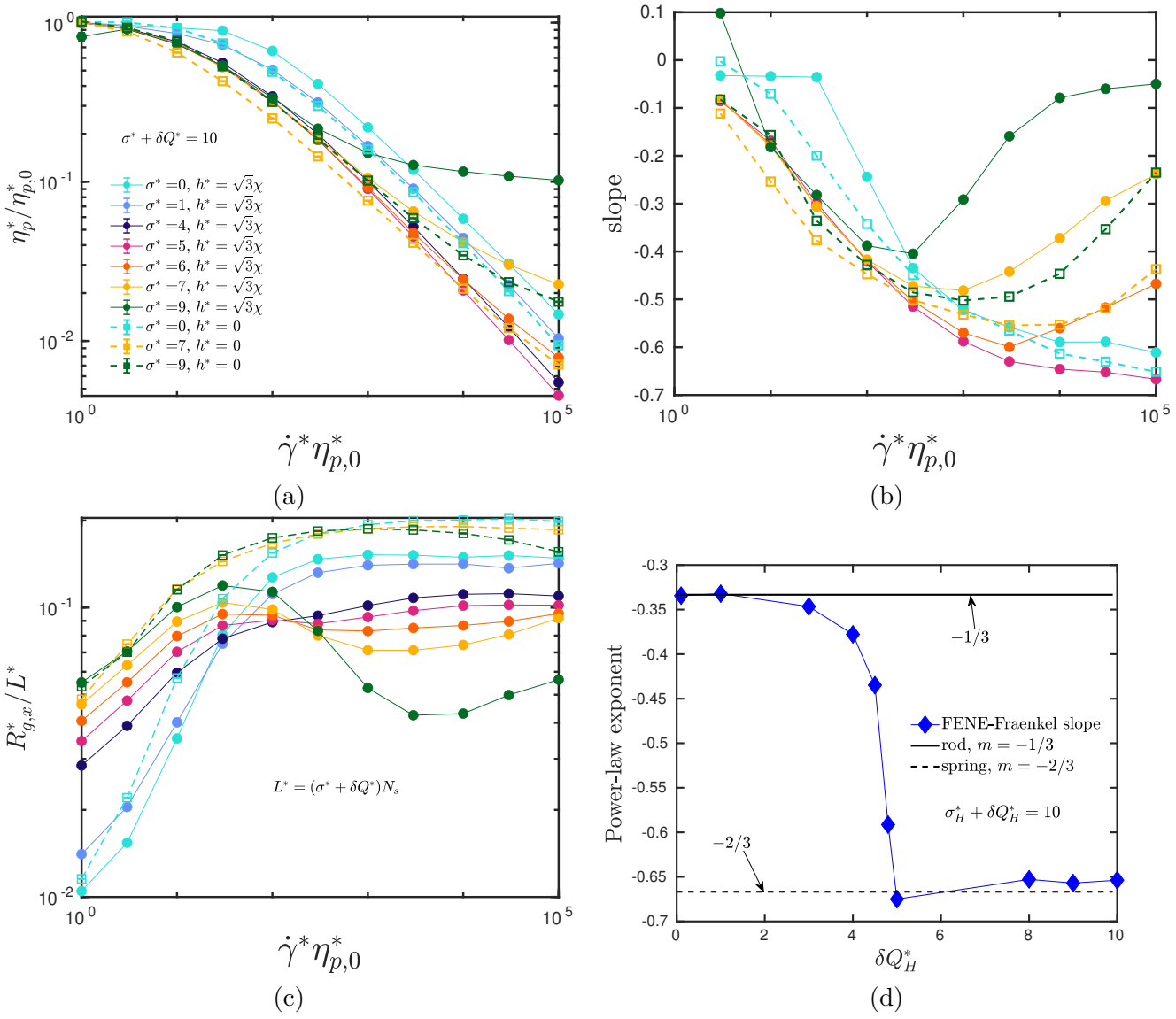

FIGURE 3.7: Calculated properties for FENE-Fraenkel springs with $\sigma^* + \delta Q^* = 10$, changing the value of σ^*. Results with HI have h^* scaled by χ calculated from Equation 3.16, such that the beads are on average osculating at equilibrium. The values of χ for $\sigma^* = 0$ to 9 are $\chi = \{0.9759, 1.2856, 2.6145, 3.1303, 3.6591, 4.1922, 5.2360\}$ respectively. Note that qualitatively similar results are seen when we set the strength of HI to a constant $h^* = 0.3$ for all springs irrespective of χ. Zero-shear viscosity is found from low-shear results, which agrees with Green-Kubo calculations to within error bars (see Appendix F). Properties for curves (a) and (c) are defined as in Equation 3.20 and Equation 3.22, while 'slope' in (c) is given by the log-log gradient of (a) at each shear rate. The total contour length L^* used to normalise $R_{g,x}$ in plot (c) is given by $L^* = (\sigma^* + \delta Q^*)N_s$. Plot (d) is reproduced here from Figure 2.13 for ease of comparison. Where not visible, error bars are smaller than symbol size.

leading to a plateauing of the viscosity at high shear rates. This is observed both with and without HI, although the effect is more pronounced with HI. The same scaling can be seen in Figure 3.7 (b), particularly for models with HI, where a compression in the flow direction at high shear rates begins roughly when $\sigma = 6$, and is more pronounced for higher σ. This was previously noted by several authors using both stiff Fraenkel springs [76, 77, 79] and true rigid

constraints [35, 37].

Interestingly, we note that since $\sigma + \delta Q = 10$, this change in behaviour occurs when $\sigma > \delta Q$, or in other words when the spring is no longer infinitely compressible. To see this, note the behaviour of the lower bound in Figure 3.4, in which the force goes to infinity at $\sigma - \delta Q$ when $\sigma > \delta Q$. This is exactly the behaviour observed for FENE-Fraenkel dumbbells [65], where the terminal slope showed a change from $(-2/3)$ to $(-1/3)$ when $\sigma > 5$. For reference, we have reproduced a key figure from Ref. [65] in Figure 3.7 (d), which gives the terminal slope at high shear for FENE-Fraenkel dumbbells as a function of δQ. These results taken together imply that even for chains, the crossover from bead-spring to bead-rod behaviour is related to the compressibility of the underlying segment, whether in the form of a rigid rod, very stiff Fraenkel spring, or the current FENE-Fraenkel spring.

To test this idea for another form of the spring potential, we use the so-called MS-WLC-Fraenkel spring, introduced in Equation 3.5. Note that for this form of the spring force law, setting a constant $\delta Q = 10$ and changing σ from $0 \rightarrow 10$ implies the same behaviour as setting $\sigma + \delta Q = 10$ for a FENE-Fraenkel spring. Additionally, unlike the FENE-Fraenkel spring, the effective spring constant (or the linear relationship between force and extension about σ) changes as $\sigma \rightarrow \delta Q$, such that one both 'stiffens' the spring and makes it less extensible for higher σ. Results are shown in Figure 3.8, without HI or EV and with constant $\delta Q = 10$ and variable σ.

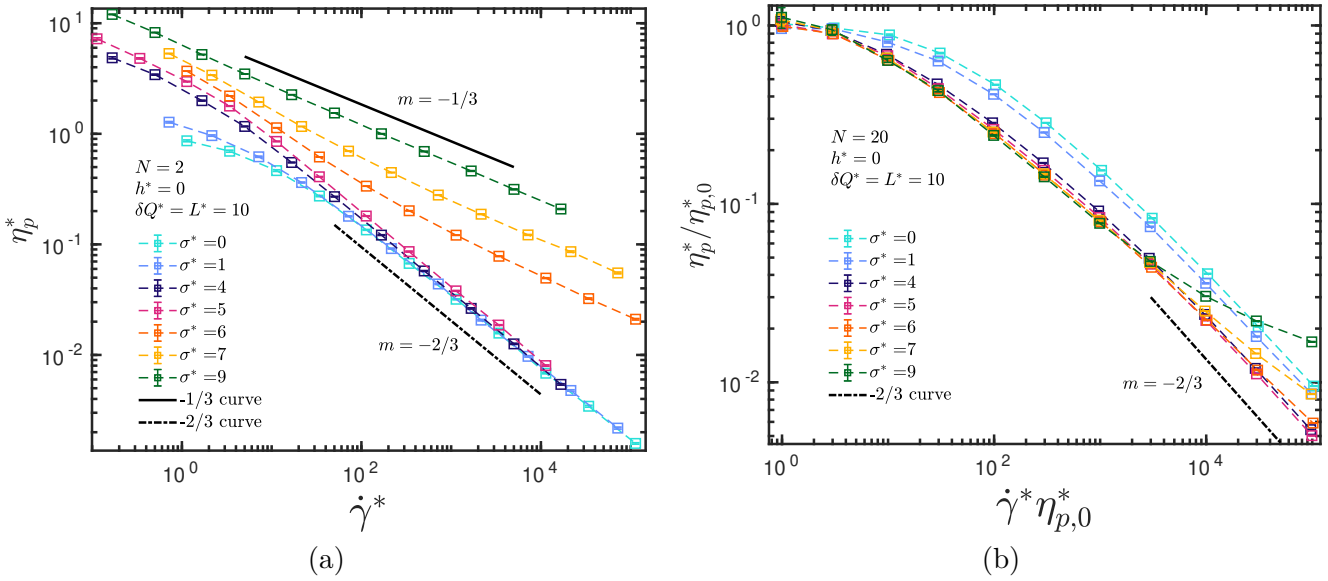

FIGURE 3.8: Viscosity scaling without HI or EV for MS-WLC-Fraenkel spring chains, as described in Equation 3.5. In this case, $\delta Q = L = 10$, giving the same total extensibility at a particular σ as for the FENE-Fraenkel spring (although not necessarily the same effective spring constant). Plot (a) gives the non-dimensional viscosity as a function of shear rate for MS-WLC dumbbells without HI. Plot (b) gives the viscosity normalised by zero-shear viscosity against Weissenberg number for 20-bead MS-WLC spring chains, also without HI. $m = -1/3$ and $m = -2/3$ lines are guides for the eye and do not imply exact terminal slopes.

For dumbbells in Figure 3.8 (a), we again see a clear $(-2/3)$ power law slope at high shear rates when $\sigma < 5$, as expected for 'spring-like' force laws. Note that in the $\sigma = 0$ limit, the traditional MS-WLC force law is recovered, as has been used by many other authors [16, 31, 115, 116], which again gives a $(-2/3)$ power law slope. However, the crossover in behaviour from $\sigma = 5$ to $\sigma = 6$ is even more pronounced than for the FF spring, possibly due to the increased effective spring stiffness H as $\sigma \to \delta Q$. The crossover from bead-spring to bead-rod behaviour again occurs when the spring can no longer compress to zero length, reinforcing the conclusion that 'rod-like' behaviour is intimately linked to spring compressibility. For the bead-spring-chain results in Figure 3.8 (b), we see a power-law slope of ≈ -0.6 for $\sigma < 5$, with a gradual plateau in viscosity at high shear rates for $\sigma > 5$, qualitatively identical to the behaviour for FF springs. The straightforward conclusion is that for shear flow, the precise form of the spring force law seems to be less qualitatively relevant than the average spring length, spring stiffness, extensibility and compressibility.

Returning briefly to Figure 3.7, one obvious feature is in the stark difference in both $R_{g,x}$ compression and high-shear plateau as one switches on HI. To investigate this effect, we have visualised the flow field caused by polymer deformation in Figure 3.9 (a), (b) and (c). First examining Figure 3.9 (a), a 20-bead chain with $\sigma = 9$, $\delta Q = 1$ at $Wi = 3000$ with $h^* = 0$, one can see the stretch of an example polymer trajectory in the flow direction caused by the background shear flow. The direction of shear flow is shown by the streamlines, while the colour represents the magnitude of velocity at each point. While the background shear flow does have a rotational component, causing tumbling, the elongational stretch leads to the classic increase in $R_{g,x}$.

We then turn to Figure 3.9 (b) and (c), where HI has been switched on. HI causes a change in the flow field at each point corresponding to:

$$\boldsymbol{v}' = [\boldsymbol{\Omega} \cdot \boldsymbol{F}] \tag{3.27}$$

where $\boldsymbol{v}'$ is the velocity perturbation due to HI, and $\boldsymbol{\Omega}$ is the RPY tensor described in Equation 3.13. In Figure 3.9 (b), we have plotted the streamlines of $\boldsymbol{v}_{\text{shearflow}} + \boldsymbol{v}'$, again with colour representing velocity magnitude at each point (and averaged over several relaxation times and trajectories). The drastic change in flow field around the center of mass of the chain is immediately obvious, demonstrating clearly why HI is often referred to as 'backflow'. This effect is highlighted in Figure 3.9 (c), which plots just $\boldsymbol{v}'$ without the background shear flow. As the flow stretches out the chain, the spring and entropic forces pull it back towards its center of mass, causing a velocity disturbance which opposes the background shear flow. It is apparently this effect which leads to a compression of bead-rod chains at high shear and with $h^* >> 0$, as the backflow disrupts elongation. This process does not occur in bead-spring models, likely due to their stretchability, which causes the effective force of HI on each bead

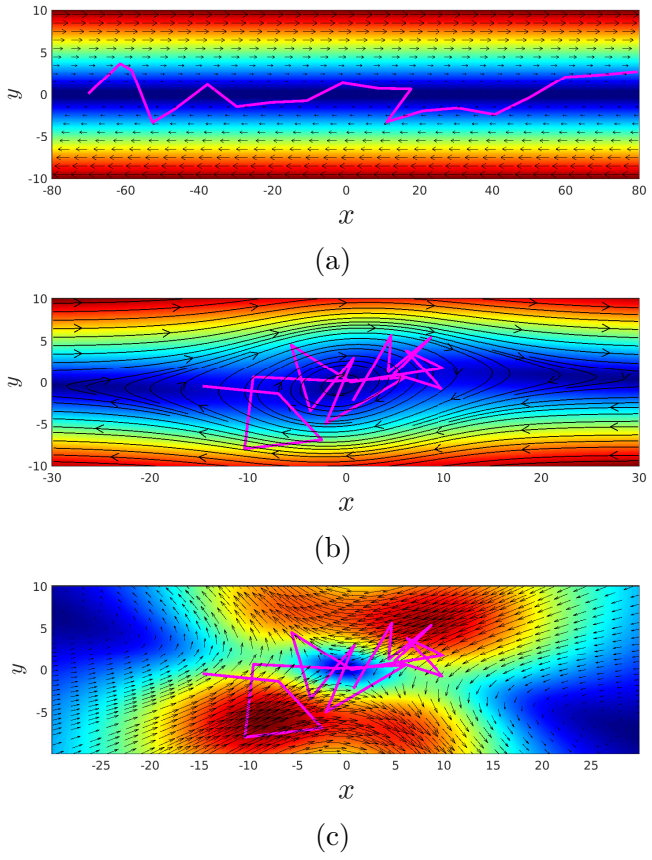

FIGURE 3.9: Velocity field due to shear flow and HI for $N = 20$, $\sigma^* = 9$, $\delta Q^* = 1$ and $Wi = 3000$. (a) is with $h^* = 0$ (no HI), (b) and (c) are with $h^* = \sqrt{3}\chi$. (c) shows the flow only due to HI, whereas (a) and (b) show the total flow. Colour scales are not the same between figures. HI perturbation is averaged over several timesteps and trajectories.

to be diminished due to increased distance between beads. Also, as we will see in Figure 3.14, the addition of a hard-core repulsion between beads disrupts this compression, likely due to increased bead-bead separation and less of a 'coiled' shape for the chain at high shear.

The behaviour of the other material functions in shear flow, the normal stress coefficients Ψ_1 and Ψ_2, are displayed in Figure 3.10. The first normal stress coefficient Ψ_1 at high shear rates is given in Figure 3.10 (a), where all σ^* values display the expected $(-4/3)$ power-law slope without HI. However, when HI is switched on, there is a slight increase in the power-law slope, but only, as we have come to expect, for the cases of $\sigma^* > 5$. While a slope of $-4/3$ has been widely reported for a variety of models [31–33, 35, 36, 71], several bead-rod simulations show an ≈ -1.1 power law slope with HI [72, 75, 100]. This again suggests that the change in behaviour is linked to the rodlike characteristics of the underlying model. We also briefly report results for the second normal stress coefficient Ψ_2 in Figure 3.10 (b). We do not report results without HI, since they are considerably smaller in magnitude and error bars overlap with 0 for a wide range of shear rates. Interestingly, Ψ_2 is negative for all σ^*, in contrast with the results for dumbbells where a crossover from positive to negative Ψ_2 was seen for

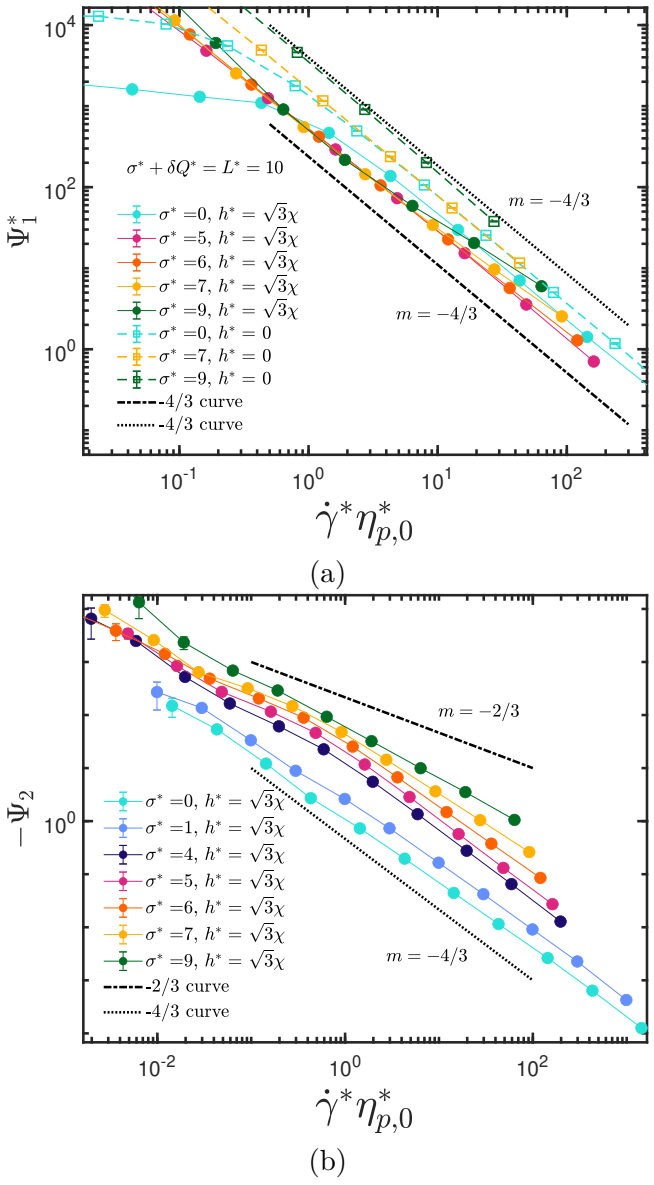

FIGURE 3.10: Normal stress coefficients (a) Ψ_1 and (b) Ψ_2 as a function of shear rate. 20-bead FENE-Fraenkel springs are used, with parameters chosen such that $\sigma^* + \delta Q^* = 10$. Error bars are unfortunately not small enough to accurately display results for Ψ_2 over a range of shear rates for models with smaller N, or for the case of $h^* = 0$. Where not visible, error bars are smaller than symbol size. Dotted lines are guides for the eye and do not imply exact terminal slopes.

sufficiently extensible springs [65]. We have attempted to calculate the magnitude of Ψ_2 for intermediate bead numbers, but results are difficult to interpret due to the large error bars (one needs significantly more sampling to observe a difference in Ψ_2 than Ψ_1). It appears that either a sufficiently 'spring-like' dumbbell, or a bead-rod chain with sufficient beads, gives a negative Ψ_2, while a bead-rod dumbbell ($N = 2$) gives a positive Ψ_2. We have discussed the history of Ψ_2 calculations in our previous paper [65] (found in Section 2.3.2.2) - to summarise, there is still no clear experimental consensus on the correct sign of Ψ_2.

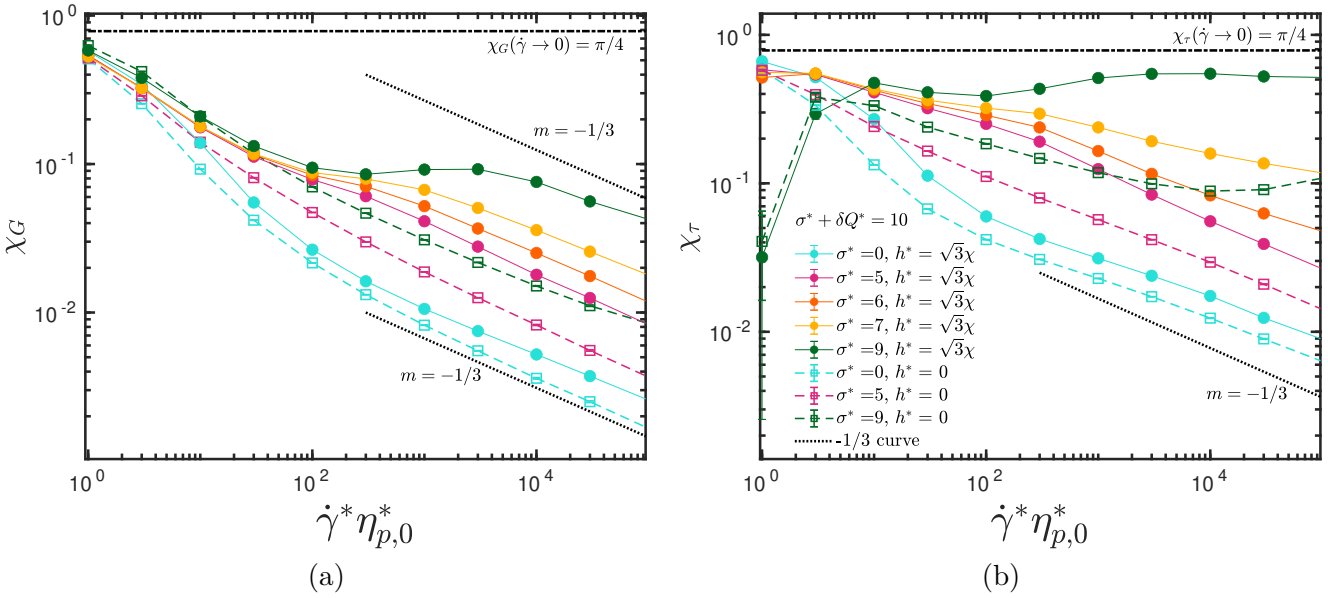

FIGURE 3.11: Orientation angles (a) χ_G and (b) χ_τ as a function of shear rate. 20-bead FENE-Fraenkel springs are used, with parameters chosen such that $\sigma^* + \delta Q^* = 10$. The zero-shear value for both χ_G and χ_τ of $\pi/4$ (since $1/2 \arctan \infty = \pi/4$) is displayed as a horizontal dotted line. First two $\sigma^* = 9$ data points for χ_τ at low shear are certainly artefacts, related to a changing sign in the denominator of Equation 3.24 due to large error in Ψ_1, but are nevertheless included for completeness. Where not visible, error bars are smaller than symbol size. Dotted lines are guides for the eye and do not imply exact terminal slopes.

The orientation or extinction angles χ_G and χ_τ from Equation 3.23 and Equation 3.24 are plotted in Figure 3.11. For χ_G, all models show a roughly $(-1/3)$ power law slope at high shear rate shear rate irrespective of σ^* or the presence of HI. However, the intermediate-shear behaviour is quite varied, with low σ^* and no-HI curves displaying a fairly monotonic decrease, while the $\sigma^* > 5$ cases with HI show an initial $\approx (-1/3)$ slope, then a slight leveling off before the final terminal slope. This is likely related to the behaviour of the components of the gyration tensor - while we have not displayed this behaviour in figures, $R_{g,y}$ tends to decrease monotonically for all non-Hookean springs irrespective of HI or EV, so a decrease in $R_{g,x}$ at intermediate shear rates is reflected in a change in behaviour of χ_G for certain FENE-Fraenkel springs. At higher shear rates, $R_{g,x}$ levels off as seen in Figure 3.7 (c), but the continuing decrease of $R_{g,y}$ leads to a further decrease in χ_G.

The stress tensor orientation χ_τ displays similar behaviour, particularly at low and intermediate shear rates. At high shear rates, the $\sigma^* > 5$ cases deviate from the other curves, with a plateau in χ_τ for $\sigma^* = 9$. This plateau implies that the terminal slopes of η_p and Ψ_1 differ by only $\dot\gamma^{-1}$, meaning that $\eta_p/\Psi_1\dot\gamma$ is a constant. For FENE-Fraenkel dumbbells, the divergence of χ_G and χ_τ was a clear marker of the change from bead-spring to bead-rod behaviour, and this seems to hold somewhat for chains. While several other authors have calculated χ_G and χ_τ [36, 72, 96, 99, 115], the only direct calculation of the power-law slope appears to be from

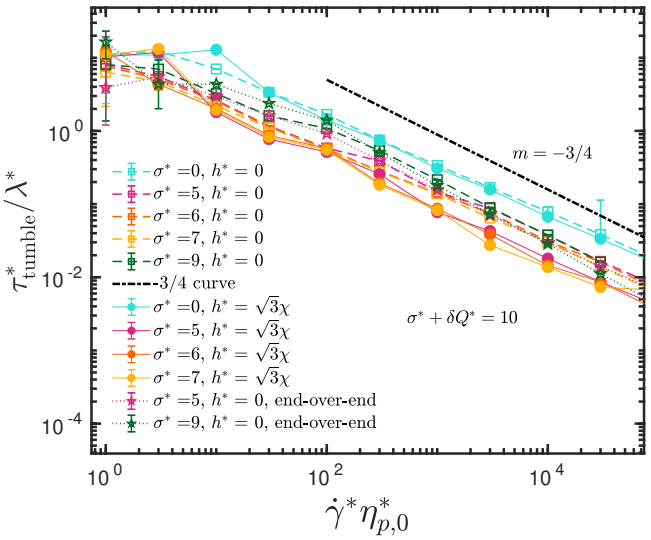

FIGURE 3.12: Tumbling calculations, using cross-correlation method as detailed in Equation G.2. Results are given as the tumbling period τ_{tumble} divided by the relaxation time λ calculated from the end-to-end auto-correlation of the radius of gyration at equilibrium. Also given are two results with the 'end-over-end' tumbling time calculations, showing nearly identical, and certainly qualitatively similar behaviour. $m = -3/4$ line is a guide for the eye and does not imply exact terminal slopes.

Schroeder et al. [31], who found a -0.43 slope in χ_G from both bead-spring simulations and direct imaging of DNA chains, albeit with rather large error bars.

Calculations of the tumbling times of our FENE-Fraenkel chains was performed using the two methods detail in Appendix G. Interestingly, we do not find any difference in the scaling of tumbling times for all FENE-Fraenkel springs in Figure 3.7. This is seen in Figure 3.12, which shows a nearly $-3/4$ power-law slope in tumbling time with shear rate irrespective of the inclusion of HI, or the stiffness of the springs. The implication is that tumbling time is a universal function of the shear rate and overall polymer relaxation time, in contrast to what we have seen for other solution properties where the included non-linear physics can lead to drastic changes in behaviour. Our finding of a $(-3/4)$ power-law slope agrees with the findings of Dalal and coworkers [79] for 100-bead Fraenkel-spring chains without HI, but their model changed to a -1.1 power law slope at high shear when HI (but not both EV and HI) was included. They used only the end-on-end method for calculating tumbling times, and so it would be enlightening to re-run the analysis for their system using the cross-correlation method. Additionally, Schroeder et al. [80] find a $-2/3$rds power law slope in the tumbling time from the peak in the power spectral density irrespective of inclusion of HI or EV, for both experiments and simulation of a bead-spring chain with HI and EV.

We also wish to check how the qualitative behaviour of our FF springs changes with number of beads. This is shown in Figure 3.13, for both $\sigma = 0$ and $\sigma = 9$. For the FENE spring, $\sigma = 0$, we see an $\approx (-2/3)$ slope in viscosity with shear rate for all chain lengths at high shear. However, the onset of shear thinning occurs at successively higher shear rates for longer

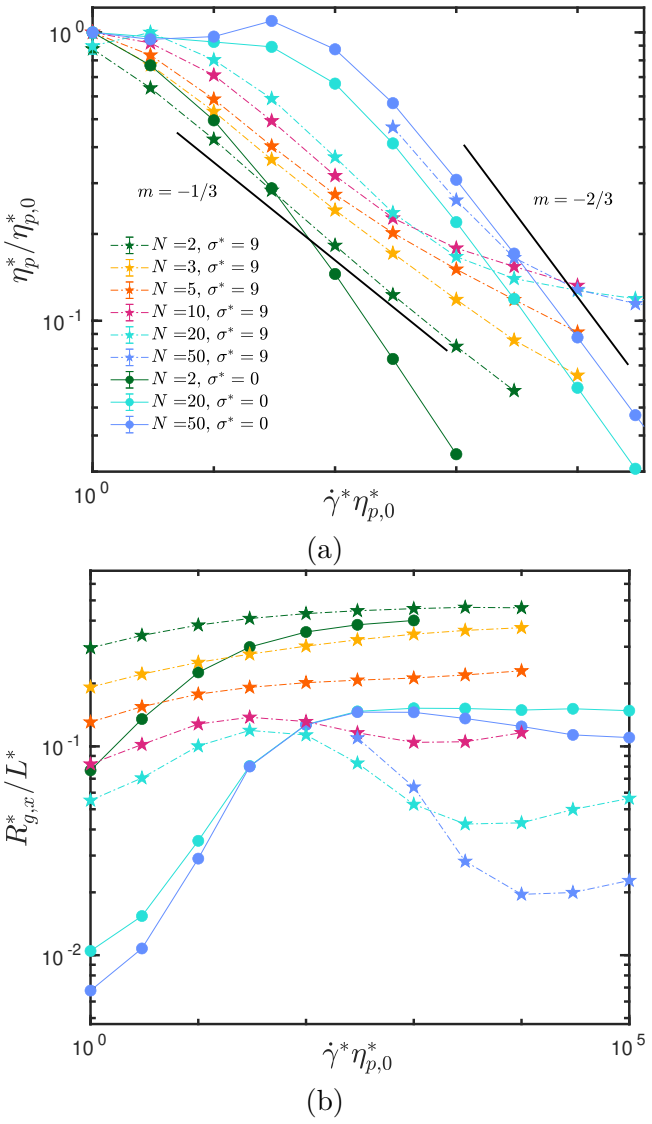

FIGURE 3.13: FENE-Frankel springs with HI but no EV and $\sigma^* + \delta Q^* = 10$, presented as a function of bead number. Plot (a) gives the viscosity divided by the zero-shear viscosity versus Weissenberg number, while plot (b) gives the xx-direction gyration tensor component divided by total contour length of the chain $L^* = (\sigma^* + \delta Q^*)N_s$. Note that $\sigma = 0$ corresponds to a FENE spring with $\delta Q = 10$, while $\sigma = 9$ is a 'rod-like' FENE-Fraenkel spring. In all cases, $h^* = \sqrt{3}\chi$. $m = -1/3$ and $m = -2/3$ lines are guides for the eye and do not imply exact terminal slopes.

chains, which matches with the later onset of shear thinning for more extensible FENE springs (larger δQ). Additionally, the $N = 50$ FENE chain with HI displays slight shear-thickening at intermediate shear rates. Overall, this suggests that for FENE springs, qualitatively one finds that changing the extensibility is equivalent in many ways to changing the number of springs, once there are enough beads (in this case, > 20) for sufficient degrees of freedom.

However, behaviour is somewhat different for bead-rod chains. The $\sigma = 9$ dumbbell of course gives the expected $-1/3$rd power law slope in viscosity, and a monotonic increase in gyration tensor component in the flow direction due to alignment. At higher bead numbers, we again

have a delayed onset of shear thinning, but also the appearance of a high-shear plateau in viscosity, which becomes more pronounced as N is increased. It's clear that the chain conformation observed in Figure 3.9 can only occur once there are sufficient numbers of chain links for significant compression to occur, and likely for significant backflow to be felt. The compression in the flow direction appears more pronounced at higher bead numbers, as seen in Figure 3.13 (b). Additionally, we do see a slight plateauing of the viscosity for $N = 5$, even though there is no apparent flow-direction compression - this compression is not a necessary condition for a change in the shear-thinning exponent. Finally, there appears to be no shear-thickening for bead-rod chains, although this may require far larger numbers of beads. For example, a 350-bead chain with HI and EV simulated using an extrememly efficient algorithm by Moghani and Khomami [75] shows slight hints of intermediate-shear thickening before the terminal shear-thinning slope is reached, however it's unclear whether this is a real result or due to lack of sufficient sampling at low shear.

3.3.2 Addition of EV and bending potentials to FF bead-spring chains

As previously mentioned, EV potentials can be given in either 'soft' or 'hard' forms. The 'hard' potential is the purely repulsive SDK (in Equation 3.9, with $\varepsilon = 0$), where the force diverges to infinity at small bead separation, preventing overlap. The 'soft' potential is the Gaussian potential (given in Equation 3.10, with $d^* = z^{*1/5}$), which has a finite force at low bead separations, pushing beads apart but not completely preventing overlap. For the Gaussian potential, there are well-developed theories of polymer swelling based on so-called two-parameter theory [90], which says that the value of some property away from the theta-point (for simulations, this implies no EV potential) can be written as the value at the theta point multiplied by some function of the universal scaling variable z, the solvent quality [12, 93]. Specifically, it has previously be shown that by calculating z^* as per Equation 3.12, one obtains universal predictions of swelling in the long chain limit (as $N \to \infty$), irrespective of the value of d^* [16]. Additionally, one finds a universal $-1/4$ power-law scaling in the viscosity with shear rate for $z \to \infty$ and $N \to \infty$ [96], a result in alignment with renormalisation group calculations [91]. In summary, we generally define our EV potential not in terms of the direct microscopic details of the polymer, but instead the measured static or dynamic swelling at equilibrium, which should be independent of fine-grained details such as the exact form of the potential in the long-chain limit.

For purely repulsive hard-core potentials, as we have used here for the case of the SDK potential with $\varepsilon = 0$, correspond to the athermal limit, where $z \to \infty$ [117]. As has been mentioned, a highly repulsive potential appears to remove the high-shear plateau in viscosity for bead-rod models [37, 75, 100], as well as the compression at high shear [79]. We wish to determine

whether the 'soft' and 'hard' potentials are equivalent in shear flow, particularly for the less extensible FENE-Fraenkel springs.

Here we present results for $N = 20$ bead chains with both Gaussian and purely repulsive SDK potentials, in order to study the differences for more rod-like models. Both of these potentials cause swelling at equilibrium, seen in the zero-shear viscosity of Figure 3.14 (a) and the equilibrium gyration radius in Figure 3.14 (b). In fact, the Gaussian potential leads to slightly more equilibrium swelling than the repulsive SKD potential.

While the two EV potentials have a similar qualitative effect near equilibrium, as the shear rate is increased there are considerable differences. The most obvious effect is the convergence in viscosity for the no-EV and Gaussian-EV cases, leading to a similar terminal shear-thinning slope for the $\sigma = 0$ (FENE) case, or a high-shear plateau for the $\sigma = 7$ and $\sigma = 9$ cases. This is also somewhat apparent in the $R_{g,x}$ scaling, which shows similar qualitative behaviour with shear rate for all three σ values with and without Gaussian EV.

However, the SDK potential, which prevents bead overlap, leads to entirely different qualitative results. The high-shear plateau is entirely absent, and $R_{g,x}$ monotonically increases to a similar value for both $\sigma = 7$ and $\sigma = 9$. Although these results are given for only $N = 20$, other authors find similar results for longer chains [79], with the longest available in the literature being Moghani and Khomami's 350-bead-rod chains with full HI and repulsive hardcore EV [75] (which shows no compression at high shear rates, and an ≈ -0.28 power-law slope in viscosity). There are several tentative conclusions which can be drawn from this result. Firstly, the swelling at equilibrium due to EV does not necessarily predict the shear-flow behaviour for finite chains (for which universal scaling results don't necessarily apply). There is a clear distinction between potentials which cause chain swelling but allow bead overlap, and those which cause the same swelling but do NOT allow bead overlap. Secondly, as seen by the similar terminal shear-thinning slopes for $\sigma = 7$ and $\sigma = 9$, and particularly the convergence of $R_{g,x}$, implies that a hard EV potential in some sense 'takes over' from the spring potential at high shear rates. An SDK potential with $d^* = 0.8\sqrt{3}\chi$, as in Figure 3.14, almost represents a 'pearl-necklace' model, where beads exclude each other on roughly the range given by half their average spring length. Finally, although not shown here, we note that these effects diminish as d^*_{SDK} is reduced (the effective range of interactions), even for 100-bead chains as previously demonstrated by Dalal et al. [79]. A more detailed study could use an SDK or LJ potential with attractive and repulsive components, carefully determine the ε which represents a θ-solvent [94], and then compare results with Gaussian EV in the long-chain limit at the same solvent quality z.

We now arrive at our final piece of qualitative physics, the bending potential, which represents polymer semiflexibility. A bending potential has been included by other authors in BD simulations [69, 71, 76, 77, 79, 97, 118], often alongside an additional torsional potential and rodlike

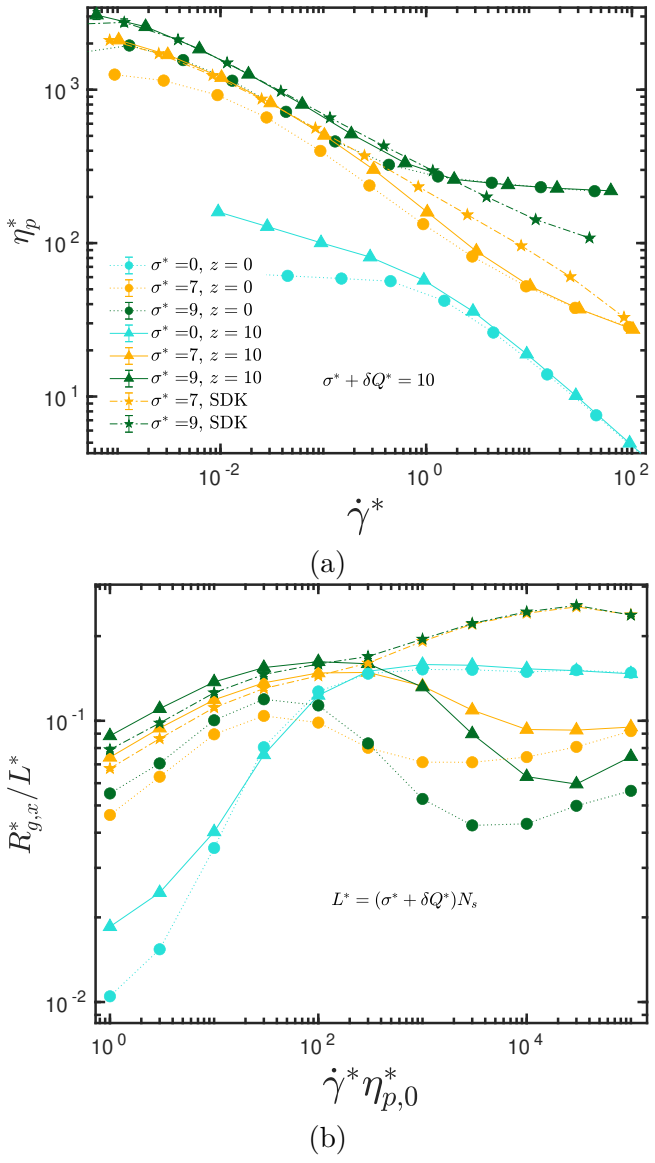

FIGURE 3.14: Effects of inclusion of excluded volume potentials on the shear-behaviour of various FENE-Fraenkel springs. Plot (a) gives the non-dimensional viscosity against the non-dimensional shear rate. Plot (b) gives the xx-component of the radius of gyration tensor normalised by the total contour length $L^* = (\sigma^* + \delta Q^*)N_s$. All examples have $\sigma^* + \delta Q^* = 10$, $N = 20$ and $h^* = \sqrt{3}\chi$. Circle symbols with dotted lines have no EV. Triangle symbols with solid lines have Gaussian potentials using parameters $z = 10$, $z^* = z\chi^3/\sqrt{N}$ and $d^* = z^{*1/5}$. Star symbols with dashed lines have an SDK potential using parameters $\varepsilon = 0$ and $d^* = 0.8\sqrt{3}\chi$.

bead-bead links. Generally, this leads to a $(-1/3)$ slope in the viscosity at high shear rates for very strong bending potentials, as expected for 'stiff' polymers, and this exponent does change towards $(-1/2)$ with the strength of the bending potential in combination with stiff Fraenkel springs [97]. Additionally, the high-shear compression in the flow direction appears to be lessened through introducing semiflexibility [77, 79].

On the other hand, semi-analytical models enforce the semiflexibility directly through an

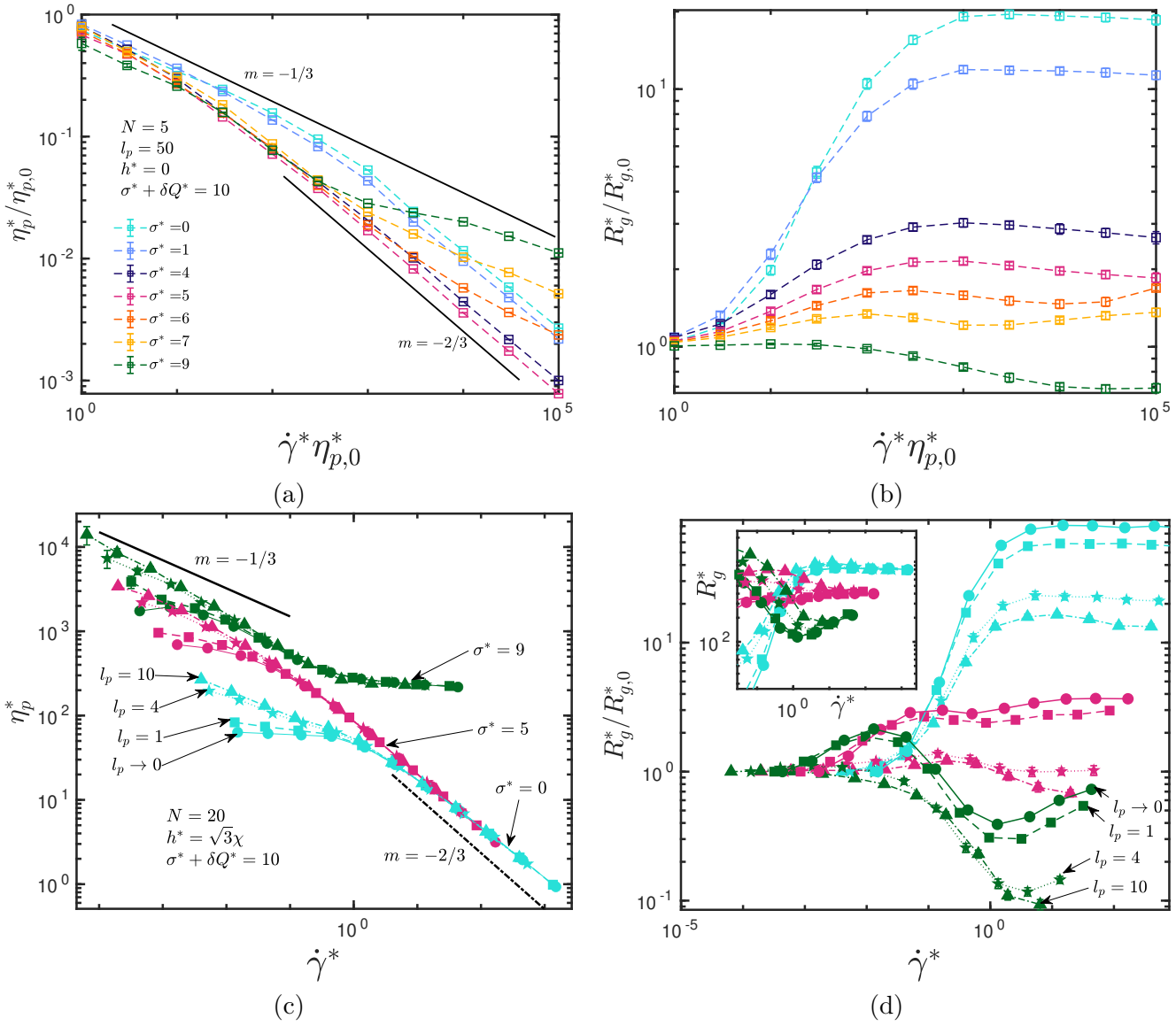

FIGURE 3.15: FENE-Fraenkel springs of bead number $N = 5$ for (a) and (b), as well as $N = 20$ for (c) and (d), with a bending potential. In all cases, l_p is defined in terms of the number of links, i.e. for $l_p = 50$ in (a), we must travel 50 springs along the chain in order for the correlations in segmental unit vectors to have decayed by 63.2%. As before, we have $\sigma^* + \delta Q^* = 10$. For (a) and (b), which display the normalised polymer viscosity and normalised gyration radius respectively against Weissenberg number, the zero-shear viscosity is calculated via Equation 3.25. Plots (c) and (d) give the dimensionless polymer viscosity and normalised gyration radius respectively against the dimensionless viscosity. Inset to plot (d) instead displays the radius of gyration without the zero-shear normalisation. $m = -1/3$ and $m = -2/3$ lines are guides for the eye and do not imply exact terminal slopes. Where not shown, error bars are smaller than symbol size.

averaged constraint on the segmental (or tangent vector) correlation along the backbone [119, 120]. However, to be analytically tractable, these models often relax the constraints on the segmental stretch and total contour length, leading to a chain which can extend and contract in response to external forces. For example, the model of Winkler [98] gives a $(-2/3)$ power law slope in viscosity at high shear irrespective of the underlying semiflexibility of the chain,

somewhat in contrast to expectations for highly inflexible polymers.

In Figure 3.15, we present results with a very stiff bending potential, where l_p is given in units of the spring length. For example, for $N = 5$ and $l_p = 50$, we have $N_{\mathrm{K,s}} = 4/(100) = 0.04$, leading to $C = 49.8$ as per Equation 3.8. Focusing firstly on the viscosity for Figure 3.15 (a) with $N = 5$, $l_p = 50$ and no HI, we see a clear initial $(-1/3)$ power-law slope at intermediate shear rates, as one would expect for a highly 'stiff' bending potential. At higher shear rates, the more 'spring-like' FENE-Fraenkel chains again give a $(-2/3)$ power-law slope in the viscosity, while the $\sigma^* > 5$ chains return to an approximately $(-1/3)$ power-law slope. Interestingly, the chains all seem to display fairly similar qualitative behaviour in the extension R_g^* in Figure 3.15 (b), and there is no clear difference in the behaviour from $\sigma^* = 5$ to $\sigma^* = 6$. The $\sigma^* = 9$ chain in fact compresses in shear flow relative to its equilibrium length, likely due to the shear flow deforming the semiflexible chain into a hairpin-like configuration observed in both experimental and simulation studies [121, 122].

The behaviour for a range of smaller l_p values is displayed in Figure 3.15 (c) and (d), using $N = 20$ bead chains and $h^* = \sqrt{3}\chi$. At low shear rates, with $l_p \geq 4$, all chains display an $\approx -1/3$ power-law slope in viscosity. However, at higher shear rates, the behaviour collapses onto the same curve irrespective of the bending stiffness, following the results without a bending potential almost exactly. This occurs for both the viscosity and radius of gyration, as can be seen in the inset to Figure 3.15 (d). This behaviour is remarkably similar to that previously observed for Gaussian EV, where the intermediate-shear behaviour is altered, but results collapse at a certain $\dot{\gamma}^*$.

3.4 Conclusions

We began by presenting the full range of behaviour seen in previous experimental and theoretical studies in Figure 3.1 and Figure 3.2 and describing a model which could supposedly reproduce this range of behaviour. The changes in simulated polymer solution properties as a function of model parameters were then studied in detail, highlighting how each piece of physics affects the observed rheology. To conclude, let us refer back to Figure 3.1 and Figure 3.2, and demonstrate that by appropriately selecting parameters, we can indeed qualitatively recover the full range of expected changes in viscosity with shear rate using our model. In other words, we wish to show that given some experimental or simulated measurements of dilute polymer solution rheology in shear flow (such as a curve of viscosity versus shear rate), as well as basic details about the polymer microstructure, we can choose our FENE-Fraenkel spring parameters, as well as bending potential, HI, and EV, in order to qualitatively match that behaviour.

We begin with Figure 3.2, pointing out which of our simulations correspond to each curve. Note that our list numbering refers to the curves in Figure 3.2, such that, for example, (a) is qualitative comparisons with FENE chains and HI: [67]:

(a) The shear-thickening is observed for sufficiently extensible FENE springs with HI (both with and without EV), as shown in Figure 3.5 and Figure 3.13.

(b) The high-shear plateau seen for bead-spring models is again recovered for sufficiently extensible FENE (or Hookean) springs with Gaussian EV, as seen in Figure 3.5 (c).

(c) The $\approx (-2/3)$rds power-law slope in viscosity with shear rate is found for any sufficiently compressible bead-spring model, as demonstrated most clearly in Figure 3.7 and Figure 3.8. This may even be the case when a strong bending potential is used, as suggested by Figure 3.15.

(d) The characteristic $(-1/3)$rd power-law slope in viscosity found in rodlike models is approached for sufficiently incompressible springs, seen here quite clearly for the dumbbell results of Figure 3.8 (a). A strong bending potential also seems to give an intermediate $(-1/3)$rd slope in the viscosity as per Figure 3.15, however the terminal slope may instead correspond to the form of the spring potential rather than bending potential.

(e) The high-shear plateau for bead-rod chains is seen for sufficiently incompressible bead-spring chains, as in Figure 3.7 (a) and Figure 3.8 (b).

Furthermore, we show that moving from the bead-spring-chain to bead-rod-chain leads to a plateauing of the viscosity at high shear rates, as well as a compression in the flow direction. This crossover occurs when $\sigma > \delta Q$ (or $\sigma > \delta Q/2$ for MS-WLC-Fraenkel spring), suggesting that the compressibility of a force law gives it either bead-rod or bead-spring-like behaviour. We also found that 'hard-core' and 'soft-core' EV potentials give considerably different results at finite shear rates for finite chain lengths, and the effects of a strong bending potential depend heavily on the form of the force law used to link beads.

We also briefly mention some features of the experimental results which can be matched onto our models, roughly corresponding to the physics expected to be important in those real polymer solutions. However, this is largely qualitative - ideally we would seek to develop a parameter-free method to obtain quantitative predictions of this experimental behaviour in future work. The following features were present in Figure 3.1 which can be seen in our FF-spring-chain simulations (again, letters represent curves in the original figure):

(a) The extremely high-molecular-weight polystyrene in a theta solvent should in theory be modelled by a highly extensible bead-spring-chain with HI but no EV (or for a value of

ε corresponding to a θ-solvent). This could correspond to the behaviour of Hookean or $\delta Q >> 0$ FENE chains seen in Figure 3.5, making the speculative assumption that the shear-thickening regime has not been reached.

(b) This polymer solution uses the same polystyrene molecule as in (a), but with a higher solvent quality, leading to a ≈ -0.1 power-law slope in viscosity. This somewhat corresponds to a highly extensible FENE chain with finite z, as per Figure 3.5 (c). For example, the Hookean $h^* = 0$, $z = 2$ curve has an initial gradient of ≈ -0.1, which is seen at intermediate shear rates before the $(-2/3)$ slope due to finite extensibility.

(c) For a shorter polystyrene chain in a close-to-theta solvent, we expect a FENE spring-chain with some relatively small δQ to be a reasonable model, leading directly to a $(-2/3)$ slope in viscosity at high shear rates, as seen in all of our highly-compressible FF springs.

(d) The three DNA chains of 24 kbp, 48.5 kbp and 165.6 kbp show slight differences in the shear-thinning exponent, as well as differences in the onset of shear thinning. Qualitatively, we have seen that all our models appear to have a later onset of shear-thinning as the chain extensibility is increased, as in Figure 3.5 and Figure 3.13. The shear rates reached are also not particularly large - it is possible that the chains are still in the crossover region between zero-shear and high-shear behaviour, leading to differences in slopes. One might also speculate that the semiflexibility of DNA causes two different slopes at intermediate and high shear rates, as in Figure 3.15, although this is again purely speculative.

Beyond presenting a unified model for examining the properties of previous bead-rod chains and spring-force laws in detail, we hope that this work will be useful in the future development of multiscale modelling approaches. While several authors have developed models which are able to represent a section of polymer chain on many length scales at equilibrium [18–21], our current results suggest that this is not sufficient to ensure correct reproduction of properties at finite shear. In future studies, we hope to present a multiscale modelling procedure based upon this FENE-Fraenkel spring. In this way, one may be able to represent both a short section of semiflexible polymer chain, as well as a very large segment of a more flexible polymer, using the same continuous fine-graining procedure.

Chapter 4

Successive Fine Graining and Static Swelling with QTP Theory

4.1 Introduction

In chapters 2 and 3 we have laid out a comprehensive method for inclusion of various pieces of physics into a polymer model such that one can, in theory, represent a polymer at length scales ranging from thousands of Kuhn steps down to the sub-Kuhn step level. Although it appears possible to use this model to qualitatively recover a wide range of previously-observed experimental and theoretical behaviour, we would ultimately aim to exactly reproduce experimental predictions. Previously, the method of successive fine graining (SFG) has been applied to obtain quantitative, parameter-free predictions of polymer rheology in extensional flow [14, 16, 123]. However, this method relies upon an accurate measure of the solvent quality, z, in our simulations, which can be expressed in terms of the number of beads and strength of excluded volume potential (as will be outlined below) [86, 92, 93, 96, 104]. As described by Yamakawa [49] using so-called quasi-two-parameter (QTP) theory, the normal relations for a flexible polymer chain do not apply to a semiflexible chain. Instead, we can use a new measure of the solvent quality, $\tilde{z}$, which is essentially a correction to z by some function of the contour length and persistence length. In this chapter, we show how QTP theory can be applied to our bead-spring model to accurately recover the expected swelling at equilibrium, as well as detail a method for obtaining parameter-free predictions of properties away from equilibrium.

4.2 Two-parameter theory and Successive Fine Graining

SFG was proposed by Prakash and coworkers [14, 16] as a method to exploit the universality of polymer solutions to obtain parameter-free predictions of static and dynamic properties

[14, 16, 123]. That is to say, our predictions should be independent of arbitrary model choices such as number of beads, the specific form of the spring/bending/EV potential, or the effective hydrodynamic interaction parameter. This is done by keeping parameters characterising the key physical properties of the underlying chain constant as the number of beads is increased, then extrapolating measured properties to some limit. If one wishes to obtain universal properties of long chains, this procedure can be used to extrapolate to $N_s \to \infty$, where N_s is the number of springs in the chain. For example, this can be used to obtain universal predictions of swelling due to EV [93, 124], or to calculate universal ratios [16, 125]. On the other hand, if one wishes to simulate a real chain, in situations where the finite contour length is important (for example in extensional flow or at high shear rates [14, 16, 126]), we can instead extrapolate to the number of Kuhn steps in the underlying chain, i.e. $N_s \to N_k$. The 'trick' is to carefully select our model parameters at each N_s such that in the extrapolated limit, accurate predictions are obtained.

We wish to illustrate the procedure via a couple of examples, first by showing how universal predictions of polymer viscosity in shear flow were obtained in the long-chain limit [96], and then how successive fine graining was applied to calculate the extension of a real DNA chain in elongational flow [16]. We will then show how this method must be slightly altered when a bending potential is used, and how we can again obtain parameter-free predictions. Specifically, we will show that one can choose the strength of the excluded volume potential such that the same swelling is found irrespective of whether a bending potential is used or not.

To begin, imagine that one would like to predict the swelling of a polymer molecule, say polystyrene of a certain molecular weight in cyclohexane at different temperatures, as measured by Miyaki and Fujita [127]. It has been found for experimental systems of long, flexible polymers, that the dependence of the size of the polymer molecule on both molecular weight (chain length) and temperature (solvent-polymer interaction strength), can be collapsed onto a single, universal curve when plotted in terms of a single variable, the so-called solvent quality z [90, 117]:

$$z = k\left(1 - \frac{T_\theta}{T}\right)\sqrt{M} \tag{4.1}$$

where M is the molecular weight, T is the solution temperature, T_θ is the theta-temperature with net-zero solvent-polymer interactions, and k is a chemistry-dependent constant. In a θ-solvent, the coil size (measured by radius of gyration, R_g) increases as $R_{g,\theta} = a\sqrt{M}$ where a depends on the polymer-solvent system, but for $T > T_\theta$ we find that:

$$\frac{R_g}{R_{g,\theta}} = f(z) = \alpha_g \tag{4.2}$$

where $f(z)$ is a universal function of the z-parameter given in Equation 4.1, R_g is the gyration radius at a particular z, $R_{g,\theta}$ is the gyration radius at the theta temperature, and α_g is the

swelling of the gyration radius. The function $f(z)$ is commonly fit in the form:

$$f(z) = \left(1 + az + bz^2 + cz^3\right)^m \tag{4.3}$$

where a, b, c and m are constants and perturbative treatments show that for α_g, $am = 1.276$ [93, 102]. An example of this fit is given in Figure 4.1 for both BD simulations and swelling of polystyrene (reprinted from Kumar and Prakash [93], who fit the measurements of Miyaki and Fujita [127]), where data for several polymer solutions are collapsed on to the same universal curve.

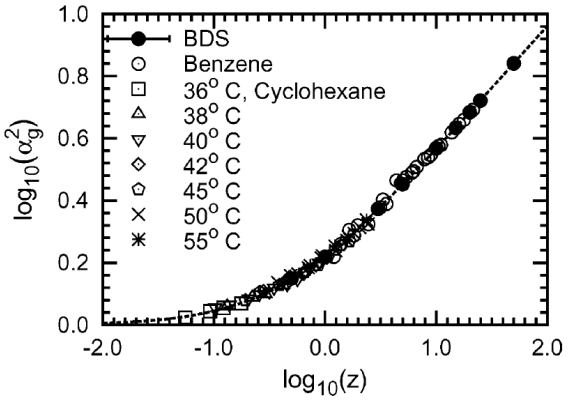

FIGURE 4.1: Reprinted with permission from Kumar and Prakash [93], showing the gyration radius swelling for polystyrene in different solvents of Miyaki and Fujita [127] as well as predictions of BD simulations. Defining the solvent quality z as in Equation 4.1, data collapses onto a universal curve. Dotted fit is Equation 4.3 with $am = 1.276$, $b = 19.48$, $c = 14.92$, $m = 0.1339$.

This universal behaviour found in experimental solutions can be analytically explained in terms of the so-called Two-Parameter (TP) theory. The TP theory for static solution properties (such as α_g) has been rigorously derived using renormalisation group (RG) methods [90]. For the application of RG methods, we have a bead-spring-chain model of N beads connected by Hookean springs (with spring constant H), which have some repulsive potential modelling the solvent quality. This repulsive potential represents the polymer-solvent interaction relative to the polymer-polymer interaction (which changes with temperature), and in the RG theory has a Dirac delta function form:

$$E(\boldsymbol{r}_{\mu\nu}) = v(T) k_{\mathrm{B}} T \delta(\boldsymbol{r}_{\mu\nu}) \tag{4.4}$$

where $\boldsymbol{r}_{\mu\nu}$ is the vector connecting two beads μ and ν, and $v(T)$ is the so-called excluded volume parameter. The key point is that due to the universality and scale invariance of a polymer in the long-chain limit, one can show that if we define a dimensionless strength:

$$z^* = v\left(2\pi \frac{k_{\mathrm{B}} T}{H}\right)^{-3/2} \tag{4.5}$$

then the temperature and chain length dependence can in fact be combined into a single parameter, just as for the experimental systems [90]:

$$z = z^* \sqrt{N} \tag{4.6}$$

This analytical result provides a powerful link between experimentally observed swelling on one hand, and the excluded volume potential in our polymer models on the other.

For simulations, it is not possible to use a Dirac delta potential. On a lattice, one can directly prevent a chain from overlapping with itself [128], while off-lattice one can use a repulsive potential such as the Lennard-Jones form to represent polymer-polymer exclusion [129]. In these cases, one cannot define the solvent quality z directly in terms of the EV potential as in Equation 4.6. Instead, the EV well depth takes the form of temperature in Equation 4.1, such that one must carefully determine both the θ-temperature and chemistry-dependent constant k [94, 129]. Data is collected for finite chain lengths, and then extrapolated to the long-chain limit, where results become independent of details such as the particular form of the potential (given a correctly defined z).

One can also apply the same ideas to Brownian dynamics simulations, which have the crucial advantage of being able to simulate systems away from equilibrium, and obtain dynamic properties. A method for doing so was described by Kumar and Prakash [93] based upon the so-called Gaussian potential, which has the form:

$$E(\boldsymbol{r}_{\mu\nu}) = \frac{v k_\mathrm{B} T}{(2\pi d^2)^{3/2}} \exp\left\{ -\frac{1}{2} \frac{{\boldsymbol{r}_{\mu,\nu}}^2}{d^2} \right\} \tag{4.7}$$

or in dimensionless units:

$$E(\boldsymbol{r}_{\mu\nu}) = k_\mathrm{B} T \frac{z^*}{d^{*3}} \exp\left\{ -\frac{1}{2} \frac{{\boldsymbol{r}^*_{\mu,\nu}}^2}{d^{*2}} \right\} \tag{4.8}$$

where d is the range of the excluded volume potential, such that as $d^* \to 0$, we recover the δ-function potential. d^* has units of length, and is non-dimensionalised as $d = d^* \sqrt{k_\mathrm{B} T / H}$. This form was first suggested by Öttinger [13], and used by Prakash and Öttinger to determine viscometric functions of dilute polymer solutions in good solvents [104]. It has the distinct advantage that it is a regularisation of the same Dirac delta potential defined for renormalisation group theories, and so can be shown to give the same results when setting $d^* \to 0$ and $N \to \infty$ [93]. Therefore, since we know that $z = z^* \sqrt{N}$, we can obtain long-chain predictions for a particular value of z by setting $z^* = z/\sqrt{N}$ at several finite values of N for some particular d^*, and finding the swelling at each of these N. We can then plot α_g against $1/\sqrt{N}$, and in the limit of $N \to \infty$, we should obtain universal results for the swelling which are independent of our particular choice of d^*. It is usually efficient to choose $d^* = K {z^*}^{1/5}$, for some constant

K, and then show that results are independent of K. An example of this scheme is shown in Figure 4.2, where we have simulated Hookean chains with two different values of K for several N, giving results which are independent of K in the limit of $1/\sqrt{N} \to 0$. In fact, one only needs to simulate up to $N \approx 35$ in order to obtain sufficient results for extrapolations of universal values, making this a highly efficient scheme [93].

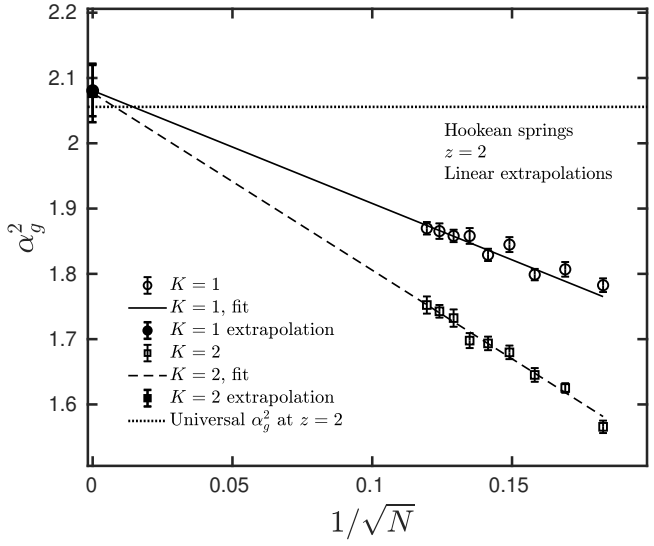

FIGURE 4.2: Extrapolations to the long-chain limit using Hookean springs. The horizontal line is the expected α_g^2 based on Equation 4.3. Note that extrapolated results agree with previous fits to within error bars [93]. Performing this extrapolation procedure for several z gives the curve in Figure 4.1

It is also possible to apply this same procedure away from equilibrium [96], for example in shear flow. In this case, one performs the same extrapolation procedure at some dimensionless shear rate β, where β is given for experimental systems by:

$$\beta = \frac{[\eta]_0 \eta_s M \dot{\gamma}}{N_A k_B T} \tag{4.9}$$

and where $[\eta]_0$ is the zero-shear intrinsic viscosity, η_s is the solvent viscosity, $\dot{\gamma}$ is the experimental shear rate, N_A is Avogadro's constant and M is the molecular mass. It is possible to non-dimensionalise the shear rate in our simulations in the same way, given we have calculated the zero-shear viscosity [96]. At this particular value of β, we perform the same extrapolations for several K at some particular z, changing the number of beads N, giving a universal prediction of the scaled viscosity η_p/η_p^R for some solvent quality z [96], where η_p^R is the Rouse viscosity. The SFG process at finite shear rates can be seen in Figure 4.3, where results for several Hookean chains at finite lengths and with different d^* are extrapolated to the same universal value of the scaled viscosity.

A similar scaling holds for HI, where results can be shown to be independent of the choice of h^* in the long-chain limit [125]. This leads to a similar 'draining parameter' $h = h^*\sqrt{N}$, and constant h^* as $N \to \infty$ is referred to as the 'non-draining limit' ($h \to \infty$) [102].

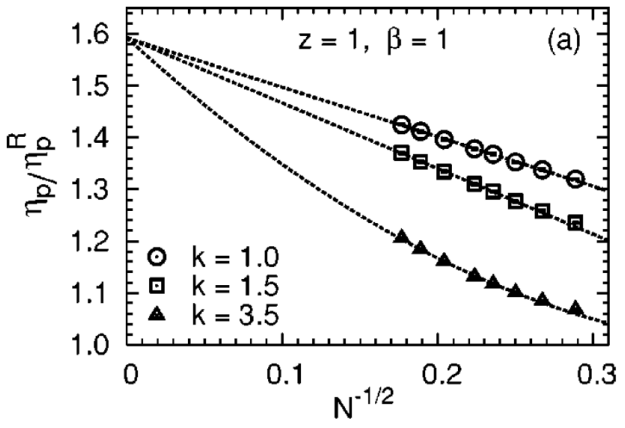

FIGURE 4.3: Reprinted with permission from Kumar and Prakash [96], showing the polymer viscosity divided by the Rouse viscosity at reduced shear rate $\beta = 1$ and solvent quality $z = 1$. The three curves each have a different value of $d^* = k(z^*)^{1/5}$, but in the long-chain limit extrapolate to the same viscosity.

4.2.1 Successive fine graining for finite chains

One may then wish to apply these ideas to obtain direct, quantitative predictions of polymer solution properties in non-equilibrium flows. This idea was first introduced by Prakash and coworkers [14, 16] for polystyrene chains in extensional flow. Here we will sketch an example of the procedure as applied by Sunthar and Prakash [16] to DNA chains of only ≈ 200 Kuhn lengths, demonstrating that the concepts of universality apply even for relatively short chains.

Imagine that we have measurements of the expansion factor:

$$E(\epsilon, \dot{\epsilon}) = \frac{\bar{x}^+(\epsilon)}{\bar{x}_{\rm eq}} \tag{4.10}$$

where $\bar{x} \equiv \max_{\mu,\nu} |r_\mu^x - r_\nu^x|$ (and r_μ^x is the x-component of vector $\boldsymbol{r}_\mu$) is the maximum extent of the chain in the flow direction, ϵ is the strain, $\dot{\epsilon}$ is the strain rate, $\bar{x}_{\rm eq}$ is the average maximum extent at equilibrium, and $\bar{x}^+(\epsilon)$ is the average maximum chain extent in flow at a particular strain and strain rate. For example, this might be for experimental data of λ-DNA in elongational flow, such as that of Smith and Chu [130]. Essentially, we apply the same extrapolation procedure as before for Hookean chains in the $N \to \infty$ limit, but instead extrapolate to $(N-1) = N_s \to N_k$, where N_k is the number of Kuhn lengths in the underlying polymer chain, N is the number of beads at each SFG step, hence with $N_s = (N-1)$ springs.

To do so, we must also account for the finite contour length of the chain, and simultaneously correct our previous calculations of z^* (and also hydrodynamic interaction parameter h^*) at each N. For this purpose, we use FENE springs, for which the total contour length of our

model chain of N beads is given by:

$$L = (N-1)\delta Q \tag{4.11}$$

where L is the contour length and δQ is the maximum extensibility of the FENE spring (usually referred to as Q_0 [34], but here given as δQ to correspond to our previous notation for FENE-Fraenkel springs). The gyration radius of this chain can be found as:

$$R_g^2 = \langle Q^2 \rangle_{\text{eq}} \frac{N^2-1}{2N} = \frac{H\delta Q^2/k_{\text{B}}T}{H\delta Q^2/k_{\text{B}}T+5} \frac{N^2-1}{2N} \frac{k_{\text{B}}T}{H} \tag{4.12}$$

where H is our Hookean spring constant and $\langle Q^2 \rangle_{\text{eq}}$ is the average spring length at equilibrium with no EV. Therefore, if we have a polymer chain with a known length and gyration radius, we can determine the parameters δQ and H by solving the equations 4.11 and 4.12 simultaneously [16]. The gyration radius of DNA can be calculated from the contour length and persistence length using the Kratky-Porod model [49, 131], giving us H and δQ for some N_s. If we define $b = H\delta Q^2/k_{\text{B}}T$ as the finite extensibility parameter, we have that:

$$b = N_k \frac{3(N+1)}{N(N-1)} \tag{4.13}$$

given the number of Kuhn steps N_k, calculated from experimental measurements as:

$$N_k = \frac{L_{\text{exp}}^2}{6{R_{g,\text{exp}}^{\theta}}^2} \tag{4.14}$$

where $R_{g,\text{exp}}^{\theta}$ is the experimental radius of gyration under θ-solvent conditions, and L_{exp} is the experimental contour length. This fully specifies our spring parameters given an experimentally-determined N_k and a choice for the number of beads N. We can apply the same procedure for some arbitrary spring force law other than the FENE spring, but the result will not necessarily have such a simple algebraic form [16]. It is useful to define a so-called 'extensibility parameter' χ, which is the ratio of average equilibrium spring length to that of a Hookean chain:

$$\chi^2 = \frac{1}{3} \frac{\int Q^{*4} e^{\phi^*}}{\int Q^{*2} e^{\phi^*}} \tag{4.15}$$

where Q^* is the non-dimensional spring length $Q^* = Q/l_H$, and ϕ^* is the non-dimensional spring potential.

For each N (with a particular b), we can then calculate the relaxation time λ (for example, from the end-to-end vector autocorrelation function), which allows us to choose $\dot{\epsilon}$ in order to recover some non-dimensional extension rate $Wi = \dot{\epsilon}\lambda$ as for our experimental system. In the absence of HI or EV, we could then run simulations for several N and extrapolate to $N \to N_k$. This should give the same predictions as a chain of N_k rods, and in fact Tri et al. [126] have

demonstrated that (at least for intermediate Wi) SFG can indeed be used to determine the material properties of a solution of bead-rod chains in shear flow.

However, real chains clearly do experience solvent-mediated hydrodynamic interactions and excluded volume effects, which we would ideally include in such a way that predictions are independent of the fine-grained details of our implementation (in other words, they are parameter-free). In order to properly include EV and HI, Sunthar and Prakash [16] showed through perturbation expansion arguments, as well as Monte-Carlo and BD simulations, that for a non-Hookean spring one should correct z^* and h^* by:

$$z^* = \frac{z\chi^3}{\sqrt{N}} \tag{4.16}$$

$$h^* = \frac{h\chi}{\sqrt{N}} \tag{4.17}$$

where h is the draining parameter and χ is defined in Equation 4.15. In other words, when a non-Hookean spring is used, the true definitions of h^* and z^* change, such that universal functions of h and z will not be accurately obtained unless Equations 4.16 and 4.17 are used. The intuitive explanation for this correction is that z^* scales like a volume while h^* scales like a length, and therefore if the spring length changes, other parameters should scale identically [16].

By way of illustration, let us follow the procedure of Sunthar and Prakash [16] and obtain universal predictions of both the universal ratio $U^{\theta}_{R\bar{D}}$ (defined below), as well as α_g (at $z = 2$), for non-Hookean springs. Rather than using FENE or Marko-Siggia springs as Sunthar and Prakash have done [16, 44], we will instead apply the method to FENE-Fraenkel springs, which can have $\chi > 1$, unlike the former spring force laws.

The universal ratio $U^{\theta}_{R\bar{D}}$ is a function of the radius of gyration and Kirkwood diffusivity at the theta-temperature [16], given in dimensionless form as [34]:

$$U^{\theta}_{R\bar{D}} = \frac{4}{\sqrt{\pi}h^*}\bar{D}^{*,\theta}R_g^{*,\theta} \tag{4.18}$$

with

$$\bar{D}^{*,\theta} = \frac{1}{4N}\left[1 + \frac{\sqrt{\pi}h^*}{N}\sum_{\substack{\mu,\nu \\ \mu\neq\nu}}^{N}\left\langle\frac{1}{r^*_{\mu\nu}}\right\rangle_{\text{eq}}\right] \tag{4.19}$$

where $r^*_{\mu\nu}$ is the linear distance between beads μ and ν. By assuming the equilibrium distribution is Gaussian for large bead separations $|\mu - \nu|$, it is possible to approximately evaluate the sum over the average inverse bead separation as an equivalent integral (we give a shortened form of this derivation in Section 4.4). By doing so, Sunthar and Prakash [16] were able to

show that $U^{\theta}_{R\bar{D}}$ obeys the expression:

$$U^{\theta}_{R\bar{D}} = \frac{8}{3\sqrt{\pi}} + \frac{1}{\sqrt{2\pi N}}\left(\frac{1}{\tilde{h}^*} - \frac{1}{h^*_f(\chi)}\right) + \mathcal{O}\left(\frac{1}{N}\right) \tag{4.20}$$

where $\tilde{h}^* = h^*/\chi$ and h^*_f is the so-called fixed-point at which order $N^{-1/2}$ corrections to $U^{\theta\infty}_{R\bar{D}} = 8/3\sqrt{\pi} \approx 1.51$ vanish. Therefore, to test the correction in Equation 4.17, we can generate equilibrium, θ-solvent configurations of FENE-Fraenkel spring chains, calculate the diffusivity as per Equation 4.19 for several $\tilde{h}^*$, and extrapolate to the $N \to \infty$ limit. This should give us the same universal prediction, but an altered fixed point and different order $N^{-1/2}$ corrections as predicted by Equation 4.20.

Configurations are generated directly by inverting the numerically-calculated cumulative distribution function for the equilibrium length of FENE-Fraenkel springs, which transforms uniform random numbers into those following the expected spring length distribution. These spring lengths are then multiplied by unit vectors randomly distributed on the surface of a sphere, and the resulting vectors are connected end-to-end one at a time, recreating the θ-solvent (no EV forces) distribution of freely jointed chains. This Monte-Carlo procedure [132] is explained more thoroughly in Appendix H. One can then calculate $\langle R_g^2 \rangle$ and $\langle 1/r_{\mu\nu} \rangle$ for an ensemble of such chains, and hence $\bar{D}^{*,\theta}$ and $U^{\theta}_{R\bar{D}}$ at each particular value of N. (As an interesting aside, we note that the calculation of $\langle 1/r_{\mu\nu} \rangle$ is by far and away the most computationally expensive step in this procedure for large N, since it requires N^2 operations. This problem has been discussed by Clisby and Dünweg, who calculate hydrodynamic radii for very large N via a pivot algorithm for a self-avoiding walk on a lattice [133]. They show that one needs only determine $1/r_{\mu\nu}$ for two random pairs of beads in each generated trajectory, which still gives a very high accuracy estimate of the sum $\sum\langle 1/r_{\mu\nu} \rangle$. We have not generated long enough chains for this to be required.) Extrapolations of this procedure to $N \to \infty$ for two sets of FENE-Fraenkel springs are shown in Figure 4.4. The correct universal value of $U^{\theta\infty}_{R\bar{D}}$ is obtained in both cases, although a higher value of χ necessitates longer chains for an accurate extrapolation.

So far, we have only considered extrapolations to the long-chain limit, where universal results are obtained. However, for finite chains, we instead extrapolate to $(N-1) \to N_k$. In this limit, results may not necessarily be universal, but one can still obtain accurate predictions of the behaviour of the underlying real chain by judicious choice of chain parameters for each fine-graining step. Specifically, one can obtain results which are independent of arbitrary parameters which do not feature in the real chain, such as the particular form of the spring potential. This idea is demonstrated in Figure 4.5 through what we call a 'double-extrapolation'. In Figure 4.5 (a), we have reproduced Figure 3 of Sunthar and Prakash [16].

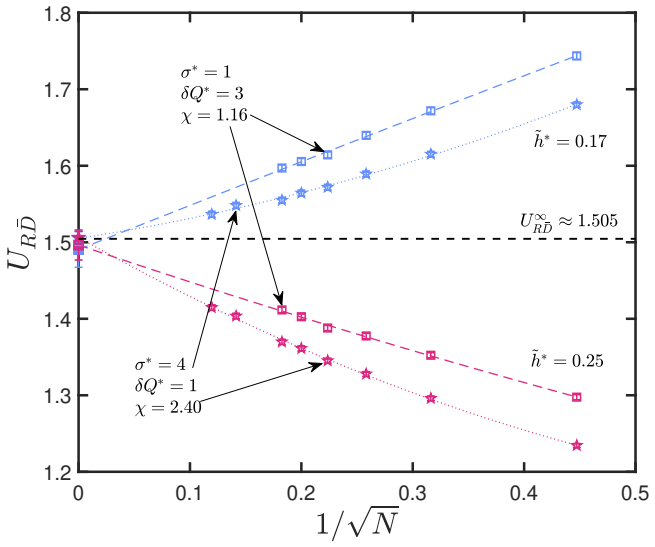

FIGURE 4.4: Extrapolation of finite-chain results to universal limit. Results are generated using equilibrium, θ-solvent distributions of FENE-Fraenkel spring-chains (as described in text) with parameters listed in figure, and $h^* = \tilde{h}^*\chi$. $U^{\theta}_{R\bar{D}}$ is calculated as per Equation 4.18 and Equation 4.19. Where not visible, error bars are smaller than symbol size.

By generating equilibrium, θ-solvent configurations of FENE bead-spring chains at several levels of fine-graining, one can extrapolate to obtain the exact prediction of the bead-rod results at that $\tilde{h}^*$. In other words, we don't necessarily need to directly simulate a 2000-rod chain, but can instead extrapolate finitely-extensible bead-spring results to the $N_{\text{rod}} = 2000$ limit and obtain the same predictions. Note that the double-extrapolation arises due to the fact that the various N_{rod} predictions themselves extrapolate to the same universal $U^{\theta\infty}_{R\bar{D}}$.

The same kind of extrapolation at $z = 2$ can be seen in Figure 4.5 (b) using BD simulations. In this case, we do not have exact results for the bead-rod chains, and so must rely upon the extrapolations to obtain $N_{\text{rod}} = 200$ and $N_{\text{rod}} = 2000$ results. As before, we accumulate data for several bead numbers with the underlying contour length, radius of gyration and solvent quality z matching that of the 200 or 2000-rod chain. In the $(N-1) \to N_k$ limit, results are clearly not independent of the choice of K, and so are not parameter-free. However, we can again extrapolate our N_{rod} results to the long-chain limit, where predictions do indeed agree with the universal result for $z = 2$, irrespective of the choice of the range of the Gaussian potential. It is useful at this point to carefully consider what these results mean. Specifically, the renormalisation group theories which predict scaling laws which are independent of the local polymer details rely on the scale invariance and self-similarity of a long polymer chain [90]. At low N_{rod}, we do not necessarily have this scale invariance, since there are not enough degrees of freedom in the model, which instead appears for longer chains due to the emerging self-similarity. This is why we see predictions converging as N_{rod} increases, since the local details of the EV and spring potentials are no longer relevant, and results depend instead on the value of z alone (they are parameter-free). Then, in the limit $N_{\text{rod}} \to \infty$, we obtain the

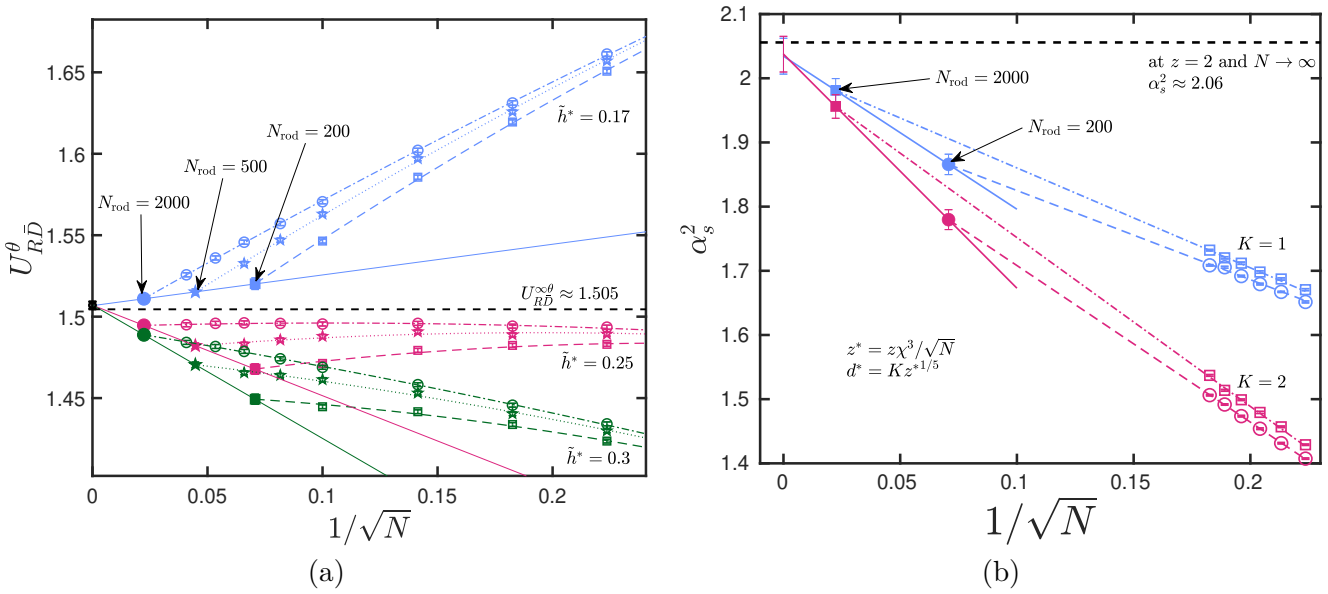

FIGURE 4.5: Double-extrapolations using FENE springs and SFG. In both cases, the FENE b-parameter is chosen as per Equation 4.13, with $N_k \equiv N_{\rm rod}$. In plot (a), $U^{\theta}_{R\bar{D}}$ is calculated as per Equation 4.18 and Equation 4.19, with $h^* = \tilde{h}^*\chi$, at equilibrium with no EV. $N_{\rm rod}$ extrapolations agree exactly with those of Sunthar and Prakash [16]. Plot (b) contains BD simulations of FENE chains at equilibrium with Gaussian EV parameters as described in the figure, with extrapolations to $(N-1) \to N_{\rm rod}$.

universal prediction, which holds experimentally for sufficiently long chains. These results are useful to inform our analysis once a bending potential is added, where we will extrapolate towards a chain with some $N_{\rm rod}$ as well as a particular persistence length l_p.

4.2.2 Quasi Two Parameter Theory

Our basic goal is to apply this same SFG method to our FENE-Fraenkel springs with a bending potential, HI and EV. However, in a similar way to the previous correction to z^* and h^* as a function of χ, we must correct for the bending potential, as it leads to independent swelling in the θ-state (with no EV). To do so, we turn to the Quasi-Two-parameter (QTP) theory introduced by Yamakawa [49]. This involves defining a perturbation expansion for the swelling of some parameter, for example the end-to-end length α_R:

$$\alpha_R^2 = 1 + K(L/2l_p)z + \cdots \tag{4.21}$$

where L is the total contour length and l_p is the persistence length, and then finding the function $K(L)$ which gives the expected first-order perturbation coefficients. This derivation is highly non-trivial, but leads to a rather straightforward conclusion. If one wishes to determine the swelling α for a semiflexible chain, we can simply define a new solvent quality $\tilde{z}$, given by:

$$\tilde{z} = \frac{3}{4}K(L/2l_p)z \tag{4.22}$$

and then the same universal swelling curve as for flexible chains should be recovered for $\alpha(\tilde{z})$ [49]. Yamakawa also gives a useful interpolation formula for $K(L)$:

$$\begin{aligned} K(L) &= \frac{4}{3} - \frac{2.711}{L^{1/2}} + \frac{7}{6L} && \text{for } L > 6 \\ &= \frac{1}{L^{1/2}} \exp\left(-\frac{6.611}{L} + 0.9198 + 0.03516L\right) && \text{for } L \leq 6 \end{aligned} \tag{4.23}$$

which has the limit $K(L) \to 4/3$ as $L \to \infty$ (the flexible-chain limit). Note that we can identify for a semiflexible WLC that $N_k = L/2l_p$ [49, 102].

This QTP theory has been tested both through comparison with experiment, and detailed Monte-Carlo simulations with EV included via a Lennard-Jones potential [49]. However, analogously with the situation for the original TP theory, these simulations have two distinct disadvantages. Firstly, the EV is not defined directly in terms of z^*, such that one must carefully determine the θ-condition and hence z for some particular EV potential. Secondly, pre-averaging or Gaussian approximations are required for dynamic and non-equilibrium scaling [49], so the scheme does not naturally extend to flow properties. Therefore, we wish to establish the universal scaling of semiflexible chains using a bending potential and the Gaussian EV potential with QTP theory, in such a way that it can be applied to SFG predictions of polymer properties away from equilibrium.

We would like to show that when we use $\tilde{z}$ instead of z with a bending potential, extrapolations to the long-chain limit are independent of L/l_p, when corrected using $K(L)$. However, in the long-chain limit, we have that $N_k \to \infty$, implying that $L/l_p \to \infty$ and hence $K(L) = 4/3$ and $z = \tilde{z}$. In other words, even with some non-zero bending potential, the long-chain limit extrapolation will be the same with and without a bending potential.

Instead, we use a slightly different scheme. Recalling our double-extrapolations in Figure 4.5, we know that applying the SFG scheme to FENE chains results in accurate predictions of bead-rod results for some N_{rod}. We also know that one can choose our bending potential C to recover a particular L/l_p, as per the formulation of Saadat and Khomami [18], namely:

$$C = \frac{1 + p_{\text{b},1}(2N_{\text{K,s}}) + p_{\text{b},2}(2N_{\text{K,s}})^2}{2N_{\text{K,s}} + p_{\text{b},3}(2N_{\text{K,s}})^2 + p_{\text{b},4}(2N_{\text{K,s}})^3} \tag{4.24}$$

where $p_{\text{b,i}} = \{-1.237, 0.8105, -1.0243, 0.4595\}$ and $N_{\text{K,s}} = L/(2N_s l_p)$. Therefore, if we express the persistence length in units of rod length (i.e. $l_p = 10$ implies that if we travel 10 rod lengths along the backbone contour, we have moved by one persistence length), then we can identify using QTP that:

$$z^* = \tilde{z}\chi^3 \sqrt{\frac{1}{N}} \frac{4}{3} \frac{1}{K(N_{\text{rod}}/2l_p)} \tag{4.25}$$

For some choice of N_{rod}, we should be able to set l_p to any aribtrary value and still recover the same swelling at a particular $\tilde{z}$ as per Equation 4.25. In other words, when we extrapolate to the limit of $(N-1) \to N_{\text{rod}}$, our results should be independent of the persistence length l_p (and hence the bending potential). This should be true irrespective of our choice of N_{rod}, although results will not be universal or necessarily parameter-free except in the $N_{\text{rod}} \to \infty$ case.

4.3 Static scaling results

We are now in a position to test our scheme for the static scaling of radius of gyration. Here we use FENE springs with a bending potential and Gaussian EV, such that the FENE b-parameter is set via Equation 4.13 given N_{rod} and N_s, the bending potential is set via Equation 4.24 given l_p, and the EV strength is set via Equation 4.25 for some $\tilde{z}$. In Figure 4.6, this is done for $N_{\text{rod}} = 500$ with $l_p = 1$, 2, and 4. In all cases, $d^* = 2z^{*1/5}$, and $N = 20$ to 30 in steps of 2. For each N, the swelling of the radius of gyration due to EV is averaged over approximately 10^4 trajectories at equilibrium, and the results extrapolated to $N_{\text{rod}} = 500$.

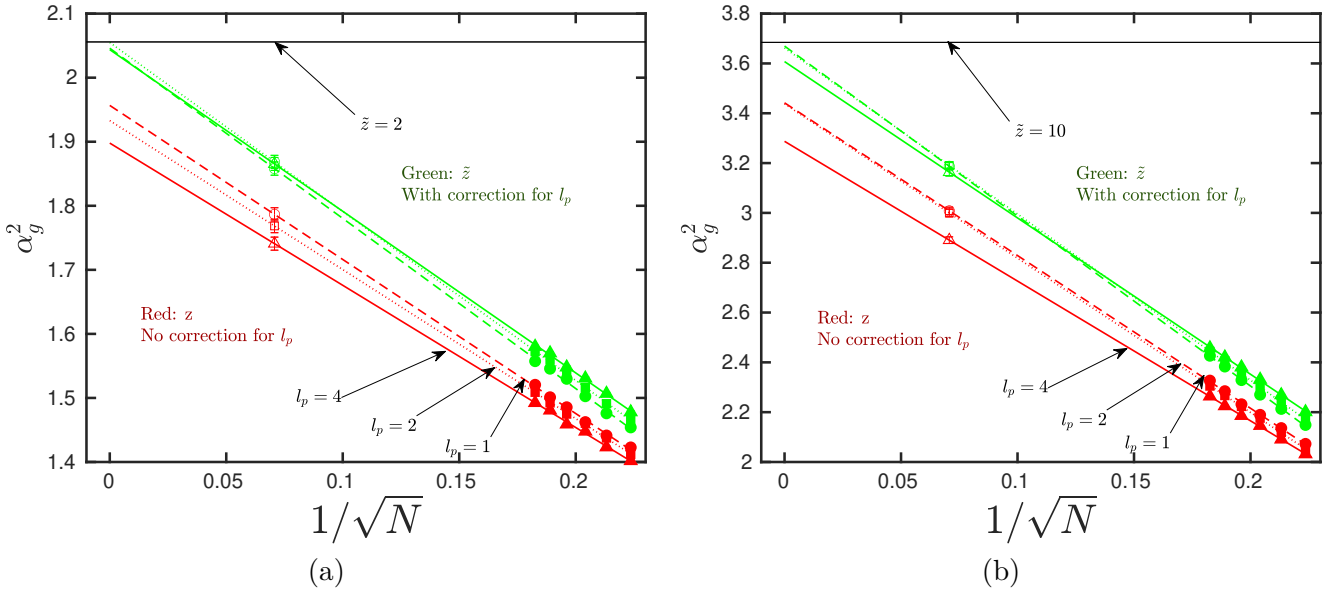

FIGURE 4.6: Comparison of using a bending potential without a correction for z (red curves), as well as correcting for the bending potential with $\tilde{z}$ (green curves). Plot (a) is for $\tilde{z}, z = 2$, while plot (b) is for $\tilde{z}, z = 10$. Dashed lines are $l_p = 1$, dotted lines are $l_p = 2$, full lines are $l_p = 4$. Symbols at $1/\sqrt{N}$ represent the results extrapolated to $N_{\text{rod}} = 500$. Here $K = 2$, and $d^* = Kz^{*1/5}$. Horizontal lines show the expected α_g^2 results for both z values based upon the fitting parameters to Equation 4.3 from Kumar and Prakash [93], namely $am = 1.276$, $b = 19.48$, $c = 14.92$, $m = 0.1339$. Error bars are approximately symbol size. Extrapolations are linear least-squared fits.

Also included are results for the swelling without the QTP correction for z, the $4/3K(L)$ factor. As can be seen, the extrapolations are identical to within error bars for $\tilde{z}$, but differ when the

correction is not applied. Let us carefully examine what these results imply, with reference to hypothetical experimental measurements of an equivalent underlying system. Experimentally, we have some θ-temperature, which corresponds to the no-EV case in our simulations. For short polymer chains, or specifically semiflexible chains with small L/l_p, the α_g vs z curves for polymers of different stiffnesses at several temperatures or lengths will not be identical if z is defined as in Equation 4.1 [49, 134]. Instead, one must correct for z by applying the $K(L/2l_p)$ factor, in which case one obtains the new solvent quality $\tilde{z}$, where the curves for different stiffnesses will lie on top of one another. If we only used T and $\sqrt{M}$ to define z, one would not obtain the same swelling at a for different l_p at a particular z, while on the other hand if one uses $\tilde{z}$, results do in fact collapse [49]. So, when we apply the QTP theory correction to our simulations, we seek to identically make our results independent of the semiflexibility, characterised by l_p. In fact, we have shown through the use of Equation 4.25 in Figure 4.6 that we don't even need to apply a post-hoc correction to the overall swelling curve, but can instead directly 'feed-in' the $K(L/2l_p)$ factor to our calculation for z^*. This ensures that $\tilde{z}$ is the same for each curve with different l_p, leading to the same extrapolated value of swelling irrespective of l_p. This allows us to incorporate semiflexibility into our SFG modelling, and still be confident that the swelling will be constant at a particular $\tilde{z}$ for a particular value of N_{rod}. Specifically, at each N_s, we have chosen our bending stiffness C via Equation 4.24 such that the underlying N_{rod}/l_p is recovered, and so we know from QTP theory that we can apply a constant $K(L/2l_p)$ correction to keep $\tilde{z}$ constant.

We have therefore shown, at least for this case, that QTP is able to correct for the change in swelling due to a bending potential (through l_p) at a particular $\tilde{z}$. However, we still have other parameters which influence the swelling, namely the range of the EV potential d^*, as well as the number of rods for our extrapolation N_{rod}. For $N_{\text{rod}} \to \infty$, we know that the swelling must necessarily approach the universal value, as it is independent of local model details such as short-range potentials (that is, short range along the polymer backbone, not in space). On the other hand, for finite N_{rod}, the results are not universal. While they are not universal, they may be parameter-free at a sufficiently high N_{rod}, at which point the chain is sufficiently long for the EV potential range to no longer determine the swelling (it is instead purely a function of $\tilde{z}$).

Extrapolations for several K, where $d^* = Kz^{*1/5}$ (not to be confused with the correction factor $K(L)$ in QTP theory), as well as four N_{rod} at $l_p = 2$ and $\tilde{z} = 2$ are displayed in Figure 4.7. For small N_{rod}, particularly the $N_{\text{rod}} = 200$ case, the two extrapolated values are clearly different, meaning that the d^* parameter still has a strong influence upon the observed swelling. However, as one successively increases N_{rod}, the two extrapolated values converge, to the point where they very nearly agree within error bars for $N_{\text{rod}} = 800$. In theory, it should be possible to perform a double-extrapolation to the universal value at $\tilde{z} = 2$, however the extrapolations do not appear precise enough to allow for this. Nevertheless, it is clear that

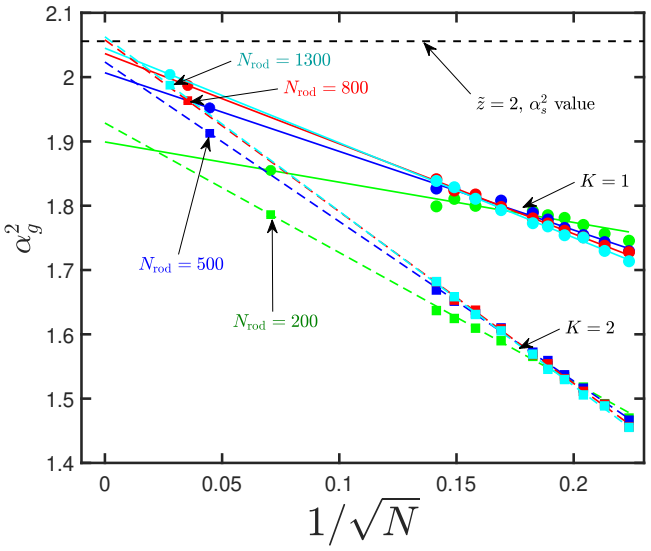

FIGURE 4.7: Extrapolations for several $N_{\rm rod}$ and K, where $d^* = Kz^{*1/5}$. In all cases, $l_p = 2$ and $\tilde{z} = 2$, with FENE sprng parameters and bending potential selected as described in the text. Lines are linear extrapolations. Where not visible, error bars are smaller than symbol size.

while results are not universal, we are able to correct for the influence of the semiflexibility l_p, and also that our results approach the universal curve as $N_{\rm rod} \to \infty$.

With this in mind, we can combine Figure 4.6 and Figure 4.7 into a single curve for several $\tilde{z}$, as in Figure 4.8. Also included in Figure 4.8 is the universal swelling curve based on a fit to Hookean spring data in the long-chain limit [93], as well as experimental data from Norisuye et al. [134] on the radius of gyration swelling for several synthetic semiflexible polymers. The experimental data has been carefully corrected for the semiflexibility using QTP theory, and so all results are plotted in terms of $\tilde{z}$.

As can be seen, simulation results do not perfectly agree with the universal curve for smaller values of $N_{\rm rod}$. However, they approach the universal curve as $N_{\rm rod}$ is increased, until they lie on the universal curve for $N_{\rm rod} = 1000$, irrespective of l_p. A considerable amount of scatter can be seen in the experimental results, all of which are at fairly low $\tilde{z}$. The range of L/l_p values for the experimental data ranges from roughly 10 to 500, so the low $\tilde{z}$ appears to be due to relatively low excluded volume strength seen in semiflexible polymers. For reference, the largest experimentally-measured swelling, for Na-HA in 0.5M NaCl, has $L/l_p \approx 200$ [134], and hence the correction to z from $3/4K(L/l_p)$ is approximately 0.86 as per Equation 4.23. Therefore, our application of the QTP theory covers a similar range to the available experimental data, and appears to lie within the regular experimental error.

Overall, in this section, we have demonstrated that we can use QTP theory to obtain parameter-free predictions of static swelling, in the sense that for a particular $N_{\rm rod}$ and $\tilde{z}$, the value of z^* can be chosen such that the swelling is independent of l_p. However, in order to apply these

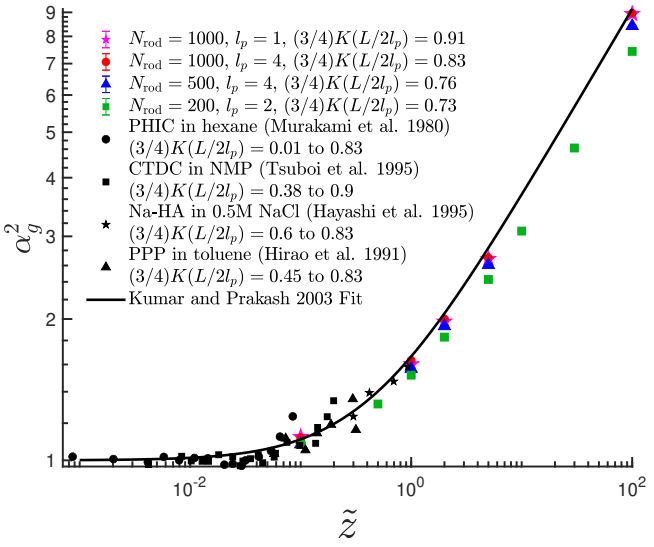

FIGURE 4.8: Coloured symbols are BD simulations with different $N_{\rm rod}$ and l_p. Where not visible, magenta symbols for $N_{\rm rod} = 1000$ and $l_p = 1$ are directly underneath the red $N_{\rm rod} = 1000$ and $l_p = 4$ symbols. Experimental data (filled black symbols) is from Norisuye et al. [134], who collated data on the swelling of semiflexible polymers (with $L/2l_p$ ranging from about 5 to 250, and hence $3/4K(L/2l_p)$ from about 0.25 to 0.88) measured by several other authors [135–138]. Line is Equation 4.3 with $am = 1.276$, $b = 19.48$, $c = 14.92$, $m = 0.1339$ [93].

ideas to obtain parameter-free predictions for dynamic quantities and away from equilibrium, we should also choose our h^* parameter such that predictions are independent of the particular choice of l_p. To do so, in the next section we will approach the corrections to z^* and h^* in a slightly different manner, drawing upon simple dimensional arguments. We will not be answering exactly the same question - namely, in this section we have asked whether one can use QTP theory to collapse swelling predictions for chains with different l_p on top of one another in the extrapolated $N_s \to N_{\rm rod}$ limit. Instead, we will show that one can derive the expected change in swelling when a bending potential is added to an arbitrary polymer model, and use this to collapse the swelling back on the freely-jointed (no bending potential) result at a particular N_s.

4.4 Corrections to swelling directly from bending potential

Let us consider the arguments used to derive Equation 4.16 and Equation 4.17, as done by Prakash and coworkers [14, 16]. The basic sketch of the procedure is as follows. Firstly, one assumes that the distance between two beads μ and ν follows a Gaussian distribution, namely:

$$\psi(r_{\mu\nu}) = \left(\frac{2}{3\pi\langle r_{\mu\nu}^2\rangle}\right)^{3/2} \exp\left(-\frac{3r_{\mu\nu}^2}{2\langle r_{\mu\nu}^2\rangle}\right) \tag{4.26}$$

where $r_{\mu\nu} = r_\nu - r_\mu$, such that the distribution is a function of the combined variable $|\nu - \mu|$, and $\langle r_{\mu\nu}^2 \rangle$ is the equilibrium average of $r_{\mu\nu}^2$. This is of course not strictly true unless the chain is composed of purely Hookean springs, but the central limit theorem guarantees that it will be approximately Gaussian for large $|\nu - \mu|$. In other words, the distance between two beads separated by large distances along the chain backbone will always be approximately Gaussian. Secondly, one gives an expression for $\langle r_{\mu\nu}^2 \rangle$, a point which we will return to shortly. Then, one evaluates some quantity which is a function of h^* or z^*. For example, for the case of HI and no EV, one can evaluate the sum:

$$\sum_{\substack{\mu,\nu \\ \mu \neq \nu}}^{N} \left\langle \frac{1}{r_{\mu\nu}^*} \right\rangle_{\text{eq}} \tag{4.27}$$

which then allows the Kirkwood diffusivity and hence $U_{R\bar{D}}^{\theta}$ to be evaluated as per Equation 4.18 and Equation 4.19. For the case of EV, one can evaluate the end-to-end distance using the covariance:

$$\left\langle R_{\text{e}}^2 \right\rangle = \sum_{\mu\nu}^{N_s} \langle \mathbf{Q}_\mu \cdot \mathbf{Q}_\nu \rangle \tag{4.28}$$

which requires a more complicated perturbation expansion in the EV [16], but ultimately still gives a similar final sum. Once the averages are determined, one can transform the sums into integrals, and then compare the expansion with the purely Hookean case to determine the required corrections to z^* and h^*.

While this is far from straightforward, it was done for non-Hookean chains by Prakash and coworkers [14, 16], giving the corrections to z^* and h^* in terms of χ. Our aim is to determine similar expressions for chains with a bending potential, ideally deriving the expected correction in terms of the average included angle between bends, namely:

$$c = \langle \cos\theta \rangle \equiv \coth C - \frac{1}{C} \tag{4.29}$$

where the final expression is for our particular form of the bending potential. While it isn't clear that this is, in general, possible, here we will present a very simple derivation of the correction to h^* and z^* based upon dimensional arguments. We then hope to show the validity of these corrections numerically, which can guide a later, more precise derivation. Such a derivation is presented for the diffusivity in Section 4.4.2.

The first step is to write out an explicit expression for $\langle r_{\mu\nu}^2 \rangle$ given a bead-spring chain with a bending potential. However, even at this stage we run into an issue. One can show that for a bead-rod chain of N_s rods with some rod length l and average bending angle $c = \langle \cos\theta \rangle$, the end-to-end distance is given by:

$$\langle r_{N_s}^2 \rangle = N_s l^2 \left(\frac{1+c}{1-c} + \frac{2c}{N_s} \frac{(c^{N_s} - 1)}{(c-1)^2} \right) \tag{4.30}$$

which was also found by Winkler, Reineker and Harnau to be identical for infinitely stiff Fraenkel springs of average length l [119] (when correcting for an apparent typographical error in the formula of Winkler, Reineker and Harnau, as they had an additional N_s factor on the second term of the brackets). However, for Hookean springs, with again average length l but fluctuations allowed about the average length l, the expression is in fact different, and has the form [119]:

$$\langle r_{N_s}^2 \rangle = N_s l^2 \left(1 + \frac{16}{3\pi} \left[\frac{c}{1-c} + \frac{c}{N_s} \frac{(c^{N_s}-1)}{(c-1)^2} \right] \right) \tag{4.31}$$

where we have again corrected for an apparent typographical error in their expression, which was missing an additional c in the first term within the square brackets.

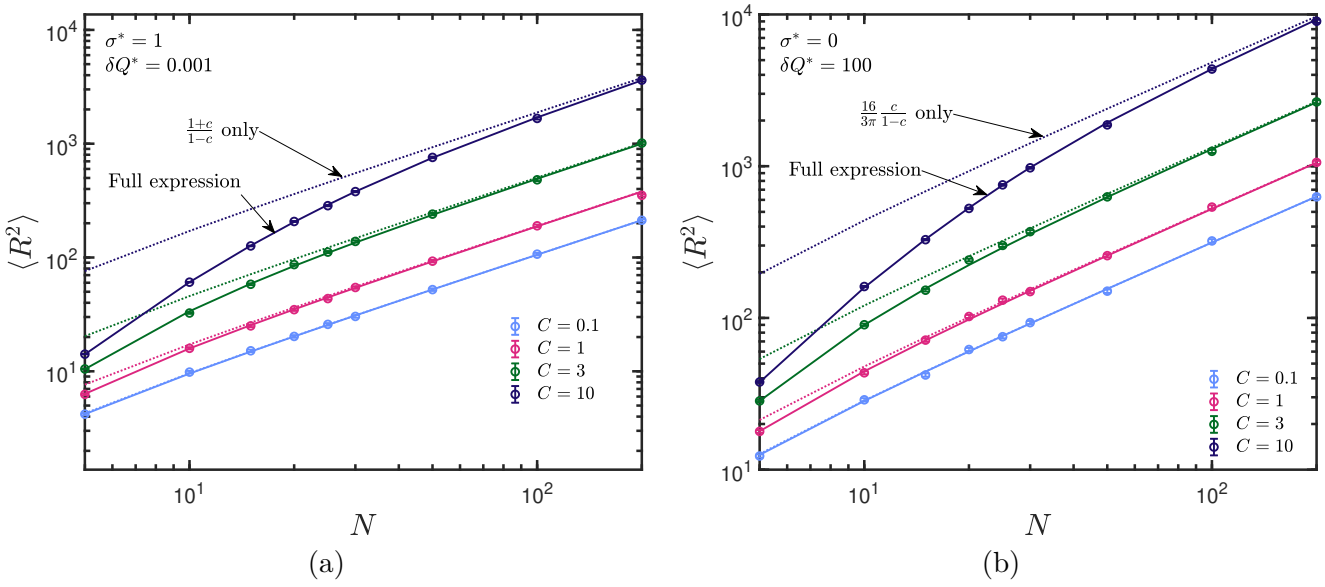

FIGURE 4.9: (a) Comparisons of $\langle R^2 \rangle$ for rodlike chains generated using a Monte-Carlo method with Equation 4.30. Dotted line only considers the first term in the brackets of Equation 4.30, in other words we assume the second term is zero. (b) Comparisons of $\langle R^2 \rangle$ for Hookean chains generated using a Monte-Carlo method with Equation 4.31. Dotted line only considers the first term in the angular brackets of Equation 4.31, in other words we assume the second term is zero.

In order to test these expressions, chains are generated using a Monte-Carlo scheme [132] outlined in Appendix H, and the average end-to-end distance of the simulated chain ensembles compared with Equation 4.30 and Equation 4.31. Several features are apparent. Firstly, there is indeed a difference between Hookean and highly constrained springs of the same l in our simulations, as the analytical results guarantee. Secondly, the difference vanishes for small C, since $C \to 0$ implies $c \to 0$ and hence $\langle r_{N_s}^2 \rangle = N_s l^2$ in both cases. Finally, one can actually approximately ignore part of the expression for small C or large N_s, namely the term which contains a power law in N_s. This means that for small C or large N_s, the end-to-end distance squared is approximately linear in N_s. As used in Equation 4.26, this means that the average bead separation is linear in $|\mu - \nu|$, which also follows from the central limit theorem for large $|\mu - \nu|$.

Now let us derive new h^* and z^* expressions using a simple dimensional argument. Note that h^* is effectively a non-dimensional bead radius, while z^* is effectively a volume over which other beads are excluded, and they scale like a length and a volume respectively. Note what happens to the root-mean-square end-to-end distance as per Equation 4.30 and Equation 4.31 when one changes the average spring length - they both scale by the same amount. Therefore, if χ is a non-dimensional spring length, we can imagine how one can see that if we decrease χ, we should increase z^* and h^* as per Equation 4.16 and Equation 4.17, namely $z^*_{\text{new}} = z^*\chi^3$ and $h^*_{\text{new}} = h^*\chi$. So, let us assume that we should apply a similar correction when we have some non-zero c, namely:

$$z^* = \frac{z\chi^3\xi^3}{\sqrt{N}} \tag{4.32}$$

$$h^* = \frac{h\chi\xi}{\sqrt{N}} \tag{4.33}$$

where for rods or very stiff springs:

$$\xi = \left(\frac{1+c}{1-c}\right)^{1/2} \tag{4.34}$$

and for Hookean springs:

$$\xi = \left(1 + \frac{16c}{3\pi(1-c)}\right)^{1/2} \tag{4.35}$$

For other springs, ξ will have some value between these two limits.

4.4.1 Tests of correction for static properties

Let us first test this correction for Hookean springs. To do so, we simulate chains with Hookean springs (where $\chi = 1$) and several C values given $z = 2$, $d^* = 2z^{*1/5}$ and no HI at equilibrium. For each C value, we either set $\xi = 1$, or alternatively calculate ξ using Equation 4.35 and then calculate z^* using Equation 4.32. The $\xi = 1$ case corresponds to 'no correction' - this is the raw swelling when we set $z^* = z/\sqrt{N}$ even though we have a bending potential. The swelling in each case can be seen in Figure 4.10, for $C = 0, 0.1, 0.5$, and 2. It is immediately obvious that the correction is causing the extrapolated values to move considerably closer to the universal result, and in fact the curves for $C = 0, 0.1$, and 0.5 agree to within error bars when the correction is applied. The $C = 2$ result has come close to the universal value, but still is not fully accurate - this may be due to a longer chain being needed, or one of our approximations used in deriving the ξ correction may be inaccurate for larger C.

Importantly, note that even for finite N_s, the results for the freely jointed Hookean chain, and those with a bending potential but corrected using ξ, have collapsed onto a similar result even for finite N_s. The result is particularly striking for $C = 2$, where the swelling differs by almost 20% without the correction, but has collapsed with the correction. Therefore, it appears

that one can use the expression in Equation 4.35 to not only obtain universal predictions when a bending potential is used, but also recover the same swelling as that of a flexible chain for finite N_s. This seems to be the key difference between the QTP theory and this new scheme - in this case, there is no fundamental underlying concept of 'chain length' which determines our correction to z, as for the $K(L/l_p)$ factor in some SFG limit. Instead, we derive a correction to the z^* value based upon the local correlation between segments, which collapses data approximately on top of the freely jointed result for an arbitrary bending potential.

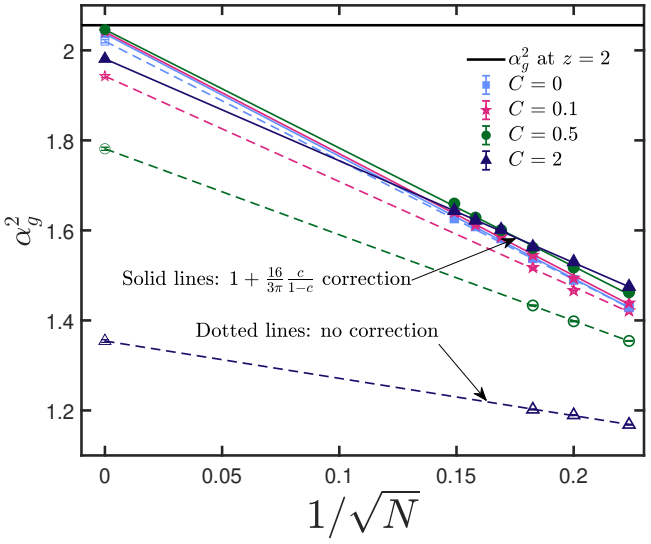

FIGURE 4.10: Radius of gyration swelling for Hookean chains with a bending potential. Dotted lines and empty symbols represent simulations without the correction for ξ as per Equation 4.35, while solid lines with filled symbols use the correction. The $z = 2$ line presents the universal value of α_g^2 at $z = 2$ from previous simulations for Hookean chains [93]. All extrapolations are linear, with the symbols at $1/\sqrt{N} = 0$ representing the long-chain limit result. Where not visible, error bars are smaller than symbol size.

We can also perform a similar test for $U_{R\bar{D}}$, this time doing a double-extrapolation using FENE springs with a bending potential. In Figure 4.11, this is done using our previous Monte-Carlo generation of equilibrium, θ-solvent configurations. Notably, when the correction is applied, the double-extrapolated value agrees with the universal value to within error bars, while the uncorrected value does not. In this case, it appears unimportant that the ξ correction is strictly accurate only for rods, since while we are using FENE springs we are still extrapolating towards the bead-rod limit. Although this is a calculation of static diffusivity, it suggests that when performing SFG simulations with a bending potential, one can correct h^* using the expression in Equation 4.33, to obtain roughly parameter-free predictions.

4.4.2 Rescaling HI parameter with bending potential

Here we give a summarised version of the calculations of Sunthar and Prakash [16]. The hydrodynamic interaction between beads in a BD simulation occurs via the RPY tensor,

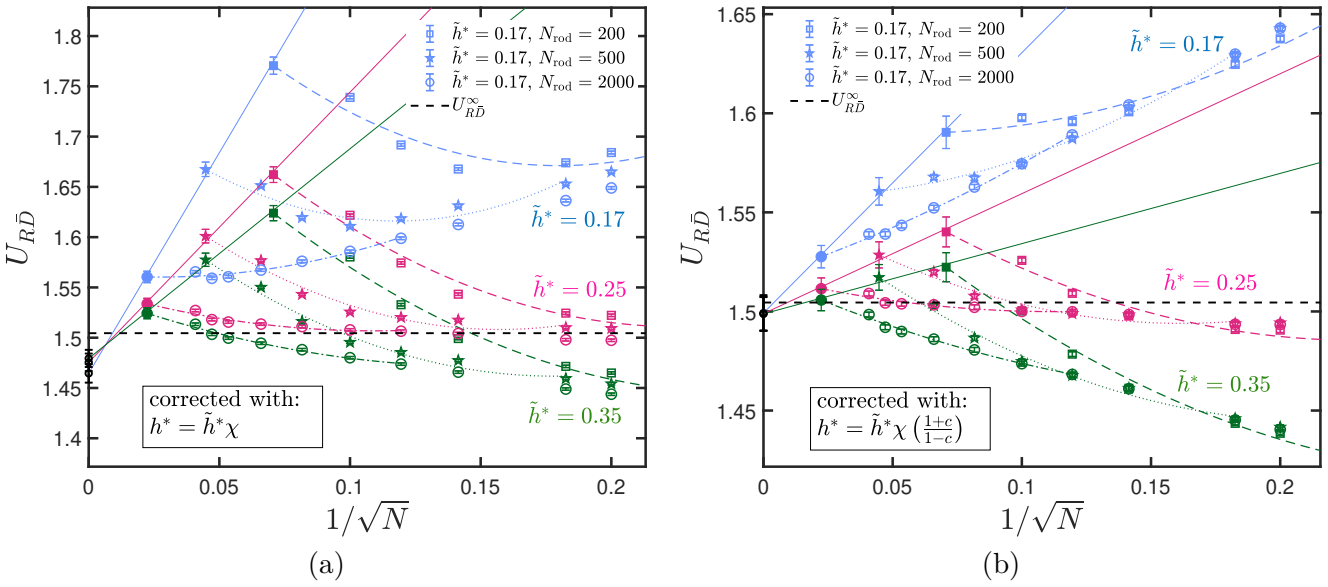

FIGURE 4.11: Double extrapolations using the same Monte-Carlo method as in Figure 4.5. In both (a) and (b), we have set $l_p = 4$ and chosen C and the FENE parameters as per our previous method for QTP theory extrapolations. For (a), h^* has been corrected only using χ, while for (b), we have also applied the β correction for rods.

which is equivalent at large distances to the Oseen tensor [34]. When preaveraged using the equilibrium distribution, we obtain the isotropic form of the Oseen tensor, specifically [34]:

$$\langle \boldsymbol{\Omega}_{\mu\nu} \rangle_{\rm eq} = \frac{1 - \delta_{\mu\nu}}{6\pi\eta_s} \left\langle \frac{1}{r_{\mu\nu}} \right\rangle_{\rm eq} \boldsymbol{\delta} \tag{4.36}$$

where we can evaluate the ensemble average over the inverse bead separation using the equilibrium distribution function. For freely jointed chains with Hookean springs, the probability density $P(\boldsymbol{r}_{\mu\nu})$ is Gaussian, but once a bending potential is included this is no longer the case. However, by definition correlations between segments reduce at a rate roughly proportional to $\langle \cos\theta \rangle^{|\mu-\nu|}$, where $\langle \cos\theta \rangle$ is the average cosine of the angle between adjacent segments due to the bending potential (and $\langle \cos\theta \rangle = 0$ for a freely jointed chain, so correlations decay instantly). As $\langle \cos\theta \rangle$ is less than 1, this is essentially an exponential decay with decay constant $\ln \langle \cos\theta \rangle$, and so after some distance $|\mu - \nu|_{\rm min}$ which depends on the bending potential, the correlations will have decayed and $P(\boldsymbol{r}_{\mu\nu})$ will be Gaussian. We have previously seen that this Gaussian has the form:

$$\psi(r_{\mu\nu}) = \left(\frac{3}{2\pi \langle r^2_{\mu\nu} \rangle} \right)^{3/2} \exp\left(-\frac{3 r^2_{\mu\nu}}{2 \langle r^2_{\mu\nu} \rangle} \right) \tag{4.37}$$

and for Hookean springs, we have that:

$$\langle r^2_{\mu\nu} \rangle = |\mu - \nu| l^2 \left(1 + \frac{16}{3\pi} \left[\frac{c}{1-c} + \frac{c}{|\mu - \nu|} \frac{(c^{|\mu-\nu|} - 1)}{(c-1)^2} \right] \right) \tag{4.38}$$

where $l = \sqrt{3}\sqrt{k_{\mathrm{B}}T/H}$ and $c = \langle \cos\theta \rangle$. However, when evaluating the average $\langle 1/r_{\mu\nu} \rangle$ using this expression, the required integral is highly complex, and it may not be possible to solve analytically. Instead, we will assume that the second term in the square brackets in Equation 4.38 is approximately zero for $|\mu - \nu| > |\mu - \nu|_{\min}$. The resulting integral is now again a straightforward Gaussian, and we can see that:

$$\left\langle \frac{1}{r_{\mu\nu}} \right\rangle_{\mathrm{eq}} = \begin{cases} \sqrt{\frac{2}{\pi}} \frac{1}{l} \left(\frac{1}{\xi}\right) \sqrt{\frac{1}{|\mu-\nu|}} & \text{for} |\mu - \nu| > |\mu - \nu|_{\min} \\ \sqrt{\frac{2}{\pi}} \frac{1}{l} \left(\frac{1}{\xi}\right) \sqrt{\frac{1}{|\mu-\nu|}} (1 + f(c, |\mu - \nu|)) & \text{otherwise} \end{cases} \tag{4.39}$$

where the first case corresponds to our average evaluated with a Gaussian potential for $|\mu - \nu| > |\mu - \nu|_{\min}$. The second case is when $|\mu - \nu| < |\mu - \nu|_{\min}$, and the function $[1 + f(c, |\mu - \nu|)]$ represents the unknown average arising from both the non-Gaussian nature of the distribution, as well as the inclusion of the full expression in Equation 4.38. The parameter ξ is defined in Equation 4.35.

Let us now obtain the Kirkwood translational diffusivity coefficient under θ-conditions, which in the preaveraged approximation is given by:

$$\bar{D}^{\theta} = \frac{k_{\mathrm{B}}T}{N\zeta} \left(1 + \frac{h^* \sqrt{\pi}}{N} \sqrt{\frac{k_{\mathrm{B}}T}{H}} \sum_{\substack{\mu,\nu \\ \mu \neq \nu}}^{N} \left\langle \frac{1}{r_{\mu\nu}} \right\rangle_{\mathrm{eq}} \right) \tag{4.40}$$

we then substitute in from Equation 4.39, convert the sum to an integral, and carefully take into account the correction due to the singularity at $\mu = \nu$ [139], the limit of $N \gg 1$ gives:

$$\bar{D}^{\theta} = \frac{k_{\mathrm{B}}T}{N\zeta} \left[1 + \frac{h^*}{\xi} \left(\frac{8}{3} \sqrt{2N} - \frac{1}{h^*_{\mathrm{Zf}}} \right) \right] + O\left(N^{3/2}\right) + \frac{k_{\mathrm{B}}T}{N\zeta} \frac{\sqrt{2} h^*}{N\xi} g(c, N) \tag{4.41}$$

where $g(c, N)$ represents the non-Gaussian contributions to the sum, and $h^*_{\mathrm{Zf}} \approx 0.24$. As for the calculation involving non-Hookean springs and χ, this differs from the Zimm result for Hookean springs only via the presence of the function $g(c, N)$ and the factor ξ.

If we now examine the behaviour of the universal ratio $U^{\theta}_{R\bar{D}}$, we can see that:

$$U_{\mathrm{R}\overline{D}} \equiv \frac{R_{\mathrm{g}}}{R_{\mathrm{H}}} \equiv \frac{6\pi\eta_{\mathrm{s}}}{kT} \overline{D}^{\theta} R_{\mathrm{g}} = \frac{1}{\sqrt{\pi} h^*} R_{\mathrm{g}} \sqrt{\frac{H}{kT}} \frac{\overline{D}^{\theta} \zeta}{kT} \tag{4.42}$$

and therefore in the limit of large N, we can write $R_g = \sqrt{N/6} l \xi$, and hence:

$$U_{R\bar{D}} = \frac{8}{3\sqrt{\pi}} + \frac{1}{\sqrt{2\pi N}} \left(\frac{\xi}{h^*} - \frac{1}{h^*_{\mathrm{Zf}}} \right) + \mathcal{O}\left(N^{-1}\right) + \frac{1}{\sqrt{\pi} N^{3/2}} g(c, N) \tag{4.43}$$

further, we know that the long chain limit must remain unchanged regardless of the bending potential or spring force law, and so we can expand $g(c, N)$ to leading order in N, and hence

determine that:

$$U_{R\bar{D}} = \frac{8}{3\sqrt{\pi}} + \frac{1}{\sqrt{2\pi N}}\left(\frac{\xi}{h^*} - \frac{1}{h^*_{\mathrm{Zf}}(c)}\right) + \mathcal{O}\left(N^{-1}\right) \tag{4.44}$$

where $h^*_{\mathrm{Zf}}(c)$ is now a function of the first order expansion term in $g(c, N)$. If we then consider the Zimm expression for Hookean springs:

$$U_{R\bar{D}} = \frac{8}{3\sqrt{\pi}} + \frac{1}{\sqrt{2\pi N}}\left(\frac{1}{h^*} - \frac{1}{h^*_{\mathrm{Zf}}}\right) + \mathcal{O}\left(N^{-1}\right) \tag{4.45}$$

we notice that the only difference between this expression and our bending potential calculation is the factor of ξ, suggesting that we can obtain a rescaled HI parameter by absorbing the ξ factor into our definition of h^*:

$$\tilde{h}^* = \frac{h^*}{\xi(c)} \tag{4.46}$$

which has an identical form to the correction for χ derived by Sunthar and Prakash [16]. It also modifies the fixed point h^*_{Zf}, which is now a function of the bending potential stiffness constant C.

We can also see that in general, this entire derivation holds for any factor which is linear in $|\mu - \nu|$. Therefore, we can in general apply the corrections for both χ and ξ, and perform a similar derivation for rodlike segments, which gives us the corrections used in Figure 4.11.

As a final point, we note that the derivation for the segment-segment correlation using a perturbation expansion in the presence of EV is similarly linear [16]. Additionally, since there is no correlation between the spring and bending potentials, we can neatly separate out these two contributions in our perturbation expansion. While we have not explicitly followed this derivation through, we hope that our simple dimensional argument, as well as the empirical proof of Figure 4.10, is sufficiently satisfying.

4.5 Conclusions and future work

Here we have shown, using the QTP theory for the static swelling of the radius of gyration at a particular z or $\tilde{z}$, that one can correct for the semiflexibility of the chain at some N_{rod} and l_p in order to obtain predictions of α_g^2 in the $N_s \to N_{\mathrm{rod}}$ limit which are independent of the choice of l_p. Further, we show how one can potentially correct for h^* in order to give full parameter-free predictions away from equilibrium with both HI and EV. Future work could extend these results to measures of dynamic swelling, such as the zero-shear viscosity [124] or the long-time diffusivity [140]. We have made some progress towards this aim, with the BD simulation code found to be slightly inaccurate if extremely precise predictions are needed, since the Chebyshev approximation used to speed up the simulations requires more terms. This has been investigated in Appendix E.

Furthermore, this now allows one to perform fully parameter-free SFG simulations of a semiflexible chain with some L and l_p, given a particular $\tilde{z}$ and with full inclusion of HI. In Chapter 5, we have performed mostly qualitative simulations of semiflexible chains in shear flow for the purpose of comparison with Linear Dichroism experimental data, but the results of the current investigation show a possible method to obtain quantitative, parameter-free predictions.

Chapter 5

Determining Linear Dichroism using Polymer Models

5.1 Introduction

There have long been attempts to use polymer models to predict or qualitatively understand the experimentally measured Linear dichroism (LD) of macromolecules in shear flow [1–7]. LD is the polarisation-dependent absorption of light by an ensemble of oriented molecules, such that

$$\mathrm{LD} = A_{\parallel} - A_{\perp} \tag{5.1}$$

where $A_{\parallel}$ and $A_{\perp}$ represent the absorption of light polarised in perpendicular directions relative to some laboratory axis (the $\parallel$ direction). The reduced linear dichroism removes dependence on concentration and path length

$$\mathrm{LD}^{r} = \frac{\mathrm{LD}}{A_{\mathrm{iso}}} \tag{5.2}$$

where A_{iso} is the isotropic absorbance of the sample. Sample orientation can be achieved in a variety of ways [9], however, in this work the focus is on shear orientation in a Couette cell, where the sample is placed in solution and sheared between concentric cylinders (as displayed in Figure 5.1). Flow LD has the advantage of being able to probe reaction kinetics such as assembly of protein fibres [141, 142], cleavage of DNA, or protein and peptide interactions with membranes [10] with relatively small sample volumes (70 μL) [143]. However, Couette flow LD has a fairly significant disadvantage, namely that sample orientation under shear flow is both imperfect and configurationally complex due to the combination of rotational and elongational velocity components. Thus, data interpretation is often restricted to being qualitative or semi-quantitative, and attempts to calculate the orientation parameter have been either crude approximations or limited to rigid rods [2, 3]. If this difficulty could be

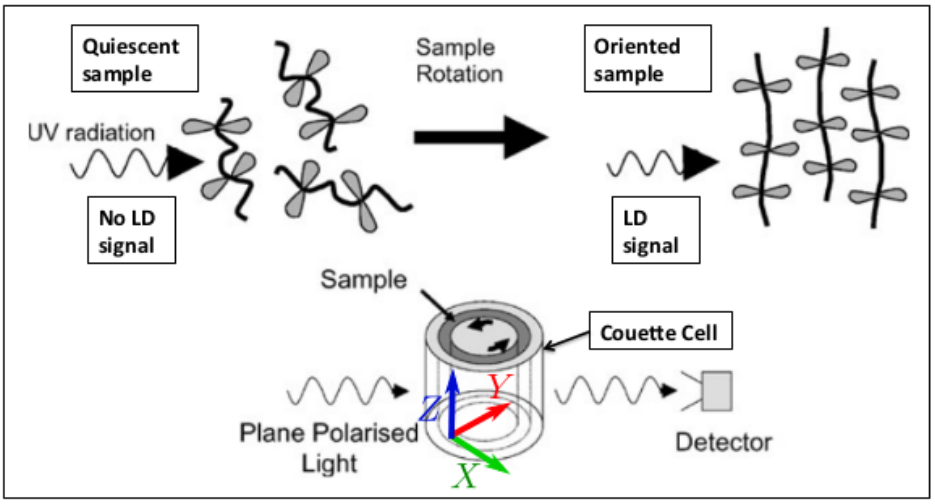

FIGURE 5.1: Use of a Couette cell for orientation of a sample. Shear flow within the cell aligns the molecules, allowing a net LD signal to be measured. In this case, as in experiments by Simonson and Kubista [17], light is propagated radially through the cell (the Y direction) and LD is measured with light polarised axially (Z direction) and perpendicular to the $Y-Z$ plane (the X direction). Relative to the flow field between the cylinders, the light is propagated along the shear gradient direction (the laboratory axis Y), while LD is measured along the flow direction (X) and neutral direction (Z).

overcome, and sample orientations determined for a particular macromolecular sample at a particular shear rate, it would be possible to considerably improve the quantitative accuracy of LD spectroscopy analysis [9, 10]. Since a full analytical theory for the conformation of a flexible polymer chain in shear flow is not possible, these treatments have previously relied on fairly significant approximations regarding the chain connectivity, perturbation due to shear flow, and physical effects such as solvent-polymer interactions and hydrodynamic forces on beads [4, 11, 12]. Recent advances in modelling of dilute polymer solutions, most notably the development and refinement of simulation methods such as Brownian dynamics (BD), allow one to avoid many of the earlier approximations [13]. It is now possible to qualitatively recover much of the key behaviour of polymers in shear flows, and even obtain quantitative, parameter-free predictions in extensional flows [12, 14–16] (although shear flows remain challenging).

BD has previously been used by Ødegaard-Jensen, Elvingson and Håkansson [8] to study the shear flow LD of short DNA fragments from 200-1000 nm (about 600-3000 base pairs), albeit at shear rates considerably higher than accessible experimentally. They used between 64 and 320 segments in their polymer model, with each segment corresponding to approximately 10 base pairs. For each polymer chain at several shear rates, they then calculated the orientation factor, defined as:

$$S = \langle u_X^2 \rangle - \langle u_Z^2 \rangle \tag{5.3}$$

where u_X and u_Z are the projection of the segment unit vectors onto the flow X and neutral Z axes respectively, and $\langle\rangle$ is an average over all chain segments and all independent chain

trajectories. As we will later show, this S-parameter is directly proportional to LD^r. Interestingly, they also calculated the same orientation parameter for the overall polymer end-to-end vector, and found it was over two times larger than the orientation parameter of the individual segments [8]. It is the former orientation, that of individual segments a few base pairs long, which determines the experimentally measured LD^r [4, 8, 9].

While LD is measurable for many relevant biopolymers, in the current work we will focus our attention on DNA, as it is widely studied and we have the experimental data of Simonson and Kubista [17] with which to compare. We will develop a model which can represent a DNA fragment of arbitrary length, from 300 bp all the way to 164 kbp, by 'coarse-graining' the underlying polymer as a chain of beads connected by springs. Specifically, rather than setting a constant 10 base pairs per segment, we will use a spring force law which can represent anything from tens of base pairs to thousands of base pairs, such that one can simulate even long DNA fragments ($>$ 100 kbp) with less than 100 springs, which allows for efficient simulation. However, the results of Ødegaard-Jensen, Elvingson and Håkansson [8] suggest that in doing so, we must be careful to ensure we can still capture the average orientation of the DNA base pairs themselves, rather than just the coarse-grained segments, as this is what ultimately determines the experimental LD. The problem of determining the LD of a real polymer chain given a coarse-grained representation has been described and investigated in the literature [1, 2, 102, 144], and we will spend some time reviewing this research and applying it to our current work.

In this chapter we first review prior work on shear flow LD calculations and then outline the multiscale polymer model we have developed based on the so-called FENE-Fraenkel spring, originally proposed by Hsieh et al. [23]. At least in theory, this approach enables us to model a DNA fragment using segments from tens of base pairs all the way up to several thousand base pairs [65]. We test our model by comparison with the data of Simonson and Kubista [17], who measured the LD in Couette flow for a wide range of DNA fragment lengths over several shear rates and salt concentrations.

5.2 Calculating Linear Dichroism from a Polymer Model

LD is an absorption spectroscopy and so arises from the coupling of the electric field vector, $\boldsymbol{E}$, of light with an electric transition dipole moment $\boldsymbol{\mu}$ of a molecule to cause transitions between molecular energy states. $\boldsymbol{\mu}$ is an integral function of the electric dipole operator and the initial and final molecular wavefunctions for the transition [55]. The oscillator strength A (or absorption magnitude) may be written:

$$A = k|\boldsymbol{\mu} \cdot \boldsymbol{E}|^2 = (\mu E \cos\Omega)^2 \tag{5.4}$$

where k is a constant with respect to $\boldsymbol{E}$ and $\boldsymbol{\mu}$ but may vary with light wavelength λ [4, 9], μ and E are the magnitudes of the $\boldsymbol{\mu}$ and $\boldsymbol{E}$ vectors, while Ω is the angle between them, as displayed schematically in Figure 5.2. The signal in a real solution is an ensemble average over the many molecules which interact with the light.

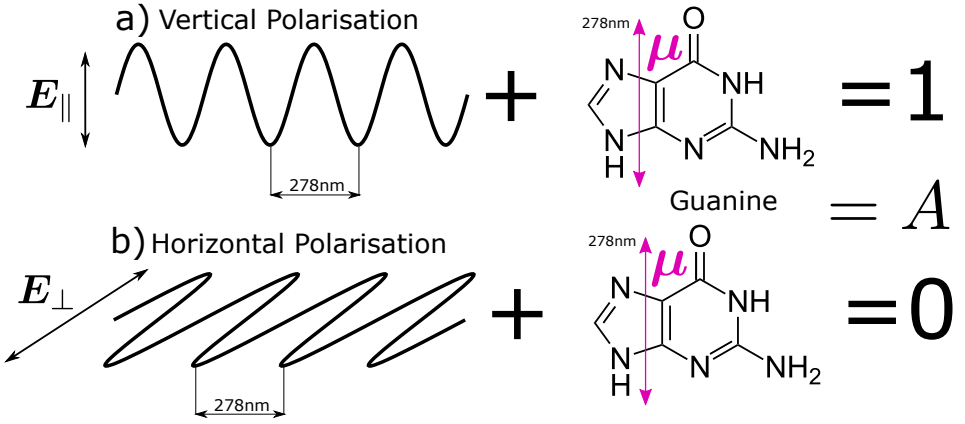

FIGURE 5.2: Differential absorption of polarised light (with electric field vector $\boldsymbol{E}$) by a representative molecule (DNA base Guanine). Magenta arrows represent the direction of the transition dipole moment $\boldsymbol{\mu}$. In (a), the 278nm light is polarised parallel to the 278nm transition dipole moment ($\hat{\boldsymbol{\mu}} \cdot \hat{\boldsymbol{E}} = 1$), so that absorption is at a maximum. In (b), the light is polarised perpendicular to the same dipole moment ($\hat{\boldsymbol{\mu}} \cdot \hat{\boldsymbol{E}} = 0$), leading to a minimum in absorption.

If one were able to somehow determine the orientation of every single transition dipole moment $\boldsymbol{\mu}$ in some solution of DNA, it would be in principle straightforward to use Equation 5.4 to calculate the LD. One can define the parallel and perpendicular absorptions in Equation 5.1 using light polarised along two orthogonal laboratory axes, such as:

$$A_X = \langle k|\boldsymbol{\mu} \cdot \boldsymbol{E}_X|^2 \rangle \tag{5.5}$$

where $\boldsymbol{E}_X$ is light polarised along the laboratory X-axis as in Figure 5.1, and $\langle\rangle$ is an average over all the $\boldsymbol{\mu}$ at the given wavelength of light. We can define a similar A_Z in terms of $\boldsymbol{\mu}$ and $\boldsymbol{E}_Z$, and hence:

$$\mathrm{LD}^r = \frac{A_X - A_Z}{A_{\mathrm{iso}}} \tag{5.6}$$

where A_{iso} is the isotropic absorption, for example at equilibrium in the absence of flow. We assume that $\boldsymbol{E}_X$ and $\boldsymbol{E}_Z$ have the same magnitude E (i.e. the same electric field strength), so that we will mainly deal with the unit vectors $\hat{\boldsymbol{E}}_X \equiv \boldsymbol{\delta}_X$ and $\hat{\boldsymbol{E}}_X \equiv \boldsymbol{\delta}_X$, where $\boldsymbol{\delta}_X$ and $\boldsymbol{\delta}_Z$ are unit vectors in the X and Z directions respectively. The challenge is of course to locate each $\boldsymbol{\mu}$, which is in general extremely complex given a long polymer chain in shear flow. However, we can simplify this process significantly by realising that each $\boldsymbol{\mu}$ is not freely floating in space, but instead 'attached' to the DNA double-helix, and so it is possible to decompose the overall LD signal into separate components.

Consider Figure 5.3, where we have representations of the DNA chain at vastly different length scales. Beginning at the 'base-pair axis' on the left, the overlapping transition moments with absorption at a particular wavelength of light λ are represented by $\boldsymbol{\mu}_1, \boldsymbol{\mu}_2, \boldsymbol{\mu}_3$. The direction of each of these transition moments can be expressed relative to the orientation of the base pair. Further, each base pair is in fact embedded within the DNA double-helix, such that the vector $\boldsymbol{u}$ is at all times parallel to this 'helix axis'. In our polymer models, we cannot individually represent every base pair, or even the entire DNA backbone, but instead split the DNA chain up into N_s segments of length Q, each with a vector $\boldsymbol{Q}$ pointing along the segment. In our model, each of these segments will be represented as a spring (connecting beads which capture the hydrodynamic friction), and the overall 'macromolecular axis' is defined in terms of the end-to-end vector $\boldsymbol{R}$.

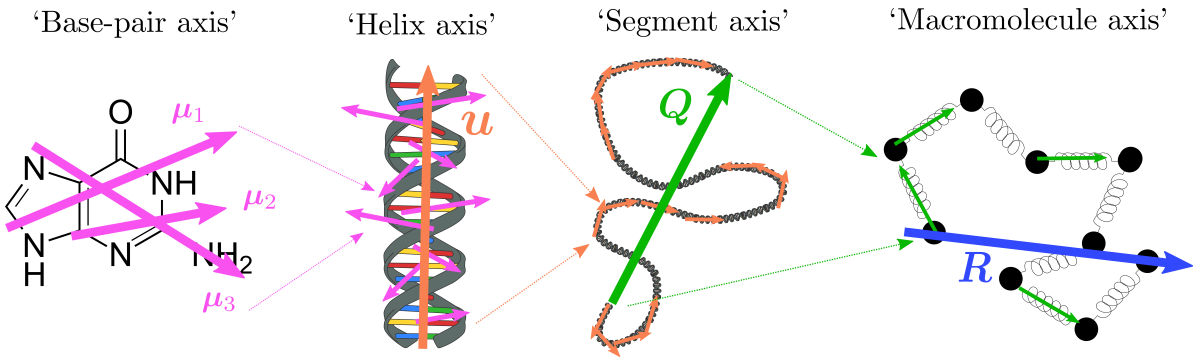

FIGURE 5.3: Different levels at which we can calculate S as per Equation 5.3. Magenta arrow is each transition dipole moment $\boldsymbol{\mu}$. The orange arrow is always tangential to the contour of the DNA helix [1], hence its designation as the helix axis. The green arrow shows the orientation of each spring in our polymer model, equivalent to each link in Figure 5.4 or Figure 5.5. Finally, the blue arrow gives the overall orientation of the end-to-end vector, which points between the first and last beads in our model chains (or the first and last monomers in a real polymer chain). The directions of the transition dipole moments $\boldsymbol{\mu}$ are purely schematic, and do not represent the real transitions in a DNA helix.

Now the question becomes, if we have some model of the DNA chain with segments $\boldsymbol{Q}$, can we write the LD^r not in terms of the individual transition moments $\boldsymbol{\mu}$, but instead in terms of the $\boldsymbol{Q}$? The answer is yes - more specifically, we can separate out the LD^r into three separate components, what we will call the segment orientation S_s, the base-pair orientation S_BP, and the optical factor O [4, 17, 145]:

$$\mathrm{LD}^r = S_s \times S_\mathrm{BP} \times O \tag{5.7}$$

all of which are dimensionless quantities. This separation is possible due to the approximate cylindrical symmetry of the base pairs within the double helix, and the chain contour $\boldsymbol{u}$ around each segment $\boldsymbol{Q}$, the mathematical details of which are derived in Appendix I. Here, we will

[1] DNA schematic adapted from Difference DNA RNA-EN.svg by Sponk based on Double-stranded DNA by MesserWoland and Chemical structures of nucleobases by Roland1952 licensed under the Creative Commons Attribution-Share Alike 3.0 Unported license and the 2.5 Generic, 2.0 Generic and 1.0 Generic licenses.

simply give the form of each component, as well as an explanation of its meaning and method of calculation.

We begin with the optical factor, O. This quantity effectively describes the average difference in absorption of light polarised parallel and perpendicular to the DNA helix (i.e. parallel and perpendicular to $\boldsymbol{u}$). This represents an average over both the overlapping transition moments in a base pair at a particular wavelength, and also over all the base pairs along the backbone of the chain. A commonly used explicit expression for O is given by [145]:

$$O = \frac{\sum_p A_p(\lambda)(3\cos^2\alpha_p - 1)}{\sum_p A_p(\lambda)} \tag{5.8}$$

where $A_p(\lambda)$ is the absorbance of the pth transition moment in the DNA chain at some wavelength λ, and α_p is the angle that transition moment makes with the helix axis $\boldsymbol{u}$. Note that $A_p(\lambda)$ (and hence O) is a function of the magnitude of the light electric field vector E as per Equation 5.4, but does not depend on its direction - the dependence on the direction of $\boldsymbol{E}$ (given by the unit vector $\hat{\boldsymbol{E}}$) is contained in the S_s factor. Other expressions are possible [146], and determination of O for a DNA fragment with either specific, or random base pair sequences has a long history [1, 4, 145]. For our purposes, it suffices to assume a random distribution of base pairs, for which O is generally thought to be $O \approx 1.48$ at 260nm, the wavelength used in the experiments of Simonson and Kubista with which we will be comparing [4, 17]. In the context of the present discussion, it is useful to intuitively think of O as a kind of 'averaged projection' of each $\boldsymbol{\mu}$ onto the tangent to the double helix $\boldsymbol{u}$.

We then turn to the base-pair orientation factor, which we have called S_BP. This factor is derived in a similar way to O, only instead of projecting $\boldsymbol{\mu}$ onto $\boldsymbol{u}$, we project the $\boldsymbol{u}$ onto $\boldsymbol{Q}$. Specifically, S_BP is given by:

$$S_\mathrm{BP} = \langle(\hat{\boldsymbol{u}} \cdot \hat{\boldsymbol{Q}}_\parallel)^2\rangle_Q - \langle(\hat{\boldsymbol{u}} \cdot \hat{\boldsymbol{Q}}_\perp)^2\rangle_Q \tag{5.9}$$

where $\hat{\boldsymbol{u}}$ represents a unit vector in the direction of $\boldsymbol{u}$, while $\hat{\boldsymbol{Q}}_\parallel$ and $\hat{\boldsymbol{Q}}_\perp$ represent unit vectors parallel and perpendicular to $\boldsymbol{Q}$ respectively. The average $\langle\rangle_Q$ is performed for a segment of a particular end-to-end distance Q over all segments in a particular solution, a concept which will hopefully become more clear once we explicitly calculate S_BP in later sections. Namely, we will later show how one can obtain S_BP for a particular average segment length $\sqrt{\langle Q^2\rangle}$ via either the analytical expression of Wilson and Schellman [1], or more generally from simple Monte-Carlo simulations. Note that S_BP must necessarily be equal to 1 if all the $\boldsymbol{u}$ point along $\hat{\boldsymbol{Q}}_\parallel$, and equal to 0 for a random orientation of $\boldsymbol{u}$ relative to $\boldsymbol{Q}$.

Finally, we come to the segment orientation factor, S_s. At this point, we project our whole polymer onto the laboratory axes along which the dichroism is measured:

$$S_s = \langle(\hat{\boldsymbol{Q}} \cdot \boldsymbol{\delta}_X)^2\rangle_{\dot{\gamma}} - \langle(\hat{\boldsymbol{Q}} \cdot \boldsymbol{\delta}_Z)^2\rangle_{\dot{\gamma}} \tag{5.10}$$

for LD with the light polarisation in the laboratory X and Z directions, which are the flow direction X and neutral direction Z (with shear gradient axis Y along which the light is propagated, as per Figure 5.1). Here the $\langle\rangle_{\dot{\gamma}}$ represents an ensemble average over all segments in the chain, and all chains in our set of simulated chain trajectories, at a particular shear rate $\dot{\gamma}$. At $\dot{\gamma} = 0$ (a quiescent solution), all the $\boldsymbol{Q}$ will point in random directions, and so $S_s = 0$, while a hypothetical flow that perfectly aligns the molecule along X will give $S_s = 1$, which is NOT necessarily the case as $\dot{\gamma} \to \infty$. Note the connection to the expression of Ødegaard-Jensen, Elvingson and Håkansson [8] in Equation 5.3. In their case, the individual segments were short enough that the base pairs were fully aligned along the 10-bp segments, such that $S_\mathrm{BP} \approx 1$ and hence $S \equiv S_s$. This would imply that each $\hat{\boldsymbol{Q}} \equiv \hat{\boldsymbol{u}}$, and since the electric field vectors point along the X and Z axes, we could write in the notation of Equation 5.3 that:

$$\hat{u}_X = \hat{\boldsymbol{Q}} \cdot \boldsymbol{\delta}_X \tag{5.11}$$

since $\hat{\boldsymbol{E}}_X \equiv \boldsymbol{\delta}_X$ is simply a unit vector along the X-direction, and so $\hat{u}_X$ is the projection of $\hat{\boldsymbol{Q}} \equiv \hat{\boldsymbol{u}}$ onto the X-axis. As previously mentioned, we have given a mathematical derivation of this expression for S in Appendix I, as well as the details of the separation of S and O factors.

Before we move onto the details of our polymer model with which we will calculate S_BP and S_s, let us first briefly reflect on what we have found and hope to determine in the rest of this chapter. We first saw that the overall LD^r can be expressed as a projection of each transition dipole moment $\boldsymbol{\mu}$ onto the orthogonal light electric field vectors $\boldsymbol{E}_X$ and $\boldsymbol{E}_Z$, as in Equation 5.5 and Equation 5.6. However, since the transition moments are constrained to sit on the DNA helix, we can separate the overall LD signal into three separate components, O, S_BP, and S_s. Intuitively, one can think of these as the projection of the transition moments $\boldsymbol{\mu}$ onto the local helix axis $\boldsymbol{u}$, the projection of the local helix axis onto the segment vectors $\boldsymbol{Q}$, and the projection of the segment vectors onto the laboratory axis. We wish to ultimately compare our predictions with the experimental data of Simonson and Kubista [17], who determined LD^r for several DNA fragment lengths at several shear rates and salt concentrations. Prior literature has already given us the value of O, so it remains to calculate the orientation factors S_BP and S_s, which we must do for a particular length of DNA at a particular shear rate. For this, we will use previously-developed polymer physics models and a combination of Brownian dynamics simulation techniques and simple Monte-Carlo methods. Further, we wish to briefly highlight some previous work on this topic by early authors [1, 2, 144, 147, 148], whose work will be crucial in carefully separating out the contributions of S_BP and S_s.

As a final note, let us give an idea of the potential significance of this work. Imagine that we wish to determine not the LD of a DNA chain, but instead the kinetics of a drug molecule, perhaps a novel antibiotic, binding to a DNA chain [10, 149]. If the drug molecule itself has some transition dipole moment $\boldsymbol{\mu}_{\text{drug}}$, then the optical factor O_{drug} for $\text{LD}^r_{\text{drug}}$ will itself be a function of the average angle α between $\boldsymbol{\mu}_{\text{drug}}$ and the DNA helix $\boldsymbol{u}$. In other words, as the drug binds to the DNA helix in solution, we will get a changing $\text{LD}^r_{\text{drug}}$ measurement. However, if one has already determined S_{BP} and S_{s} for the DNA, then it is in principle possible to 'back-out' the numerical value of the O_{drug} factor, given a known LD^r in Equation 5.7. Therefore, one could in theory determine binding properties quantitatively, such as the binding angle that the drug molecule makes with the DNA helix, providing a new avenue for early in-vitro pharmacological characterisation [10, 149].

5.3 DNA modelling scheme

Our overall goal is to develop a polymer model to predict LD for a wide variety of DNA fragment lengths, all the way from 239 base pairs up to 164000 base pairs (164 kbp), which is the range studied by Simonson and Kubista [17]. Our modelling scheme will be based upon the FENE-Fraenkel bead-spring chain, as well as a bending potential and full hydrodynamic interaction (HI) and excluded volume (EV) [23, 65], as described in Chapter 2 and Chapter 3. The qualitative behaviour of this model has been studied in shear flow in Chapters 2 and 3, and we note that it has previously been used to directly model the LD of an M13 bacteriophage in Chapter 2 [65]. Our method for determining the parameters follows from the results of Chapter 4, however here we will use FENE-Fraenkel springs instead of FENE springs. We will briefly review the main steps here, with details in Chapters 3 and 4.

We assume each DNA fragment can be characterised by three experimentally measured parameters, the total contour length L (which is a function of the number of base pairs), the persistence length l_p (related to the stiffness of the double helix), and the relaxation time λ (which depends on the chain dynamics in a particular solvent). We generally give all lengths in units of base pairs, for example describing a particular chain as having $L = 25$kbp and $l_p = 147$bp. This specific choice of l_p will be used throughout this chapter, based on the generally-accepted value of $l_p = 50$nm in excess salt, and a base pair length of ≈ 0.34nm [9, 17, 124]. In fact, Simonson and Kubista measured the LD at various salt concentrations, which both affects the effective persistence length and can introduce additional physical effects from charges along the DNA backbone [17, 124]. For simplicity, we have assumed that the main results of Simonson and Kubista are at a high enough salt concentration for charges to be screened, and for l_p to be 147 base pairs.

Before we give the specifics of our modelling scheme, we can get a feel for the form of the chain configurations at different DNA fragment lengths L by first studying the results. In Figure 5.4 we have displayed four generated configurations of a 294 base pair DNA fragment at equilibrium, given $N_s = 30$ springs are used in the model. Note that both the total contour length L, as well as the effective bending rigidity l_p, is set to be the same as the underlying DNA fragment.

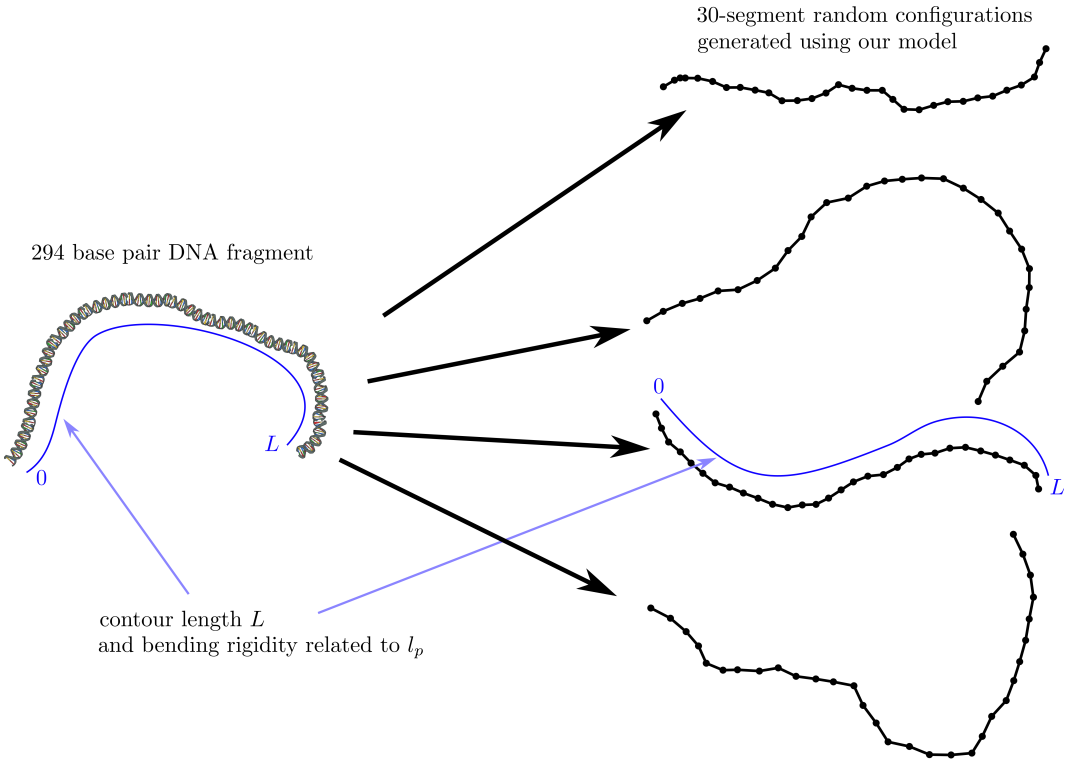

FIGURE 5.4: Realisations of a 294 base pair fragment of DNA generated using our model. In this case, $L = 294$ base pairs, $l_p = 147$ base pairs, and we have used $N_s = 30$ springs in our model. The DNA fragment is schematic - we have assumed the DNA is well represented by a Kratky-Porod chain.

Equilibrium bead-spring chain configurations for other DNA fragment lengths L and number of springs N_s are given in Figure 5.5. There are several features we wish to highlight. Firstly, as one moves from the 0.1 kbp fragment to the 100 kbp fragment, the configurations become more coiled, as opposed to the elongated configuration at low L. A reasonable macroscopic analogy of this behaviour is that of a long, flexible rubber tube, which appears quite rigid over short distances, but a random configuration many meters long will tend to loop back on itself. Secondly, and particularly for the longer chains of $L = 10$ kbp or $L = 100$ kbp and $N_s \leq 40$, the springs do not necessarily follow the DNA fragment contour. Instead, they are an approximation of the restoring force that separated points on the chain feel due to the combination of elastic and entropic effects from both the chain bending rigidity and Brownian motion of the polymer through the solvent. Therefore, their average length will necessarily be very different from their total stretched length for large L. Thirdly, even for quite short DNA

fragments, one cannot hope to recover the behaviour of the chain contour down to the base-pair level unless computationally intractable numbers of beads are used. In our BD simulations, we will not consider more than $N_s = 80$ springs, and even then only under limiting assumptions. This is an important consideration, since we have seen that the LD for a DNA chain is defined at the base-pair level, and so we must be careful to correct for the larger length scales. Finally, although the bead sizes in Figure 5.5 should not be taken literally and are certainly not to scale, we note that the effective hydrodynamic radius of each bead must indeed be larger for smaller N_s to correctly recover the relaxation time λ of the real underlying DNA fragment. When we integrate these configurations over time to recover trajectories in shear flow, the bead dynamics play a crucial role in the behaviour.

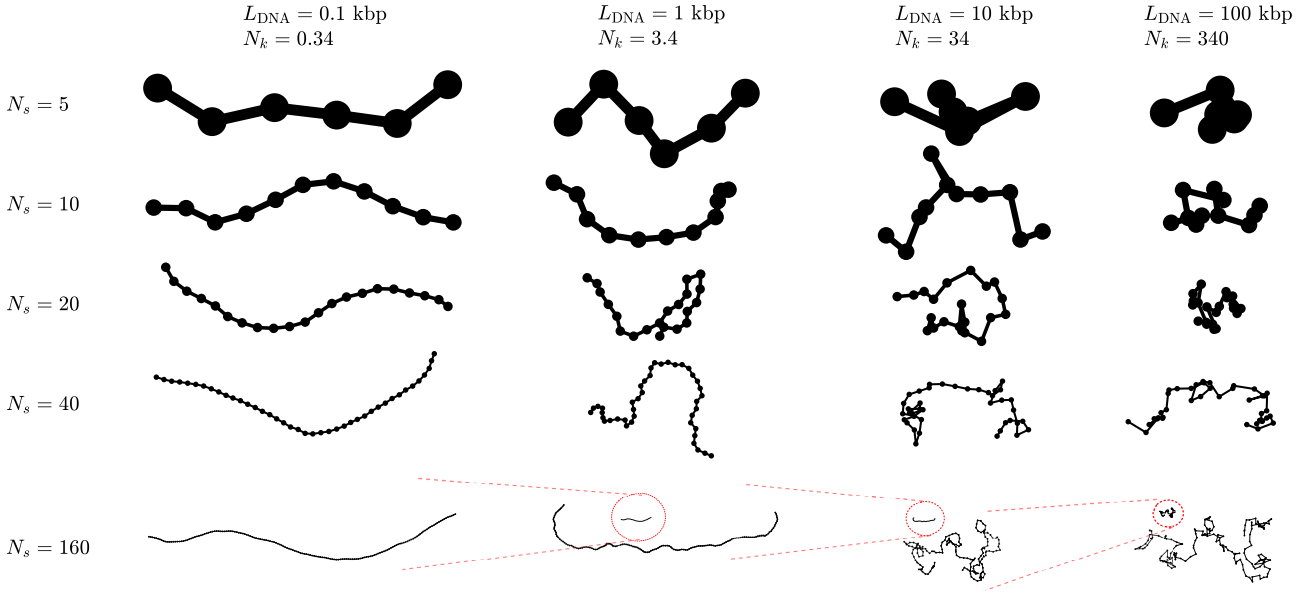

FIGURE 5.5: Example equilibrium configurations generated using our multiscale modelling procedure. Overall 3D structures have been projected onto the principal gyration axes for ease of comparison (as shown in Figure 5.8). Columns correspond to different lengths of DNA, while rows are the number of springs used to represent the DNA fragment. Note that although solid lines are used to connect beads in this schematic, in reality each connection is a spring of variable length. Final row of $N_s = 160$ shows comparisons of coil sizes between columns, such that each circled configuration represents the previous configuration at the same scale as the next.

As before, our model is a bead-spring chain of N beads and $N_\mathrm{s} = N - 1$ segments with bead μ at position $\boldsymbol{r}_\mu$ relative to the chain center of mass, bead-bead vectors $\boldsymbol{Q}_\mu = \boldsymbol{r}_\mu - \boldsymbol{r}_{\mu-1}$ and segment angles θ_μ as illustrated schematically in Figure 3.3, which also gives the numbering scheme for beads, segments and angles. We impose a connector force law $\boldsymbol{F}_\mu^{(c)}(\boldsymbol{Q}_\mu)$ which acts along the segments, as well as bending forces between segments, EV forces between every set of nearby beads, and HI perturbations to represent the effects of the implicit solvent, all of which will be described in detail shortly. The solvent is represented implicitly such that beads have solvent friction $\zeta = 6\pi\eta_s a$, where η_s is the solvent viscosity and a is the effective hydrodynamic bead radius. Flow is imposed through the tensor $\boldsymbol{\kappa}$, where the velocity field of

the Newtonian solvent is $\boldsymbol{v} = \boldsymbol{\kappa} \cdot \boldsymbol{r}$, assuming the background flow $\boldsymbol{v}_0 = 0$. For the case of shear flow considered here, the only non-zero component of $\boldsymbol{\kappa}$ is $\kappa_{x,y} = \dot{\gamma}$, the shear rate.

In this chapter we exclusively use the FENE-Fraenkel force law, which we have discussed in great detail in Chapter 3 - for clarity, it has the form:

$$\boldsymbol{F}^{(c)} = \frac{H(Q-\sigma)}{1-(Q-\sigma)^2/(\delta Q)^2}\frac{\boldsymbol{Q}}{Q} \tag{5.12}$$

We will also employ a bending potential as in Equation 5.13, with the bending stiffness chosen through Saadat and Khomami's expression in Equation 3.8. Again, we repeat both here for clarity:

$$\phi_{\mathrm{b},\mu}/k_{\mathrm{B}}T = C(1-\cos\theta_\mu) \tag{5.13}$$

$$C = \frac{1 + p_{\mathrm{b},1}(2N_{\mathrm{K,s}}) + p_{\mathrm{b},2}(2N_{\mathrm{K,s}})^2}{2N_{\mathrm{K,s}} + p_{\mathrm{b},3}(2N_{\mathrm{K,s}})^2 + p_{\mathrm{b},4}(2N_{\mathrm{K,s}})^3} \tag{5.14}$$

As we will see later in Figure 5.6, choosing C in this way to fit the nearest neighbour correlation does not necessarily capture the full end-to-end distribution function, particularly around $N_{k,s} = 1$, but is qualitatively suitable for our purposes.

Before we turn to our final pieces of physics to include in the polymer model (namely HI and EV, for which we will follow the method of Chapter 4), we wish to show how the combination of a FENE-Fraenkel spring and bending potential can accurately model a DNA segment of arbitrary length. Assuming that the Kratky-Porod wormlike chain (KP WLC) is an accurate representation of the underlying chain with contour length L and persistence length l_p, we seek to discretise the chain using N_s FENE-Fraenkel springs and a bending potential such that we recover the correct end-to-end vector magnitude distribution function $\psi(R)$ (given via a fit to the even moments of the KP chain derived by Hamprecht and Kleinert [150]).

We perform this discretisation in two stages. Firstly, for each of the N_s segments with length $l_s = L/N_s$ (which is the same as choosing $N_{\mathrm{K,s}} = L/(2N_{\mathrm{s}}l_p)$ from earlier), we set our FENE-Fraenkel spring parameters such that the total spring extensibility is equal to l_s, and also that the average spring length at equilibrium is equal to that for the underlying WLC segment. The total spring extensibility condition is easy to satisfy by setting $\sigma + \delta Q = l_s$. This gives us a single free polymer chain feature, the average length of the DNA segment, as compared to the two parameters for our FENE-Fraenkel spring (our natural length σ and spring constant H). In the limit of $N_{\mathrm{K,s}} >> 1$, this is not an issue, as we can choose our spring constant H to obtain the correct average spring length in the FENE-spring limit, as suggested by Sunthar and Prakash [16] and previously used in Chapter 4:

$$H = \frac{k_{\mathrm{B}}T}{\delta Q^2}\left(\frac{3l_s^2}{\langle R^2\rangle} - 5\right) \tag{5.15}$$

where $\langle R^2 \rangle$ is given by Equation 5.16:

$$\langle R^2 \rangle = 2Ll_p - 2l_p^2 \left(1 - e^{-L/l_p}\right) \tag{5.16}$$

As previously stated, this formula works well for $N_{\mathrm{K,s}} >> 1$, where a FENE spring is appropriate and we can set $\sigma = 0$. However, as $N_{\mathrm{K,s}}$ becomes smaller, the distribution function for Q, namely $\psi(Q)$, differs from that for the end-to-end distance of the KP chain. In this case, it is possible to fit σ such that the spring length $\langle Q^2 \rangle = \langle R^2 \rangle$, which gives an improved fit. However, note that when $l_s^2/\langle R^2 \rangle > 5/3$, the spring constant becomes negative, which is clearly nonphysical. To remedy this, we make the assumption that as $N_{\mathrm{K,s}} = l_s/2l_p \to 0$, the section of WLC will behave approximately like a elastic rod, meaning that the spring force should again increase with l_s/l_p. Therefore, we simply add l_s/l_p to the expression for H in Equation 5.15, giving:

$$H = \frac{k_{\mathrm{B}}T}{\delta Q^2}\left(\frac{3l_s^2}{\langle R^2 \rangle} - 5 + K\frac{l_s}{l_p}\right) \tag{5.17}$$

for some constant K (the choice of $K = 5$ is used here).

This appears a fairly ad hoc methodology, which we justify as follows. For $N_{\mathrm{K,s}} >> 1$, the KP chain end-to-end distribution function is approximately Gaussian, and the FENE-Fraenkel spring with $\sigma = 0$ (the FENE spring) has been shown to match it with reasonable accuracy [16]. In the limit of $N_{\mathrm{K,s}} \to 0$, the segment of DNA is expected to behave much like a rigid rod. Importantly, we have previously shown that in the $\delta Q \to 0$, $H \to \infty$ limit, the behaviour of the FENE-Fraenkel spring is largely insensitive to the specific choice of H and δQ, in that it functions as a bead-rod dumbbell in shear flow (see Figure 2.18) [65]. Therefore, in both limits $N_{\mathrm{K,s}} >> 1$ and $N_{\mathrm{K,s}} << 1$, our FENE-Fraenkel spring model gives the correct behaviour.

The second step is straightforward, namely to utilise the expression of Saadat and Khomami in Equation 3.8 with our choice of $N_{\mathrm{K,s}}$ to determine the bending potential strength C. Two examples of end-to-end distribution functions calculated using this procedure for 24kbp and 7kbp DNA are displayed in Figure 5.6 for several N_s. Here we have assumed that the persistence length of DNA is 147 base pairs. Note that the distribution functions seem to get worse for higher N_s when modelling the shorter DNA fragment. This is apparently due to a crudely chosen bending potential, such that matching only nearest-neighbor correlations is not sufficient to capture the full end-to-end distribution function when $N_{k,s} \approx 1$ (but it again becomes accurate in the $N_{k,s} \to 0$ limit [18]). Since there is no simple analytical expression to capture this behaviour over the full range of L and l_p, we will nevertheless use this scheme despite its shortcomings, noting that it would be possible to construct an iterative scheme to choose C such that the correct end-to-end distance distribution is captured.

Finally, the hydrodynamic interactions between beads (HI) and excluded volume forces (EV) follow the same general methodology as in Chapter 3, namely using the RPY tensor for HI and

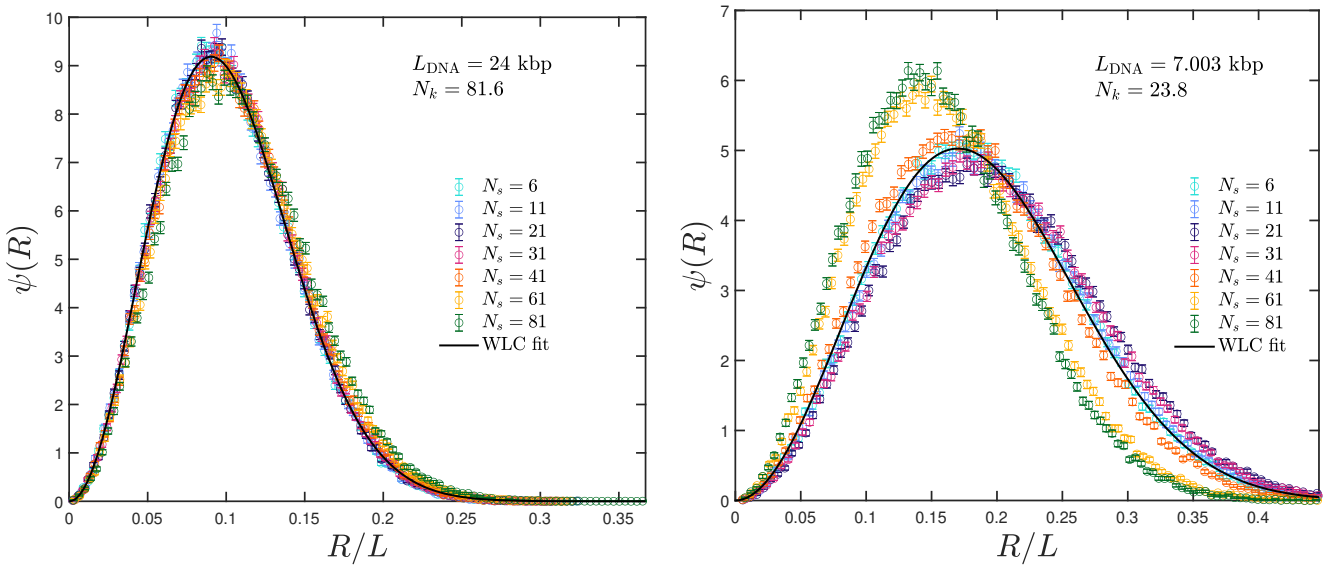

FIGURE 5.6: End-to-end distribution function fits using our modelling scheme for FENE-Fraenkel springs and Saadat and Khomami's form of the bending potential. Analytical WLC distributions are given by the method of Hamprecht and Kleinert [150]. Here we have assumed $l_p = 147$ base pairs.

the Gaussian potential for EV. As per the discussion in Chapter 4, we choose our dimensionless parameters h^* and z^* as per the following equations:

$$h^* = \tilde{h}^* \chi \xi \tag{5.18}$$

$$z^* = \tilde{z} \frac{\chi^3}{\sqrt{N}} \frac{4}{3K(N_k)} \tag{5.19}$$

where we have carefully defined χ and ξ in Chapter 4. We choose z^* and h^* at each level of successive fine graining in order to keep $\tilde{h}^*$ and $\tilde{z}$ constant.

At equilibrium, and in the absence of EV, we do not have to perform BD simulations, but can instead use our simple Monte-Carlo method as described in Appendix H to generate equilibrium configurations. This is considerably less computationally intense, particularly for very stiff FENE-Fraenkel springs at high bead numbers. Our Monte-Carlo scheme takes $\mathcal{O}(N)$ time to generate chain configurations, and this time is almost completely independent of the spring and bending parameters. On the other hand, our BD scheme is $\mathcal{O}(N^{2.25})$ when full fluctuating HI is turned on [53]. Additionally, since the relaxation time scales as $\mathcal{O}(N^{1.5})$ and also increases with stiffer FENE-Fraenkel springs, it quickly becomes totally infeasible to simulate short DNA fragments with $N > 30$. There are several far more efficient BD algorithms which have been developed [75], but for the current investigation our scheme has proven acceptable.

5.3.1 Matching parameters with experimental results

While we have specified the length scale, l_H, such that our FENE-Fraenkel springs correspond to a real DNA chain, our time scale, λ_H, requires one to know the effective bead friction ζ, which is not directly accessible experimentally. Without knowledge of the true λ_H, it is difficult to match the shear rates between experiment and simulation. This problem can be avoided by calculating the relaxation time of our polymer model, and then matching this relaxation time to the experimentally measured relaxation time. More precisely, we determine the Weissenberg number $Wi = \lambda\dot{\gamma}$ at each shear rate $\dot{\gamma}$ using the DNA relaxation time λ. We then find the relaxation time for our polymer model, and run simulations at the same Weissenberg numbers, such that $\dot{\gamma}_{\text{model}} = Wi_{\text{experiment}}/\lambda_{\text{model}}$. In our case, we have done this using the zero-shear viscosity, from which a relaxation time can be derived [34]:

$$\lambda_\eta = \frac{\eta_0 - \eta_s}{n_p k_{\text{B}} T} = \frac{[\eta]_0 \eta_s M}{N_A k_{\text{B}} T} \tag{5.20}$$

where λ_η is the relaxation time calculated from viscosity, η_0 is the zero-shear viscosity from our simulations, η_s is the Newtonian solvent viscosity, $k_{\text{B}}T$ is the Boltzmann constant multiplied by the solution temperature, n_p is the number density of polymer molecules, $[\eta]_0$ is the experimentally measured intrinsic viscosity, M is the polymer molecular mass and N_A is Avogadro's constant. Careful calculations of λ_η for 25 kbp and 48 kbp DNA at several temperatures in excess salt has been performed by Pan et al. [124]. Usefully, Simonson and Kubista calculated LD^r for these DNA fragment lengths, at a temperature within the range of Pan et al.'s measurements [17]. This is an imprecise measure of the relaxation time for the LD^r data, since the salt concentrations and temperatures are different - Pan et al. used 500mM NaCl at temperatures 15°C to 35°C, while Simonson and Kubista used 2mM to 250mM NaCl at 22°C (as well as slightly different buffer solutions). In principle, it would be possible to calculate new λ_η values by interpolating based on a scaling law, but as we will see, we have obtained reasonable predictions even from the approximate nearest λ_η. Specifically, we will use the values of $\lambda_\eta = 0.058\text{s}^{-1}$ for 25kbp DNA, and $\lambda_\eta = 0.2\text{s}^{-1}$ for 48.5kbp DNA [22].

For our polymer models without HI, the zero-shear viscosity can be found very simply from the radius of gyration at equilibrium:

$$\eta_{p,0} = \frac{n_p \zeta}{6} N \langle R_g^2 \rangle_{\text{eq}} \tag{5.21}$$

where N is the number of beads and $\langle R_g^2 \rangle_{\text{eq}}$ is the equilibrium gyration radius. When HI is included, the viscosity can instead be calculated by performing a step-strain simulation and measuring the decay in the x, y component of the stress tensor, namely:

$$G(t) = \lim_{\gamma \to 0} \frac{\tau_{x,y}(t)}{\gamma} \tag{5.22}$$

and the zero-shear viscosity is then given by the integral of $G(t)$, specifically:

$$\eta_{p,0} = \int_0^\infty G(t)dt \tag{5.23}$$

which, combined with variance-reduction techniques [13], allows one to obtain an accurate measure for the zero-shear viscosity. This method, along with other procedures one can use to determine relaxation times from simulations, are discussed in Appendix F.

For other DNA fragment lengths, we unfortunately do not have an accurate measurement of the experimental zero-shear viscosity with which to calculate the relaxation time. We have currently only simulated those fragment lengths for which we have measures of λ_η. However, there are measurements of other characteristic relaxation times - for example, λ_D, the relaxation time calculated from the hydrodynamic radius using dynamic light scattering [124]. There are two ways one could, in principle, use this alternate relaxation time. The first is to use universal ratios to convert between different measures of relaxation time, for example $U_{\eta D}$ relates the viscosity radius to the hydrodynamic radius [125], from which relaxation times can be extracted. Secondly, one could directly measure the diffusivity via BD simulations and directly determine λ_D for our polymer models.

5.4 Determining orientation parameter from our model

5.4.1 Calculating orientation parameter of segments

We are now in a position to directly determine S_s and S_BP for our DNA chains. We will mainly study the 25 kbp chain, at first with no HI or EV for simplicity, after which we will present results for both 25kbp and 48.5kbp chains with HI and EV. For the 25kbp chain, we have chosen $N_s = \{5, 10, 20, 30, 40, 60, 80\}$, with FENE-Fraenkel spring parameters for each segment as per earlier discussion. For each N_s, we calculate the zero-shear viscosity, and hence extract a relaxation time. As previously stated, 25kbp DNA has a $\lambda_\eta \approx 0.058$s [22], and so the $\approx 10\mathrm{s}^{-1}$ to $\approx 3000\mathrm{s}^{-1}$ shear rate range studied by Simonson and Kubista [17] corresponds to $Wi \approx 0.6 \to 175$. Therefore, determining S_s is reasonably straightforward - we simulate approximately 500 independent trajectories at a range of shear rates $\dot{\gamma}$ corresponding to $Wi \approx 0.6 \to 175$ for each N_s, ensuring that they are run long enough to reach steady state. Note that this is equivalent to running at $\dot{\gamma} = Wi/\lambda(N_s)$, where λ is different for each chain discretisation. Measurements of S_s are then taken as per Equation 5.10, averaged over all segments and trajectories for several relaxation times at steady state.

Results are given for S_s in Figure 5.7. While the simulated S_s has roughly the same shape as the experimental results, it is still clearly quantitatively incorrect, as we expect without

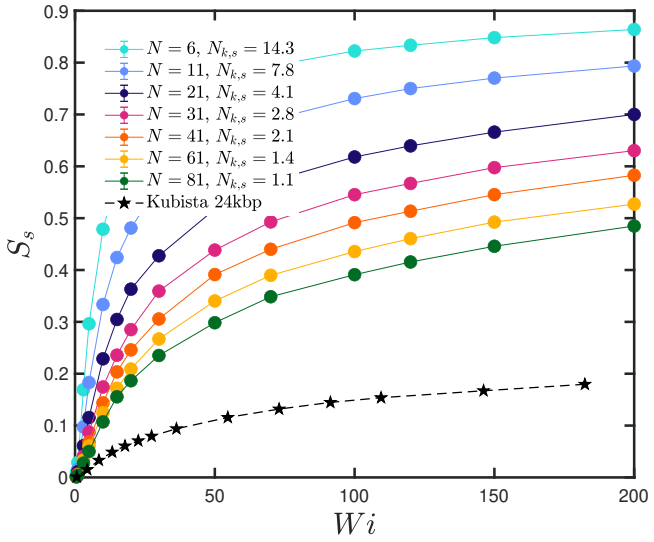

FIGURE 5.7: Curves with no HI or EV for S_s calculated as per Equation 5.10. Experimental data is from Simonson and Kubista [17], with an assumed $O = -1.48$ and $\lambda_\eta = 0.058$s.

incorporating the contribution from S_BP. Note that as N_s increases, S_s decreases, approaching the experimental results. This is expected, and in fact in the limit where N_s is sufficiently large that each segment is made up of only several base pairs, we would expect $S_\mathrm{BP} \approx 1$ and hence only S_s is required.

5.4.2 Calculating orientation parameter of base pairs

We now finally come to the task of calculating S_BP. To do so, we turn to some of the early theory on the subject, specifically the work of Wilson and Schellman [1, 2]. These authors were investigating precisely the same problem that we have in front of us today, namely the use of polymer physics models to determine the flow LD of DNA [2]. They understood that it was not possible to directly write down an analytical model for the conformation of the whole DNA helix in shear flow, and so instead approximations were required. The basic idea was as follows - first relate the dichroism of a chain to the end-to-end extension of a chain, and then use the Rouse model to determine the end-to-end extension at a particular shear rate. In current notation, we would write the relationship between dichroism and extension in terms of the orientation parameter S_BP, such that:

$$S_\mathrm{BP}(\dot{\gamma}) = m\frac{\langle R^2\rangle_{\dot{\gamma}}}{\langle R^2\rangle_\mathrm{eq}} \tag{5.24}$$

where m is assumed constant (so the relation is linear), $\langle\rangle_{\dot{\gamma}}$ represents the average end-to-end distance over all trajectories and segments at a particular shear rate, and $\langle\rangle_\mathrm{eq}$ is the same average end-to-end distance at equilibrium. This relationship has actually long been worked out by authors such as Kuhn [144], Nagai [148], and Flory [147], with Wilson and

Schellman deriving a similar expression specifically for DNA [1]. The key insight is that while we cannot directly determine the constant m in shear flow, it is possible to derive an equivalent relationship at equilibrium, namely [1]:

$$S_{\mathrm{BP}}(R) = \frac{3}{5}\left[\frac{3\langle c^2\rangle + 1}{3 - 3\langle c^2\rangle} + \frac{2\langle c\rangle}{1 - \langle c\rangle^2}\right]\frac{R^2}{\langle R^2\rangle_0 N_s} \tag{5.25}$$

for a chain where $c = \cos\theta$ (with θ the angle from one segment to the next), $S_{\mathrm{BP}}(R)$ is the average S_{BP} of all chain configurations at a particular end-to-end distance squared R^2, with $\langle R^2\rangle_0$ the average chain end-to-end distance squared over all possible extensions. This S_{BP} is calculated relative to the chain end-to-end vector, not relative to some laboratory axes - this is why one obtains a non-zero S_{BP} even in a quiescent solution.

While Equation 5.25 is calculated at equilibrium and makes a number of assumptions (such as a sufficiently long chain, and relatively small extensions), the key idea is that the same expression can be applied to a general perturbation of the chain, such as that caused by shear flow. For example, when a polymer chain is sheared, its average end-to-end distance will usually increase. The assumption is then that this increase in R^2 relative to its value at equilibrium (specifically, $\langle R^2\rangle_{\dot\gamma}/\langle R^2\rangle_{\mathrm{eq}}$) is related to S in the same way as in Equation 5.25 for $R^2/\langle R^2\rangle_0$. In other words, the prefactor m in Equation 5.24 is exactly the same as the prefactor to $R^2/\langle R^2\rangle_0$ in Equation 5.25. Using this relationship, Wilson and Schellman were able to to use the Rouse model to determine $\langle R^2\rangle_{\dot\gamma}/\langle R^2\rangle_{\mathrm{eq}}$, and hence predict the LD^r for some experimental systems [2]. Of course, we know that the Rouse chain is a poor model in shear flow, leading to nonphysical extensions even at moderate shear rates, and so the predictions of Wilson and Schellman were only qualitatively accurate, and then only at low shear rates [2]. We are now in a position to do somewhat better with our current model.

By way of example, let us test the predictions of Wilson and Schellman in Equation 5.25. To do so, we will use our Monte-Carlo procedure to generate thousands of equilibrium bead-rod-chain (actually, very stiff FENE-Fraenkel springs, which are equivalent) configurations with some bending stiffness C as per Equation 5.13 and $N_s = 1000$. We then calculate S_{BP} for each configuration as per Equation 5.9, with $\hat{\boldsymbol{Q}}_{\parallel}$ along the end-to-end vector $\boldsymbol{R}$, and $\hat{\boldsymbol{Q}}_{\perp}$ some randomly selected unit vector orthogonal to $\boldsymbol{R}$ (precisely, we choose some random vector on the unit sphere and take its cross product with respect to $\hat{\boldsymbol{R}}$, which gives a random unit vector orthogonal to $\boldsymbol{R}$). An example of this procedure is shown in Figure 5.8, where we have the axes directions $\hat{\boldsymbol{Q}}_{\parallel}$ along the end-to-end vector, and $\hat{\boldsymbol{Q}}_{\perp}$ orthogonal to $\hat{\boldsymbol{Q}}_{\parallel}$.

Results are shown in Figure 5.9. From Figure 5.9 (a), we can see that there is significant variability in S_{BP} between different configurations, even at the same R^2, such that it is difficult to determine a trend. In order to make the trends clearer, we bin data into ranges of R^2 as shown in Figure 5.9 (a), giving a particular S_{BP} around some approximate R^2. We can then

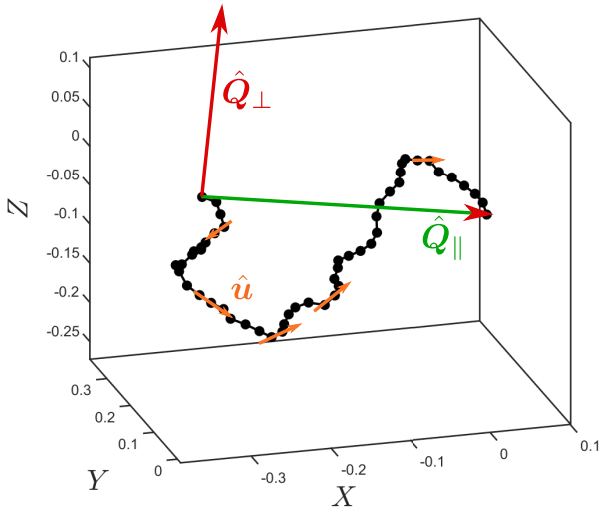

FIGURE 5.8: Example vectors $\hat{\boldsymbol{Q}}_\parallel$ and $\hat{\boldsymbol{Q}}_\perp$ for which S_{BP} is defined. Each bead-bead vector has an associated $\hat{\boldsymbol{u}}$, allowing S_{BP} to be calculated as per Equation 5.9.

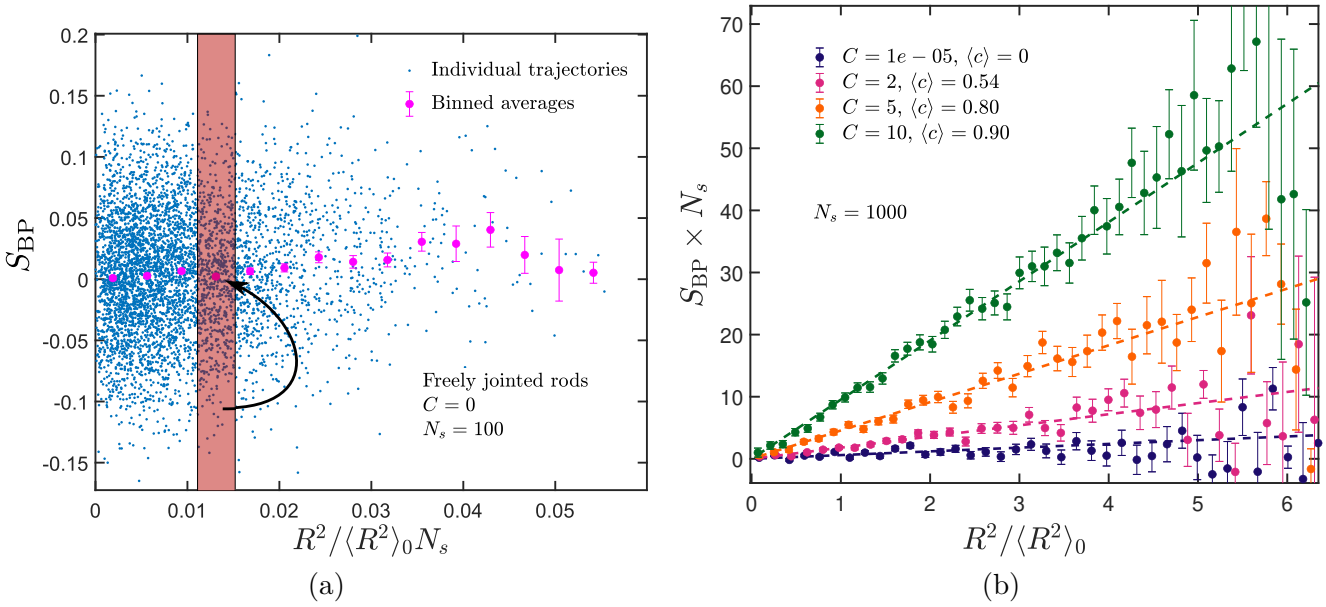

FIGURE 5.9: (a) 10000 configurations of freely jointed bead-rod chains with $N_s = 100$. Each blue point is a particular trajectory with some S and R^2. Individual configurations are binned as shown in the figure, with all the points within the red band averaged along both axes. (b) $S\times N_s$ plotted against $R^2/\langle R^2\rangle_0$. Points are binned configurations as in (a), while lines are linear fits as per Equation 5.25. Example values of $\langle c\rangle$ calculated from C based on Equation 5.13 are shown in the legend of plot (b).

plot SN_s against $R^2/\langle R^2\rangle_0$, where $\langle R^2\rangle_0$ is an average over all trajectories, not just in a particular bin. This is done in Figure 5.9 (b), where curves for several C values are given. The lines are the predictions of Equation 5.25, using the formulation of Wilson and Schellman [1]. The predictions of Equation 5.25 compare favourably with Monte-Carlo results, both validating Equation 5.25 as well as supporting our general approach.

However, Equation 5.25 still requires several assumptions, most notably that it is only strictly valid for long chains at small extensions. Since we have a Monte-Carlo scheme which can directly produce S_{BP} vs $Q^2/\langle Q^2\rangle_0$ curves for an arbitrary DNA segment, we generate these curves for each segment length. Let us demonstrate our full procedure with a specific example. For our 25kbp DNA chain, imagine that we are using $N_s = 40$ segments (each of which is a FENE-Fraenkel spring) for our BD simulations, and so therefore each segment represents 625 base pairs. We then want to use our Monte-Carlo scheme to generate chain configurations where each segment is only several base pairs long. This requires $N_s = 125$ rods (which are modelled as stiff FENE-Fraenkel springs), such that each rod in our Monte-Carlo scheme is now only 5bp. We then generate a plot of S_{BP} vs $Q^2/\langle Q^2\rangle_0$ as shown in Figure 5.8 and Figure 5.9.

We then perform BD simulations of our chain at several $\dot{\gamma}$, and measure not only S_{s} as in Figure 5.7, but also $\langle Q^2\rangle_{\dot{\gamma}}$ at each shear rate. We then take $\langle Q^2\rangle_{\dot{\gamma}}/\langle Q^2\rangle_{\mathrm{eq}}$, and use it to calculate S_{BP} at each shear rate. The key assumption is that the average $\langle Q^2\rangle_{\dot{\gamma}}$ in shear flow can take the place of Q^2 at equilibrium, but as we will see, this procedure appears adequate to collapse data. This full procedure is shown in Figure 5.10 for $L = 25$kbp, $N_s = 40$ and $Wi = 50$.

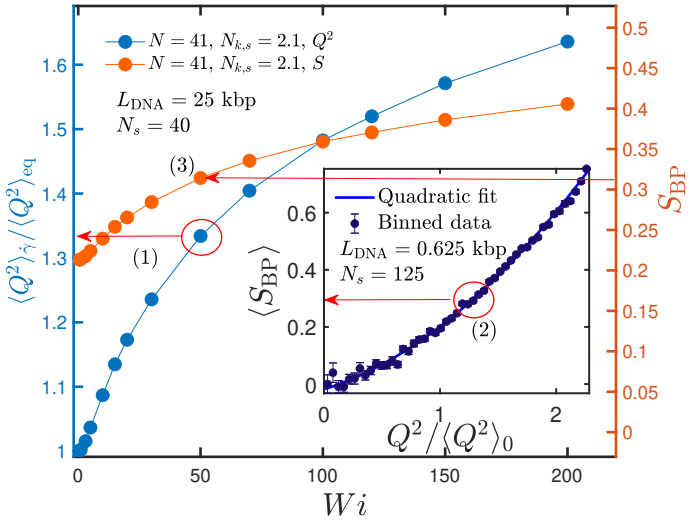

FIGURE 5.10: Main plot is BD simulation of a 25kbp DNA chain with $N_s = 40$. Left axis (blue) is $\langle Q^2\rangle_{\dot{\gamma}}/\langle Q^2\rangle_{\mathrm{eq}}$ at each Wi. Inset contains Monte-Carlo simulation at equilibrium for a 625bp segment with $N_s = 125$, corresponding to the segment length in the BD simulations. To obtain S_{BP} (right axis, orange), the steps are (1) calculate $\langle Q^2\rangle_{\dot{\gamma}}/\langle Q^2\rangle_{\mathrm{eq}}$ at a particular shear rate, (2) obtain S_{BP} corresponding to that Q^2 at equilibrium, (3) use this to plot S_{BP} vs Wi.

We also note the close analogy between our current methodology and the simplifications for type-B polymer solutions undergoing dielectric relaxation [151, 152]. Another way of understanding our procedure is that we are splitting the chain up into many sub-molecules, and then assuming that the end-to-end vector of each submolecule (represented by a single spring

in our BD simulations) can be related to the average dipole of that submolecule. For a type-A polymer, this dipole is *equal* to the end-to-end vector [151], but for type-B polymers, one must find some relation between the dipoles of the monomers and the dipoles of the submolecular units used in the modelling, as we have done. The other key assumption made in deriving type-A polymer dielectric relaxation expressions is that results are independent of sub-molecule size, which implicitly depends upon the assumption that the polymer chain obeys equilibrium statistics on length scales larger than the sub-molecules.

In other words, we are implicitly determining the equilibrium partition function for a particular submolecule in order to find the weighted distribution functions which allows one to relate S and Q at equilibrium. This is done using a Monte-Carlo scheme with Boltzmann weights for each configuration proportional to the bending and spring potentials, as detailed in Appendix H. We then assume that the partition function at equilibrium also holds in flow for the submolecules (but of course not for the overall chain of submolecules). This approximation will become less accurate at high shear rates or for large sub-molecules. This is related to the size of a so-called Pincus blob [12, 153], where effectively the number of monomers within a 'blob' is internally under equilibrium θ-conditions decreases with shear rate [22]. The higher the shear rate, the smaller the submolecule must be in order to still obey equilibrium statistics. However, for sufficiently small submolecules at sufficiently small shear rates, we should expect that the equilibrium and non-equilibrium partition functions for the submolecules are identical, and so one can assume that Q relates to S_{BP} in the same way for both flow and equilibrium.

5.4.3 Comparisons with experimental data

Results for $S = S_{\mathrm{BP}} \times S_s$ are given in Figure 5.11, with both S_{s} and $S_{\mathrm{BP}} \times S_s$. The data collapse is somewhat remarkable, although the results are still some ways off from the experimental data of Simonson and Kubista [17]. In the next section, we will give results for chains with HI and EV, showing slightly better agreement with experimental results.

We also wish to briefly touch on why this procedure appears to work so well. The most important assumption that we have made throughout this procedure is that the extension of a segment is directly proportional to its LD (or S-parameter) in shear flow, which is an assumption we can test, at least for our 25kbp chain BD simulations. In Figure 5.12, we have plotted S_{s} against $\langle R^2 \rangle / \langle R^2 \rangle_{\mathrm{eq}} - 1$, and while the agreement is certainly not perfectly linear, the correlation is striking for all N_s. In other words, even for a chain with relatively low N_s, the measured S_s is reasonably well-captured purely by the extension of the chain due to shear flow, in that one could determine only $\langle R^2 \rangle / \langle R^2 \rangle_{\mathrm{eq}}$ and still obtain quite an accurate prediction of S_s. If we think about the geometry of a chain in shear flow, the velocity field is

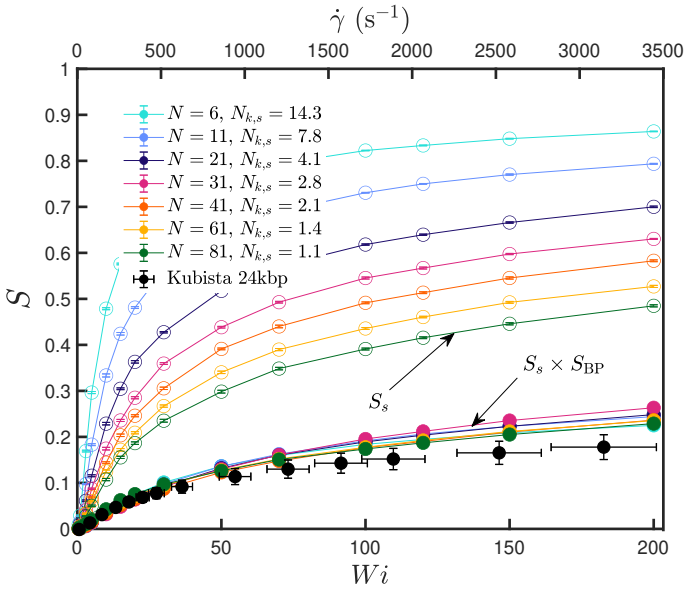

FIGURE 5.11: BD simulations of S_{s} and $S_{\mathrm{BP}} \times S_s$ for several Wi of a 25kbp chain following the procedure in the text, alongside the experimental data of Kubista and Simonson [17] with $Wi = \lambda\dot{\gamma}$, where $\lambda = 0.058$s. For the experimental data, it is assumed that $S = \mathrm{LD}^r/O$, with $O \approx 1.48$. BD simulations have no HI or EV. Error bars of 10% in Wi and 15% in S have been added to the experimental data to approximately represent uncertainty in λ and variation in LD due to salt concentration and temperature.

really doing two things, namely stretching the molecule out, and also aligning its principle axes towards the shear flow direction. We have actually previously seen this effect in Chapter 3, namely Figure 3.11, where the isocline angle χ_G, representing the orientation of the gyration axes, decreases in shear flow with increasing shear rate. In other words, we might think about our calculations as follows. When we do a BD simulation to measure LD, we are really obtaining two important pieces of information. The first is how the whole molecule orients itself in flow, which affects the average projection of each segment onto the polarisation axes $\boldsymbol{E}_X$ and $\boldsymbol{E}_Z$. The second is how each segment stretches due to the flow, which causes the base pairs making up the segment to align themselves along the extension direction, increasing the net alignment of the entire macromolecule. Therefore, our results are useful not only due to the almost quantitative agreement with experimental data, but also because they inform our understanding of deformation of a chain at different length scales in shear flow.

5.4.4 Results with HI and EV

Real polymer chains experience hydrodynamic interactions and excluded volume forces between beads, as we have seen in Chapters 3 and 4. While it is difficult to get an exact measure of the solvent quality for Simonson and Kubista's data [17], Pan et al. have previously found that DNA of similar lengths has $\tilde{z} \approx 1$ to 3 [124]. Therefore, to investigate the effects of the addition of HI and EV, we have performed simulations with $h^* = 0.3$ and $\tilde{z} = 2$ for both

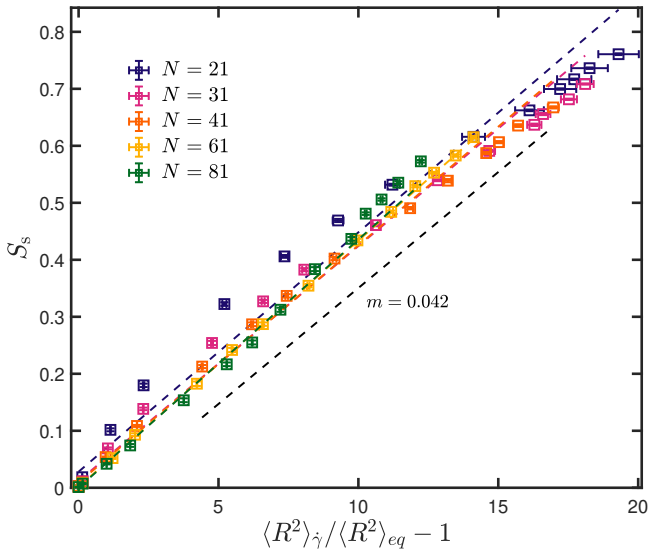

FIGURE 5.12: S_s calculated for the 25kbp chain model plotted against $\langle R^2\rangle_{\dot\gamma}/\langle R^2\rangle_{\text{eq}} - 1$, where each point represents a different shear rate. Lines are linear fits to data, which have slopes of ≈ 0.042.

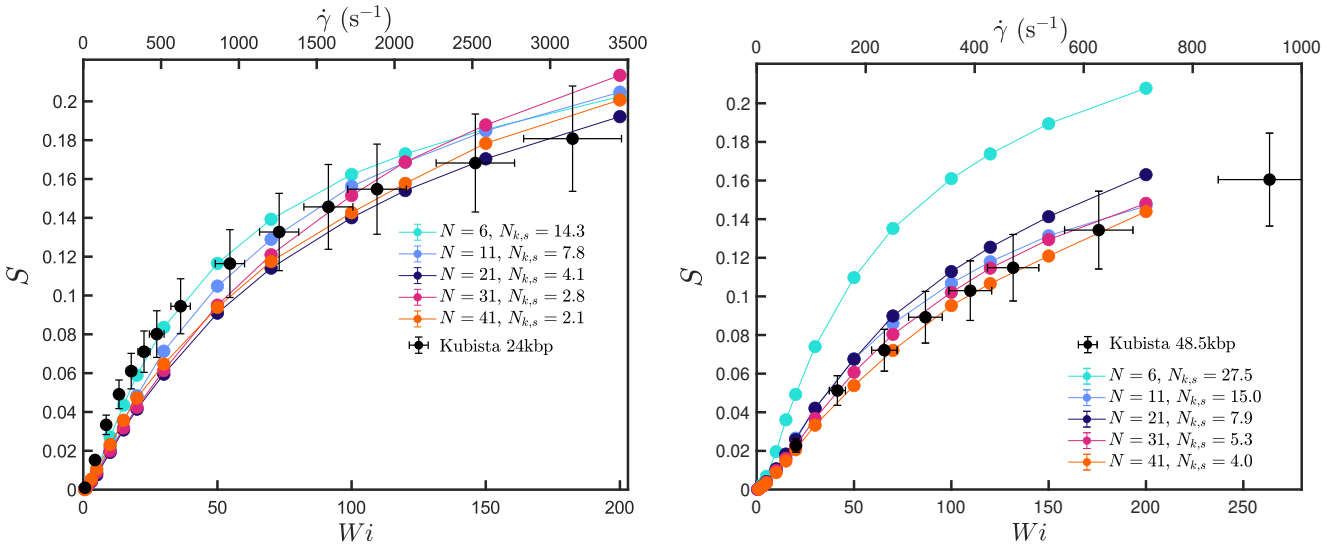

FIGURE 5.13: Comparisons with the data of Simonson and Kubista [17] as in Figure 5.11. (a) 25kbp DNA with $h^* = 0.3$ and $\tilde z = 2$, using $\lambda_{25\text{kbp}} = 0.058$s. (b) 48.5kbp DNA with $h^* = 0.3$ and $\tilde z = 2$, using $\lambda_{48.5\text{kbp}} = 0.2$s. For the experimental data, it is assumed that $S = \text{LD}^r/O$, with $O \approx 1.48$. Error bars of 10% in Wi and 15% in S have been added to the experimental data to approximately represent uncertainty in λ and variation in LD due to salt concentration and temperature.

25kbp and 48.5kbp DNA chains. While EV will change the equilibrium distribution for the purposes of calculating S_{BP} vs Q^2, we have assumed that the segments are short enough that the curves are the same with and without EV. Comparisons with experimental data are given in Figure 5.13.

Despite the apparent close agreement, particularly for the 48.5kbp DNA chains, we would

caution against over-interpreting the results. The exact relaxation times used to calculate Weissenberg numbers are unlikely to be fully accurate, and furthermore Simonson and Kubista [17] found considerable changes in LD with salt concentration, with the measured LD dropping by almost half from 1mM NaCl to 250mM NaCl. It would be insightful to perform simulations with a range of values for l_p to test the sensitivity of the comparisons to the particular value chosen. There is also still some inherent experimental uncertainty, as well as potential variation in the exact value of the optical factor O for DNA chains [4, 145]. We also note that the shape of the curve for the 25kbp chains is not completely accurate, which may be e.g. due to a poor choice of $\tilde{z}$ or incorrectly scaled shear rates.

5.5 Conclusions

By separately calculating the contributions to the LD^r due to S_s and S_BP, we have been able to achieve quantitative agreement between BD simulations and the experimental data of Simonson and Kubista [17]. Qualitatively, we have also seen that the overall LD signal is due to both orientation of the chain (related to S_s) and stretching of the chain segments (which can be used to derive S_BP). These results are useful not only in that they may allow for improved quantitative analysis of flow LD data, but also in that they enhance our understanding of the overall orientation of a polymer chain in shear flow. It seems likely that the same basic principles apply to the behaviour of any macromolecule in solution.

However, we note that there are several major sources of uncertainty affecting our comparisons, which could be mitigated by future experiments or simulations:

- We have assumed that the persistence length of DNA is 147 base pairs at the given salt concentration based on previous data [124], but this is likely not exact given that Simonson and Kubista's data shows factor-of-two changes in predicted LD with changing salt concentration, which affects the persistence length.
- We have assumed a value for the 25kbp DNA relaxation time of 0.058 seconds [22], but this is in a solution of different salt concentration, at a slightly different temperature.
- Our results have only included HI and EV qualitatively, when ideally one would obtain fully parameter-free predictions [12, 14, 16].
- There is still some debate regarding the exact optical parameter O [9], which we use to convert experimental LD^r data to S.
- There may be inherent systematic experimental uncertainties in the LD measurements.

In an ideal experiment, one would perform measurements similar to that of Simonson and Kubista in excess salt, while at the same time accurately measuring the chain relaxation time using an orthogonal technique, such as the zero-shear viscosity (although other measures are available [34]). This would provide an excellent opportunity to accurately test many of the techniques and comparisons with BD described here.

Chapter 6

Conclusions

6.1 Summary

This thesis has developed a model of dilute polymer solutions based upon a FENE-Fraenkel bead-spring chain with a bending potential, hydrodynamic interactions between the beads, and excluded volume forces.

We firstly show that the FENE-Fraenkel spring can capture the behaviour of a both a rod and a spring using a simple dumbbell model. The FENE-Fraenkel spring contains three parameters, the natural length σ, the extensibility δQ about the natural length and the spring stiffness H. It is constructed such that when $\sigma = 0$, it has the exact form of a FENE spring, while when $\sigma > \delta Q$, the spring length is constrained to lie between $\sigma - \delta Q$ and $\sigma + \delta Q$. This allows it to represent both an entropic FENE spring, as well as an inextensible rod, and the crossover between them. There has long been discussion [13, 25–27] about the relative merits of a very stiff spring versus a rigid rod to model bond length constraints. Rods show behaviour such as an instantaneous stress jump at start up of flow, or non-uniform included angle distribution, which cannot be captured even by an infinitely stiff spring. However, as the FENE-Fraenkel extensibility δQ gets arbitrarily small at large spring stiffness H, rheological, orientational and optical properties of a rigid rod are recovered both at steady state and during startup of flow. Additionally, by relaxing the extensibility towards the FENE limit, the shear-thinning viscosity exponent goes from the classic $-1/3$ power law slope for rods to the $-2/3$ slope for FENE springs, with the interesting finding that this crossover occurs when $\sigma > \delta Q$. We also find a change from positive to negative for the second normal stress coefficient Ψ_2 with sufficiently low H and large δQ (in other words, as one moves from a stiff rod to a highly extensible spring). Finally, comparisons with experimental data reveal the FENE-Fraenkel spring can accurately recover the flow behaviour of short, rigid molecules.

This model is then extended to bead-spring chains with HI and EV. We show agreement with a variety of previous results for rodlike models, such as those by Petera and Muthukumar [37], as well as the original results of Larson and coworkers using appropriate parameters and timesteps [23]. We demonstrate that our model can reproduce the behaviour of Hookean and FENE springs with EV and HI, such as shear-thickening due to HI, intermediate shear-thinning due to EV, and differences in onset of shear thinning due to finite extensibility. By then keeping the total extensibility fixed while increasing σ towards the 'Rodlike' limit as for dumbbells, we again show that the same crossover behaviour is observed once $\sigma > \delta Q$. For example, the high-shear Newtonian plateau and compression in the flow direction observed by other authors [37, 79] coincides with this compressibility condition. We show how the backflow effect due to HI compounds this compression for sufficiently stiff springs, and also investigate other properties such as tumbling frequency, orientation angles, and distribution functions. This informs not only the qualitative behaviour of polymer models and gives insight into the behaviour of experimental systems, but also provides necessary conditions for multiscale approaches which seek to capture both bead-rod and bead-spring behaviour.

While the role of EV on equilibrium static and dynamic swelling has been well-established through careful application of two-parameter (TP) theory and the Gaussian potential [12], the methods developed cannot be properly applied to models with a bending potential. The TP theory states that the change in chain properties due to EV can be represented purely by the equilibrium value under θ-conditions multiplied by a function of the so-called solvent quality z. The solvent quality z is a function of the relative solvent-polymer interactions (generally related to temperature or EV potential) and the chain length. However, polymer semiflexibility changes the swelling behaviour, as described by Yamakawa's quasi-two-parameter (QTP) theory [49]. This theory states that the TP theory solvent quality z should be modified by a function $K(L/l_p)$ of the bending stiffness, giving $\tilde{z} = Kz$, and it is this $\tilde{z}$ which correctly describes semiflexible chain swelling. We show that so-called successive fine graining [16] techniques to recover polymer properties can be applied to models with a bending potential if $\tilde{z}$ is used as the solvent quality in place of z. Specifically, the equilibrium swelling of a model polymer coil collapses to a fixed value irrespective of the choice for l_p for a particular value of $\tilde{z}$, giving a universal curve. This allows the method of successive fine graining to be applied to arbitrary semiflexible polymer models, including both our FENE-Fraenkel scheme as well as that of other authors [18].

One of the major aims of this project was to correctly model the Linear Dichroism (LD) of a polymer molecule in shear flow. LD is an optical technique which uses the difference in absorption of perpendicularly polarised light through an oriented sample to obtain structural information. However, LD requires an accurate knowledge of the sample orientation in order to obtain quantitative data. When the sample is aligned using Couette flow, simple models are unable to correctly predict orientation of long, semiflexible polymer such as DNA [3].

By applying the methods of early authors such as Wilson and Schellman [1, 2], who derived expressions for the LD of a chain in terms of the extension of its end-to-end distance, we are able to correctly identify the average orientation of the DNA helix even for a coarse-grained BD simulation. In doing so, we achieve quantitative agreement between our simulations and the experimental data of Simonson and Kubista [17].

Overall, this work has clarified the shear flow behaviour of dilute polymer solution models when a variety of physical effects are included. Additionally, it has provided a framework for quantitative multiscale modelling of an arbitrary experimental system, using the FENE-Fraenkel spring and QTP theory. We hope that this work will be useful both in future modelling efforts, and in the qualitative and quantitative analysis of experimental polymer solution behaviour, particularly with regards to Linear Dichroism measurements.

6.2 Future work

While we have characterised the static swelling of semiflexible polymer models in Chapter 4, the same theories should quite naturally extend to dynamic properties, such as the swelling of the viscosity or hydrodynamic radii [49, 140, 154]. This would reinforce the validity of the QTP theory, particularly since the scaling of dynamic properties under the QTP framework has not been investigated with full hydrodynamic interactions, which are known to be crucially important [140]. Additionally, the method of Chapter 5 could be applied to a wider range of DNA fragment lengths, as it should extend to an arbitrary number of base pairs given a correctly chosen measure of the experimental relaxation time. The effects of solvent quality and persistence length could also be more carefully studied, to test for the sensitivity of results to the underlying assumptions about the DNA properties and experiments of Simonson and Kubista [17].

Although we have included a wide range of physical effects into our polymer model, there are wide classes of polymer solutions which we have not considered here. The most natural extension would be to semidilute, rather than infinitely dilute solutions. Our current BD algorithms and polymer models extend quite naturally to multi-chain simulations [123], and so it would be interesting to extend the FENE-Fraenkel spring to more concentrated solutions, which are often more experimentally relevant. Finally, DNA, and many other biopolymers, display ionic effects which are screened at high salt concentrations. It is in principle possible to include charges into our BD simulations [155], which would in principle allow one to model a DNA chain at arbitrary salt concentration. Combined with our current model, and used in multi-chain simulations, it may be possible to simulate a vast array of polymer solutions even away from equilibrium.

Appendix A

Supporting information for dumbbell models

A.1 Dumbbell Models

A.1.1 Diffusion equation for springs

We begin with the equation of continuity for the bead-bead connector vector distribution function $\psi(\boldsymbol{Q}, t)$, given as [34]:

$$\frac{\partial \psi}{\partial t} = -\left(\frac{\partial}{\partial \boldsymbol{Q}} \cdot [\![\dot{\boldsymbol{Q}}]\!]\psi\right) \tag{A.1}$$

which says that the rate of change of ψ at a particular $\boldsymbol{Q}$ is equal to the spatial derivative of ψ times the velocity-averaged connector vector velocity $[\![\dot{\boldsymbol{Q}}]\!]$. For the spring, we can find $[\![\dot{\boldsymbol{Q}}]\!]$ by considering a force balance over each bead. The overall force on each bead at a given moment is the sum of three general forces, the hydrodynamic force $\boldsymbol{F}^{(h)}$, the Brownian or random force $\boldsymbol{F}^{(b)}$ and the connector vector spring force $\boldsymbol{F}^{(c)}$. By assuming a Maxwellian velocity distribution for the Brownian force and including hydrodynamic interactions, it can be shown that [34]:

$$[\![\dot{\boldsymbol{Q}}]\!] = [\boldsymbol{\kappa} \cdot \boldsymbol{Q}] + \left[(\boldsymbol{\delta} - \zeta\boldsymbol{\Omega}) \cdot \left(-\frac{2kT}{\zeta}\frac{\partial}{\partial \boldsymbol{Q}} \ln \psi - \frac{2}{\zeta}\boldsymbol{F}^{(c)}\right)\right] \tag{A.2}$$

where $\zeta = 6\pi\eta_s a$ (Stokes drag) and $\boldsymbol{\Omega}$ is the tensor describing hydrodynamic interactions between the beads. The beads then have hydrodynamic radius a and the solvent has Newtonian viscosity η_s. $\boldsymbol{\Omega}$ has the general form

$$\boldsymbol{\Omega}(\boldsymbol{Q}) = \frac{3a}{4\zeta Q}\left(A\boldsymbol{\delta} + B\frac{\boldsymbol{Q}\boldsymbol{Q}}{Q^2}\right) \tag{A.3}$$

where the constants A and B must be chosen carefully to ensure the tensor correctly describes the bead-bead interaction while also remaining positive-semidefinite [13]. A common choice is the Rotne-Prager-Yamakawa (RPY) tensor, which has two separate branches depending on whether the bead separation is greater or less than $2a$:

$$A = 1 + \frac{2}{3}\left(\frac{a}{Q}\right)^2, B = 1 - 2\left(\frac{a}{Q}\right)^2 \text{ for } Q \geq 2a \tag{A.4a}$$

$$A = \frac{4}{3}\left(\frac{Q}{a}\right) - \frac{3}{8}\left(\frac{Q}{a}\right)^2, B = \frac{1}{8}\left(\frac{Q}{a}\right)^2 \text{ for } Q < 2a \tag{A.4b}$$

We have used the RPY form throughout this study for both spring-dumbbells and rod-dumbbells. Another form suggested by Öttinger [13] for the specific case of dumbbells is the regularised Oseen-Burgers (ROB) tensor, and we have verified that our results are indistinguishable to within simulation error between the ROB and RPY tensors.

Upon substitution of Eq. (A.2) into Eq. (A.1), we arrive at the diffusion equation for the configurational distribution function:

$$\frac{\partial \psi}{\partial t} = -\frac{\partial}{\partial \boldsymbol{Q}} \cdot [\boldsymbol{\kappa} \cdot \boldsymbol{Q}]\psi + \frac{\partial}{\partial \boldsymbol{Q}} \cdot \left[(\boldsymbol{\delta} - \zeta \boldsymbol{\Omega}) \cdot \frac{2kT}{\zeta} \frac{\partial}{\partial \boldsymbol{Q}} \ln \psi\right] \psi + \frac{\partial}{\partial \boldsymbol{Q}} \cdot \left[(\boldsymbol{\delta} - \zeta \boldsymbol{\Omega}) \cdot \frac{2}{\zeta} \boldsymbol{F}^{(c)}\right] \psi \tag{A.5}$$

The aim is then to get the equation above into the general form of the Fokker-Planck equation, as it can then be interpreted as a stochastic differential equation using Îto's method. To do so we apply the identity [43]:

$$\frac{\partial}{\partial \boldsymbol{Q}} \cdot \left[\boldsymbol{L} \cdot \frac{\partial f}{\partial \boldsymbol{Q}}\right] = \frac{\partial}{\partial \boldsymbol{Q}} \frac{\partial}{\partial \boldsymbol{Q}} : [\boldsymbol{L}^T f] - \frac{\partial}{\partial \boldsymbol{Q}} \cdot \left[f \frac{\partial}{\partial \boldsymbol{Q}} \cdot \boldsymbol{L}^T\right] \tag{A.6}$$

where $\boldsymbol{L}$ is a rank-2 tensor and f is some scalar function. Then, by noting that $(\boldsymbol{\delta} - \zeta \boldsymbol{\Omega})$ is symmetric, and further that $\boldsymbol{\nabla} \cdot \boldsymbol{\Omega} = 0$ for the Oseen-Burgers tensor [13] (which is also the case for the ROB and RPY tensors):

$$\frac{\partial \psi}{\partial t} = -\frac{\partial}{\partial \boldsymbol{Q}} \cdot \left\{\boldsymbol{\kappa} \cdot \boldsymbol{Q} - (\boldsymbol{\delta} - \zeta \boldsymbol{\Omega}) \cdot \frac{2}{\zeta} \boldsymbol{F}^{(c)}\right\} \psi + \frac{2k_\mathrm{B}T}{\zeta} \frac{\partial}{\partial \boldsymbol{Q}} \frac{\partial}{\partial \boldsymbol{Q}} : [\boldsymbol{\delta} - \zeta \boldsymbol{\Omega}]\psi \tag{A.7}$$

This Fokker-Planck equation forms the basis of the Brownian Dynamics simulations, which are used to solve for ψ.

A.1.2 Diffusion Equation for Rods

Note that for a rod, the connector vector has a fixed length, and so can be written as $\boldsymbol{Q} = L\boldsymbol{u}$, where $\boldsymbol{u}$ is the radial unit vector in spherical coordinates. The continuity equation then reduces

to the form

$$\frac{\partial \psi}{\partial t} = -\left(\frac{\partial}{\partial \boldsymbol{u}} \cdot [\![\dot{\boldsymbol{u}}]\!]\psi\right) \tag{A.8}$$

when $\psi = \psi(\boldsymbol{u}(t), t)$.

The expression for $[\![\dot{\boldsymbol{u}}]\!]$ for the rod is similar to that for the spring, except that there is no spring force $\boldsymbol{F}^{(c)}$, and the forces must be projected onto the ϕ and θ components through multiplication by $(\boldsymbol{\delta} - \boldsymbol{uu})$ (where $\boldsymbol{\delta}$ is the unit rank-2 tensor). It can be shown [34] that this force projection gives the following expression for the velocity-averaged radial unit vector velocity, when the hydrodynamic interaction is mediated via the RPY tensor as per Eq. (A.4):

$$[\![\dot{\boldsymbol{u}}]\!] = [\boldsymbol{\kappa} \cdot \boldsymbol{u}] - [\boldsymbol{\kappa} : \boldsymbol{uuu}] - \frac{2kT(1 - Ah)}{\zeta L^2} \frac{\partial}{\partial \boldsymbol{u}} \ln \psi \tag{A.9}$$

where $h_R^* = 3a/4L$ is the hydrodynamic interaction parameter for a bead-rod dumbbell and A is the same as that given in Eq. (A.4) with $Q = L$. This expression can then be substituted in to the continuity equation (A.8), giving

$$\frac{\partial}{\partial t}\psi = \frac{2}{\lambda_2^{(1)}}\left(\frac{\partial}{\partial \boldsymbol{u}} \cdot \frac{\partial}{\partial \boldsymbol{u}}\psi\right) - \left(\frac{\partial}{\partial \boldsymbol{u}} \cdot [\boldsymbol{\kappa} \cdot \boldsymbol{u} - \boldsymbol{\kappa} : \boldsymbol{uuu}]\psi\right) \tag{A.10}$$

in which we have used the time constant $\lambda_2^{(1)} = (\zeta L^2/kT)[1 - h_R^*(1 + 2a^2/3L^2)]^{-1}$ for bead-rod dumbbells with RPY HI. Here we use $\lambda_2^{(1)}$ to refer to the diffusion equation time constant for a dumbbell (with two beads). Note that we actually obtain the same general form of the diffusion equation for any rigid system with only two degrees of (orientational) freedom, such as a multibead-rod, prolate spheroid, cylinder or slender-body. These models differ only in the form of λ, which varies with the rotational friction. Furthermore, there are two time constants which characterise these systems, $\lambda^{(1)}$, which appears in diffusion equations similar to Eq. (A.10), and $\lambda^{(2)}$, which determines how the stress tensor varies with the distribution function in flow, as in Eq. A.23. For a multibead-rod model, we can further denote $\lambda_N^{(1)}$ and $\lambda_N^{(2)}$ as the time constants for an N-bead rigid rod.

A.2 Simulation Methodology

Here we use a semi-implicit predictor-corrector scheme based on solving a cubic polynomial, as suggested by Öttinger [13] and then applied to multi-bead chains with HI by Hsieh et al. [52] as well as Prabhakar and Prakash [53], who also included excluded-volume interactions. Here we assume that all quantities are in the Hookean non-dimensional form, and so drop the * and $_{\mathrm{H}}$ superscripts and subscripts. Additionally, we will define $\alpha = \delta Q_{\mathrm{H}}^{*2}$, such that α is equivalent to the FENE-spring b-parameter (see [34], section 13.5).

We begin with the Fokker-Planck Eq. (A.7) non-dimensionalised via Hookean units. In Îto's interpretation, there is an equivalence between the above Fokker-Planck equation and the following stochastic differential equation [13]:

$$d\boldsymbol{Q} = \left(\boldsymbol{\kappa}\cdot\boldsymbol{Q} - [\boldsymbol{B}(\boldsymbol{Q})\cdot(\boldsymbol{B}(\boldsymbol{Q}))^T]\cdot\frac{1}{2}\boldsymbol{F}^{(c)}\right)dt + \boldsymbol{B}(\boldsymbol{Q})d\boldsymbol{W} \tag{A.11}$$

where $d\boldsymbol{W}$ is a Wiener process and $\boldsymbol{B}(\boldsymbol{Q})\cdot(\boldsymbol{B}(\boldsymbol{Q}))^T = \boldsymbol{\delta} - \zeta\boldsymbol{\Omega}$. In this case we can choose $\boldsymbol{B}(\boldsymbol{Q})$ to have the form [13]:

$$\boldsymbol{B}(\boldsymbol{Q}) = \boldsymbol{\delta}\sqrt{1-\frac{3a}{4Q}A} + \frac{\boldsymbol{QQ}}{(Q)^2}\left(\sqrt{1-\frac{3a}{4Q}(A+B)} - \sqrt{1-\frac{3a}{4Q}A}\right) \tag{A.12}$$

Note that A and B (defined in Eq. (A.4)) are already dimensionless, so converting them to A^*_{H} and B^*_{H} is simply a matter of substituting $a \to a^*_{\mathrm{H}}$ and $Q \to Q^*_{\mathrm{H}}$.

We can now describe our numerical integration method for the above stochastic differential equation. This is broken into 3 main parts, the first of which is a predictor step based on the value of variables at the beginning of the timestep. We adopt the convention that any quantity with a bar (e.g. $\bar{\boldsymbol{Q}}$) represents a predicted quantity, while the subscripts j and $j+1$ refer to the beginning and the end of the timestep. We can then write Eq. (A.11) in the following approximate finite difference form:

$$\begin{aligned}\bar{\boldsymbol{Q}}_{j+1} &= \boldsymbol{Q}_j + \left(\boldsymbol{\kappa}\cdot\boldsymbol{Q}_j - \frac{1}{2}[\boldsymbol{B}(\boldsymbol{Q}_j)\cdot(\boldsymbol{B}(\boldsymbol{Q}_j))^T]\cdot\boldsymbol{F}^{(c)}_j\right)\Delta t + \boldsymbol{B}(\boldsymbol{Q}_j)\cdot\Delta\boldsymbol{W}_j \\ &\equiv \boldsymbol{Q}_j + \left(\boldsymbol{\kappa}\cdot\boldsymbol{Q}_j - \frac{1}{2}[\boldsymbol{\delta}-\zeta\boldsymbol{\Omega}]\cdot\boldsymbol{F}^{(c)}_j\right)\Delta t + \boldsymbol{B}(\boldsymbol{Q}_j)\cdot\Delta\boldsymbol{W}_j\end{aligned} \tag{A.13}$$

We then apply a corrector step using the previous predictor value, treating the force law implicitly. We don't recalculate the HI tensor, since the change is negligible over the course of a timestep and doing so was found to have no effect upon accuracy. The predictor step can be expressed as follows:

$$\begin{aligned}\boldsymbol{Q}_{j+1} + \frac{\Delta t}{4}\boldsymbol{F}^{(c)}_{j+1} = \boldsymbol{Q}_j + \frac{1}{2}\Big(&\boldsymbol{\kappa}\cdot(\boldsymbol{Q}_j + \bar{\boldsymbol{Q}}_{j+1}) \\ &- [\boldsymbol{B}(\boldsymbol{Q}_j)\cdot(\boldsymbol{B}(\boldsymbol{Q}_j))^T]\cdot\boldsymbol{F}^{(c)}_j + \frac{1}{2}\boldsymbol{F}^{(c)}_j\Big)\Delta t + \boldsymbol{B}(\boldsymbol{Q}_j)\cdot\Delta\boldsymbol{W}_j\end{aligned} \tag{A.14}$$

where all terms depending on the final spring force have been moved to the LHS. This makes the implicit assumption that the spring force is approximately equal at the beginning and end of the timestep, such that $-[\boldsymbol{B}\cdot\boldsymbol{B}^T]\cdot\boldsymbol{F}^{(c)}_j + \boldsymbol{F}^{(c)}_{j+1} \approx -[\boldsymbol{\delta}-\zeta\boldsymbol{\Omega}]\cdot\boldsymbol{F}^{(c)}_j + \boldsymbol{F}^{(c)}_j = \zeta\boldsymbol{\Omega}\cdot\boldsymbol{F}^{(c)}_j$. If we

then denote the RHS of Eq. (A.14) by $\boldsymbol{Y}$ and give the full form of $\boldsymbol{F}_{j+1}^{(c)}$, then:

$$\boldsymbol{Q}_{j+1} + \frac{\Delta t}{4}\left[\frac{Q_{j+1}-\sigma}{1-(Q_{j+1}-\sigma)^2/\alpha}\frac{\boldsymbol{Q}_{j+1}}{Q_{j+1}}\right] = \boldsymbol{Y} \tag{A.15}$$

If we denote $\hat{\boldsymbol{u}}$ as a unit vector in the $\boldsymbol{Y}$ direction, then we can take the magnitude of both sides and solve implicitly for Q_{j+1} using the following cubic equation:

$$0 = Q^3 - Q^2[2\sigma + Y] - Q[\alpha - \sigma^2 - 2Y\sigma + \beta] + [\beta\sigma + Y\alpha - Y\sigma^2] = g(Q) \tag{A.16}$$

where $\beta = 0.25\alpha\Delta t$ and $Q \equiv Q_{j+1}$. If we give Eq. (A.16) the label $g(Q) = 0$, then we can evaluate $g(Q)$ at different points to determine the ranges for the roots:

- $g(\infty) > 0$
- $g(\sigma + \sqrt{\alpha}) = -\beta\sqrt{\alpha} < 0$
- $g(\sigma - \sqrt{\alpha}) = \beta\sqrt{\alpha} > 0$
- $g(0) = \beta + (\alpha - \sigma^2)\cdot Y$, so if $\sqrt{\alpha} \geq \sigma$, then $g(0) > 0$
- $g(-\infty) < 0$

Therefore, one of the roots of the equation is always positive with an upper bound of $\sigma + \sqrt{\alpha}$ and a lower bound of the larger of 0 or $\sigma - \sqrt{\alpha}$, which is chosen as the value of Q. This is displayed graphically in figure (A.1). The other two roots will be outside of this range, but also real. Note that this implies that when $\sigma = 0$, we recover the behaviour of a FENE spring, where we can say $\alpha \equiv b$, and clearly $\sqrt{b} > \sigma = 0$.

Finally, we set $\boldsymbol{Q} = Q\hat{\boldsymbol{u}} \equiv Q\boldsymbol{Y}/Y$, giving us the new position vector of the bead-spring dumbbell at the next timestep.

A.2.1 Solving for Distributions and Material Functions of Rodlike Models

Here we summarise a general numerical method for solving for the transient distribution function of a rodlike model in shear flow based on a spherical harmonic expansion, as originally given by Stewart and Sorensen [32]. The same method can be used for bead-rod dumbbells, multibead-rods [34] and prolate spheroids [3]. In general, we simply require that the distribution function ψ of the system can be characterised by two generalised coordinates (the azimuthal angle ϕ and the polar angle θ) and a time constant $\lambda^{(1)}$ which can be derived from the rotational friction of the body (we also have a time constant $\lambda^{(2)}$ which is related to the

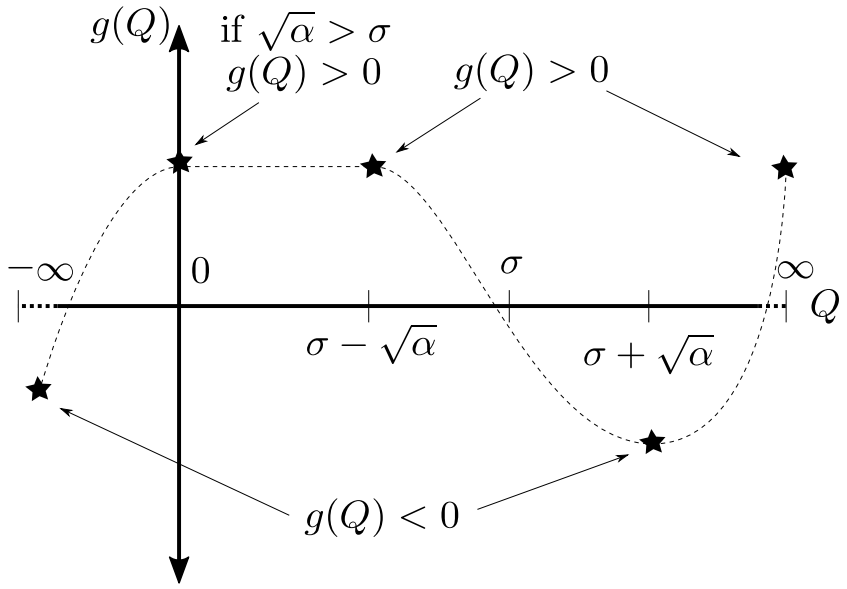

FIGURE A.1: Visualisation of the range of the cubic equation, showing why there must be a real root between $\sigma - \sqrt{\alpha}$ and $\sigma + \sqrt{\alpha}$. The key insight is that $g(Q)$ must be negative at $\sigma + \sqrt{\alpha}$ and must be positive at the larger of $\sigma - \sqrt{\alpha}$ and 0, with no inflection points within this range. Therefore, we know that one root must lie in that range.

stress tensor). We can then write the configurational diffusion equation in shear flow with shear rate $\dot{\gamma}$ as [32, 34]

$$\frac{\partial \psi}{\partial t} = \frac{1}{\lambda^{(1)}} \Lambda \psi - \dot{\gamma} \Omega_s \psi \tag{A.17}$$

where Λ and Ω_s are operators which generalise the diffusion equation given in Eq. (A.10) for a rodlike model in shear flow. Since $\psi = \psi(\phi, \theta, t)$, we can expand this distribution function as a set of spherical harmonics in the form

$$\psi(\theta, \phi, t) = \frac{1}{4\pi} \sum_{n=0}^{N} \sum_{m=0}^{n} \left[A_{0n}^{m}(t) P_n^m(\cos\theta) \cos(m\phi) + A_{1n}^{m}(t) P_n^m(\cos\theta) \sin(m\phi) \right] \tag{A.18}$$

where N gives the expansion order, $P_n^m(\cos\theta)$ are the associated Legendre polynomials (such that $P_n^m(\cos\theta)\cos(m\phi)$ or $P_n^m(\cos\theta)\sin(m\phi)$ are spherical harmonics), and the amplitudes $A_{in}^m(t)$ can be solved for via the diffusion equation. The operators Λ and Ω_s both act on spherical harmonics as follows:

$$\Lambda P_n^m s_m = -n(n+1) P_n^m s_m \tag{A.19a}$$

$$\Lambda P_n^m c_m = -n(n+1) P_n^m c_m \tag{A.19b}$$

$$\Omega_s P_n^m s_m = \sum_{j=m-2}^{m+2} \sum_{k=n-2}^{n+2} a_{nk}^{mj} P_k^j c_j \ (m > 0) \tag{A.20a}$$

$$\Omega_s P_n^m c_m = -\sum_{j=m-2}^{m+2}\sum_{k=n-2}^{n+2} a_{nk}^{mj} P_k^j s_j \ (m>0) \tag{A.20b}$$

where $s_m \equiv \sin m\phi$, $c \equiv \cos m\phi$, P_n^m is the $n-m$ associated Legendre polynomial acting on $\cos\theta$, and a_{nk}^{mj} are given as follows:

$$a_{n,n-2}^{m,m-2} = \frac{(n-2)(n+m)!\,(1-\delta_{m0})}{4(2n+1)(2n-1)(n+m-4)!} \tag{A.21a}$$

$$a_{n,n}^{m,m-2} = \frac{3(n-m+2)!(n+m)!\,(1-\delta_{m0})}{4(2n-1)(2n+3)(n+m-2)!(n-m)!} \tag{A.21b}$$

$$a_{n,n+2}^{m,m-2} = -\frac{(n+3)(n-m+4)!\,(1-\delta_{m0})}{4(2n+1)(2n+3)(n-m)!} \tag{A.21c}$$

$$a_{n,n}^{m,m} = -m/2 \tag{A.21d}$$

$$a_{n,n-2}^{m,m+2} = -\frac{(n-2)\,(1+\delta_{m0})}{4(2n+1)(2n-1)} \tag{A.21e}$$

$$a_{n,n}^{m,m+2} = -\frac{3\,(1+\delta_{m0})}{4(2n-1)(2n+3)} \tag{A.21f}$$

$$a_{n,n+2}^{m,m+2} = \frac{(n+3)\,(1+\delta_{m0})}{4(2n+1)(2n+3)} \tag{A.21g}$$

This spherical harmonic expansion along with the above operator defintions creates a set of coupled ODEs, which we have integrated using built-in differential equation solvers in MATLAB.

The unit vector $\boldsymbol{u}$ can be given in component form as follows:

$$\boldsymbol{u} = [\cos\phi\sin\theta, \sin\phi\sin\theta, \cos\theta] \tag{A.22}$$

To calculate material functions for a rodlike model, we use the following form of the stress tensor:

$$\boldsymbol{\tau} = -\eta_s\dot{\boldsymbol{\gamma}} - 6nkT\lambda_N^{(2)}\boldsymbol{\kappa} : \langle \boldsymbol{uuuu}\rangle - 3nkT\langle \boldsymbol{uu}\rangle + nkT\boldsymbol{\delta} \tag{A.23}$$

where θ is the polar angle and ϕ is the azimuthal angle. The averages are given by:

$$\langle \boldsymbol{A}\rangle = \int \boldsymbol{A}\psi d\boldsymbol{u} = \int_0^{\pi}\int_0^{2\pi} \boldsymbol{A}\psi\sin\theta d\phi d\theta \tag{A.24}$$

and we re-arrange the double dot product $\boldsymbol{\kappa} : \langle \boldsymbol{uuuu}\rangle$ as $\langle(\boldsymbol{\kappa} : \boldsymbol{uu})\boldsymbol{uu}\rangle$. Therefore, for shear stress with $\boldsymbol{\kappa}_{x,y} = \dot{\gamma}$ and all other components 0, we can expanded the stress tensor into

averages over sines and cosines as follows:

$$\boldsymbol{\kappa} : \boldsymbol{uuuu} = \dot{\gamma} \begin{pmatrix} \cos^3(\phi)\sin(\phi)\sin^4(\theta) & \cos^2(\phi)\sin^2(\phi)\sin^4(\theta) & \cos^2(\phi)\cos(\theta)\sin(\phi)\sin^3(\theta) \\ \cos^2(\phi)\sin^2(\phi)\sin^4(\theta) & \cos(\phi)\sin^3(\phi)\sin^4(\theta) & \cos(\phi)\cos(\theta)\sin^2(\phi)\sin^3(\theta) \\ \cos^2(\phi)\cos(\theta)\sin(\phi)\sin^3(\theta) & \cos(\phi)\cos(\theta)\sin^2(\phi)\sin^3(\theta) & \cos(\phi)\cos^2(\theta)\sin(\phi)\sin^2(\theta) \end{pmatrix} \tag{A.25}$$

$$\boldsymbol{uu} = \begin{pmatrix} \cos^2(\phi)\sin^2(\theta) & \cos(\phi)\sin(\phi)\sin^2(\theta) & \cos(\phi)\cos(\theta)\sin(\theta) \\ \cos(\phi)\sin(\phi)\sin^2(\theta) & \sin^2(\phi)\sin^2(\theta) & \cos(\theta)\sin(\phi)\sin(\theta) \\ \cos(\phi)\cos(\theta)\sin(\theta) & \cos(\theta)\sin(\phi)\sin(\theta) & \cos^2(\theta) \end{pmatrix} \tag{A.26}$$

By way of example, if we now specialise to a bead-rod dumbbell with hydrodynamic interaction between the beads given via the RPY tensor (as per Eq. (A.4) with $Q = L$), we find that [34]:

$$\lambda_2^{(1)}(L,a) = (\zeta L^2/12k_\mathrm{B}T)[1-(6a)/(4L)(1+2/3(a/L)^2]^{-1} \tag{A.27}$$

while

$$\lambda_2^{(2)}(L,a) = (\zeta L^2/12k_\mathrm{B}T)[1-(12a)/(4L)(1-2/3(a/L)^2]^{-1} \tag{A.28}$$

We then further define $\lambda_R^* = (L^2\zeta)/(k_\mathrm{B}T)$ (identical to the λ_R^* for bead-FF-spring dumbbells, with $L \equiv \sigma$) and $\mu = 1 - 2h_R^*(1 - 32/27{h_R^*}^2)$ where $h_R^* = (3a)/(4L)$ so that the unit system is indentical to the rodlike non-dimensionalisation of the bead-spring dumbbells. After some algebra, we have for the material functions:

$$\frac{-(\eta-\eta_s)}{nkT\lambda_R^*} = -\frac{6}{5\lambda_R^*\dot{\gamma}}A_{12}^2 - \frac{1}{12\mu}\left[\frac{2}{5}A_{00}^0 - \frac{4}{35}A_{02}^0 + \frac{2}{105}A_{04}^0 - 16A_{04}^4\right] \tag{A.29a}$$

$$\frac{-\Psi_1}{nkT{\lambda_R^*}^2} = -\frac{12}{5{\lambda_R^*}^2\dot{\gamma}^2}A_{02}^2 - \frac{8}{3\lambda\dot{\gamma}\mu}A_{14}^4 \tag{A.29b}$$

$$\frac{-\Psi_2}{nkT{\lambda_R^*}^2} = +\frac{3}{{\lambda_R^*}^2\dot{\gamma}^2}\left[-\frac{1}{5}A_{02}^0 - \frac{2}{5}A_{02}^2\right] + \frac{1}{4\lambda\dot{\gamma}\mu}\left[\frac{8}{35}A_{12}^2 - \frac{4}{7}A_{14}^2 - \frac{16}{3}A_{14}^4\right] \tag{A.29c}$$

$$S = \frac{1}{3}A_{00}^0 - \frac{1}{15}A_{02}^0 + \frac{2}{5}A_{02}^2 \tag{A.29d}$$

A.3 Code Validation

A.3.1 Comparison with FENE Spring Simulations

There is no previous work in the literature on FENE-Fraenkel dumbbells with which we can compare our results, as Larson et al. [23] only reports results for 10-bead chains. Therefore, we

compare our results with other studies using the semi-implicit predictor-corrector algorithm for FENE dumbbells, as our code should give identical results when setting $\sigma = 0$ in the FENE-Fraenkel force law. One such example is the work by Kailasham et al. [43], who also used an RPY tensor to mediate hydrodynamic interactions. Some comparisons between their work and our own are shown Fig. A.2, with almost perfect agreement.

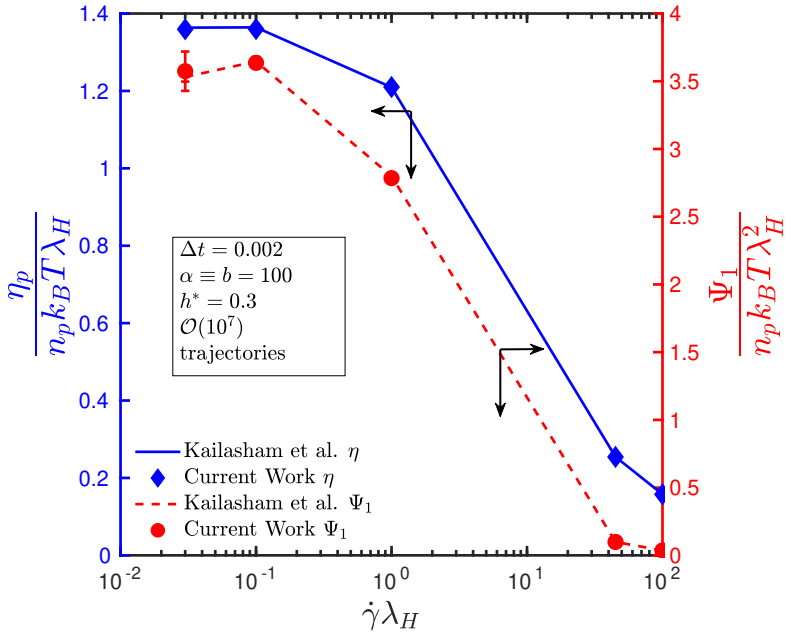

FIGURE A.2: Comparison of steady-state shear viscosity and first normal stress difference with shear rate against the results of Kailasham et al. [43]. Note that with $\sigma = 0$, the α dimensionless parameter used in this paper is equivalent to the dimensionless parameter b characterising the extensibility of a FENE spring. Error bars, when not visible, are smaller than symbol size.

A.3.2 FENE-Fraenkel Distribution Functions

As an analytical result for the equilibrium end-to-end vector distribution $\psi(\boldsymbol{Q})$ can be derived (section A.4), histograms of simulated dumbbell vectors in the absence of flow can be used as an initial check of timestep convergence. The dumbbell vector can be represented in spherical coordinates and the angular distribution plotted separately from the length distribution. An example of the angular distribution is shown in Fig. A.3, where the simulated distribution follows the expected sin curve for θ and is constant for ϕ. This angular distribution remains spherically symmetric irrespective of the value of h^*, δQ, H, σ or even the timestep Δt. This is of course to be expected, as even when numerically unstable, the algorithm treats all three Cartesian coordinates identically.

The length distribution $\psi(Q)$ is somewhat more complicated, as the distribution function convergence with decreasing Δt depends somewhat on the spring parameters δQ, H, σ, as

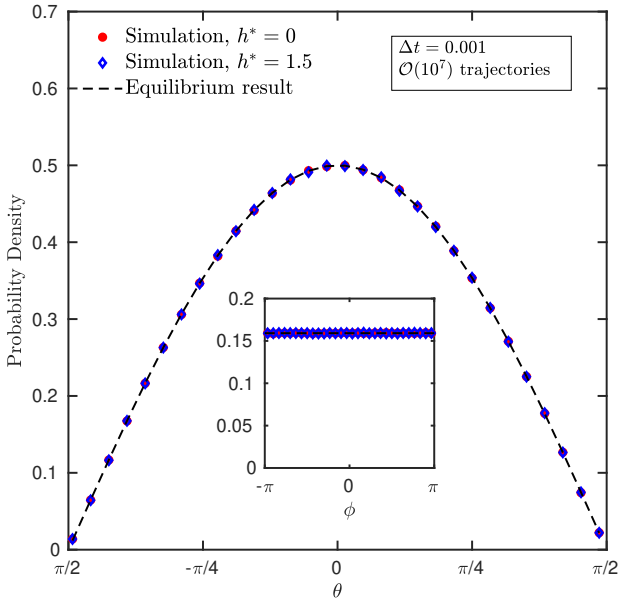

FIGURE A.3: Comparison of the azimuthal (ϕ, inset) and polar (θ) angle distributions with those expected at equilibrium, i.e. a perfectly spherical distribution. The simulated distribution is spherical at equilibrium both with and without HI, with error bars smaller than symbol size.

well as the hydrodynamic interaction parameter h^*. In order to analyse the convergence, two measurements are computed. Firstly, the Kolmogorov-Smirnov test, which is a hypothesis test on the null hypothesis that the two distributions are the same. This returns a p-value, which we denote p_{KS}, such that a large p_{KS} implies that the null hypothesis likely holds, and the two distributions are likely the same. This is simple to calculate in MATLAB using an inbuilt function. Secondly, the summed difference between the analytical and simulated $\psi(Q)$. This is the equivalent of the following integral

$$\mathcal{D}_\psi = \delta Q \int_{-\infty}^{\infty} (\psi_{\text{sim}}(Q) - \psi_{\text{ana}}(Q))^2 dQ = \delta Q \int_{-\infty}^{\infty} (\Delta\psi)^2 dQ \tag{A.30}$$

which in discrete form, with the simulated lengths binned into N_{bin} segments, is

$$\mathcal{D}_\psi = \delta Q \sum_{i}^{N_{\text{bins}}} (\psi_{\text{sim}}(Q_i) - \psi_{\text{ana}}(Q_i))^2 (\Delta Q_i) = \delta Q \sum_{i}^{N_{\text{bins}}} (\Delta\psi_i)^2 (\Delta Q_i) \tag{A.31}$$

where $\mathcal{D}_\psi$ is the 'summed difference', denoted $\sum(\Delta\psi)^2$ in Fig. A.4 below. Note the multiplication by δQ, which is necessary to non-dimensionalise the summed difference. Since $\Delta\psi$ has units of inverse length, a direct integral over this quantity squared will have units of inverse length, so it must be multiplied by a quantity with units of length to obtain a dimensionless form. By multiplying by δQ, the summed difference should be independent of the specific

choice of δQ, but instead simply a function of the difference in shape between the two distributions. For example, see Fig. A.4, which shows two plots with the same Δt_H^*, δQ_H^* and h_R^*. Both plots are converged by the Kolmogorov-Smirnov test, but if they were not normalised by δQ_R^*, the calculated differences would differ by an order of magnitude. Essentially, this ensures that with identical binning and sample size, two distributions which are similarly 'accurate' should give similar summed differences, irrespective of the FENE-Fraenkel spring parameters.

The error in this summed difference can also be computed, by assuming the counts in each bin are Poisson-distributed, and hence the error in each measurement is the square root of the bin count, normalised by the same factor c as to transform from raw counts to a PDF.

$$\sigma_{bin} = \sqrt{n}/c \tag{A.32}$$

The total error is then, when propagated:

$$\sigma_T = \sqrt{\sum_i^{N_{\text{bins}}} (2\Delta\psi_i \Delta Q_i \sigma_{bin,i})^2} \tag{A.33}$$

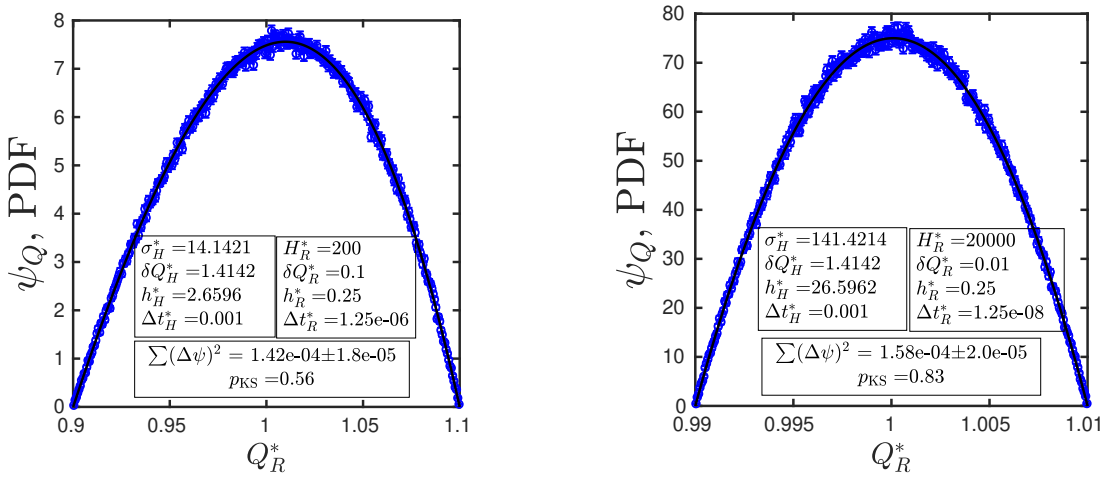

(a) (b)

FIGURE A.4: Distribution functions at two δQ_R^*.

A.4 Analytical Results

We begin with the spring potential of the dumbbell, which is:

$$\phi_{\text{eq}} = -\frac{H\delta Q^2}{2} \ln\left[1 - \frac{(Q-\sigma)^2}{\delta Q^2}\right] \tag{A.34}$$

In general, the distribution function has the form (in spherical coordinates) [34]:

$$\psi_{\mathrm{eq}}(Q) = \frac{Q^2 e^{-\phi_{\mathrm{eq}}/k_{\mathrm{B}}T}}{4\pi J_{\mathrm{eq}}} \tag{A.35}$$

where J_{eq} is a normalisation factor (after already integrating over the isotropic angular distribution, giving the 4π factor). The normalisation must be over all possible values of Q, which in this case has one upper bound, $\sigma + \delta Q$ and two possible lower bounds, the larger of 0 and $\sigma - \delta Q$. For now we will restrict our calculation to the $\sigma - \delta Q$ lower bound. The normalisation factor will have the form:

$$J_{\mathrm{eq}} = \int_{\sigma-\delta Q}^{\sigma+\delta Q} \left[1 - \frac{(Q-\sigma)^2}{\delta Q^2}\right]^{\frac{H\delta Q^2}{2k_{\mathrm{B}}T}} Q^2 dQ \tag{A.36}$$

We can split this integral into two halves as follows:

$$A_1 = \int_{\sigma}^{\sigma+\delta Q} \left[1 - \frac{(Q-\sigma)^2}{\delta Q^2}\right]^{c} Q^2 dQ \tag{A.37a}$$

$$A_2 = \int_{\sigma-\delta Q}^{\sigma} \left[1 - \frac{(Q-\sigma)^2}{\delta Q^2}\right]^{c} Q^2 dQ \tag{A.37b}$$

$$J_{\mathrm{eq}} = A_1 + A_2 \tag{A.37c}$$

where we have set $c = H\delta Q^2/2k_{\mathrm{B}}T$. For A_1, we make the substitution $t = (Q-\sigma)^2/\delta Q^2$, so that $Q = \sigma + \delta Q\sqrt{t}$, $dQ = 2\sqrt{t}/\delta Q dt$, and the integral becomes:

$$A_1 = \int_0^1 (1-t)^c (\delta Q\sqrt{t} + \sigma)^2 \frac{\delta Q}{2\sqrt{t}} dt \tag{A.38}$$

For A_2, we can make the same substitution $t = (Q - \sigma + \delta Q)^2/\delta Q^2$, only we use the other solution for Q, giving $Q = \sigma - \delta Q\sqrt{t}$, $dQ = -2\sqrt{t}/\delta Q dt$, so that the integral is:

$$A_2 = \int_1^0 (1-t)^c (-\delta Q\sqrt{t} + \sigma)^2 \frac{-\delta Q}{2\sqrt{t}} dt \tag{A.39}$$

While it is possible to expand the brackets and manipulate the integrals into a form which is equivalent to the Beta function, Mathematica can symbolically solve the combined integral for us, giving:

$$J_{\mathrm{eq}} = \frac{\delta Q(\delta Q^2 + (3+2c)\sigma^2)}{3+2c} \mathrm{B}\left(\frac{1}{2}, 1+c\right) \tag{A.40}$$

With this Mathematica script, it is trivial to compute equilibrium averages over Q, such as:

$$\langle Q^2 \rangle_{\mathrm{eq}} = \frac{\delta Q(3\delta Q^4 + 6(5-2c)\delta Q^2\sigma^2 + (-5+2c)(-3+2c)\sigma^4)}{(5-2c)(3-2c)} \mathrm{B}\left(\frac{1}{2}, 1-c\right) \tag{A.41}$$

A.5 Selection of Parameters for Experimental Comparisons

A.5.1 Choosing Bead Radius

Here we show how bead radii are calculated for the FENE-Fraenkel spring to properly compare with experimental results for rigid macromolecules as in section 3.4 of the main paper. This is performed primarily based on the results in section 14.6 of Dynamics of Polymeric Liquids Vol.2 by Bird et al [34]. The full form of Eq. (A.17) for a multibead-rod is given in Bird et al. by Eq. (14.6-13), which is as follows:

$$\frac{\partial}{\partial t}\psi = \frac{1}{6\lambda_N^{(1)}}\left(\frac{\partial}{\partial \boldsymbol{u}}\cdot\frac{\partial}{\partial \boldsymbol{u}}\psi\right) - \left(\frac{\partial}{\partial \boldsymbol{u}}\cdot[\boldsymbol{\kappa}\cdot\boldsymbol{u} - \boldsymbol{\kappa}:\boldsymbol{uuu}]\psi\right) \tag{A.42}$$

with the stress tensor given by:

$$\boldsymbol{\tau} = -\eta_s\dot{\boldsymbol{\gamma}} - 6nkT\lambda_N^{(2)}\boldsymbol{\kappa}:\langle\boldsymbol{uuuu}\rangle - 3nkT\langle\boldsymbol{uu}\rangle + nkT\boldsymbol{\delta} \tag{A.43}$$

with $\lambda_N^{(2)}$ and $\lambda_N^{(1)}$ defined as:

$$\lambda_N^{(1)}(h_N^*,\xi) = \frac{\zeta d^2}{12kT}\left(\sum_{v=-(N-1)}^{N-1} v\phi_v\left(h_N^*,\xi^2,N\right)\right) \tag{A.44}$$

$$\lambda_N^{(2)}(h_N^*,\xi) = \frac{\zeta d^2}{12kT}\left(\sum_{v=-(N-1)}^{N-1} v\phi_v\left(2h_N^*,-\xi^2,N\right)\right) \tag{A.45}$$

with ϕ_v defined by the following equation:

$$\phi_v(\alpha,\beta,N) + 2\alpha\sum_{\mu}{}'\left(\frac{1}{|v-\mu|} + \tfrac{2}{3}\beta_{|v-\mu|^3}\right)\phi_\mu(\alpha,\beta,N) = \frac{1}{2}v \tag{A.46}$$

where $\sum_\mu'$ runs over $-(N-1)$ to $+(N+1)$, omitting terms $\mu=\nu$ and using even (odd) values of μ if N is odd (even). The parameters are $\xi = a/d$ where a is the bead radius and d is the distance between bead centers, N is the number of beads, $L = d(N-1)$ is the total length of the rod, and h_N^* is given as $h_N^* = \zeta/8\pi\eta_s d$.

These expressions can be solved for the values of $\lambda_N^{(1)}$, which essentially defines the rotational friction of the molecule, and $\lambda_N^{(2)}$, which gives the stress response to orientation. Note that explicit expressions have already been given in Eqs. (A.27) and (A.28) for a bead-rod dumbbell (the $N=2$ case), albeit with slightly different definitions of L and h. The key is that for purely orientational measurements, such as the S-parameter characterising Linear Dichroism, the effective bead radius for the bead-rod dumbbell can be chosen such that $\lambda_2^{(1)} = \lambda_N^{(1)}$, meaning that the diffusion equation for the two cases is identical. This same bead radius can

then be used for FENE-Fraenkel simulations to give a spring which approximately behaves hydrodynamically like a multibead-rod.

For viscosity measurements, the situation is slightly more complicated. In this case, it's not possible to choose a single bead radius such that both $\lambda_2^{(1)} = \lambda_N^{(1)}$ and $\lambda_2^{(2)} = \lambda_N^{(2)}$. Therefore, the bead radius was chosen to sit somewhere between the radius such that $\lambda_2^{(1)} = \lambda_N^{(1)}$ and the radius such that $\lambda_2^{(2)} = \lambda_N^{(2)}$, so that the bead-rod viscosity data gives a reasonable fit to the multibead-rod viscosity data. This is able to once again give a reasonable overall hydrodynamic approximation of a multibead-rod, as can be seen in Fig. (18) of the main paper.

Appendix B

Semi-Implicit Predictor-Corrector Scheme and Lookup Tables

There are three steps in the semi-implicit predictor-corrector algorithm. Firstly, an Euler predictor step is used to obtain the bead positions $\tilde{\boldsymbol{R}}_{n+1}$ at the $n+1$ time step.

$$\tilde{\boldsymbol{R}}_{n+1} = \boldsymbol{R}_n + \left[\boldsymbol{K}\cdot\boldsymbol{R}_n + \frac{1}{4}\boldsymbol{D}_n\cdot\boldsymbol{F}_n^{\mathrm{S}} + \frac{1}{4}\boldsymbol{D}_n\cdot\boldsymbol{F}_n^{\mathrm{E}}\right]\Delta t^* + \frac{1}{\sqrt{2}}\Delta\boldsymbol{S}_n \tag{B.1}$$

where $\Delta\boldsymbol{S}_n = \boldsymbol{B}_n\cdot\Delta\boldsymbol{W}_n$ is the diffusion term, made up of the random Weiner process $\Delta\boldsymbol{W}_n$ with zero mean and variance Δt^*, as well as the square root of the diffusion tensor $\boldsymbol{D} = \boldsymbol{B}\cdot\boldsymbol{B}^{\mathrm{T}}$. The 'Gaussian' random numbers are not truly Gaussian, but are instead generated from the following distribution:

$$X = \sqrt{\Delta t^*}\left(Y - \frac{1}{2}\right)\left[c_1\left(Y - \frac{1}{2}\right)^2 + c_2\right] \tag{B.2}$$

where Y is a uniform random number in the range $[0,1]$ (generated using the ran_1 algorithm in Numerical Recipes [156]), and c_1 and c_2 are the constants 14.14855378 and 1.21569221 respectively, as suggested by Öttinger [13]. This distribution still has the correct second and fourth moments, which is adequate to obtain average values from BD simulations [13] for considerably reduced computational cost. Additionally, the bead force term $\boldsymbol{F}_n^{\phi}$ has been split up into a spring contribution, $\boldsymbol{F}_n^{\mathrm{S}}$ and a non-spring contribution $\boldsymbol{F}_n^{\mathrm{E}}$ (currently excluded volume and bending potential forces).

A corrector step is then constructed as follows:

$$\begin{aligned}\boldsymbol{R}_{n+1} =& \boldsymbol{R}_n + \left[\frac{1}{2}\left\{\boldsymbol{K}\cdot\boldsymbol{R}_n + \boldsymbol{K}\cdot\tilde{\boldsymbol{R}}_{n+1}\right\} + \frac{1}{8}\boldsymbol{D}_n\cdot\left\{\boldsymbol{F}_n^{\mathrm{S}} + \boldsymbol{F}_{n+1}^{\mathrm{S}}\right\}\right.\\ &\left. + \frac{1}{8}\boldsymbol{D}_n\cdot\left\{\boldsymbol{F}_n^{\mathrm{E}} + \tilde{\boldsymbol{F}}_{n+1}^{\mathrm{E}}\right\}\right]\Delta t^* + \frac{1}{\sqrt{2}}\Delta\boldsymbol{S}_n\end{aligned} \tag{B.3}$$

where the non-spring force $\tilde{\boldsymbol{F}}^{\mathrm{E}}_{n+1}$ has been evaluated using the predicted bead positions $\tilde{\boldsymbol{R}}_{n+1}$. Note, however, that the spring force $\boldsymbol{F}^{\mathrm{S}}_{n+1}$ is being treated implicitly. The solution to this equation will then give the bead positions for the next timestep, $\boldsymbol{R}_{n+1}$.

The final step then involves solving for the connector vectors $\boldsymbol{Q}^*_\nu$ from bead ν to bead $\nu+1$, where $\boldsymbol{Q}^*_\nu = \boldsymbol{r}^*_{\nu+1} - \boldsymbol{r}^*_\nu$. This is described theoretically by Prabhakar and Prakash [53], but here we will give a description in terms of the data structures used in the code. Firstly, we construct the following $\tilde{\boldsymbol{\Upsilon}}_{n+1}$ term:

$$\tilde{\boldsymbol{\Upsilon}}_{n+1} = \boldsymbol{R}_n + \left[\frac{1}{2}\left\{\boldsymbol{K}\cdot\boldsymbol{R}_n + \boldsymbol{K}\cdot\tilde{\boldsymbol{R}}_{n+1}\right\} + \frac{1}{8}\boldsymbol{D}_n\cdot\boldsymbol{F}^{\mathrm{S}}_n + \frac{1}{8}\boldsymbol{D}_n\cdot\left\{\boldsymbol{F}^{\mathrm{E}}_n + \tilde{\boldsymbol{F}}^{\mathrm{E}}_{n+1}\right\}\right]\Delta t^* + \frac{1}{\sqrt{2}}\Delta\boldsymbol{S}_n \tag{B.4}$$

Note that this definition contains everything on the RHS of (B.3) besides the $\boldsymbol{F}^{\mathrm{S}}_{n+1}$ term, which is the part we wish to solve for implicitly. This Upsilon vector is stored as a $3\times N$ matrix, so that $\tilde{\boldsymbol{\Upsilon}}_{\nu,n+1}$ refers to the 3-component vector corresponding to the νth element of $\tilde{\boldsymbol{\Upsilon}}_{n+1}$. We can then write the connector vector between beads ν and $\nu+1$ for the next timestep as follows:

$$\boldsymbol{Q}^*_{\nu,n+1} = \left(\tilde{\boldsymbol{\Upsilon}}_{\nu,n+1} - \tilde{\boldsymbol{\Upsilon}}_{\nu,n}\right) + \frac{1}{8}\left(\left[\boldsymbol{D}_n\cdot\boldsymbol{F}^{\mathrm{S}}_{n+1}\right]_{\nu+1} - \left[\boldsymbol{D}_n\cdot\boldsymbol{F}^{\mathrm{S}}_{n+1}\right]_{\nu}\right)\Delta t^* \tag{B.5}$$

We can identify this $(\tilde{\boldsymbol{\Upsilon}}_{\nu,n+1} - \tilde{\boldsymbol{\Upsilon}}_{\nu,n})$ operation (and the equivalent for the $\boldsymbol{D}_n\cdot\boldsymbol{F}^{\mathrm{S}}_{n+1}$ term) as $\mathcal{D}_\nu[\tilde{\boldsymbol{\Upsilon}}_{n+1}]$, in order to correspond to the notation of Prabhakar and Prakash [53].

We now notice that the second term on the RHS of Eq. (B.5) contains a term of the form $-(1/4)(\boldsymbol{F}^{S*}_{v+1,n+1} - \boldsymbol{F}^{S*}_{v,n+1})\Delta t^* = -(1/4)\boldsymbol{F}^{c*}_{v,n+1}\Delta t^*$, where $\boldsymbol{F}^{c*}_{v,n+1}$ is the force in the νth spring, which is a function of $\boldsymbol{Q}^*_{\nu,n+1}$. We can transpose this term to the LHS by adding $\boldsymbol{F}^{c*}_{v,n+1}$ to both sides of the equation, which then gives the following iterative form:

$$\boldsymbol{Q}^{*(j)}_{v,n+1} + \frac{\Delta t^*}{4}\boldsymbol{F}^{c*(j)}_v = \boldsymbol{\Gamma}^{(j-1)}_{v,n+1} \tag{B.6}$$

where j is an iteration index, and

$$\boldsymbol{\Gamma}^{(j-1)}_{v,n+1} = \mathcal{D}_v\left[\tilde{\boldsymbol{\Upsilon}}_{n+1}\right] + \frac{1}{8}\mathcal{D}_v\left[\boldsymbol{D}_n\cdot\boldsymbol{F}^{S(j-1)}_{n+1}\right]\Delta t^* + \frac{1}{4}\boldsymbol{F}^{\mathrm{c}*(j-1)}_v\Delta t^* \tag{B.7}$$

Since $\boldsymbol{F}^{c*}_{v,n+1}$ is a function of $\boldsymbol{Q}^*_{\nu,n+1}$, and the RHS of Eq. (B.6) depends only on $\boldsymbol{Q}$ from the previous iteration, this should converge on the correct solution for large j. Note that $\boldsymbol{D}_n$ and $\tilde{\boldsymbol{\Upsilon}}_{n+1}$ do not change during the iterative solution, as they are not dependent on the iteration index.

In order to exit this iteration, we need some stopping criteria based on the difference between the bead positions in two subsequent iterations. It's not clear what stopping criteria is ideal, and exact definitions seem to be different between almost every implementation of this

method. Currently, the code uses the total sum of squares of the differences between all $3 \times N$ components of the bead vectors divided by the number of beads, which seems to give just as accurate results as a relative error (although may not be as universally applicable).

The final remaining step is the actual solution of Eq. B.6. Since both $\boldsymbol{F}^{(c)}$ and $\boldsymbol{Q}$ are aligned along the same axis, we can see that the direction of $\boldsymbol{Q}$ must be the same as the direction of $\boldsymbol{\Gamma}$. We can then solve for the magnitude by using:

$$\left(1 + \frac{\Delta t^*}{4} f(Q)\right) \boldsymbol{Q}^{*(j)}_{v,n+1} = \boldsymbol{\Gamma}^{(j-1)}_{v,n+1} \tag{B.8}$$

for a force law of the general form:

$$\boldsymbol{F}(Q) = H\boldsymbol{Q}f(Q) \tag{B.9}$$

where H is the spring stiffness, $\boldsymbol{Q}$ is the spring connector vector, and $f(Q)$ is some function of the connector vector length (the simple Hookean spring has $f(Q) = 1$). For example, for the FENE spring, if we set $x \equiv \|\boldsymbol{Q}^{*(j)}_{v,n+1}\|$ and $G \equiv \|\boldsymbol{\Gamma}^{(j-1)}_{v,n+1}\|$, then we have:

$$x^3 - Gx^2 - Q_0^{2*}\left(1 + \frac{\Delta t^*}{4}\right)x + Q_0^{2*}G = 0 \tag{B.10}$$

which is actually guaranteed to have exactly one root in the range $\{0, Q_0^*\}$. The solution to this equation is somewhat more complicated for a FENE-Fraenekl spring, and follows the method detailed in Section A.2.

For a modified WLC potential, we end up with a (non-dimensional) equation like this:

$$\frac{6G}{\Delta t \delta Q} = \frac{6x}{\Delta t} + \frac{1}{4}\left(\frac{1-\sigma}{1-x}\right)^2 - \frac{1}{4} + \frac{x-\sigma}{1-\sigma} - \frac{\sigma}{4}\left(\frac{1-\sigma}{1+x}\right)^2 + \frac{\sigma}{4} - \sigma\frac{-x-\sigma}{1-\sigma} \tag{B.11}$$

which is then solved using a numerical root-finding algorithm, namely 'rtsafe' in Numerical Recipes [157].

B.1 Cubic equation solvers

For the FENE-Fraenkel spring, we can directly calculate the roots of the cubic polynomial to find the value within the range of the spring force law, as described above. For other force laws (besides modified-MS), we can approximate the root and then polish it using the Newton-Raphson method.

For the modified-MS algorithm, we can use 'rtsafe' from Numerical Recipes [157]. This requires both the expression itself Equation B.11, as well as the derivative of this function with respect

to x, which is trivial to derive. However, since this is a very expensive operation, these roots are only calculated once at the start of the simulation for several values of G, and then a lookup table is used throughout normal operation.

B.2 Lookup tables

The lookup table is implemented using the 'hunt' and 'polint' methods of numerical recipes [157], giving an extension x for some value of G. However, the construction of the table is not simple, since the slope can change very rapidly around certain points. In other words, a simple equal division of the range is not appropriate. Instead, we apply the following algorithm to generate the table, where $g^{-1}(G)$ is the inverse of Equation B.11:

$$x_1 = g^{-1}(G_1), \quad x_2 = g^{-1}(G_2), \quad G_1 = 0, G_2 = \Delta G \tag{B.12}$$

and then loop over the following steps:

$$G_i = G_{i-1} + \Delta G \tag{B.13}$$

$$x_i = g^{-1}(G_i), \quad G_i = G_{i-1} + \Delta G \tag{B.14}$$

$$x_{i-1/2} = g^{-1}(G_{i-1/2}), \quad G_{i-1/2} = G_{i-1} + \Delta G/2 \tag{B.15}$$

We then do a polynomial interpolation using $x_{i,i-1,i-2}$ and $G_{i,i-1,i-2}$ to give the expected value $\tilde{x}_{i-1/2}$ at $G_{i-1/2}$. Our calculated error ϵ_x is then:

$$\epsilon_x = \|\tilde{x}_{i-1/2} - x_{i-1/2}\| \tag{B.16}$$

If our error is greater than some tolerance, we set $\Delta G = 0.7\Delta G$. If not, we set $\Delta G = 1.6\Delta G$ and exit our loop, moving on to the next i. Finally, we finish the construction of the lookup table when G_i reaches some value G_{exit}. An example graph of this lookup table is given in Figure B.1. The set of parameters given in this figure appears to give a reasonable number of lookup table entries for a wide range of Δt and σ^*.

The advantage of this method is that we are almost certain that our error during a simulation step will never be greater than the tolerance, since we're ensuring this is the case in the construction of our lookup table. However, the number of points in the table is variable, meaning that the amount of time a given lookup takes will vary from simulation to simulation. Since the 'hunt' algorithm takes $\mathcal{O}(\log n)$ time, where n is the number of entries in the table, a large table doesn't lead to much difference in performance. Timing tests reveal that this implementation does in fact save significant computational time, since as much as $15 - 20\%$ of the total compute time goes into solving Equation B.11, which is reduced to $< 5\%$ when

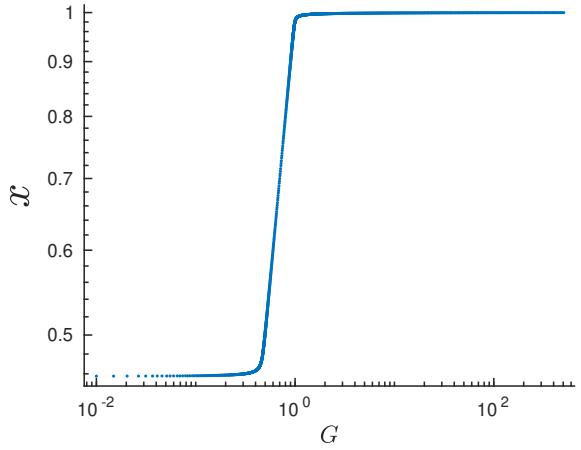

FIGURE B.1: Example lookup table in the case where $\sigma^* = 8/11$, $\Delta t = 0.002$, $\Delta G = 0.01$, the tolerance is 10^{-9} and $G_{\text{exit}} = 500$.

pre-computed. It's very likely that considerable subsequent improvements in speed could be found with better optimisation of the lookup table and interpolation algorithm.

Appendix C

Calculation of solvent perturbation due to HI

In BD simulations, the hydrodynamic interactions are transferred instantly from bead to bead, essentially coupling the motion of different beads together directly. Unlike in explicit-sovlent MD, this means we cannot directly visualise the flow around a polymer molecule in our simulations. However, we can use the same RPY tensor which transmits the solvent velocity perturbation to calculate the effective force each point in space would feel in our simulations. This can give insight into how HI is influencing the overall conformation of the polymer molecule.

The Oseen-Burgers tensor (or regularised form in RPY tensor, given in Equation A.3, and also reproduced in 'Hookean' units below in Equation C.2) describes how a spherical point source moving through the origin creates a velocity perturbation at a different point [59]:

$$\boldsymbol{v}' = [\boldsymbol{\Omega} \cdot \boldsymbol{F}] \tag{C.1}$$

where $\boldsymbol{\Omega}$ is the Oseen-Burgers tensor, $\boldsymbol{F}$ is the force exerted by the sphere on the fluid, and $\boldsymbol{v}'(\boldsymbol{r})$ is the velocity perturbation at $\boldsymbol{r}$ caused by that force. This velocity perturbation is visualised in the $x-y$ plane for a couple of simple situations in Figure C.1. It is worth at this point remarking upon a couple of interesting features. Firstly, a single force in Figure C.1 (a) actually has somewhat the appearance of the field of an electric dipole, and in fact the flow field around a sphere in the frame of reference of a sphere is a dipole. Secondly, the opposing forces of Figure C.1 (b) behave somewhat like a quadrupole, with flow moving in the direction of 'tension' and then circulating out perpendicularly.

As we have information on both the bead locations and bead forces at each sample time for each trajectory, this enables us to plot the flow field disturbance due to HI. It is also possible

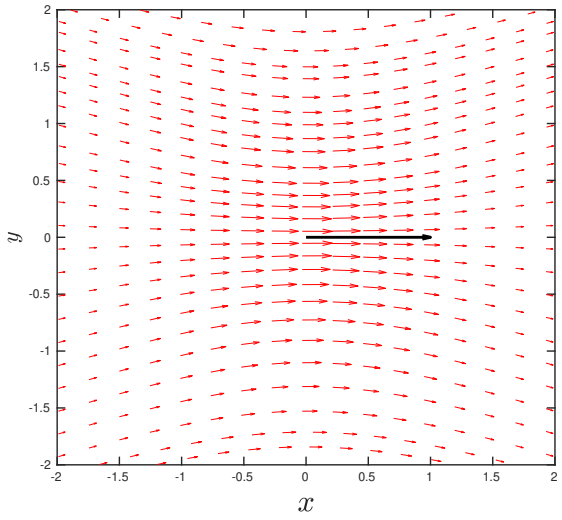

(a)

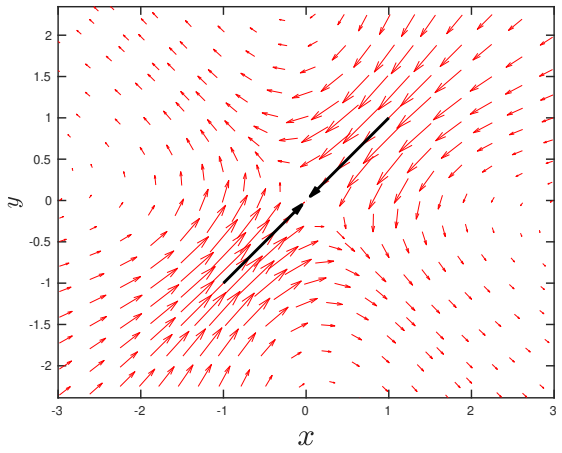

(b)

FIGURE C.1: Visualisation of the flow field in the $x - y$ plane for two simple force vector arrangements. The direction and magnitude of the velocity disturbance are shown through red arrows, while the larger black arrows give the direction of the applied force on the fluild. In case (a), the force is purely in the x-direction, leading to a 'Stokeslet' like flow field. In case (b), the flow field looks rather like a quadropole.

to add onto this the background shear flow vectors, giving a sense of the overall change in flow due to HI. This is shown in Figure C.2, which has a somewhat different visual form from Figure C.1. Essentially, the disturbance due to HI is added to the background shear flow, and the total streamlines are plotted, with the magnitude of the velocity as the colour gradient. This gives a sense of the imposed re-circulation due to HI, which is why HI is referred to as 'backflow' in many texts.

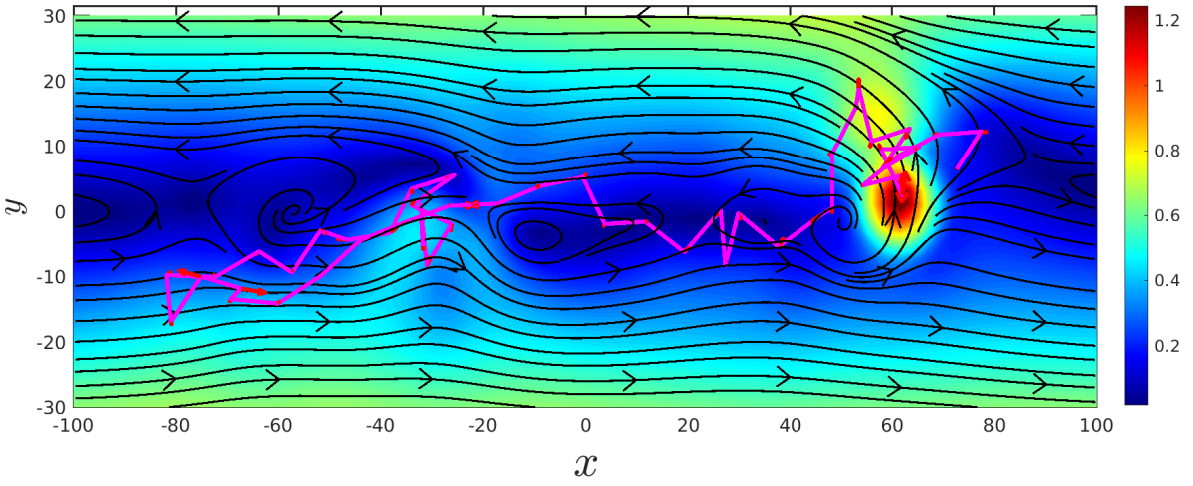

FIGURE C.2: Visualisation of the flow field in the $x-y$ plane for a FENE-Fraenkel bead-spring chain. Magenta lines show projection of chain contour into $x-y$ plane, with the same for red arrows showing forces on beads. Direction of flow is given by black streamlines, while colour is used for total magnitude of velocity at each point.

C.1 Equations in Hookean units

When written in terms of h^*, the RPY tensor reads:

$$\boldsymbol{\Omega}(\boldsymbol{R}) = \frac{3\sqrt{\pi}h^*}{4\zeta R}\left(A\boldsymbol{\delta} + B\frac{\boldsymbol{RR}}{R^2}\right) \tag{C.2}$$

with

$$A = 1 + \frac{2\pi}{3}\left(\frac{h^*}{R}\right)^2, B = 1 - 2\pi\left(\frac{h^*}{R}\right)^2 \text{ for } R \geq 2\sqrt{\pi}h^* \tag{C.3a}$$

$$A = \frac{4}{3\sqrt{\pi}}\left(\frac{R}{h^*}\right) - \frac{3}{8\pi}\left(\frac{R}{h^*}\right)^2, B = \frac{1}{8\pi}\left(\frac{R}{h^*}\right)^2 \text{ for } R < 2\sqrt{\pi}h^* \tag{C.3b}$$

where $h^* \equiv h^*_H$ and $R \equiv R^*_H$.

Additionally, with our Hookean unit system, and setting $\boldsymbol{\Omega}^* \equiv \boldsymbol{\Omega}\zeta$, the true velocity disturbance is given by:

$$\begin{aligned} \boldsymbol{v}' &= [\boldsymbol{\Omega}\cdot\boldsymbol{F}] \\ \boldsymbol{v}'^*\frac{l_H}{\lambda_H} &= \left[\frac{\boldsymbol{\Omega}^*}{\zeta}\cdot\boldsymbol{F}^*F_H\right] \\ \boldsymbol{v}'^*\sqrt{\frac{k_BT}{H}}\frac{4H}{\zeta} &= \left[\frac{\boldsymbol{\Omega}^*}{\zeta}\cdot\boldsymbol{F}^*\sqrt{k_BTH}\right] \end{aligned} \tag{C.4}$$

finally giving:

$$\boldsymbol{v}'^* = \frac{[\boldsymbol{\Omega}^*\cdot\boldsymbol{F}^*]}{4} \tag{C.5}$$

Appendix D

Bending potential implementation details

D.1 Theory

We denote the bending potential by $\phi_{\mathrm{b},\mu}$, where ϕ_{b} refers to the potential energy due to bending, while the μ subscript references segmental angle μ. In this case we will firstly deal with a bending potential of the form [18]:

$$\phi_{\mathrm{b},\mu}/k_{\mathrm{B}}T = C(1 - \cos\theta_{\mu}) \tag{D.1}$$

where C is a rigidity constant.

Now consider bead μ in Fig. Figure 3.3. It has angle θ_{μ} associated with it, which we can calculate by the dot product:

$$\theta_{\mu} = \arccos(\boldsymbol{u}_{\mu-1} \cdot \boldsymbol{u}_{\mu}) \tag{D.2}$$

where the unit vectors $\boldsymbol{u}_i$ can be expressed as $\boldsymbol{Q}_i/Q_i$, and the connector vectors $\boldsymbol{Q}$ can be expressed in terms of bead position vectors $\boldsymbol{r}_i$ as:

$$\boldsymbol{Q}_{\mu} = \boldsymbol{r}_{\mu+1} - \boldsymbol{r}_{\mu} \tag{D.3}$$

Now consider the force due to the bending potential on bead μ. This will actually be a combination of the force from θ_{μ}, as well as adjacent angles $\theta_{\mu\pm1}$. Specifically, we can denote the force on bead μ due to potential μ' as $\boldsymbol{F}^{\mathrm{b}}_{\mu,\mu'}$, and then identify the total force as:

$$\boldsymbol{F}^{\mathrm{b}}_{\mu} = \boldsymbol{F}^{\mathrm{b}}_{\mu,\mu} + \boldsymbol{F}^{\mathrm{b}}_{\mu,\mu-1} + \boldsymbol{F}^{\mathrm{b}}_{\mu,\mu+1} \tag{D.4}$$

We can further find each of these forces as a gradient of the potential (in other words, the force can be found by determining how energy changes with bead position), namely:

$$\boldsymbol{F}^{\mathrm{b}}_{\mu,\mu} = -\frac{\partial \phi_{\mathrm{b},\mu}}{\partial \boldsymbol{r}_\mu} = -\frac{\partial \phi_{\mathrm{b},\mu}}{\partial \theta_\mu}\left\{\frac{\partial \theta_\mu}{\partial \boldsymbol{u}_\mu}\cdot\frac{\partial \boldsymbol{u}_\mu}{\partial \boldsymbol{r}_\mu} + \frac{\partial \theta_\mu}{\partial \boldsymbol{u}_{\mu-1}}\cdot\frac{\partial \boldsymbol{u}_{\mu-1}}{\partial \boldsymbol{r}_\mu}\right\} \tag{D.5a}$$

$$\boldsymbol{F}^{\mathrm{b}}_{\mu,\mu-1} = -\frac{\partial \phi_{\mathrm{b},\mu-1}}{\partial \boldsymbol{r}_\mu} = -\frac{\partial \phi_{\mathrm{b},\mu-1}}{\partial \theta_{\mu-1}}\frac{\partial \theta_{\mu-1}}{\partial \boldsymbol{u}_{\mu-1}}\cdot\frac{\partial \boldsymbol{u}_{\mu-1}}{\partial \boldsymbol{r}_\mu} \tag{D.5b}$$

$$\boldsymbol{F}^{\mathrm{b}}_{\mu,\mu+1} = -\frac{\partial \phi_{\mathrm{b},\mu+1}}{\partial \boldsymbol{r}_\mu} = -\frac{\partial \phi_{\mathrm{b},\mu+1}}{\partial \theta_{\mu+1}}\frac{\partial \theta_{\mu+1}}{\partial \boldsymbol{u}_\mu}\cdot\frac{\partial \boldsymbol{u}_\mu}{\partial \boldsymbol{r}_\mu} \tag{D.5c}$$

where expansions arise from application of the multivariate chain rule to Eq. (D.2). The task now is to derive the form of the total force given a particular potential.

Firstly we can derive the parts which do not depend on the form of the potential. We have the following results:

$$\frac{\partial \theta_\mu}{\partial \boldsymbol{u}_\mu} = \frac{\partial \arccos(\boldsymbol{u}_{\mu-1}\cdot\boldsymbol{u}_\mu)}{\partial(\boldsymbol{u}_{\mu-1}\cdot\boldsymbol{u}_\mu)}\frac{\partial(\boldsymbol{u}_{\mu-1}\cdot\boldsymbol{u}_\mu)}{\partial \boldsymbol{u}_\mu} = -\frac{1}{\sqrt{1-\cos^2\theta_\mu}}\boldsymbol{u}_{\mu-1} = -\frac{1}{\sin\theta_\mu}\boldsymbol{u}_{\mu-1} \tag{D.6a}$$

$$\frac{\partial \theta_\mu}{\partial \boldsymbol{u}_{\mu-1}} = -\frac{1}{\sin\theta_\mu}\boldsymbol{u}_\mu \tag{D.6b}$$

$$\frac{\partial \theta_{\mu-1}}{\partial \boldsymbol{u}_{\mu-1}} = -\frac{1}{\sin\theta_{\mu-1}}\boldsymbol{u}_{\mu-2} \tag{D.6c}$$

$$\frac{\partial \theta_{\mu+1}}{\partial \boldsymbol{u}_\mu} = -\frac{1}{\sin\theta_{\mu+1}}\boldsymbol{u}_{\mu+1} \tag{D.6d}$$

For the $\partial\boldsymbol{u}/\partial\boldsymbol{r}$ terms, this will give a symmetric tensor with different diagonal and cross terms. To demonstrate, consider the following derivative:

$$\frac{\partial u_{\mu,x}}{\partial r_{\mu,x}} = \frac{\partial\left[r_{\mu+1,x}-r_{\mu,x}\right]/\sqrt{(r_{\mu+1,x}-r_{\mu,x})^2+\ldots}}{\partial r_{\mu,x}} \tag{D.7a}$$

$$\frac{\partial u_{\mu,x}}{\partial r_{\mu,x}} = \frac{\partial Q_{\mu,x}/\sqrt{Q^2_{\mu,x}+\cdots}}{\partial Q_{\mu,x}}\frac{\partial Q_{\mu,x}}{\partial r_{\mu,x}} \tag{D.7b}$$

$$\frac{\partial u_{\mu,x}}{\partial r_{\mu,x}} = -1\left[\frac{1}{\sqrt{Q^2_{\mu,x}+\ldots}} - \frac{Q^2_{\mu,x}}{(Q^2_{\mu,x}+\ldots)^{3/2}}\right] \tag{D.7c}$$

$$\frac{\partial u_{\mu,x}}{\partial r_{\mu,x}} = \frac{Q^2_{\mu,x}}{Q^3_\mu} - \frac{1}{Q_\mu} = \frac{1}{Q_\mu}\left(u^2_{\mu,x}-1\right) \tag{D.7d}$$

Similarly, the cross terms can be shown to be:

$$\frac{\partial u_{\mu,x}}{\partial r_{\mu,y}} = \frac{\partial\left[r_{\mu+1,x}-r_{\mu,x}\right]/\sqrt{(r_{\mu+1,x}-r_{\mu,x})^2+(r_{\mu+1,y}-r_{\mu,y})^2+\ldots}}{\partial r_{\mu,y}} \tag{D.8a}$$

$$\frac{\partial u_{\mu,x}}{\partial r_{\mu,y}} = \frac{\partial Q_{\mu,x} / \sqrt{Q_{\mu,x}^2 + Q_{\mu,y}^2 + \cdots}}{\partial Q_{\mu,y}} \frac{\partial Q_{\mu,y}}{\partial r_{\mu,y}} \tag{D.8b}$$

$$\frac{\partial u_{\mu,x}}{\partial r_{\mu,y}} = \frac{Q_{\mu,x} Q_{\mu,y}}{Q_\mu^3} = \frac{1}{Q_\mu} \left(u_{\mu,x} u_{\mu,y} \right) \tag{D.8c}$$

Therefore, overall due to symmetry we have that:

$$\frac{\partial \boldsymbol{u}_\mu}{\partial \boldsymbol{r}_\mu} = \frac{1}{Q_\mu} \left(\boldsymbol{u}_\mu \boldsymbol{u}_\mu - \boldsymbol{\delta} \right) \tag{D.9}$$

where $\boldsymbol{\delta}$ is the diagonal unit tensor. Similarly, we can show that:

$$\frac{\partial \boldsymbol{u}_{\mu-1}}{\partial \boldsymbol{r}_\mu} = \frac{1}{Q_{\mu-1}} \left(-\boldsymbol{u}_{\mu-1} \boldsymbol{u}_{\mu-1} + \boldsymbol{\delta} \right) \tag{D.10}$$

We then evaluate the dot products in Eq. (D.5). These are as follows:

$$\begin{aligned} \frac{\partial \theta_\mu}{\partial \boldsymbol{u}_\mu} \cdot \frac{\partial \boldsymbol{u}_\mu}{\partial \boldsymbol{r}_\mu} &= -\frac{1}{\sin \theta_\mu} \frac{1}{Q_\mu} \boldsymbol{u}_{\mu-1} \cdot \left(\boldsymbol{u}_\mu \boldsymbol{u}_\mu - \boldsymbol{\delta} \right) \\ &= -\frac{1}{\sin \theta_\mu} \frac{1}{Q_\mu} \left(\cos \theta_\mu \boldsymbol{u}_\mu - \boldsymbol{u}_{\mu-1} \right) \end{aligned} \tag{D.11a}$$

$$\begin{aligned} \frac{\partial \theta_\mu}{\partial \boldsymbol{u}_{\mu-1}} \cdot \frac{\partial \boldsymbol{u}_{\mu-1}}{\partial \boldsymbol{r}_\mu} &= -\frac{1}{\sin \theta_\mu} \frac{1}{Q_{\mu-1}} \boldsymbol{u}_\mu \cdot \left(-\boldsymbol{u}_{\mu-1} \boldsymbol{u}_{\mu-1} + \boldsymbol{\delta} \right) \\ &= -\frac{1}{\sin \theta_\mu} \frac{1}{Q_{\mu-1}} \left(-\cos \theta_\mu \boldsymbol{u}_{\mu-1} + \boldsymbol{u}_\mu \right) \end{aligned} \tag{D.11b}$$

$$\begin{aligned} \frac{\partial \theta_{\mu-1}}{\partial \boldsymbol{u}_{\mu-1}} \cdot \frac{\partial \boldsymbol{u}_{\mu-1}}{\partial \boldsymbol{r}_\mu} &= -\frac{1}{\sin \theta_{\mu-1}} \frac{1}{Q_{\mu-1}} \boldsymbol{u}_{\mu-2} \cdot \left(-\boldsymbol{u}_{\mu-1} \boldsymbol{u}_{\mu-1} + \boldsymbol{\delta} \right) \\ &= -\frac{1}{\sin \theta_{\mu-1}} \frac{1}{Q_{\mu-1}} \left(-\cos \theta_{\mu-1} \boldsymbol{u}_{\mu-1} + \boldsymbol{u}_{\mu-2} \right) \end{aligned} \tag{D.11c}$$

$$\begin{aligned} \frac{\partial \theta_{\mu+1}}{\partial \boldsymbol{u}_\mu} \cdot \frac{\partial \boldsymbol{u}_\mu}{\partial \boldsymbol{r}_\mu} &= -\frac{1}{\sin \theta_{\mu+1}} \frac{1}{Q_\mu} \boldsymbol{u}_{\mu+1} \cdot \left(\boldsymbol{u}_\mu \boldsymbol{u}_\mu - \boldsymbol{\delta} \right) \\ &= -\frac{1}{\sin \theta_{\mu+1}} \frac{1}{Q_\mu} \left(\cos \theta_{\mu+1} \boldsymbol{u}_\mu - \boldsymbol{u}_{\mu+1} \right) \end{aligned} \tag{D.11d}$$

Therefore, in general we have that:

$$\boldsymbol{F}_\mu^{\mathrm{b}} = \boldsymbol{F}_{\mu,\mu}^{\mathrm{b}} + \boldsymbol{F}_{\mu,\mu-1}^{\mathrm{b}} + \boldsymbol{F}_{\mu,\mu+1}^{\mathrm{b}} \tag{D.12a}$$

$$\boldsymbol{F}_{\mu}^{\mathrm{b}} = \frac{\partial \phi_{\mathrm{b},\mu}}{\partial \theta_{\mu}} \frac{1}{\sin\theta_{\mu}} \left[\frac{1}{Q_{\mu}} \left(\cos\theta_{\mu} \boldsymbol{u}_{\mu} - \boldsymbol{u}_{\mu-1} \right) + \frac{1}{Q_{\mu-1}} \left(-\cos\theta_{\mu} \boldsymbol{u}_{\mu-1} + \boldsymbol{u}_{\mu} \right) \right] + \frac{\partial \phi_{\mathrm{b},\mu-1}}{\partial \theta_{\mu-1}} \frac{1}{\sin\theta_{\mu-1}} \left[\frac{1}{Q_{\mu-1}} \left(-\cos\theta_{\mu-1} \boldsymbol{u}_{\mu-1} + \boldsymbol{u}_{\mu-2} \right) \right] + \frac{\partial \phi_{\mathrm{b},\mu+1}}{\partial \theta_{\mu+1}} \frac{1}{\sin\theta_{\mu+1}} \left[\frac{1}{Q_{\mu}} \left(\cos\theta_{\mu+1} \boldsymbol{u}_{\mu} - \boldsymbol{u}_{\mu+1} \right) \right] \tag{D.12b}$$

For our particular form of the bending potential detailed in Eq. (D.1), we can see that:

$$-\frac{\partial \phi_{\mathrm{b},i}}{\partial \theta_i} = -k_{\mathrm{B}} T C \sin\theta_i \tag{D.13}$$

Therefore, we can see that the sin terms will cancel in Eq. (D.11), and we are left with the following equation for the force on bead μ:

$$\frac{\boldsymbol{F}_{\mu}^{\mathrm{b}}}{k_{\mathrm{B}} T C} = \left[\frac{1}{Q_{\mu}} \left(\cos\theta_{\mu} \boldsymbol{u}_{\mu} - \boldsymbol{u}_{\mu-1} \right) + \frac{1}{Q_{\mu-1}} \left(-\cos\theta_{\mu} \boldsymbol{u}_{\mu-1} + \boldsymbol{u}_{\mu} \right) \right] + \left[\frac{1}{Q_{\mu-1}} \left(-\cos\theta_{\mu-1} \boldsymbol{u}_{\mu-1} + \boldsymbol{u}_{\mu-2} \right) \right] + \left[\frac{1}{Q_{\mu}} \left(\cos\theta_{\mu+1} \boldsymbol{u}_{\mu} - \boldsymbol{u}_{\mu+1} \right) \right] \tag{D.14}$$

which is nearly, but not quite the same as Saadat and Khomami's expression. The difference arises in our $-\cos\theta_{\mu-1}\boldsymbol{u}_{\mu-1}$ term, which is positive in Saadat and Khomami's expression [18]. Given the subsequent comprehensive tests, it seems very likely that Saadat and Khomami's expression has a typographical error, and the above expression is correct.

D.2 Alternate forms of bending potential

One alternate form of the bending potential is described by Yamakawa [49] as a discrete analogue of the wormlike chain for a bead-rod model. In this case, the bending potential is given as:

$$\phi_{\mathrm{b},\mu} = \frac{\alpha}{2} \theta_{\mu}^2 \tag{D.15}$$

where α is the bending force constant, which in this case is dimensional unlike the previous definition of C in Eq. (D.1). This follows from the definition of the bending energy in the continuous WLC as $U = 1/2\alpha[\partial \boldsymbol{u}(s)/\partial s]^2$, where $\boldsymbol{u}(s)$ is the chain contour as a function of path length s. However, in this case the stiffness parameter λ^{-1} (twice the persistence length)

is defined as:

$$\lambda^{-1} = l\frac{1+\langle\cos\theta\rangle}{1-\langle\cos\theta\rangle} \tag{D.16}$$

where l is the rod length and:

$$\langle\cos\theta\rangle = \int_0^\pi e^{-\alpha\theta^2/2k_\mathrm{B}T}\cos\theta\sin\theta d\theta / \int_0^\pi e^{-\alpha\theta^2/2k_\mathrm{B}T}\sin\theta d\theta \tag{D.17}$$

This integral should be evaluated numerically to give λ as a function of α, or alternatively one can solve for α given a particular persistence length. It's unclear whether the same chain statistics would be obtained if the earlier form of the bending potential given in Eq. (D.1) was used, with the same persistence length given by the $\cos\theta$ averages.

D.3 Updating semi-implicit scheme to use bending potential

Here I want to highlight the changes made to the semi-implicit scheme so that it works with the bending potential. We follow Prakash and Prabhakar's paper [53], which the code reproduces. This begins with the following overall stochastic differential equation:

$$\mathrm{d}\boldsymbol{R} = \left[\boldsymbol{K}\cdot\boldsymbol{R} + \frac{1}{4}\boldsymbol{D}\cdot\boldsymbol{F}^\phi\right]\mathrm{d}t^* + \frac{1}{\sqrt{2}}\boldsymbol{B}\cdot\mathrm{d}\boldsymbol{W} \tag{D.18}$$

where $\boldsymbol{K}$ is a block matrix of flow field tensors, $\boldsymbol{R}$ is the position vector block matrix, $\boldsymbol{D}$ is the diffusion tensor block matrix, $\boldsymbol{F}^\phi$ is the total force on each bead due to potentials, $\boldsymbol{B}$ is a block matrix such that $\boldsymbol{B} = \boldsymbol{D}\cdot\boldsymbol{D}^\mathrm{T}$, and $d\boldsymbol{W}$ is a block matrix describing a random Weiner process. In general, $\boldsymbol{F}^\phi$ can be split into spring forces, $\boldsymbol{F}^\mathrm{s}$, and other forces, which may be excluded volume, bending or torsional potentials, external forces etc. We'll denote these other forces by $\boldsymbol{F}^\mathrm{O}$. Now in step 1 of the semi-implicit solution, we get a halfway step of the position vectors as follows:

$$\tilde{\boldsymbol{R}}_{n+1} = \boldsymbol{R}_n + \left[\boldsymbol{K}\cdot\boldsymbol{R}_n + \frac{1}{4}\boldsymbol{D}_n\cdot\boldsymbol{F}_n^\mathrm{S} + \frac{1}{4}\boldsymbol{D}_n\cdot\boldsymbol{F}_n^\mathrm{O}\right]\Delta t^* + \frac{1}{\sqrt{2}}\Delta\boldsymbol{S}_n \tag{D.19}$$

Where we have replaced $\boldsymbol{F}_n^\mathrm{E}$ in the original by $\boldsymbol{F}_n^\mathrm{O}$ to denote the additional bending potential forces, rather than simply the excluded volume forces. The basic principle is then to construct a semi-implicit solution to this equation, where we must construct the following term made up of all the explicit parts of the equation:

$$\tilde{\boldsymbol{\Upsilon}}_{n+1} = \boldsymbol{R}_n + \left[\frac{1}{2}\left\{\boldsymbol{K}\cdot\boldsymbol{R}_n + \boldsymbol{K}\cdot\tilde{\boldsymbol{R}}_{n+1}\right\} + \frac{1}{8}\boldsymbol{D}_n\cdot\boldsymbol{F}_n^\mathrm{S} + \frac{1}{8}\boldsymbol{D}_n\cdot\left\{\boldsymbol{F}_n^\mathrm{O} + \tilde{\boldsymbol{F}}_{n+1}^\mathrm{O}\right\}\right]\Delta t^* + \frac{1}{\sqrt{2}}\Delta\boldsymbol{S}_n \tag{D.20}$$

Previously, the code was using the total force $\boldsymbol{F}^\phi$ for the $1/8\boldsymbol{D}_n\cdot\boldsymbol{F}_n^\mathrm{S}$ and $1/8\boldsymbol{D}_n\cdot\boldsymbol{F}_n^\mathrm{E}$ parts, but was not adding in the additional contribution from the bending potential to the predictor

step contribution $1/8\boldsymbol{D}_n \cdot \tilde{\boldsymbol{F}}^{\mathrm{O}}_{n+1}$. Once this was added in, the bending potential seems to be working correctly!

D.4 Tests to check code

Here I'll list the tests I've written to check that the code works. These are divided into two sections. The unit tests basically check some edge cases for the bending potential function itself and ensure the results for some low-bead cases are what we expect, while the validation tests essentially check that the average angles match the expected distribution for an actual BD simulation.

D.4.1 Unit tests

1. The force is zero for the two-bead case

   This one is straightforward, for the $N_{\mathrm{beads}} = 2$ case there are no bending potentials and hence we should get zero bending force.

2. No bending potential gives no force

   Also straightforward, I have an option for no bending potential.

3. The force should be zero when the beads are co-linear

   When the beads are co-linear, we have that all $\theta = \pi$, meaning that the potential should be zero and there should be no force. This is implemented by a chain of 5 beads arranged along the x-axis, then checking the force is zero.

4. For a 3-bead chain, we should be able to check the forces by hand

   Here I'm running two tests. The first is with the three beads, with the two connector vectors perpendicular to each other:

   $$\begin{aligned}\boldsymbol{r}_1 &= \{0, 1, 0\}\\ \boldsymbol{r}_2 &= \{0, 0, 0\}\\ \boldsymbol{r}_3 &= \{1, 0, 0\}\end{aligned}$$

   which for a $1 - \cos(\theta)$ bending potential, should give the forces (as per Eq. (D.14)):

   $$\begin{aligned}\boldsymbol{F}_1 &= \{-1, 0, 0\}\\ \boldsymbol{F}_2 &= \{1, 1, 0\}\\ \boldsymbol{F}_3 &= \{0, -1, 0\}\end{aligned}$$

Note that these forces are aligned such that the force vector is perpendicular to the connector unit vector $\boldsymbol{u}$ for the end beads. This is generally true for the end-beads of a chain, since this direction of movement gives the fastest rate of change of the angle, and hence is the line of steepest decent for the bending potential (which defines the direction of the force).

I'll also test a second case with the connector vectors 30° apart:

$$\begin{aligned}\boldsymbol{r}_1 &= \{-\sqrt{3}/2, 1/2, 0\}\\ \boldsymbol{r}_2 &= \{0, 0, 0\}\\ \boldsymbol{r}_3 &= \{1, 0, 0\}\end{aligned}$$

which for a $1 - \cos(\theta)$ bending potential, should give the forces (as per Eq. (D.14)):

$$\begin{aligned}\boldsymbol{F}_1 &= \{-1/4, -\sqrt{3}/4, 0\}\\ \boldsymbol{F}_2 &= \{1/4, (2+\sqrt{3})/4, 0\}\\ \boldsymbol{F}_3 &= \{0, -1/2, 0\}\end{aligned}$$

Once again, the end bead forces are perpendicular to the connector vector. This also provides a reasonable test of the final bead force equation, since we can compare our geometric intuition with the algebraic equation.

5. For a 4-bead chain, we can compare a simple case with the calculated result

   We have the following bead positions:

$$\begin{aligned}\boldsymbol{r}_1 &= \{0, 0, 0\}\\ \boldsymbol{r}_2 &= \{1, 0, 0\}\\ \boldsymbol{r}_3 &= \{1, -1, 0\}\\ \boldsymbol{r}_4 &= \{1+\sqrt{2}/2, -1+\sqrt{2}/2, 0\}\end{aligned}$$

   This is the same as the following diagram, where all connector vector lengths are equal to 1:

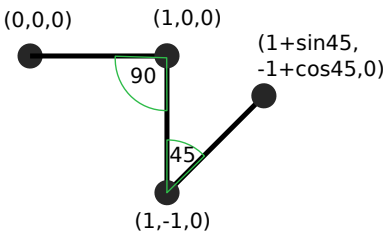

which for a $1-\cos(\theta)$ bending potential, should give the forces (as per Eq. (D.14)):

$$\begin{aligned}
\boldsymbol{F}_1 &= \{0, 1, 0\} \\
\boldsymbol{F}_2 &= \{-1-\sqrt{2}/2, -1, 0\} \\
\boldsymbol{F}_3 &= \{(1+\sqrt{2})/2, 1/2, 0\} \\
\boldsymbol{F}_4 &= \{1/2, -(2+\sqrt{2})/2, 0\}
\end{aligned}$$

6. For a 5-bead chain, we can compare a simple case with the calculated result

   We have the following bead positions:

$$\begin{aligned}
\boldsymbol{r}_1 &= \{0, 0, 0\} \\
\boldsymbol{r}_2 &= \{\sqrt{2}/2, \sqrt{2}/2, 0\} \\
\boldsymbol{r}_3 &= \{\sqrt{2}/2+1, \sqrt{2}/2, 0\} \\
\boldsymbol{r}_4 &= \{\sqrt{2}/2+1+\sqrt{3}/2, \sqrt{2}/2+1/2, 0\} \\
\boldsymbol{r}_5 &= \{\sqrt{2}/2+1+\sqrt{3}, \sqrt{2}/2, 0\}
\end{aligned}$$

   This is the same as the following diagram, where all connector vector lengths are equal to 1:

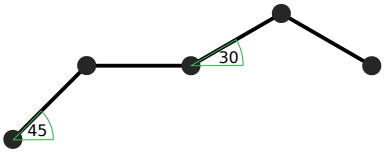

   which for a $1-\cos(\theta)$ bending potential, should give the forces (as per Eq. (D.14)):

$$\begin{aligned}
\boldsymbol{F}_1 &= \{-1/2, 1/2, 0\} \\
\boldsymbol{F}_2 &= \{1/2, -\sqrt{2}/2-1, 0\} \\
\boldsymbol{F}_3 &= \{-1/4-\sqrt{3}/4, 5/4+\sqrt{3}/4+\sqrt{2}/2, 0\} \\
\boldsymbol{F}_4 &= \{1/4, -3/2-\sqrt{3}/4, 0\} \\
\boldsymbol{F}_5 &= \{\sqrt{3}/4, 3/4, 0\}
\end{aligned}$$

7. Finally, a randomly generated initial condition and result was created on MATLAB, and then checked against the Fortran result as an additional check for both 4-bead and 5-bead cases. This should cover > 5 bead cases as well, as we only want to check inner beads.

D.4.2 Validation tests

1. Compare with expected vector-vector correlation for a wormlike chain

This one is straightforward, for the $N_{\text{beads}} = 2$ case there are no bending potentials and hence we should get zero bending force.

2. For a Rouse chain with bending potential, compare with analytical result for angular distribution

   In general we can express the angular distribution as the sum of the spring force law and the bending potential:

$$\phi = \frac{1}{2}H \sum_{k}^{N-1} \boldsymbol{Q}_k^2 + \sum_{k}^{N-2} C(1 - \boldsymbol{u}_k \cdot \boldsymbol{u}_{k+1}) \tag{D.21}$$

   This would mean that we can write out the equilibrium configurational distribution function as:

$$\psi_{\text{eq}}(\boldsymbol{Q}^{N-1}) = \frac{e^{-\phi/k_{\text{B}}T}}{\int e^{-\phi/k_{\text{B}}T} d\boldsymbol{Q}^{N-1}} \tag{D.22}$$

   So that then we have the following integral for a 3-bead chain:

$$\int\int\int\int e^{-H/2k_{\text{B}}TQ_1^2 \boldsymbol{u}_1\cdot\boldsymbol{u}_1} e^{-H/2k_{\text{B}}TQ_2^2 \boldsymbol{u}_2\cdot\boldsymbol{u}_2} e^{-C/k_{\text{B}}T(1-\boldsymbol{u}_1\cdot\boldsymbol{u}_2)} dQ_1 dQ_2 d\boldsymbol{u}_1 d\boldsymbol{u}_2 \tag{D.23}$$

   There are two things we can do to simplify this equation. Firstly, we note that $\boldsymbol{u}_i \cdot \boldsymbol{u}_i = 1$, since the dot product of a unit vector with itself must be the scalar 1. This allows us to separate the spring integral parts of the expression from the part which depends upon the angle between the beads. This is in general true as long as the spring force law depends purely upon the spring length and not orientation. The second simplification is to orient our co-ordinate system along $\boldsymbol{u}_1$, such that $\theta \equiv \boldsymbol{u}_1 \cdot \boldsymbol{u}_2$ is the polar angle in spherical co-ordinates. The result is that when we take an average which depends only on the angle θ between the springs, we can greatly simplify the resulting expression:

$$\langle \cos\theta \rangle = \frac{\int_{Q_1}\int_{Q_2} e^{-H/2k_{\text{B}}T(Q_1^2+Q_2^2)} dQ_1 dQ_2 \int_\theta \int_\beta \cos\theta e^{-\phi_{\text{b}}/k_{\text{B}}T} d\theta d\beta}{\int_{Q_1}\int_{Q_2} e^{-H/2k_{\text{B}}T(Q_1^2+Q_2^2)} dQ_1 dQ_2 \int_\theta \int_\beta e^{-\phi_{\text{b}}/k_{\text{B}}T} d\theta d\beta} \tag{D.24}$$

$$= \frac{\int_\theta \sin\theta\cos\theta e^{-\phi_{\text{b}}/k_{\text{B}}T} d\theta}{\int_\theta \sin\theta e^{-\phi_{\text{b}}/k_{\text{B}}T} d\theta} \tag{D.25}$$

   where β is the azimuthal angle and θ runs from 0 to π. For our current bending potential of $\phi_{\text{b}}/k_{\text{B}}T = C(1 - \cos\theta)$, we have that:

$$\langle \cos\theta \rangle = \frac{-1 + C + (C+1)\, e^{-2C}}{C\,(1 - e^{-2C})} \tag{D.26}$$

$$= -\frac{1}{C} + \coth(C) \tag{D.27}$$

   and also that:

$$\langle \cos^2\theta \rangle = \frac{2e^{-C}\left[(C^2+2)\sinh C - 2C\cosh C\right]}{C^2(1 - e^{-2C})} \tag{D.28}$$

Furthermore, we can integrate out the other factors to obtain the distribution in θ, which gives us:

$$\psi_{eq}(\theta) = \frac{\sin\theta e^{-\phi_b/k_BT}}{\int_\theta \sin\theta e^{-\phi_b/k_BT} d\theta} = \left[\frac{C}{1-e^{-2C}}\right] \sin\theta e^{-\frac{C}{k_BT}(1-\cos\theta)} \tag{D.29}$$

Therefore, we should expect the distribution of angles for our trimer at equilibrium to follow this distribution.

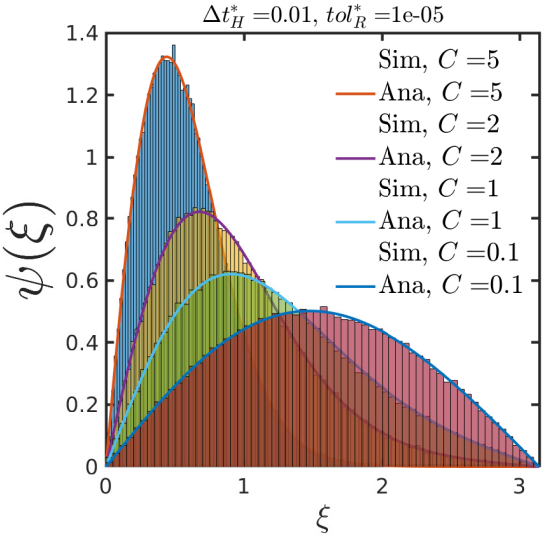

FIGURE D.1: Comparison of analytical and simulated bending angles ξ against bending stiffness value C.

Fig. D.1 gives an example of this correct distribution function. Additionally, we can see from Fig. D.2 that for a 10-bead chain with HI and a FENE-Fraenkel spring potential ($H_R^* = 200$, $\delta Q_R^* = 0.1$), the average bending angle still follows exactly the same distribution.

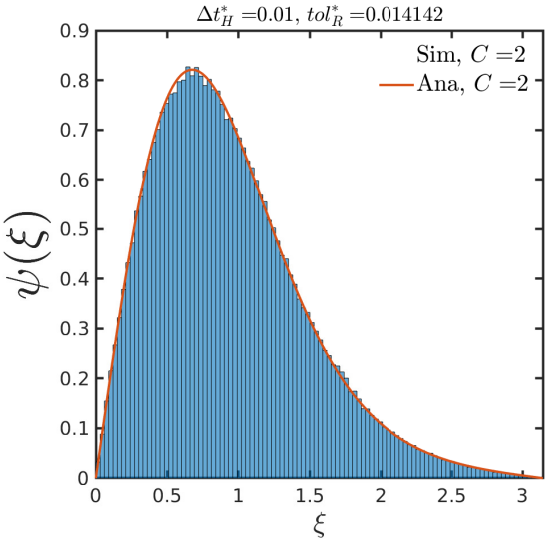

FIGURE D.2: FENE-Frankel spring 10-bead chain with HI and a bending potential. FENE-Fraenkel spring parameters are $H_R^* = 200$, $\delta Q_R^* = 0.1$.

Appendix E

Implementing Cholesky Decomposition into Single-Chain Code

E.1 Discrepancy at Equilibrium with HI

As previously discussed, Brownian dynamics simulations with hydrodynamic interactions require taking the square root of the diffusion matrix $\boldsymbol{D}$, which is then dotted with the random force to recover the correct behaviour. If this is done correctly, with a carefully chosen diffusion tensor (such that it is positive-semidefinite [13]) and an accurate method for taking the tensor square root, the equilibrium static properties of a polymer chain should be unaffected by the presence and magnitude of Hydrodynamic interactions. However, in the course of simulations with the single-chain code, some small discrepancies were noticed. For example, the equilibrium radius of gyration of a 20-bead chain was found to be incorrect when HI was turned on, irrespective of the timestep, as seen in Figure E.1. The distribution functions for a very simple system, a Hookean trumbbell (3 beads, 2 Hookean springs, no EV, no bending potential) were examined for different values of h^*.

E.2 Implementation of Cholesky Decomposition

Previously, the code used Fixman's approximation method [105] for the square root of the diffusion tensor, as it has $\approx N^{2.25}$ scaling as opposed to N^3 scaling for Cholesky decomposition of a matrix. However, it is of course an approximate method, so in order to test whether this approximation was causing the discrepancies, a Cholesky decomposition was implemented into

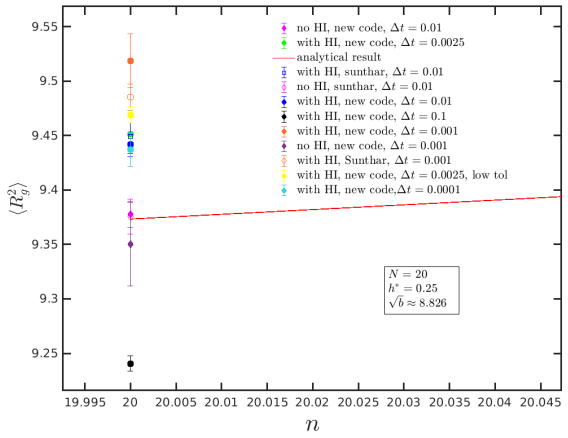

FIGURE E.1: When HI is turned on, the radius of gyration for a 20-bead FENE chain (with no EV) is incorrect irrespective of timestep. This is compared with a previous version of the code, in order to show that this has not been recently introduced.

the code with a toggle to choose either method while running. For testing purposes, the entire treatment of HI in the Fortran code was re-implimented in MATLAB, with unit tests written in Fortran (for the diffusion matrices and d$\boldsymbol{S}$ terms) to ensure exact equivalence to machine precision.

As previously discussed, in the code the 4th-order diffusion tensor is represented as a $3N \times 3N$ block matrix, and it is required to find the term:

$$\mathrm{d}\boldsymbol{S} = \boldsymbol{B} \cdot \mathrm{d}\boldsymbol{W} \tag{E.1}$$

where d$\boldsymbol{W}$ is an (approximately) Gaussian random vector represented as a matrix of size $3N$, and $\boldsymbol{B}$ is given by:

$$\boldsymbol{D} = \boldsymbol{B} \cdot \boldsymbol{B}^{\intercal} \tag{E.2}$$

Or perhaps more insightfully, as expressed by Hsieh et al. [52]:

$$\mathrm{d}\underline{\mathcal{S}}_i = \sum_{j=1}^{i} \underline{\underline{\mathcal{B}}}_{ij} \cdot \mathrm{d}\underline{\mathcal{W}}_j \tag{E.3}$$

$$\underline{\underline{\mathcal{D}}}_{ij} = \sum_{l=1}^{N} \underline{\underline{\mathcal{B}}}_{il} \cdot \underline{\underline{\mathcal{B}}}^{\intercal}_{jl} \tag{E.4}$$

where here we have re-expressed the 4th-order tensors such that $\underline{\underline{\mathcal{A}}}_{ij}$ is essentially itself a 2nd-order tensor, namely the i,j-th block of the 4th-order tensor $\boldsymbol{A}$. Note that Equation E.2 and Equation E.4 are exactly the same equation with two different representations of the underlying matrix, provided for the purpose of showing that the decomposition of the block matrix $\boldsymbol{D}$ does in fact give the correct block matrix $\boldsymbol{B}$ such that the block vector d$\boldsymbol{S}$ is correctly specified in Equation E.1. Computing this matrix is then very straightforward with

a LAPACK implementation of a Cholesky decomposition, which gives the matrix $\boldsymbol{B}$ directly from $\boldsymbol{D}$.

However, one must still be careful with the matrix ordering and transpositions. Explicitly, if $\boldsymbol{D}$ is expressed as an upper-diagonal block matrix, the following subroutine correctly calculates d$\boldsymbol{S}$:

```
subroutine get_delS_cholesky(Nbeads, &
    Diffusion_sup, delts, Dels)
  Integer, intent(in) :: Nbeads
  Real (DBprec), intent(in) :: diffusion_sup(:,:,:,:)
  Real (DBprec), intent(in) :: delts
  Real (DBprec), intent(out) :: Dels(:,:)

  Real (DBprec) :: X_0(Ndim, Nbeads)
  Real (DBprec) :: chol_matrix(Ndim,Nbeads,Ndim,Nbeads)
  Integer :: Ndof, lda, info

  external :: dpotrf, dgemv

  Ndof = Ndim*Nbeads
  lda = Ndof

  DelS = 0.d0
  !Generate the random vector X_0

  X_0 = 0.d0
  Call ran_1(Ndof, X_0)
  X_0 = X_0 - 0.5d0
  X_0 = (X_0*X_0*C5 + C6)*X_0

  If (Hstar.Gt.0) Then
    ! get the cholesky factorisation
    chol_matrix = diffusion_sup
    call dpotrf('U', Ndof, chol_matrix, lda, INFO)

    alpha = 1.D0
    beta = 0.D0

    ! multiply lower cholesky matrix by dW
```

```
    call dgemv('t', Ndof, Ndof, alpha,chol_matrix, &
    lda, X_0,incx,beta,delS,incy)
  else
    DelS = X_0
  end if

  DelS = DelS * sqrt(delts)

end subroutine
```

where diffusion_sup ($\boldsymbol{D}$) has the same dimension as chol_matrix ($\boldsymbol{B}$), X_0 (d$\boldsymbol{W}$) is a random, appoximately Gaussian block vector, and delts (Δt) is required to correctly scale d$\boldsymbol{S}$. Note that the Cholesky block matrix, as calculate here, must be transposed before multiplication by d$\boldsymbol{W}$, otherwise Equation E.1 will not be properly satisfied. As a final check, the computed block matrices satisfy Equations E.1-E.4.

E.3 Chebyshev approximation description

Here we show how the Chebyshev polynomial approximation can be made more accurate by essentially including more terms in the approximation at certain points in the simulation, if very high accuracy is desired.

E.3.1 Notes on Chebyshev Polynomial Approximation

The following is largely a transcription of unpublished notes originally written by Prabhakar Ranganathan on the Chebyshev approximation for Brownian Dynamics simulations - they are not the work of the current author (besides several additions and clarifications), but are reproduced here so as to elucidate the underlying theory.

For every real function $f(x)$ defined over $x \in [-1, 1]$, the Chebyshev polynomial approximation of $f(x)$ is:

$$f(x) \approx f_a(x) = -\frac{C_0}{2} + \sum_{p=0}^{N_T-1} C_p T_p(x), \qquad N_T \geq 1 \tag{E.5}$$

where $T_p(x)$ is a Chebyshev polynomial of index p and C_p are the Chebyshev coefficients for $f(x)$ determined from:

$$C_0 = \frac{2}{N_T} \sum_{k=1}^{N_T} f(x_k) = \frac{2}{N_T} \sum_{k=1}^{N_T} f(x_k) T_0(x_k) \tag{E.6}$$

$$C_p = \frac{2}{N_T} \sum_{k=1}^{N_T} f(x_k) T_p(x_k), \qquad 1 \leq p \leq N_T - 1 \tag{E.7}$$

Here $x_k, k = 1, \cdots, N_T$ are the zeros of T_{N_T}. For any index m, the zeros of $T_m(x)$ are given as:

$$x_k = \cos\left[\frac{\pi(k - 1/2)}{m}\right], \qquad 1 \leq k \leq m \tag{E.8}$$

For any given x, the value of $T_m(x)$ can be generated using the recurrence relation:

$$T_m(x) = 2xT_{m-1}(x) - T_{m-2}(x) \tag{E.9}$$

with $T_0(x) = 1$ and $T_1(x) = x$. Note that such recurrence relations are available for all series of orthogonal polynomials. Given this, let us now outline the rationale behind the approximation of the square root functions given the previous relations, and then describe the specific method for doing so.

Let us say we choose N_T as some very large number. Then we must approximate $f(x)$ as:

$$f(x) \cong \sum_{p=0}^{N_T - 1} C_p T_p(x) - \frac{C_0}{2} \tag{E.10}$$

Because of the large N, we can assume that the approximation is very good. Instead of the above, we may choose to truncate the summation and write:

$$f(x) \approx \sum_{p=0}^{m} C_p T_p(x) - \frac{C_0}{2}, \qquad m < N_T - 1 \tag{E.11}$$

The error between the two expressions is of course:

$$\epsilon(x) = \sum_{p=m+1}^{N_T - 1} C_p T_p(x) \tag{E.12}$$

But all the $T_p(x)$ are bounded between -1 and $+1$ and therefore $\epsilon(x)$ oscillates. In fact the maximum value it can possibly have is:

$$\sum_{p=m+1}^{N_T - 1} C_p \tag{E.13}$$

Typically, C_p's decrease rapidly with p, and the error is dominated by $C_{m+1}T_{m+1}(x)$. If m itself is large then the r.m.s. error goes as $\|C_{m+1}[T_{m+1}(x)]\|$, which is in fact nearly uniform across the whole domain of x.

If we then have some function $f(y)$ defined over $y \in [y_{\min}, y_{\max}]$, then we set:

$$y(x) = y_{\min} + \frac{x+1}{2}(y_{\max} - y_{\min}) \tag{E.14}$$

$$= \frac{1}{2}(y_{\max} + y_{\min}) + \frac{x}{2}(y_{\max} - y_{\min}) \tag{E.15}$$

or for a given y, we can find x as:

$$x = 2\left(\frac{y - y_{\min}}{y_{\max} - y_{\min}}\right) - 1 \tag{E.16}$$

$$= \frac{2y}{y_{\max} - y_{\min}} - \left(\frac{y_{\max} + y_{\min}}{y_{\max} - y_{\min}}\right) \tag{E.17}$$

So to approximate $f(y)$, we first calculate x and then approximate as before. To calculate the C_p's, we first calculate the x_k's, transform them to y_k's and then calculate $f(y_k)$'s.

Consider the function $f(y) = \sqrt{y}$ in $y \in [y_{\min}, y_{\max}]$. Then for some N_T:

$$x_k = \cos\left[\frac{\pi(k - 1/2)}{m}\right], \qquad 1 \le k \le m \tag{E.18}$$

$$y_k = \frac{1}{2}(y_{\max} + y_{\min}) + \frac{x_k}{2}(y_{\max} - y_{\min}) \tag{E.19}$$

$$C_0 = \frac{2}{N_T}\sum_{k=1}^{N_T}\sqrt{y} \tag{E.20}$$

$$C_p = \frac{2}{N_T}\sum_{k=1}^{N_T}\sqrt{y}T_p(x_k), \qquad p = 0, \cdots, N_T - 1 \tag{E.21}$$

$$T_p(x_k) = 2x_kT_{p-1}(x_k) - T_{p-2}(x_k) \tag{E.22}$$

$$T_1(x_k) = x_k, \qquad T_0(x_k) = 1 \tag{E.23}$$

$$\sqrt{y} \approx \sum_{p=0}^{N_T-1} C_pT_p(x_k) - \frac{C_0}{2} \tag{E.24}$$

where

$$x = \frac{2y}{y_{\max} - y_{\min}} - \left(\frac{y_{\max} + y_{\min}}{y_{\max} - y_{\min}}\right) \tag{E.25}$$

So we have developed a procedure for approximating the square root of a variable using Chebyshev polynomials.

We now turn to approximating the matrix square root of $\boldsymbol{D}$, which we denote as $\boldsymbol{B} = \sqrt{\boldsymbol{D}}$. Note that the matrix square root can be determined exactly from the eigenvalues and eigenvectors of $\boldsymbol{D}$, which we denote as λ_k and $\boldsymbol{v}_k$ respectively. The matrix $\boldsymbol{D}$ is given by the spectral

representation:

$$\boldsymbol{D} = \sum_{k=1}^{3N} \lambda_k \boldsymbol{v}_k \boldsymbol{v}_k \tag{E.26}$$

and if $\boldsymbol{D}$ is positive-definite, then λ_k are all finite and positive, so $\boldsymbol{B} = \sqrt{\boldsymbol{D}}$ exists and is given by:

$$\boldsymbol{B} = \sum_{k=1}^{3N} \lambda_k^{1/2} \boldsymbol{v}_k \boldsymbol{v}_k \tag{E.27}$$

We can then give a polynomial approximation (which will be Chebyshev polynomials) for the square root of eigenvalue λ, which we denote $b(\lambda)$:

$$b = \sum_{p=0}^{N_T} a_p T_p(\lambda) \tag{E.28}$$

where a_p are our polynomial coefficients, equivalent to C_p for Chebyshev polynomials, while T_p are the polynomials themselves. Since the eigenvectors of a matrix $\boldsymbol{B}$ are also eigenvectors of a polynomial $T(\boldsymbol{B})$ of that matrix, and furthermore that the eigenvalues of the polynomial are $T(\lambda)$, we can see that the if the same polynomial coefficients are used for each λ_k, we must have that:

$$\boldsymbol{B} \cong \sum_{k=1}^{3N} b(\lambda_k) \boldsymbol{v}_k \boldsymbol{v}_k \tag{E.29}$$

or alternatively, that we can write the approximation as powers of $\boldsymbol{D}$:

$$\boldsymbol{B} \sum_{p=0}^{N_T} a_p T_p(\boldsymbol{D}) \tag{E.30}$$

In other words, we see that developing an approximation for a square root function of a matrix is essentially equivalent to developing an approximation for the scalar eigenvalues, so we can use the same machinery as was developed for scalar functions. Additionally, the range of the 'function' is given by the range of the eigenvalues of $\boldsymbol{D}$, which we use to shift the Chebyshev polynomials.

We first calculate $\boldsymbol{x}$, which is a tensor of the same order as $\boldsymbol{D}$ corresponding to our previous scalar x:

$$\boldsymbol{x} = \frac{2}{d_{\max} - d_{\min}} \boldsymbol{D} - \left(\frac{d_{\max} + d_{\min}}{d_{\max} - d_{\min}} \right) \boldsymbol{\delta} \tag{E.31}$$

where $\boldsymbol{\delta}$ is the unit tensor. Here the eigenvalues of $\boldsymbol{D}$ (which must be positive-definite) must lie between $d_{\min}$ and $d_{\max}$. Then:

$$\sqrt{\boldsymbol{D}} \cong \sum_{p=0}^{N_T - 1} C_p \boldsymbol{T}_p(\boldsymbol{x}) - C_0 \boldsymbol{\delta} \tag{E.32}$$

and C_p are calculated as in the scalar square-root example before. In fact we are actually interested in the vector:

$$\boldsymbol{S} = \sqrt{\boldsymbol{D}} \cdot \boldsymbol{W} \tag{E.33}$$

where $\boldsymbol{S}$ and $\boldsymbol{W}$ are our d$\boldsymbol{S}$ and d$\boldsymbol{W}$ from the stochastic differential equation. We then identify that:

$$\boldsymbol{S} \cong \sum_{p=0}^{N_T-1} C_p \boldsymbol{V}_p(\boldsymbol{x}) - C_0 \boldsymbol{\delta} \tag{E.34}$$

where

$$\boldsymbol{V}_p(\boldsymbol{x}) = \boldsymbol{T}_p(\boldsymbol{x}) \cdot \boldsymbol{W} \tag{E.35}$$

since

$$\boldsymbol{T}_p(\boldsymbol{x}) = 2\boldsymbol{x} \cdot \boldsymbol{T}_{p-1}(\boldsymbol{x}) - \boldsymbol{T}_{p-2}(\boldsymbol{x}) \tag{E.36}$$

with

$$\boldsymbol{T}_0(\boldsymbol{x}) = \boldsymbol{\delta}, \qquad \boldsymbol{T}_1(\boldsymbol{x}) = \boldsymbol{x} \tag{E.37}$$

we must have

$$\boldsymbol{V}_p = 2\boldsymbol{x} \cdot \boldsymbol{V}_{p-1} - \boldsymbol{V}_{p-2} \tag{E.38}$$

$$\boldsymbol{V}_0 = \boldsymbol{W}, \qquad \boldsymbol{V}_1 = \boldsymbol{x} \cdot \boldsymbol{W} \tag{E.39}$$

The computational cost now only scales as $N_T N^2$ where $\boldsymbol{D}$ is an $N \times N$ matrix. Fixman showed that N_T scales as $(d_{\max}/d_{\min})^{1/2}$ if roughly constant relative error is desired [105]. We choose:

$$N_T = \text{int}\left\{ \left[\frac{d_{\max}}{d_{\min}} \right]^{1/2} \right\} + 1 \tag{E.40}$$

For polymer simulations, near equilibrium:

$$\frac{d_{\max}}{d_{\min}} \sim \frac{\lambda_{\max}}{\lambda_{\min}} \sim N^{1/2} \tag{E.41}$$

where $\lambda_{\max}$ and $\lambda_{\min}$ are the maximum and minimum eigenvalues of the mobility matrix $\boldsymbol{D}$. When chains are stretched, we expect:

$$\frac{d_{\max}}{d_{\min}} \sim \frac{\lambda_{\max}}{\lambda_{\min}} \sim N \tag{E.42}$$

Therefore, the computational cost for the Chebyshev approximation scales as $N^{2.25}$ to $N^{2.5}$, less than the Cholesky decomposition which scales as N^3. Instead of calculating the exact

eigenvalues $\lambda_{\max}$ and $\lambda_{\min}$, we instead use Fixman's suggestion:

$$d_{\max} = \frac{2}{N}\boldsymbol{D} : \boldsymbol{u}^{+}\boldsymbol{u}^{+} \tag{E.43}$$

$$d_{\min} = \frac{1}{2N}\boldsymbol{D} : \boldsymbol{u}^{-}\boldsymbol{u}^{-} \tag{E.44}$$

where $\boldsymbol{u}^{+}$ is a $3N$ vector with all components equal to $+1$, and $\boldsymbol{u}^{-}$ is a similar vector with alternating $+1$ and -1 components, repetitively starting with $+1$. The intuitive reasoning for the vectors $\boldsymbol{u}^{+}$ and $\boldsymbol{u}^{-}$ is that the maximum eigenvalue for $\boldsymbol{D}$ arises when the chain is diffusing fastest, i.e. we have fully cooperative motion of segments ($\boldsymbol{u}^{+}$), while the minimum eigenvalue occurs when we have the opposite situation ($\boldsymbol{u}^{-}$).

E.3.2 Including additional Chebyshev terms

Given the above description, there are essentially two possible sources of inaccuracy in the approximation. The first is simply the number of terms in the Chebyshev polynomial N_T, which Fixman [105] empirically found must scale as roughly $(\lambda_{\max}/\lambda_{\min})^{0.5}$ to obtain a constant relative error of about 1%. If we desire a higher accuracy of $\sim 0.1\%$, Fixman claims we must roughly double the number of Chebyshev terms. The second is in the actual determination of the eigenvalues, as in Equation E.43. We must check that these eigenvalues are reasonably accurate over a range of possible chain conformations.

In order to test these predictions, we first calculate the square root exactly, which we can then compare to the approximations. As can be seen from Equation E.27, the matrix square root is straightforward to compute if one has the eigenvalues and eigenvectors of $\boldsymbol{D}$. The LAPACK subroutines to calculate eigenvalues are somewhat more sophisticated than those for the Cholesky decomposition, and require the following code:

```
subroutine get_delS_exact(Nbeads, hstar, &
    Diffusion_sup, delts, Dels)
  Integer, intent(in) :: Nbeads
  Real (DBprec), intent(in) :: diffusion_sup(:,:,:,:)
  Real (DBprec), intent(in) :: delts, hstar
  Real (DBprec), intent(out) :: Dels(:,:)

  Real (DBprec) :: dummy_D(Ndim,Nbeads,Ndim,Nbeads)
  Real (DBprec), dimension(Ndim, Nbeads) :: X_0
  Real (DBprec), dimension(Ndim*Nbeads,Ndim*Nbeads) :: &
  eig_vec_matrix, sqrtD
  Real (DBprec), dimension(Ndim*Nbeads) :: eig_vector
  Integer :: Neigs
```

```
Integer :: Ndof, lda, info, ii, ldz
Integer, save :: lwork, liwork
Integer, parameter :: LWMAX = 1000
Real (DBprec), dimension(LWMAX) :: work
Integer, dimension(LWMAX) :: iwork
Integer, dimension(Ndim*Nbeads) :: ifail
Real (DBprec) :: eigenvalues_tolerance = -1.d-4

logical, save :: workspace_queried = .false.

external ::  dger, dgemv
external :: dsyevx

Ndof = Ndim*Nbeads
lda = Ndof
ldz = Ndof

dummy_D = diffusion_sup

DelS = 0.d0

!Generate the random vector X_0
X_0 = 0.d0
Call ran_1(Ndof, X_0)
X_0 = X_0 - 0.5d0
X_0 = (X_0*X_0*C5 + C6)*X_0! Element-wise multiplications

If (Hstar.Gt.0) Then
  ! first find the optimal workspace with a dummy run,
  ! and save results
   if (.not.workspace_queried) then
      workspace_queried = .true.
      lwork = -1
      liwork = -1
      call dsyevx('V', 'A', 'U', Ndof, dummy_D, lda, &
      1.d0, 2.d0, 1, 2, eigenvalues_tolerance, &
      Neigs,eig_vector,eig_vec_matrix,ldz, &
      work,lwork,iwork,ifail,INFO)
      lwork = min(LWMAX, INT(work(1)))
```

```
      end if

      ! do the real calculation
      call dsyevx('V', 'A', 'U', Ndof, dummy_D, lda,&
         1.d0, 2.d0, 1, 2, eigenvalues_tolerance, &
         Neigs,eig_vector,eig_vec_matrix,ldz,&
         work,lwork,iwork,ifail,INFO)

      ! this next step can probably be
      ! vectorised in a clever way,
      ! if performance is important
      sqrtD = 0.d0
      do ii=1,Ndof
         call dger(Ndof, Ndof, eig_vector(ii)**(0.5d0), &
                               eig_vec_matrix(:,ii), 1, &
                               eig_vec_matrix(:,ii), 1, &
                               sqrtD, lda)
      end do

      alpha = 1.D0
      beta = 0.D0

      ! multiply sqrtD matrix by X_0
      call dgemv('n', Ndof, Ndof, alpha,sqrtD,lda, X_0,incx, &
             beta,delS,incy)

   else
      DelS = X_0
   end if

   DelS = DelS * sqrt(delts)

end subroutine
```

This subroutine is useful for testing purposes, as the Chebyshev approximation approaches this construction of $\boldsymbol{B}$ as the number of Chebyshev terms approaches infinity (given that $d_{\max}$ and $d_{\min}$ do in fact bound the eigenvalues of $\boldsymbol{B}$). This is verified by a simple unit test in the code, which proves that the two d$\boldsymbol{S}$ matrices do in fact get arbitrarily close as $N_T \to \infty$.

E.4 Results

Comparisons between the various methods of calculating the square root of the diffusion tensor, or the $\boldsymbol{B} \cdot d\boldsymbol{W}$ term, are given in Figure E.2. The case with the number of Chebyshev terms calculated as per Equation E.42 times only 1.5 (magenta lines) appears distinctly different from the analytical distribution. As the number of Chebyshev terms is increased, the simulations approach the analytical values. The direct Cholesky decomposition is almost indistinguishable from the no HI case. Direct calculation of the square root of the diffusion tensor using the eigenvalues and eigenvectors gives similar results to the Cholesky decomposition, but is not shown in Figure E.2.

It seems that if one wishes to obtain extremely precise estimates of properties via BD simulation, it is always worth checking whether a Cholesky decomposition, or an increase in the number of Chebyshev terms, appears to change the results.

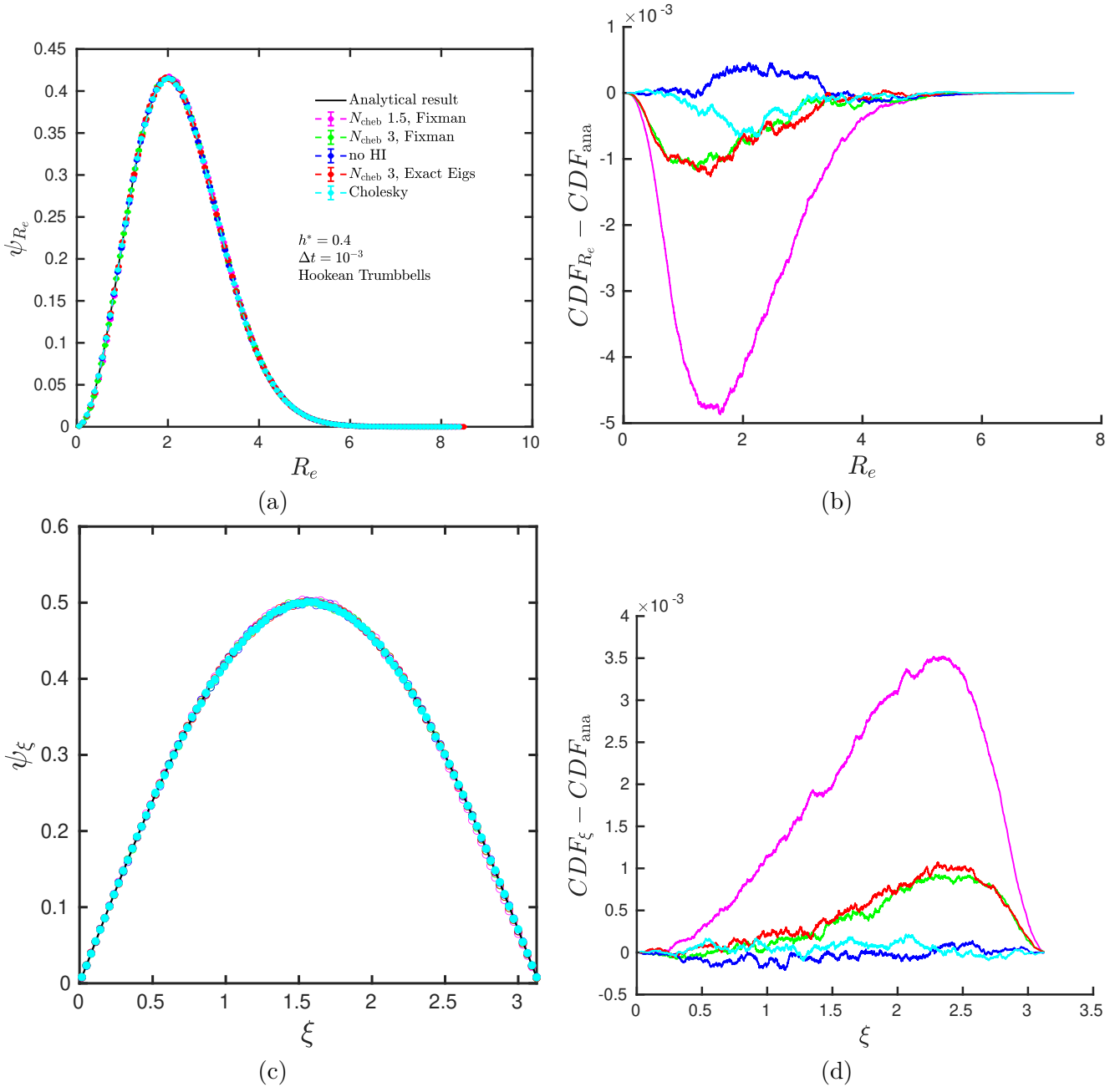

FIGURE E.2: Comparisons of distribution functions at equilibrium for BD simulations with various calculation methods for the square root of the diffusion tensor. Black line is the analytical result, blue lines represent the case with no HI, cyan lines give results for a Cholesky decomposition, red lines have three times as many Chebyshev terms as in Equation E.42, as well as the exact eigenvalues used to determine the chebyshev polynomial, and finally green and magenta lines have the eigenvalues approximated via Equation E.43, with 3 and 1.5 times as many Chebyshev terms as in Equation E.42 respectively. All results are for Hookean Trumbbells with $h^* = 0.4$ and $\Delta t^* = 10^{-3}$ (no bending potential or EV). (a) End-to-end length distribution function. (b) Difference between cumulative distribution function (CDF) of end-to-end distance and the analytical CDF. (c) Included angle distribution function. (d) Difference between cumulative distribution function (CDF) of included angle and the analytical CDF.

Appendix F

Zero-shear viscosity Calculations

There are several possible methods to obtain the zero-shear viscosity and/or relaxation times from BD simulations. Relaxation times can be found from:

- The exponential decay of the chain size (either end-to-end distance, radius of gyration, or stretch [112]) after imposing some external force and then letting the system return to equilibrium.
- The autocorrelation of the chain size at equilibrium, which should also exhibit an exponential decay.
- The value of some other dynamic property at or near equilibrium, such as the zero-shear viscosity, or hydrodynamic radius [34].

In general, these may be sums of exponentials, and we are usually interested in the longest relaxation time. The zero-shear viscosity can be determined in several ways [34]:

- Simulations at low but finite shear rate, potentially including extrapolation to zero shear.
- Green-Kubo relations, which give the zero-shear viscosity in terms of the stress autocorrelation at equilibrium.
- Finite-shear extensions of Green-Kubo, namely the Transient Time Correlation Functions (TTCF).
- The stress decay after a step strain.

Finally, although we will not describe them in detail here, we note that there are similar relations for the diffusivity. Diffusivity can be calculated directly using the mean-squared

displacement, as well as Kirkwood's static expression with Fixman's correction for fluctuating hydrodynamic interactions [140].

We will describe how we have applied the methods listed above to calculate relaxation times and zero-shear viscosity with two examples. The first is that of a FENE spring with Gaussian EV, hydrodynamic interactions and a bending potential, including nearly all of the physical effects mentioned in the body of this paper. The second is a stiff FENE-Fraenkel spring of $\sigma^* = 9$ and $\delta Q^* = 1$ with $h^* = \sqrt{3}\chi$, for which it is considerably harder to obtain accurate predictions.

While we have already given explicit expressions for the viscosity at finite shear rate in Equation 3.20, the zero-shear viscosity can be calculated using integrals over the stress autocorrelation at equilibrium $C(t)$, or the relaxation modulus $G(t)$. These are defined as [34, 124, 158]:

$$C(t) = \langle \tau_{xy}(0)\tau_{xy}(t) \rangle \tag{F.1}$$

where τ_{xy} is given by Equation 3.19. At equilibrium, the configuration is isotropic and so the average is also taken over τ_{xz} and τ_{yz}. Additionally,

$$G(t) = \lim_{\gamma_0 \to 0} \frac{\langle \tau_{xy}(t) \rangle}{\gamma_0} \tag{F.2}$$

where an instantaneous strain of γ_0 is applied at $t = 0$, such that $\dot{\gamma} = \gamma_0 \delta(t)$, and $\delta(t)$ is the dirac delta function. We then find that:

$$\eta_0 = \int_0^\infty \{G(t), C(t)\}\, dt \tag{F.3}$$

where by $\{G(t), C(t)\}$ we mean either $G(t)$ or $C(t)$.

In our simulations, we can measure both $G(t)$ and $C(t)$ at the same time through a variance reduction procedure [13, 93, 113]. An equilibrium configuration is simulated along two separate trajectories using the same set of random numbers. In one trajectory, there is a very rapid step-strain applied at $t = 0$, while the other is kept at equilibrium. The equilibrium trajectory can be used to calculate $C(t)$, while the decay of the stress after the step-strain gives us $G(t)$. Since the average stress at equilibrium is zero, we can subtract the stress for the equilibrium trajectory from the stress for the strained trajectory at each timestep to obtain the same $G(t)$ curve with considerably reduced error. We cannot impose a truly instantaneous step strain, so we instead apply an extremely rapid shear at some large shear rate $\dot{\gamma} \gg 1$, and check that results are independent of $\dot{\gamma}$.

This is shown in Figure F.1 for a FENE spring with HI, EV and a bending potential. Results are independent of $\dot{\gamma}$, but have not converged in $G(t)$ for $\gamma_0 = 0.1$ and $\gamma_0 = 1$. It is immediately obvious that error bars are considerably larger for $C(t)$ due to the lack of variance reduction.

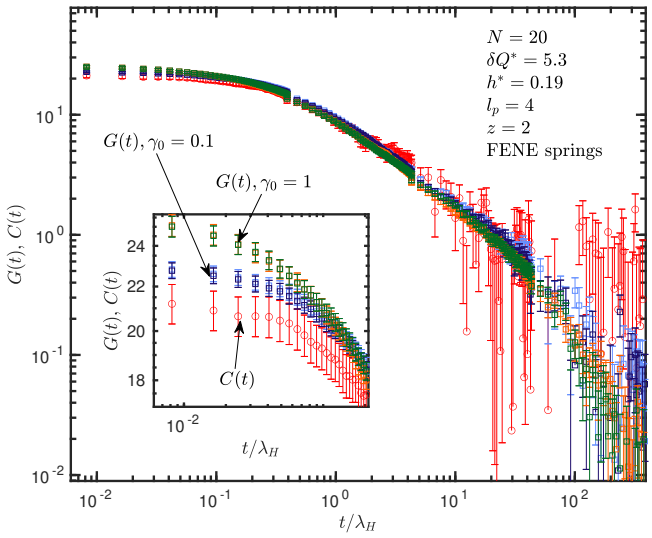

FIGURE F.1: Plot of $G(t)$ and $C(t)$ for two different step strain magnitudes, at two different shear rates for the step strain. Light and dark blue curves are $G(t)$ at $\gamma_0 = 0.1$ with $\dot{\gamma}^* = 10^3$ and $\dot{\gamma}^* = 10^5$ respectively. Green and yellow curves are $G(t)$ at $\gamma_0 = 0.1$ with $\dot{\gamma}^* = 10^3$ and $\dot{\gamma}^* = 10^5$ respectively. Red curve is $C(t)$ calculated using the equilibrium trajectories. Inset is curves at small time, showing the variation with γ_0.

The integrals are computed using simple trapezoidal integration:

$$\eta_0 = \frac{1}{2} \sum_{i=1}^{N_{\text{samples}}-1} (t_{i+1} - t_i) \left[G(t_{i+1}) + G(t_i) \right] \tag{F.4}$$

where the error is:

$$\Delta\eta_0 = \frac{1}{2} \sqrt{\sum_{i=1}^{N_{\text{samples}}-1} (t_{i+1} - t_i)^2 \left[\Delta G(t_{i+1})^2 + \Delta G(t_i)^2 \right]} \tag{F.5}$$

with $\Delta G(t)$ as the standard error in $G(t)$ over the ensemble of trajectories. Since errors accumulate monotonically when integrating an equilibrated trajectory, we often truncate this sum at some $t_{\max}$ which is less than the total simulated period to obtain reasonable precision.

It is also possible to fit some function to $G(t)$ or $C(t)$ and then analytically integrate the resulting function to infinity, as done by Pan et al. [124]. We have used the peeling method to fit a sum of exponentials. This involves first fitting a single exponential to the tail of the data, subtracting this fit away from the data, and then fitting a new exponential to the tail of the modified data. This process is continued for however many exponentials is needed for a reasonable fit, generally found to be 3 to 6. An example fit is shown in Figure F.2 for the $G(t)$ data in Figure F.1 with a sum of 5 exponential functions. Despite the apparent accuracy of this fit, we generally find that direct trapezoidal integration is sufficient, and simply use the exponential fit as a check against the direct result.

An extension of the Green-Kubo relations, the so-called Transient Time Correlation Functions (TTCF), can be used to obtain the viscosity at finite shear rates without the associated

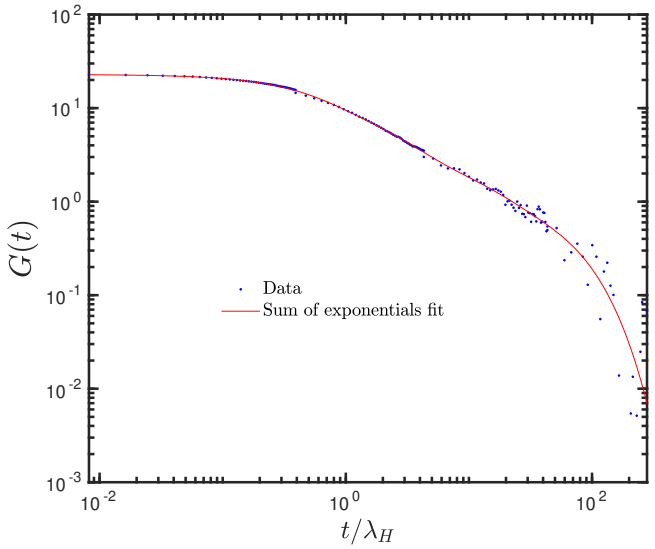

FIGURE F.2: $\gamma_0 = 0.1$, $G(t)$ curve in Figure F.1 fit with a sum of 5 exponentials.

increase in error at very low shear rates. These functions have been used in non-equilibrium molecular dynamics (NEMD) simulations for years, but have not (as far as we are aware) been applied to BD simulations to date. A excellent review of NEMD simulations, as well as the statistical mechanical foundations of TTCFs, can be found in the textbook by Daivis and Todd [109]. Essentially, the technique involves integrating the correlation between some phase space variable at equilibrium and after the inception of an external field. For the specific case of shear flow, the time-dependent behaviour of some phase variable B is given by:

$$\langle B(t)\rangle = \langle B(0)\rangle - \frac{1}{k_{\mathrm{B}}T}\dot{\gamma}V\int_0^t \langle B(s)\tau_{xy}(0)\rangle \,\mathrm{d}s \tag{F.6}$$

where V is the system volume, $\dot{\gamma}$ is the flowrate, and $\tau_{x,y}$ is the component of the stress tensor in the flow and gradient directions. For the specific case of viscosity, we can find the average over τ_{xy} and apply Newton's law of viscosity [109]:

$$\eta(t;\dot{\gamma}) = -\frac{V}{k_{\mathrm{B}}T}\int_0^t \langle \tau_{xy}(s;\dot{\gamma})\tau_{xy}(0;\dot{\gamma}=0)\rangle \,\mathrm{d}s \tag{F.7}$$

where $\tau_{xy}(t,\dot{\gamma})$ is the xy component of the stress tensor at time t and shear rate $\dot{\gamma}$. Notably, we do not have to explicitly divide by shear rate in this expression. For the direct calculation where τ_{xy} becomes smaller and smaller at steady state, divided by a smaller and smaller shear rate, leading to very large relative errors as the absolute error in τ_{xy} stays constant.

Comparison of these results is given in Figure F.3. It is clear that for a stiff spring with $\sigma^* = 9$, although the direct calculation is difficult to fully extrapolate to zero shear, it has considerably smaller error bars than the alternate methods. Therefore, generally estimates of the zero-shear viscosity for the relaxation time are made using $C(t)$ or $G(t)$, and then exact results plotted using the viscosity at low Wi.

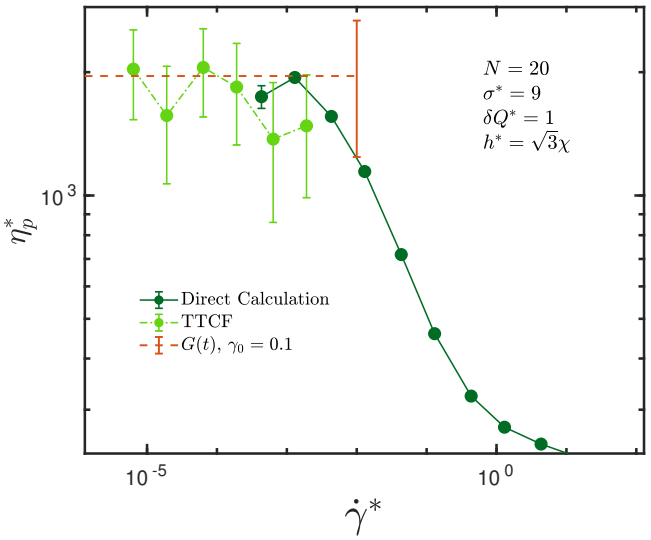

FIGURE F.3: Comparison of listed methods to obtain zero-shear viscosity. The $C(t)$ result is similar to that for $G(t)$, but with considerably larger error bars.

Appendix G

Methods for calculating tumbling times

When a polymer chain undergoes shear flow, the rotational component of the velocity field causes end-on-end tumbling of the chain. Since this is an integral feature of shear flow, we wish to have a method to quantify this tumbling frequency (or its inverse, tumbling time τ_{tumble}). There are three general methods for doing so in the literature. The first, which we will not describe in detail, is to use the peak in the power spectral density (PSD), which was often calculated in early BD studies [31]. The other two methods are what we will call direct end-on-end calculation, and the cross-correlation of the gyration tensor.

The direct calculation method is straightforward - one simply finds the end-to-end vector of the total polymer chain, and calculates its total average rotational velocity. This method was employed by Dalal et al. in a BD simulation study [78], and also by Huber et al. in an experimental study directly imaging actin molecules [106]. To demonstrate the procedure, we display a schematic of a polymer chain stretched in shear flow in Figure G.1. The angle θ is of the end-to-end vector with respect to the flow direction at a particular timestep.

To find the tumbling time, we first plot the cumulative angle the end to end vector has swept out in some time t. This is displayed in Figure G.2, which shows θ as a function of dimensionless time. Note the clear 'steps' in θ, which are of π radians, corresponding to half a revolution of the chain. An example revolution is shown in Figure G.3, where one can clearly identify the half-revolution of the end-to-end vector. It is this half-revolution that we call a 'tumble', and the tumbling period is simply given by:

$$\tau_{\text{tumble}} = \frac{\Delta\theta}{\Delta t}\frac{1}{\pi} \tag{G.1}$$

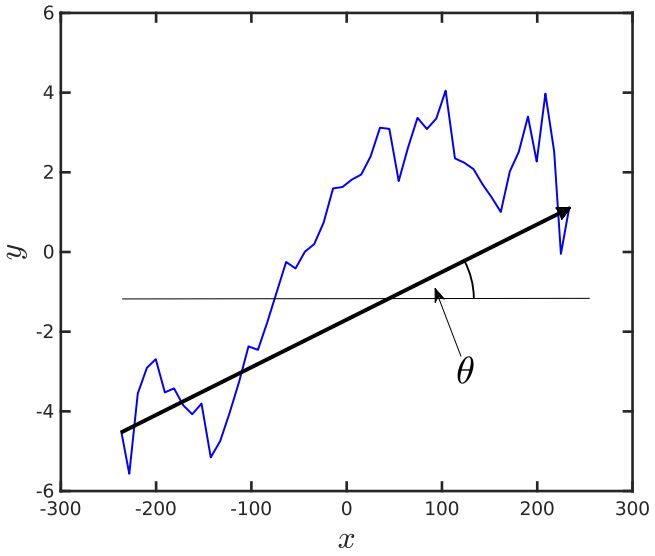

FIGURE G.1: Schematic of polymer chain in shear flow, showing the angle the end-to-end vector makes with the flow direction for calculation of the tumbling period. This angle is plotted over time for a single trajectory in Figure G.2

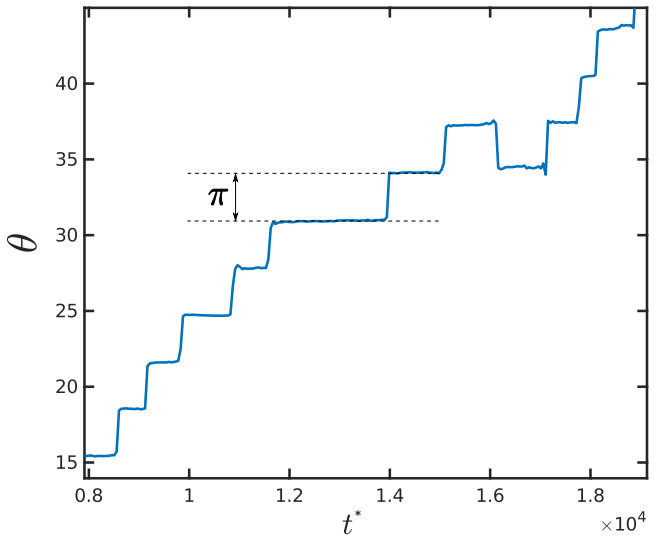

FIGURE G.2: Cumulative change in θ over time for a single example trajectory in shear flow, as per the definition of θ in Figure G.1. A single 'tumble' is identified by a change of θ by π radians, shown on the figure for a tumble at $t^* \approx 1.4 \times 10^4$. An example trajectory during a tumbling step, when the end-on-end vector rotates by π, is given in Figure G.3.

where $\Delta\theta$ is the cumulative change in the rotation angle θ, and Δt is the total time over which sums the change in θ. For example, in Figure G.2 the total change $\Delta\theta \approx 30$, while the change in time $\Delta t \approx 1 \times 10^4$, so we have $\tau_{\text{tumble}} \approx 3 \times 10^3$. This is then averaged over all trajectories to obtain a mean tumbling time.

The second method is to use the cross-correlation of the flow and gradient components of the gyration tensor [30, 107, 108]. We first define a function $C_{x,y}(t)$, given by the following

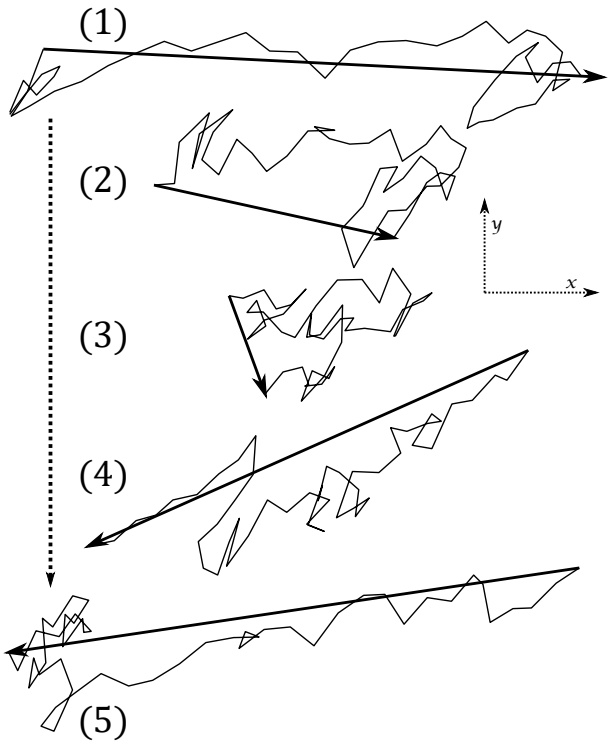

FIGURE G.3: Example of chain contour during an end-on-end tumbling event. Numbers represent successive times, where (1) represents the state prior to a 'step' in Figure G.2, while (5) represents the state after the 'step'. The x and y axes correspond to flow and gradient directions respectively. End-to-end vector is displayed via an arrow from bead $\mu = 1$ to bead $\mu = N$.

formula:

$$C_{x,y}(t) = \frac{\langle \delta G_{xx}(t_0) \delta G_{yy}(t_0 + t) \rangle}{\sqrt{\langle \delta G_{xx}^2(t_0) \rangle \langle \delta G_{yy}^2(t_0) \rangle}} \tag{G.2}$$

where $G_{\alpha\alpha}$ for $\alpha = \{x, y, z\}$ is the given component of the gyration tensor, and $\delta G_{\alpha\alpha} = G_{\alpha\alpha} - \langle G_{\alpha\alpha} \rangle$. We can imagine that as a polymer chain tumbles, it begins in an extended state in the flow direction, and then coils up and expands slightly in the gradient direction as it flips end on end. This can be seen in Figure G.3, where the stretched chain conformations before and after the tumble at (1) and (5) have a greater x-extent and slightly smaller y-extent, while the conformations during the tumble, particularly (3), are far more compact. Therefore, the time lag in the peaks of this correlation function should give us some sense of the tumbling time. This can be seen in Figure G.4, which gives an example $C_{x,y}(t)$ in shear flow. The locations of two peaks around $t = 0$ have been labelled as t^+ and t^-, and it is the difference between these two values which gives us our tumbling time.

In general, these times have similar qualitative behaviour (particularly in terms of scaling with shear rate), although they are not necessarily exactly identical. Both of these methods have been employed in the study of ring polymers [107], in which the cross-correlation defines tumbling motion, while picking a point on the ring and observing the cumulative angle it

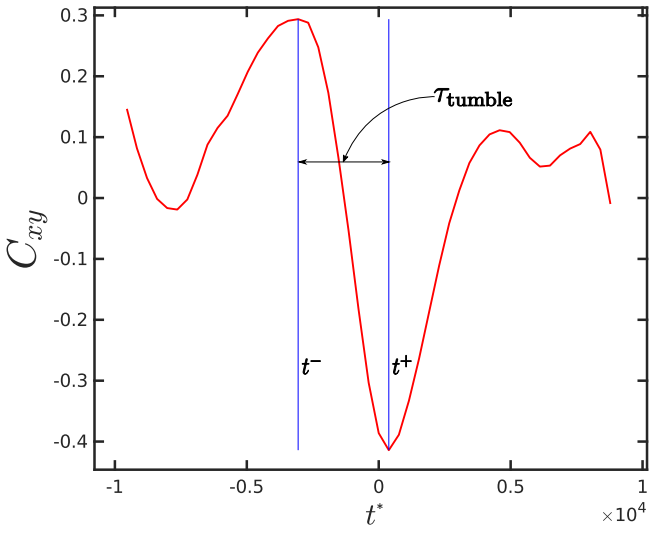

FIGURE G.4: Plot of the cross-correlation function $C_{x,y}$ as described in Equation G.2, for an ensemble of trajectories in shear flow. The locations of the peak and trough around $t = 0$, labelled as t^- and t^+, are given as vertical blue lines on the figure. The difference in t^- and t^+ is identified as the tumbling period.

sweeps out could also be associated with tank-treading motion, rather than pure tumbling.

Appendix H

Simple Monte-Carlo method for generating equilibrium distributions

Here we describe a method to generate equilibrium configurations of chains with an arbitrary spring force law and bending potential. This involves building the chain up one step at a time, such that both the average spring length and average included angle between springs matches the expected underlying distribution. We first note that for a 1D distribution $p(X)$, one can sample from this distribution by taking the inverse of the cumulative distribution function $P^{-1}(X)$. A random number Y uniformly distributed from 0 to 1 can then be transformed into a number sampling the distribution p using:

$$X = P^{-1}(Y) \tag{H.1}$$

In fact, this is very nearly the definition of the cumulative distribution function, since it should give the probability that a randomly chosen value from the distribution will be less than or equal to a given number, namely $p(X < x) = P(x)$. This result is found in many statistics textbooks, but can be intuitively (or perhaps geometrically) understood as follows. Imagine that we choose some random number y from our uniform distribution Y (let's say $y \approx 0.6915$), and interpret this as a probability. This corresponds to the y-axis of a cumulative distribution function, as in Figure H.1 (a). If we then find the corresponding inverse $x = P^{-1}(y)$, this is the number such that y fraction of the time a random number drawn from $p(X)$ will be smaller than x, and $1 - y$ fraction of the time it will be larger than x, as in Figure H.1 (b). In other words, each y maps onto some x such that $p(X < x) = y = P(x)$, and hence $x = P^{-1}(x)$.

We can now imagine that we have some spring potential $\phi_s(Q)$ in the spring length Q, as well as a bending potential $\phi_b(\theta)$ in the included angle θ. The probability distribution functions of

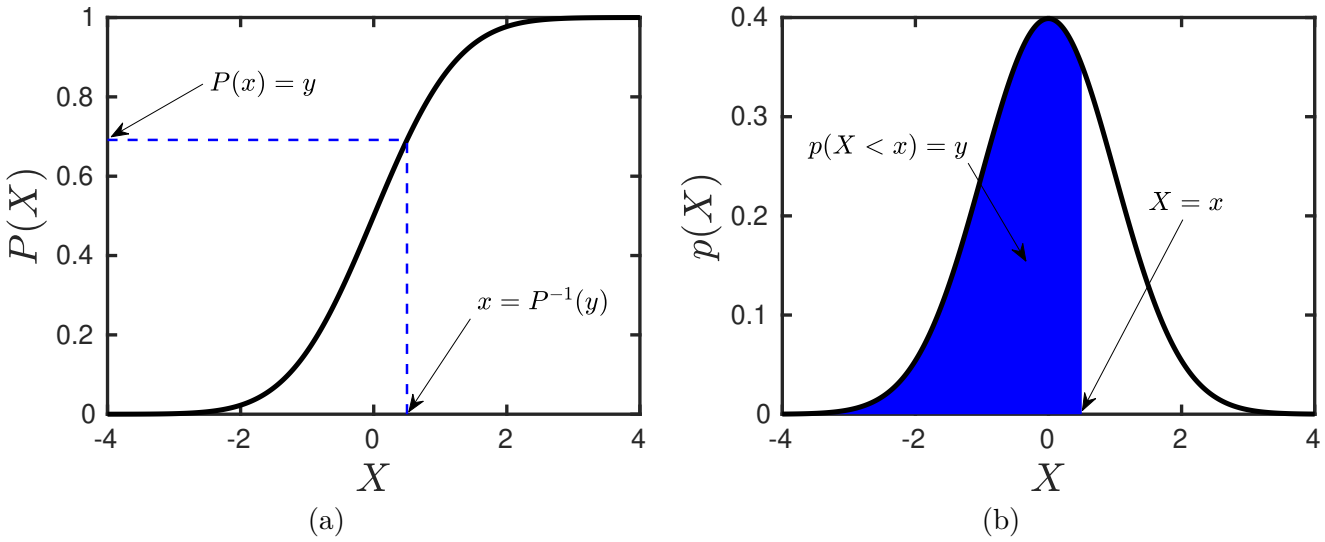

FIGURE H.1: (a) Cumulative probability distribution function of Gaussian distribution. We choose some random y from Y, and this corresponds to some $x = P^{-1}(y)$. (b) The Gaussian probability distribution, showing the area under the curve such that $p(X < x) = P(X) = y$.

Q and θ are given by:

$$\psi = \frac{e^{-\phi/k_{\mathrm{B}}T}}{Z(\phi)} = \frac{e^{-\phi/k_{\mathrm{B}}T}}{\int e^{-\phi/k_{\mathrm{B}}T}} \tag{H.2}$$

where the integration is over the range of Q or θ respectively, ψ is the probability distribution function with cumulative distribution function Ψ, and $Z(\phi)$ is the partition function corresponding to the potential ϕ in a heat bath at temperature T. This is often possible to calculate explicitly, but in general must be done numerically. For example, Appendix D gives the exact form of $\psi_b(\theta)$ for a particular form of $\phi_b(\theta)$.

When Ψ is calculated analytically, it is straightforward to generate spring lengths Q and spring-spring angles θ by generating uniform random numbers Y, then simply calculating, for example, $\theta = \Psi_b^{-1}(y)$. For numerical Ψ, we generate a table of θ and corresponding cumulative probabilities $\Psi_b(\theta)$ by numerical integration, then for each uniform random number y we determine the two $\Psi_b(\theta)$ values which bracket y, and determine θ through linear interpolation.

We are essentially attempting to calculate the joint partition function $Z(\phi_s, \phi_b)$, where ϕ_s and ϕ_b are the spring and bending potentials respectively. The partition function of course corresponds to the denominator in Equation H.2 for either ϕ_s or ϕ_b. This partition function is given as a sum over the Boltzmann weight associated with each chain conformation. Since the contributions of ϕ_s and ϕ_b to this sum are separable, it is possible for certain forms of the bending and spring potentials to directly calculate this partition function analytically [119]. However it is, as far as we know, not possible in general, and so we must calculate this partition function using a Monte-Carlo methodology, essentially generating chain configurations with the correct Boltzmann weights and then summing over the generated trajectories.

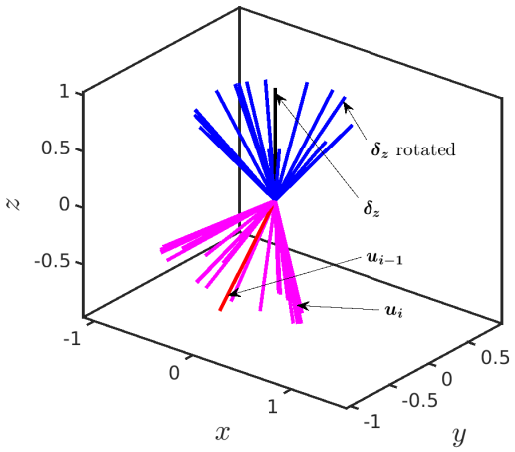

FIGURE H.2: Schematic showing rotation of vectors from one axis to another.

We then generate chains of length N_s as follows. For each spring $i = 1, \ldots, N_s$ we generate a length Q_i, and similarly for each angle $j = 1, \ldots, N_s - 1$ we generate some θ_μ as above. For the first spring, $i = 1$, we choose its direction from a random vector $\boldsymbol{u}_i$ on the surface of the unit sphere. This can be done by setting the azimuthal angle to a random uniform value between 0 and 2π, and then noting that the probability distribution of the elevation is a sine function (allowing one to sample from this distribution as described above). We then multiply this unit vector by the spring length to obtain $\boldsymbol{Q}_1$. For subsequent springs $\boldsymbol{Q}_i$, we take a unit vector along the z-axis, rotate it about the x-axis by θ_i, and then rotate it about the z-axis by some random angle between 0 and 2π. Finally, we transform this new unit vector to the coordinates of the previous unit vector $\boldsymbol{u}_{i-1}$ using rotation matrix from the z-axis to $\boldsymbol{u}_{i-1}$. We then multiply our new unit vector $\boldsymbol{u}_i$ by Q_i, giving the next spring vector $\boldsymbol{Q}_i$, and repeat the process until $i = N_s$. One can then add the vectors $\boldsymbol{Q}_i$ together to obtain the bead positions $\boldsymbol{R}_\mu$ (noting that, for example, the spring $i = 1$ runs from bead $\mu = 1$ to $\mu = 2$).

Appendix I

Separation of optical and orientational components

Here we wish to show that it is possible to separate the LD signal for DNA into optical (O) and orientational (S) components. Specifically, we assumed that we have a polymer chain made up of N_s segments $\boldsymbol{u}$ with uniaxial symmetry, each of which have a transition dipole moment $\boldsymbol{\mu}$ at angle α to $\boldsymbol{u}$. This is displayed schematically in Figure I.1, where the polymer segment orientation is given relative to the background shear flow. We will not describe explicitly how the S component can be further split into S_s and S_{BP} as in Chapter 5, but as we will see, the derivation can be quite naturally continued to arbitrary 'levels' of polymer superstructure.

Imagine that we have a coordinate system as in Figure I.1, where the unit vector of some segment $\boldsymbol{u}$ (which points along the molecular z axis) is defined in terms of the elevation θ and azimuthal angle ψ. As we have noted, Ω is the angle from the transition dipole moment axis to some laboratory axis along which we measure absorption, in this case the Z axis. The azimuthal angle is measured from the X axis towards the Y axis. The transition dipole moment is then embedded at some elevation α and azimuthal angle β from the segmental coordinate system $\{x, y, z\}$.

Therefore, the overall unit vector along $\boldsymbol{\mu}$ can be written in terms of the angles θ, ψ, α and β via four independent rotations. Essentially, we take a vector in the Z direction, rotate it about the Y axis by θ, then rotate it about the Z axis by ψ - it now points in the direction of $\boldsymbol{u}$ (or the axis z). Independently, we can take a vector in the z direction, rotate it about the y axis by α, then rotate it about the z axis by β, so that it now points along z' in the molecular coordinate system. If we represent these rotations as matrices $\boldsymbol{T}_\theta$, $\boldsymbol{T}_\psi$, $\boldsymbol{T}_\alpha$, and $\boldsymbol{T}_\beta$, and further the unit vector along the Z axis as $\boldsymbol{\delta}_Z$, then we can define the unit vector $\hat{\boldsymbol{\mu}}$ as:

$$\hat{\boldsymbol{\mu}} = \boldsymbol{T}_\psi \cdot \boldsymbol{T}_\theta \cdot \boldsymbol{T}_\beta \cdot \boldsymbol{T}_\alpha \cdot \boldsymbol{\delta}_Z \tag{I.1}$$

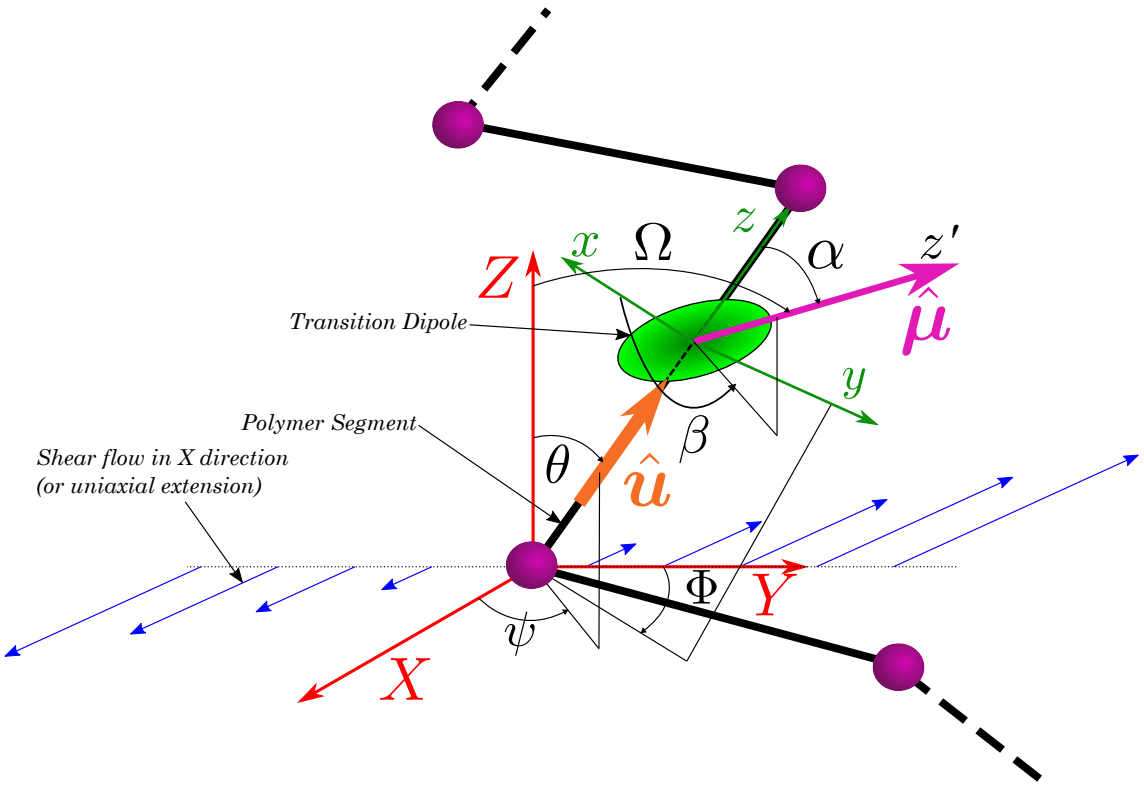

FIGURE I.1: The transition dipole of a polymer segment is represented as an ellipse, with the long axis oriented at an angle α to z. The laboratory frame is defined by the axes XYZ and is chosen to align with the shear flow direction, while the molecular axis is defined by xyz. The transition dipole is aligned along the z' direction. The Couette flow is defined by the shear flow axis (X), shear gradient axis (Y) and neutral axis (Z). Generally, the light will be propagated along the Y-axis for LD measurements in a Couette cell, as seen in Figure 5.1 (meaning that LD is given by $A_Z - A_X$).

which is the vector:

$$\hat{\boldsymbol{\mu}} = \begin{pmatrix} \sin(\alpha)[\cos(\beta)\sin(\theta)\cos(\psi) - \sin(\beta)\sin(\psi)] + \cos(\alpha)\cos(\theta)\cos(\psi) \\ \sin(\psi)[\sin(\alpha)\cos(\beta)\sin(\theta) + \cos(\alpha)\cos(\theta)] + \sin(\alpha)\sin(\beta)\cos(\psi) \\ \cos(\alpha)\sin(\theta) - \sin(\alpha)\cos(\beta)\cos(\theta) \end{pmatrix} \tag{I.2}$$

We first note that $\hat{\boldsymbol{\mu}}$ is in fact still a unit vector, which can be verified by calculating its length and applying trigonometric identities - this means that the isotropic absorbance of this system is 1/3. In order to find the LD_{ZX}, we simply take the distributional average over the components of $\hat{\boldsymbol{\mu}}$

$$\mathrm{LD}_{ZX} = \langle \hat{\mu}_Z^2 - \hat{\mu}_X^2 \rangle \tag{I.3}$$

where $\langle \quad \rangle$ is essentially an integral over θ, ψ, α and β, which is a linear operation. In fact, it is possible to explicitly perform this integral for β, which is uniformly distributed from 0 to 2π, and does not depend on any of the other angles. When we take this integral and normalise

the result, we obtain the following expression:

$$\mathrm{LD}_{ZX} = \frac{1}{16}\left\langle (3\cos(2\alpha)+1)\left(-2\sin^2(\theta)\cos(2\phi)+3\cos(2\theta)+1\right)\right\rangle \tag{I.4}$$

next note that α is not dependent on the distribution of θ and ψ, so it can be separated into its own term. By applying the double-angle formula, and simplifying the expression using trigonometric identities, we arrive at the following expression:

$$\mathrm{LD}_{ZX} = \frac{1}{2}\left\langle 3\cos^2\alpha - 1\right\rangle\left\langle \cos^2\theta - \cos^2\psi\sin^2\theta\right\rangle \tag{I.5}$$

If we assume that α is a constant α_{eff}, and further note that $\cos^2\theta \equiv u_Z^2$ and $\cos^2\psi\sin^2\theta \equiv u_X^2$, we finally obtain a slightly altered form of Equation 5.7 when combined with Equation 5.10 and Equation 5.8. We can also appreciate how this expression could be simplified for a uniaxial extension - in that case, we could eliminate terms by assuming a cylindrical distribution about X.

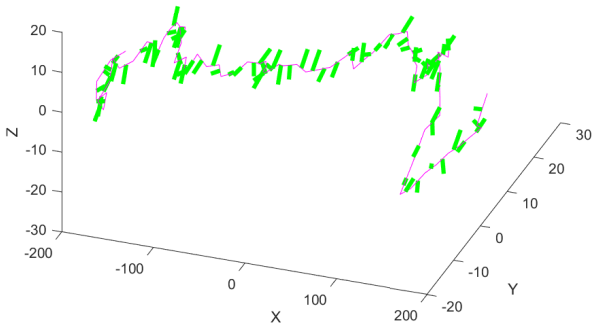

FIGURE I.2: 3D conformation of a sample polymer trajectory in magenta. Green lines are the embedded transition dipole moments at an angle of 86^o to the segments.

We can even check the expression numerically for one of our simulations at finite shear rates. To do so, we embed a transition dipole moment at some fixed angle α and random angle β to each polymer segment in shear flow. This is displayed in Figure I.2 for $\alpha = 86^o$, with the transition dipole moments displayed as green arrows. When one does this for a sufficiently large ensemble of trajectories, and further notes that $S \equiv \mathrm{LD}^r(\alpha = 0^o)/3$, we can iterate over several α and produce a plot such as Figure I.3, which confirms that it is sufficient to calculate S and then multiply by O to arrive at the reduced LD^r. This is of course an analytical certainty given the uniaxial symmetry of our segments and transition dipole moments, but it is a useful check on our procedure for calculation of S.

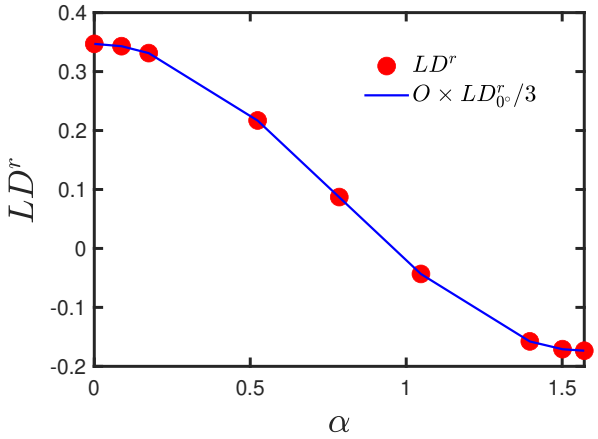

FIGURE I.3: Plot of calculated LD^r as a function of α, both directly calculating the LD (red symbols) and using the S-parameter definition for shear flow multiplied by O_{eff}

Note that this procedure can quite easily be extended to a further 'level', if we have the $\hat{\boldsymbol{u}}$ embedded in some more coarse-grained segment $\boldsymbol{Q}$. As long as the distribution of the $\boldsymbol{\mu}$ is uniaxial with respect to the $\boldsymbol{u}$, and the distribution of $\boldsymbol{u}$ is uniaxial with respect to the $\boldsymbol{Q}$, we can simply add another transformation matrix to Equation I.1 corresponding to the transformation from $\boldsymbol{u}$ coordinates to $\boldsymbol{Q}$ coordinates, then take the corresponding averages. This gives us the separation in Equation 5.7.

Bibliography

[1] Robert W Wilson and John A Schellman. The dichroic tensor of flexible helices. *Biopolymers: Original Research on Biomolecules*, 16(10):2143–2165, 1977.

[2] Robert W Wilson and John A Schellman. The flow linear dichroism of dna: Comparison with the bead-spring theory. *Biopolymers: Original Research on Biomolecules*, 17(5): 1235–1248, 1978.

[3] James R.A. McLachlan, David J. Smith, Nikola P. Chmel, and Alison Rodger. Calculations of flow-induced orientation distributions for analysis of linear dichroism spectroscopy. *Soft Matter*, 9(20):4977–4984, 2013.

[4] Bengt Norden, Mikael Kubista, and Tomas Kurucsev. Linear dichroism spectroscopy of nucleic acids. *Quarterly Reviews of Biophysics*, 25(1):51–170, 1992.

[5] Martyn Rittman, Emma Gilroy, Hashem Koohy, Alison Rodger, and Adair Richards. Is DNA a worm-like chain in Couette flow? In search of persistence length, a critical review. *Science progress*, 92(2):163–204, 2009.

[6] Christer Håkansson and Christer Elvingson. Semiflexible chain molecules with nonuniform curvature, 2. brownian dynamics simulations of electric dichroism orientation dynamics. *Macromolecular theory and simulations*, 6(1):13–27, 1997.

[7] Akira Onuki and Masao Doi. Flow birefringence and dichroism of polymers. i. general theory and application to the dilute case. *The Journal of Chemical Physics*, 85(2): 1190–1197, 1986.

[8] Arvid Ødegaard-Jensen, Christer Elvingson, and Christer Håkansson. Computer simulation of DNA orientation and deformation in a shear flow field. *Macromolecular Theory and Simulations*, 5(4):663–672, 1996.

[9] A. Rodger. Linear dichroism spectroscopy: Techniques and applications. *Advances in Biomedical Spectroscopy*, 1:150–164, 2009.

[10] Alison Rodger, Glen Dorrington, and Dale L Ang. Linear dichroism as a probe of molecular structure and interactions. *Analyst*, 141(24):6490–6498, 2016.

[11] R G Larson. The rheology of dilute solutions of flexible polymers: Progress and problems. *Journal of Rheology*, 49(1):1–70, 2005.

[12] J Ravi Prakash. Universal dynamics of dilute and semidilute solutions of flexible linear polymers. *Current Opinion in Colloid & Interface Science*, 43:63–79, 2019.

[13] Hans Christian Öttinger. *Stochastic processes in polymeric fluids: Tools and examples for developing simulation algorithms*. Springer-Verlag, Berlin Heidelberg, 1996.

[14] R Prabhakar, J Ravi Prakash, and T Sridhar. A successive fine-graining scheme for predicting the rheological properties of dilute polymer solutions. *Journal of Rheology*, 48(6):1251–1278, 2004.

[15] Amir Saadat and Bamin Khomami. Molecular based prediction of the extensional rheology of high molecular weight polystyrene dilute solutions: A hi-fidelity Brownian dynamics approach. *Journal of Rheology*, 59(6):1507–1525, 2015.

[16] P Sunthar and J Ravi Prakash. Parameter free prediction of DNA conformations in elongational flow by successive fine graining. *Macromolecules*, 38(2):617–640, 2005.

[17] T Simonson and M Kubista. DNA orientation in shear flow. *Biopolymers*, 33(8):1225–1235, 1993.

[18] Amir Saadat and Bamin Khomami. A new bead-spring model for simulation of semiflexible macromolecules. *Journal of Chemical Physics*, 145(20):204902, 2016.

[19] Elena F. Koslover and Andrew J. Spakowitz. Multiscale dynamics of semiflexible polymers from a universal coarse-graining procedure. *Physical Review E - Statistical, Nonlinear, and Soft Matter Physics*, 90(1):1–5, 2014.

[20] Patrick T Underhill and Patrick S Doyle. Alternative spring force law for bead-spring chain models of the worm-like chain. *Journal of Rheology*, 50(4):513–529, 2006.

[21] Patrick T Underhill and Patrick S Doyle. On the coarse-graining of polymers into bead-spring chains. *Journal of Non-Newtonian Fluid Mechanics*, 122(1-3):3–31, 2004.

[22] Sharadwata Pan, Duc At Nguyen, Burkhard Dünweg, P Sunthar, T Sridhar, and J. R Prakash. Shear thinning in dilute and semidilute solutions of polystyrene and DNA. *Journal of Rheology*, 62(4):845–867, 2018.

[23] Chih Chen Hsieh, Semant Jain, and Ronald G. Larson. Brownian dynamics simulations with stiff finitely extensible nonlinear elastic-Fraenkel springs as approximations to rods in bead-rod models. *Journal of Chemical Physics*, 124(4), 2006.

[24] H A Kramers. The viscosity of macromolecules in a streaming fluid. *Physica*, 11(1):1–9, 1944.

[25] N G Van Kampen. Statistical mechanics of trimers. *Applied Scientific Research*, 37(1-2): 67–75, 1981.

[26] N. G. van Kampen and J. J. Lodder. Constraints. *American Journal of Physics*, 52(5): 419–424, 1984.

[27] J M Rallison. The role of rigidity constraints in the rheology of dilute polymer solutions. *Journal of Fluid Mechanics*, 93(2):251–279, 1979.

[28] E S G Shaqfeh. The dynamics of single-molecule DNA in flow. *Journal of Non-Newtonian Fluid Mechanics*, 130(1):1–28, 2005.

[29] C C Hua and M S Wu. Viscometric properties of dilute polystyrene/dioctyl phthalate solutions. *Journal of Polymer Science Part B: Polymer Physics*, 44(5):787–794, 2006.

[30] Rodrigo E Teixeira, Hazen P Babcock, Eric SG Shaqfeh, and Steven Chu. Shear thinning and tumbling dynamics of single polymers in the flow-gradient plane. *Macromolecules*, 38(2):581–592, 2005.

[31] Charles M Schroeder, Rodrigo E Teixeira, Eric SG Shaqfeh, and Steven Chu. Dynamics of DNA in the flow-gradient plane of steady shear flow: Observations and simulations. *Macromolecules*, 38(5):1967–1978, 2005.

[32] W E Stewart and J P Sorensen. Hydrodynamic interaction effects in rigid dumbbell suspensions. II. Computations for steady shear flow. *Transactions of the Society of Rheology*, 16:1–13, 1972.

[33] X J Fan. Viscosity, first normal-stress coefficient, and molecular stretching in dilute polymer solutions. *Journal of Non-Newtonian Fluid Mechanics*, 17(2):125–144, 1985.

[34] R. B. Bird, C. F. Curtiss, R. C. Armstrong, and O. Hassager. *Dynamics of Polymeric Liquids - Volume 2: Kinetic Theory*. John Wiley, New York, 2nd edition, 1987.

[35] T W Liu. Flexible polymer chain dynamics and rheological properties in steady flows. *Journal of Chemical Physics*, 90(10):5826–5842, 1989.

[36] Patrick S Doyle, Eric SG Shaqfeh, and Alice P Gast. Dynamic simulation of freely draining flexible polymers in steady linear flows. *Journal of Fluid Mechanics*, 334:251–291, 1997.

[37] D Petera and M Muthukumar. Brownian dynamics simulation of bead-rod chains under shear with hydrodynamic interaction. *Journal of Chemical Physics*, 111(16):7614–7623, 1999.

[38] Richard M Jendrejack, Juan J de Pablo, and Michael D Graham. Stochastic simulations of DNA in flow: Dynamics and the effects of hydrodynamic interactions. *Journal of Chemical Physics*, 116(17):7752–7759, 2002.

[39] M E Mackay, C H Liang, and P J Halley. Instrument effects on stress jump measurements. *Rheologica Acta*, 31(5):481–489, sep 1992.

[40] Patrick S Doyle and Eric SG Shaqfeh. Dynamic simulation of freely-draining, flexible bead-rod chains: Start-up of extensional and shear flow. *Journal of Non-Newtonian Fluid Mechanics*, 76(1-3):43–78, 1998.

[41] Charles W Manke and Michael C Williams. Stress jumps predicted by the internal viscosity model with hydrodynamic interaction. *Journal of Rheology*, 36(7):1261–1274, 1992.

[42] Linda J Gerhardt and Charles W Manke. Relationships among shear stress jumps and high-frequency dynamic viscosity of viscoelastic fluids. *Journal of Rheology*, 38(5):1227–1234, 1994.

[43] R Kailasham, Rajarshi Chakrabarti, and J Ravi Prakash. Rheological consequences of wet and dry friction in a dumbbell model with hydrodynamic interactions and internal viscosity. *Journal of Chemical Physics*, 149(9):094903, 2018.

[44] JF Marko and ED Siggia. Statistical mechanics of supercoiled DNA. *Physical Review E*, 52(3):2912, 1995.

[45] D W Mead and R G Larson. Rheooptical study of isotropic solutions of stiff polymers. *Macromolecules*, 23(9):2524–2533, 1990.

[46] Eiichi Wada. Effect of rate of shear on viscosity of a dilute linear polymer and of tobacco mosaic virus in solution. *Journal of Polymer Science*, 14(75):305–307, 1954.

[47] Jen Tsi Yang. Non-Newtonian viscosity of poly-γ-benzyl-L-glutamate solutions. *Journal of the American Chemical Society*, 80(8):1783–1788, 1958.

[48] J.K.G. Dhont and Willem J. Briels. Rod-like Brownian particles in shear flow. In B. Cichocki, M. Napiorkowski, and J. Piasecki, editors, *Institute of Theoretical Physics, University of Warsaw and Pro Physica*, pages 7–73. Warsaw University Press, 2007. ISBN 978-83-235-0319-4.

[49] Hiromi Yamakawa and Takenao Yoshizaki. *Helical wormlike chains in polymer solutions*. Springer-Verlag, Berlin Heidelberg, second edition, 2016.

[50] MARB Castanho, S Lopes, and M Fernandes. Using UV-Vis. linear dichroism to study the orientation of molecular probes and biomolecules in lipidic membranes. *Journal of Spectroscopy*, 17(2-3):377–398, 2003.

[51] Madan Somasi, Bamin Khomami, Nathanael J Woo, Joe S Hur, and Eric SG Shaqfeh. Brownian dynamics simulations of bead-rod and bead-spring chains: numerical algorithms and coarse-graining issues. *Journal of Non-Newtonian Fluid Mechanics*, 108 (1-3):227–255, 2002.

[52] Chih Chen Hsieh, Lei Li, and Ronald G. Larson. Modeling hydrodynamic interaction in brownian dynamics: Simulations of extensional flows of dilute solutions of DNA and polystyrene. *Journal of Non-Newtonian Fluid Mechanics*, 113(2-3):147–191, 2003.

[53] R. Prabhakar and J. Ravi Prakash. Multiplicative separation of the influences of excluded volume, hydrodynamic interactions and finite extensibility on the rheological properties of dilute polymer solutions. *Journal of Non-Newtonian Fluid Mechanics*, 116(2-3):163–182, 2004. ISSN 03770257.

[54] Hermann Janeschitz-Kriegl. *Polymer melt rheology and flow birefringence*, volume 6. Springer Science & Business Media, 2012.

[55] Gerald G Fuller. *Optical rheometry of complex fluids*. Oxford University Press, 1995.

[56] Bengt Nordén. Applications of linear dichroism spectroscopy. *Applied Spectroscopy Reviews*, 14(2):157–248, 1978.

[57] R. Prabhakar and J. Ravi Prakash. Viscometric functions for hookean dumbbells with excluded volume and hydrodynamic interactions. *Journal of Rheology*, 46(5):1191–1220, 2002.

[58] M Keentok, AG Georgescu, AA Sherwood, and RI Tanner. The measurement of the second normal stress difference for some polymer solutions. *Journal of Non-Newtonian Fluid Mechanics*, 6(3-4):303–324, 1980.

[59] R. B. Bird, R. C. Armstrong, and O. Hassager. *Dynamics of Polymeric Liquids - Volume 1: Fluid Mechanics*. John Wiley, New York, 2nd edition, 1987.

[60] Mataz Alcoutlabi, SG Baek, JJ Magda, Xiangfu Shi, SA Hutcheson, and GB McKenna. A comparison of three different methods for measuring both normal stress differences of viscoelastic liquids in torsional rheometers. *Rheologica acta*, 48(2):191–200, 2009.

[61] RF Ginn and AB Metzner. Measurement of stresses developed in steady laminar shearing flows of viscoelastic media. *Transactions of the Society of Rheology*, 13(4):429–453, 1969.

[62] S-G Baek, JJ Magda, and RG Larson. Rheological differences among liquid-crystalline polymers. I. the first and second normal stress differences of PBG solutions. *Journal of Rheology*, 37(6):1201–1224, 1993.

[63] Ahmad S Khalil, Jorge M Ferrer, Ricardo R Brau, Stephen T Kottmann, Christopher J Noren, Matthew J Lang, and Angela M Belcher. Single M13 bacteriophage tethering and stretching. *Proceedings of the National Academy of Sciences*, 104(12):4892–4897, 2007.

[64] Jan Wilhelm and Erwin Frey. Radial distribution function of semiflexible polymers. *Physical Review Letters*, 77(12):2581, 1996.

[65] I Pincus, Alison Rodger, and J Ravi Prakash. Viscometric functions and rheo-optical properties of dilute polymer solutions: Comparison of FENE-Fraenkel dumbbells with rodlike models. *Journal of Non-Newtonian Fluid Mechanics*, 285:104395, 2020.

[66] Ichiro Noda, Yoshihiko Yamada, and Mitsuru Nagasawa. Rate of shear dependence of the intrinsic viscosity of monodisperse polymer. *The Journal of Physical Chemistry*, 72 (8):2890–2898, 1968.

[67] A J Kishbaugh and A J McHugh. A discussion of shear-thickening in bead-spring models. *Journal of Non-Newtonian Fluid Mechanics*, 34(2):181–206, 1990.

[68] Kyung Hyun Ahn, John L Schrag, and Seung Jong Lee. Bead-spring chain model for the dynamics of dilute polymer solutions: Part 2. Comparisons with experimental data. *Journal of Non-Newtonian Fluid Mechanics*, 50(2-3):349–373, 1993.

[69] J F Ryder and J M Yeomans. Shear thinning in dilute polymer solutions. *Journal of Chemical Physics*, 125(19):194906, 2006.

[70] Yoshihiro Mochimaru. Fast squeezing flow of viscoelastic fluids. *Journal of Non-Newtonian Fluid Mechanics*, 9(1-2):157–178, 1981.

[71] Alexey V Lyulin, David B Adolf, and Geoffrey R Davies. Brownian dynamics simulations of linear polymers under shear flow. *Journal of Chemical Physics*, 111(2):758–771, 1999.

[72] C Aust, M Kröger, and S Hess. Structure and dynamics of dilute polymer solutions under shear flow via nonequilibrium molecular dynamics. *Macromolecules*, 32(17):5660–5672, 1999.

[73] C.-C. Hsieh and R G Larson. Modeling hydrodynamic interaction in Brownian dynamics: Simulations of extensional and shear flows of dilute solutions of high molecular weight polystyrene. *Journal of Rheology*, 48(5):995–1022, 2004.

[74] R H Colby, D C Boris, W E Krause, and S Dou. Shear thinning of unentangled flexible polymer liquids. *Rheologica Acta*, 46(5):569–575, 2007.

[75] Mahdy Malekzadeh Moghani and Bamin Khomami. Computationally efficient algorithms for brownian dynamics simulation of long flexible macromolecules modeled as bead-rod chains. *Physical Review Fluids*, 2(2):1–16, 2017.

[76] C Sendner and R R Netz. Single flexible and semiflexible polymers at high shear: Non-monotonic and non-universal stretching response. *The European Physical Journal E*, 30 (1):75, sep 2009.

[77] I S Dalal, N Hoda, and R G Larson. Multiple regimes of deformation in shearing flow of isolated polymers. *Journal of Rheology*, 56(2):305–332, 2012.

[78] Indranil Saha Dalal, Alex Albaugh, Nazish Hoda, and Ronald G. Larson. Tumbling and deformation of isolated polymer chains in shearing flow. *Macromolecules*, 45(23): 9493–9499, 2012.

[79] Indranil Saha Dalal, Chih-Chen Hsieh, Alex Albaugh, and Ronald G Larson. Effects of excluded volume and hydrodynamic interactions on the behavior of isolated bead-rod polymer chains in shearing flow. *AIChE Journal*, 60(4):1400–1412, 2014.

[80] Charles M. Schroeder, Rodrigo E. Teixeira, Eric S.G. Shaqfeh, and Steven Chu. Characteristic periodic motion of polymers in shear flow. *Physical Review Letters*, 95(1):1–4, 2005.

[81] R Kailasham, Rajarshi Chakrabarti, and J Ravi Prakash. How important are fluctuations in the treatment of internal friction in polymers? *Soft Matter*, 17(30):7133–7157, 2021.

[82] R Kailasham, Rajarshi Chakrabarti, and J Ravi Prakash. Rouse model with fluctuating internal friction. *Journal of Rheology*, 65(5):903–923, 2021.

[83] R. Kailasham, Rajarshi Chakrabarti, and J. Ravi Prakash. Shear viscosity for finitely extensible chains with fluctuating internal friction and hydrodynamic interactions, 2022.

[84] Charles W Manke and Michael C Williams. Stress jump at the inception of shear and elongational flows of dilute polymer solutions due to internal viscosity. *Journal of Rheology*, 31(6):495–510, 1987.

[85] R Kailasham, Rajarshi Chakrabarti, and J Ravi Prakash. Wet and dry internal friction can be measured with the jarzynski equality. *Physical Review Research*, 2(1):013331, 2020.

[86] R Prabhakar and J R Prakash. Gaussian approximation for finitely extensible bead-spring chains with hydrodynamic interaction. *Journal of Rheology*, 50:561–593, 2006.

[87] H C Öttinger. Gaussian approximation for Rouse chains with hydrodynamic interaction. *Journal of Chemical Physics*, 90:463, 1989.

[88] W Zylka. Gaussian approximation and Brownian dynamics simulations for Rouse chains with hydrodynamic interaction undergoing simple shear flow. *Journal of Chemical Physics*, 94(6):4628–4636, 1991.

[89] Marie-Noëlle Layec-Raphalen and Claude Wolff. On the shear-thickening behaviour of dilute solutions of chain macromolecules. *Journal of Non-Newtonian Fluid Mechanics*, 1(2):159–173, 1976.

[90] Lothar Schäfer. *Excluded volume effects in polymer solutions: as explained by the renormalization group*. Springer Science & Business Media, 2012.

[91] Hans Christian Öttinger. Renormalization-group calculation of excluded-volume effects on the viscometric functions for dilute polymer solutions. *Physical Review A*, 40(5):2664, 1989.

[92] J. Ravi Prakash. Rouse chains with excluded volume interactions in steady simple shear flow. *Journal of Rheology*, 46(6):1353–1380, 2002.

[93] K S Kumar and J R Prakash. Equilibrium swelling and universal ratios in dilute polymer solutions: Exact Brownian dynamics simulations for a Delta function excluded volume potential. *Macromolecules*, 36(20):7842–7856, 2003.

[94] Aritra Santra, Kiran Kumari, Ranjith Padinhateeri, Burkhard Dünweg, and J Ravi Prakash. Universality of the collapse transition of sticky polymers. *Soft Matter*, 15(39): 7876–7887, 2019.

[95] T. Soddemann, B. Dünweg, and K. Kremer. A generic computer model for amphiphilic systems. *The European Physical Journal E*, 6(5):409–419, 2001.

[96] K. Satheesh Kumar and J. Ravi Prakash. Universal consequences of the presence of excluded volume interactions in dilute polymer solutions undergoing shear flow. *Journal of Chemical Physics*, 121(8):3886–3897, 2004.

[97] N. C. Andrews, A. J. McHugh, and J. D. Schieber. Conformational and rheological dynamics of semiflexible macromolecules undergoing shear flow: A nonequilibrium Brownian dynamics study. *Journal of Rheology*, 42(2):281–305, 1998.

[98] R G Winkler. Semiflexible polymers in shear flow. *Physical Review Letters*, 97(12), 2006.

[99] Roland G. Winkler. Conformational and rheological properties of semiflexible polymers in shear flow. *Journal of Chemical Physics*, 133(16), 2010.

[100] S. Liu, B. Ashok, and M. Muthukumar. Brownian dynamics simulations of bead-rod-chain in simple shear flow and elongational flow. *Polymer*, 45(4):1383–1389, 2004.

[101] Joe S Hur, Eric S G Shaqfeh, and Ronald G Larson. Brownian dynamics simulations of single DNA molecules in shear flow. *Journal of Rheology*, 44(4):713–742, 2000.

[102] H Yamakawa. *Modern Theory of Polymer Solutions*. Harper and Row, London, 1971.

[103] Hans C Andersen, John D Weeks, and David Chandler. Relationship between the hard-sphere fluid and fluids with realistic repulsive forces. *Physical Review A*, 4(4):1597, 1971.

[104] J Ravi Prakash and Hans Christian Öttinger. Viscometric functions for a dilute solution of polymers in a good solvent. *Macromolecules*, 32(6):2028–2043, 1999.

[105] Marshall Fixman. Construction of langevin forces in the simulation of hydrodynamic interaction. *Macromolecules*, 19(4):1204–1207, 1986.

[106] Benjamin Huber, Markus Harasim, Bernhard Wunderlich, Martin Kröger, and Andreas R. Bausch. Microscopic origin of the non-newtonian viscosity of semiflexible polymer solutions in the semidilute regime. *ACS Macro Letters*, 3(2):136–140, 2014.

[107] Wenduo Chen, Jizhong Chen, and Lijia An. Tumbling and tank-treading dynamics of individual ring polymers in shear flow. *Soft Matter*, 9(16):4312–4318, 2013.

[108] C. C. Huang, G. Sutmann, G. Gompper, and R. G. Winkler. Tumbling of polymers in semidilute solution under shear flow. *EPL (Europhysics Letters)*, 93(5), 2011.

[109] Billy D Todd and Peter J Daivis. Statistical Mechanical Foundations. In *Nonequilibrium molecular dynamics: theory, algorithms and applications*, pages 31–58. Cambridge University Press, 2017.

[110] István Borzsák, Peter T. Cummings, and Denis J. Evans. Shear viscosity of a simple fluid over a wide range of strain rates. *Molecular Physics*, 100(16):2735–2738, 2002.

[111] J Ravi Prakash. Rouse chains with excluded volume interactions: Linear viscoelasticity. *Macromolecules*, 34(10):3396–3411, 2001.

[112] P Sunthar, D A Nguyen, R Dubbelboer, J Ravi Prakash, and T Sridhar. Measurement and prediction of the elongational stress growth in a dilute solution of DNA molecules. *Macromolecules*, 38(24):10200–10209, 2005.

[113] Norman J Wagner and Hans Christian Öttinger. Accurate simulation of linear viscoelastic properties by variance reduction through the use of control variates. *Journal of Rheology*, 41(3):757–768, 1997.

[114] Praphul Kumar and Indranil Saha Dalal. Fraenkel springs as an efficient approximation to rods for brownian dynamics simulations and modelling of polymer chains. *Macromolecular Theory and Simulations*, page 2200008, 2022.

[115] Lei Li and Ronald G Larson. Comparison of Brownian dynamics simulations with microscopic and light-scattering measurements of polymer deformation under flow. *Macromolecules*, 33(4):1411–1415, 2000.

[116] Christopher Stoltz, Juan J de Pablo, and Michael D Graham. Concentration dependence of shear and extensional rheology of polymer solutions: Brownian dynamics simulations. *Journal of Rheology*, 50(2):137–167, 2006.

[117] R C Hayward and W W Graessley. Excluded volume effects in polymer solutions. 1. Dilute solution properties of linear chains in good and theta solvents. *Macromolecules*, 32(10):3502–3509, 1999.

[118] Semant Jain, Indranil Saha Dalal, Nicholas Orichella, Jeremy Shum, and Ronald Gary Larson. Do bending and torsional potentials affect the unraveling dynamics of flexible polymer chains in extensional or shear flows? *Chem. Eng. Sci.*, 64(22):4566–4571, 2009.

[119] Roland G. Winkler, Peter Reineker, and Ludger Harnau. Models and equilibrium properties of stiff molecular chains. *Journal of Chemical Physics*, 101(9):8119–8129, 1994.

[120] Ludger Harnau, Roland G Winkler, and Peter Reineker. Dynamic properties of molecular chains with variable stiffness. *Journal of Chemical Physics*, 102(19):7750–7757, 1995.

[121] Markus Harasim, Bernhard Wunderlich, Orit Peleg, Martin Kröger, and Andreas R. Bausch. Direct observation of the dynamics of semiflexible polymers in shear flow. *Physical Review Letters*, 110(10):1–5, 2013.

[122] Arash Nikoubashman and Michael P. Howard. Equilibrium Dynamics and Shear Rheology of Semiflexible Polymers in Solution. *Macromolecules*, 50(20):8279–8289, 2017.

[123] Chandi Sasmal, Kai-Wen Hsiao, Charles M Schroeder, and J Ravi Prakash. Parameter-free prediction of DNA dynamics in planar extensional flow of semidilute solutions. *Journal of Rheology*, 61(1):169–186, 2017.

[124] S Pan, D A Nguyen, P Sunthar, T Sridhar, and J R Prakash. Universal solvent quality crossover of the zero shear rate viscosity of semidilute DNA solutions. *Journal of Rheology*, 58(2):339–368, 2014.

[125] M Kröger, A Alba-Pérez, M Laso, and H C Öttinger. Variance reduced Brownian simulation of a bead-spring chain under steady shear flow considering hydrodynamic interaction effects. *Journal of Chemical Physics*, 113(11):4767–4773, 2000.

[126] Tri Thanh Pham, P. Sunthar, and J. Ravi Prakash. An alternative to the bead-rod model: Bead-spring chains with successive fine graining. *Journal of Non-Newtonian Fluid Mechanics*, 149(1-3):9–19, 2008.

[127] Y Miyaki and H Fujita. Excuded-volume effects in dilute polymer solutions. 11. Tests of the two-parameter theory for radius of gyration and intrinsic viscosity. *Macromolecules*, 14(3):742–746, 1981.

[128] Peter Grassberger, Peter Sutter, and Lothar Schäfer. Field theoretic and Monte Carlo analysis of the Domb-Joyce model. *Journal of Physics A: Mathematical and General*, 30 (20):7039–7056, 1997.

[129] William W. Graessley, Ryan C. Hayward, and Gary S. Grest. Excluded-volume effects in polymer solutions. 2. Comparison of experimental results with numerical simulation data. *Macromolecules*, 32(10):3510–3517, 1999.

[130] Douglas E Smith and Steven Chu. Response of flexible polymers to a sudden elongational flow. *Science*, 281(5381):1335–1340, 1998.

[131] O Kratky and G Porod. Röntgenuntersuchung gelöster fadenmoleküle. *Recueil des Travaux Chimiques des Pays-Bas*, 68(12):1106–1122, 1949.

[132] David P Landau. *A guide to Monte Carlo simulations in statistical physics*. Cambridge University Press, Cambridge ; New York, 2000.

[133] Nathan Clisby and Burkhard Dünweg. High-precision estimate of the hydrodynamic radius for self-avoiding walks. *Physical Review E*, 94(5):052102, 2016.

[134] Takashi Norisuye, Akihiko Tsuboi, and Akio Teramoto. Remarks on excluded-volume effects in semiflexible polymer solutions. *Polymer journal*, 28(4):357–361, 1996.

[135] Hirochika Murakami, Takashi Norisuye, and Hiroshi Fujita. Dimensional and hydrodynamic properties of poly (hexyl isocyanate) in hexane. *Macromolecules*, 13(2):345–352, 1980.

[136] Akihiko Tsuboi, Mikiya Yamasaki, Takashi Norisuye, and Akio Teramoto. Dilute-solution behavior of cellulose tris (3, 5-dimethylphenylcarbamate). *Polymer journal*, 27(12):1219–1229, 1995.

[137] Kanako Hayashi, Kikuko Tsutsumi, Fumio Nakajima, Takashi Norisuye, and Akio Teramoto. Chain-stiffness and excluded-volume effects in solutions of sodium hyaluronate at high ionic strength. *Macromolecules*, 28(11):3824–3830, 1995.

[138] Takayuki Hirao, Akio Teramoto, Takahiro Sato, Takashi Norisuye, Toshio Masuda, and Toshinobu Higashimura. Stiff-chain nature of poly (1-phenyl-1-propyne) in dilute solution. *Polymer journal*, 23(8):925–932, 1991.

[139] Hans Christian Öttinger. Generalized Zimm model for dilute polymer solutions under theta conditions. *Journal of Chemical Physics*, 86(6):3731–3749, 1987.

[140] P Sunthar and J Ravi Prakash. Dynamic scaling in dilute polymer solutions: The importance of dynamic correlations. *EPL (Europhysics Letters)*, 75:77–83, 2006.

[141] Caroline Beryl Montgomery. *The self-assembly of diphenylalanine fibres.* PhD thesis, University of Warwick, nov 2015.

[142] Timothy R Dafforn, Jacindra Rajendra, David J Halsall, Louise C Serpell, and Alison Rodger. Protein Fiber Linear Dichroism for Structure Determination and Kinetics in a Low-Volume, Low-Wavelength Couette Flow Cell. *Biophysical Journal*, 86(1):404–410, 2004.

[143] Rachel Marrington, Timothy R Dafforn, David J Halsall, and Alison Rodger. Micro-volume couette flow sample orientation for absorbance and fluorescence linear dichroism. *Biophysical journal*, 87(3):2002–2012, sep 2004.

[144] W Kuhn and F Grun. Relationships between elastic constants and stretching double refraction of highly elastic substances. *Kolloid Z.*, 101:248, 1942.

[145] Bengt Nordén, Alison Rodger, and Tim Dafforn. *Linear dichroism and circular dichroism: a textbook on polarized-light spectroscopy.* Royal Society of Chemistry, 2019.

[146] Yukio Matsuoka and Bengt Nordén. Linear dichroism studies of nucleic acids. iii. reduced dichoism curves of dna in ethanol–water and in poly (vinyl alcohol) films. *Biopolymers: Original Research on Biomolecules*, 22(7):1731–1746, 1983.

[147] Paul J Flory and M Volkenstein. Statistical mechanics of chain molecules, 1969.

[148] Kazuo Nagai. Photoelastic property of cross-linked amorphous polyethylene. *The Journal of Chemical Physics*, 40(10):2818–2826, 1964.

[149] Claire E Broughton, Hugo A Van Den Berg, Alan M Wemyss, David I Roper, and Alison Rodger. Beyond the discovery void: new targets for antibacterial compounds. *Science progress*, 99(2):153–182, 2016.

[150] B Hamprecht and H Kleinert. End-to-end distribution function of stiff polymers for all persistence lengths. *Physical Review E*, 71(3):031803, 2005.

[151] Hiroshi Watanabe. Dielectric relaxation of type-a polymers in melts and solutions. *Macromolecular Rapid Communications*, 22(3):127–175, 2001.

[152] Walter H Stockmayer. Dielectric dispersion in solutions of flexible polymers. *Pure and Applied Chemistry*, 15(3-4):539–554, 1967.

[153] P Pincus. Excluded volume effects and stretched polymer chains. *Macromolecules*, 9(3): 386–388, 1976.

[154] S Pan, D Ahirwal, D A Nguyen, P Sunthar, T Sridhar, and J R Prakash. Viscosity radius in dilute polymer solutions: Universal behaviour from DNA rheology and Brownian dynamics simulations. *Macromolecules*, 47(21):7548–7560, 2014.

[155] W Chamath Soysa, B Dünweg, and J Ravi Prakash. Size, shape, and diffusivity of a single Debye-Hückel polyelectrolyte chain in solution. *The Journal of Chemical Physics*, 143(6):64906, 2015.

[156] William T Vetterling and William H Press. *Numerical recipes in Fortran: the art of scientific computing*, volume 1. Cambridge University Press, 1992.

[157] William H Press, Saul A Teukolsky, William T Vetterling, and Brian P Flannery. *Numerical recipes 3rd edition: The art of scientific computing*. Cambridge university press, 2007.

[158] M Fixman. Inclusion of hydrodynamic interaction in polymer dynamical simulations. *Macromolecules*, 14(6):1710–1717, 1981.